MODELLING OF ECC AND SMA-REINFORCED CONCRETE MEMBERS

AUSTIN MARTINS-ROBALINO

A THESIS SUBMITTED TO

THE FACULTY OF GRADUATE STUDIES

IN PARTIAL FULFILLMENT OF THE REQUIREMENTS

FOR THE DEGREE OF

MASTER OF APPLIED SCIENCE

GRADUATE PROGRAM IN CIVIL ENGINEERING

YORK UNIVERSITY

TORONTO, ONTARIO

APRIL 2023

Abstract

Changes in codes which emphasize performance-based design have increased interest in the use of novel high-performance materials such as Shape Memory Alloys (SMAs) and Engineered Cementitious Composites (ECC). This work looks to model the response of ECC at both small-and large-scale sizes based on experimental data of ECC flexural prisms and shear walls reinforced with ECC. Modelling was conducted using VecTor2, a FEA modelling program widely applied in literature and industry. The applicability of built-in models for fibre-reinforced concrete (FRC), a concrete classification that includes ECC, was examined at a small scale. Lessons learned were applied in large scale modelling of hybrid SMA-steel slender shear walls in original condition and repaired with ECC. Results of small- and large-scale modelling demonstrated the need for further refinement of FRC models to better reflect ECC and allowed for a modelling methodology that provided more accurate load and ductility predictions in examined shear walls.

Acknowledgements

I would like to express my deepest appreciation and thanks to my supervisor Professor Dan Palermo for consistently guiding me over the last two and a half years during an unprecedent pandemic. Through all the safety measures, pandemic restrictions, online meetings, and every headache in between he remained committed to providing mentorship and support. Without his wealth of knowledge and experience in both experimental and numerical matters, trouble shooting certain challenges would have been orders of magnitude more difficult.

I would also like to thank Dr. Stavroula Pantazopoulou and Dr. John Gales for always indulging my curiosity in matters and projects outside of my own and providing another viewpoint when I ran into unforeseen issues. Gaining insight into their own fields of expertise often pushed me to want to strive for my own excellence and reminded me of the importance of fostering a collaborative environment.

I had the privilege of taking one of Dr. Anca Ferche's graduate courses on the use of VecTor2. Her assistance during and after the course helped immensely in my journey with VecTor2.

A significant portion of my time as a graduate student was spent in the High Bay Lab with my colleagues in Dr. Palermo's research group, Adrien Sparling and Alessandro (Alex) Paglia. Adrien spent countless hours imparting knowledge on nearly every piece of equipment and testing apparatus in the lab. Alex provided brutal honesty and sharp wit in equal parts so I am glad to have poured blood, sweat, and tears into our time and work together, I likely would have gone insane without a lab partner like him especially around Allen keys. I must also mention Mena Morcos and Michael Soto who even after finishing their work took time to answer questions I had into their experiments and data.

Acknowledgements would not be complete without paying my thanks to my family who have supported me well before my graduate studies, especially my mother Barbara Martins and my grandmother, Maria Armanda Martins. I will never be able to quantify all the ways you have and continue to support me but everyday I strive to live a life that honours all you have done. Thank you for always being there through all my success and especially all my failures, for reminding me to always remember my roots, but also making sure to let me know I am free to follow my passions wherever they may lead.

Table of Contents

List of Tables

List of Figures

1 Introduction

1.1 Background

The work presented in this thesis looks to improve the understanding of how to incorporate two novel and emerging materials, Shape Memory Alloys (SMAs) and Engineered Cementitious Composites (ECCs), within numerical models. This would allow these materials to be effectively and economically utilized and improve the resilience of structures to seismic events. Seismic events can be some of the most sudden and costly natural disasters that infrastructure can be subjected to during service life. This cost is not solely monetary as failure of structures can cause the loss of human life as well as reduce the quality of life of surrounding communities should the structure be used for day-to-day services.

Within Canada one of the most utilized seismic force resisting systems are shear walls. Shear walls can be placed into one of two categories, slender or squat, based on a ratio of their height and length. Slender shear walls have a height greater than twice the length and are typically found in medium and high-rise structures most commonly being traditional steel reinforced concrete (RC). Since mid- and high-rise structures consist of either commercial or housing uses that prioritize open floor plans which can be subdivided based on planned tenants, slender shear walls are often incorporated into the building layout as elevator shafts or stairwell walls. Squat shear walls have a height that is less than twice their length and can be found in low-rise structures. Due to the compartmentalized nature of these structures, squat shear walls can often be incorporated as separating walls between units, exterior walls, and stairwell/elevator shafts.

When considering shear wall construction under a performance-based design one of the approaches could consist of increasing the amount of reinforcing and concrete used to ensure that the response under seismic event stays within the elastic range of the materials. Though this may ensure that residual displacements and drifts are left to a minimum there would be a significant increase in the cost that make it financially unsustainable. A more complex and appealing approach to improving performance-based design of slender shear walls involves integrating novel materials which can improve the durability and recentering ability of the walls. Within slender shear walls the predominate modes are rupture of steel in flexure, crushing of concrete in wall toes leading to localized bucking, and sliding failure. Beyond these failure modes RC shear walls can be considered to have failed due to large permanent drifts resulting from degradation of concrete

material, which helps provide a confining pressure on reinforcing bars, and steel accumulating permanent strain and deformation. These failure methods demonstrate two areas of concern that can be improved using novel materials demonstrating improved mechanical properties. Shape Memory Alloys (SMAs) due to their superelastic properties could replace steel reinforcement within boundary regions, where reinforcement is subjected to the greatest stresses, addressing the rupture or permanent deformation of steel reinforcement. Engineered Cementitious Composites compliment the superealasticity of SMAs due to their own ductility which is significantly higher than that of normal concrete (NC) as a result of their fibres. These same fibres and the material's microstructure allow for greater resistance against spalling and crushing which often degreed NC during seismic events.

1.1.1 Shape Memory Alloys

Shape memory alloys (SMA) are a group of smart materials which can demonstrate two important behaviours, a shape memory effect (SME) and superelasticity(SE). First discovered in 1932, as a gold-cadmium alloy it was not until 1962 that the most common and researched SMA, Nitinol, a nickel titanium (Niti) alloy created at the Naval Ordnance Laboratory (nol) was created by Buechler and co-researchers (Song et al., 2006). Since then, other SMA alternatives such as copper (Cu) and iron (Fe) based SMAs have been developed and tested. The reason for both the SME and SE behaviours of SMAs is due to the alloys having two distinct phases, a weaker Martensite and stronger Austenite phase which are stable at lower and higher temperatures respectively. In SME the alloy is initially in its weaker Martensite phase which is easy to deform due to the crystal structure of the phase. However, should enough heat be applied to the SMA it will transitions to it Austinite phase at which point the crystal orientation rights itself to its original shape which is kept once it is cooled and returns to the Martensite phase. The SE behaviour is observed when an SMA is kept at a temperature above its Austinite phase. When a stress is induced in the material it will cause the crystal structure to change to its weaker Martensite phase to accommodate the greatest displacement possible. However, once the applied stress is removed the martensite phase will transform back into the stronger more stable Austinite phase resulting in the stress strain response shown below in Figure 1.1(Song et al., 2006). In the case of Nitinol this superelastic effect can result in a recoverable strain of between 5-10% compared to the 0.2% of traditional steel reinforcement (Abdulridha et al., 2011). This superelasticity and shape memory effect combined with corrosion resistance makes Nitinol an attractive material for uses in structures in seismic areas

with work done by Zareie et al. (2020) demonstrating there is still ongoing and increasing interest and research regarding the use of SMAs in buildings and bridges.

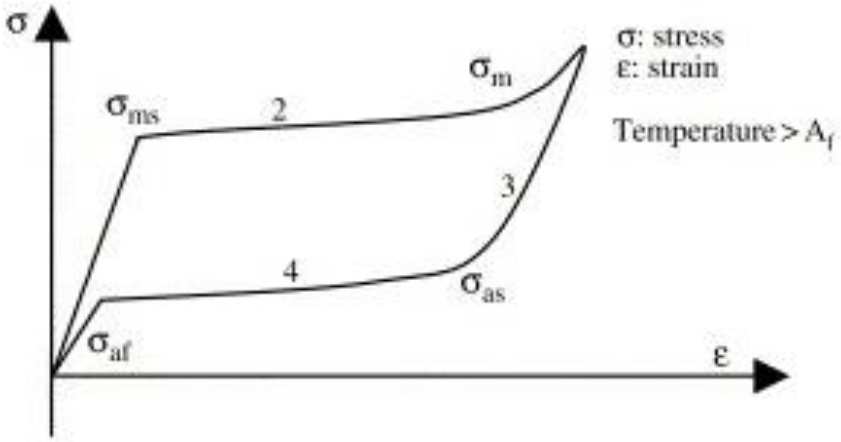

Figure 1.1 Stress-strain response of a SE-SMA at constant temperature (Song et al., 2006).

1.1.2 Engineered Cementitious Composites

Engineered Cementitious Composites (ECC) are a classification of fibre reinforced concrete (FRC) which differs from normal concrete (NC) due to modification of the constituent materials. NC typically consists of five constituents: water, large aggregate (gravel), small aggregate (sand), cement, and air. ECC on the other hand removes all large aggregate and includes short plastic fibres typically made from polyethylene (PE) or polyvinyl alcohol (PVA) with the later being the more common of the two. Additionally, ECC commonly includes fly ash, a waste by product of coal energy production, that is a pozzolan known to reduce the temperature of hydration, increase setting time, and provide increased flowability due to the spherical shape of induvial grains. ECC mixes can also make use of other pozzolans such as slag and silica fume. The fact that these pozzolans are all waste by-produce provide ECC with the additional benefit of having less embodied carbon dioxide in their production. A final addition to most ECC mixes is use of a super plasticizer to ensure self consolidating behaviour in the presence of lower water to cementitious ratios.

Naaman (2018) provides a through review of the development and evolution of FRCs over their 50 year history since the first modern scientific study in 1963 while providing insight on how different FRCs can be classified. The first FRCs allowed the material to undergo a gradual strain-softening under tensile loading, as show in Figure 1.2, compared the sudden failure exhibited by

NC. More advanced FRCs which demonstrate a strain-hardening behaviour prior to strain softening characterized by the formation of multiple cracks before localization and failure are often termed HPFRC for high performance FRC. A properly designed ECC can be categorized as a HPFRC and is capable of this strain-hardening characteristic by ensuring that the bond strength between fibres and the mortar matrix is less than the tensile strength of the fibres themselves. This condition allows for fibres to undergo pullout from the surrounding matrix instead of fracture allowing for development of multiple micro-cracks.

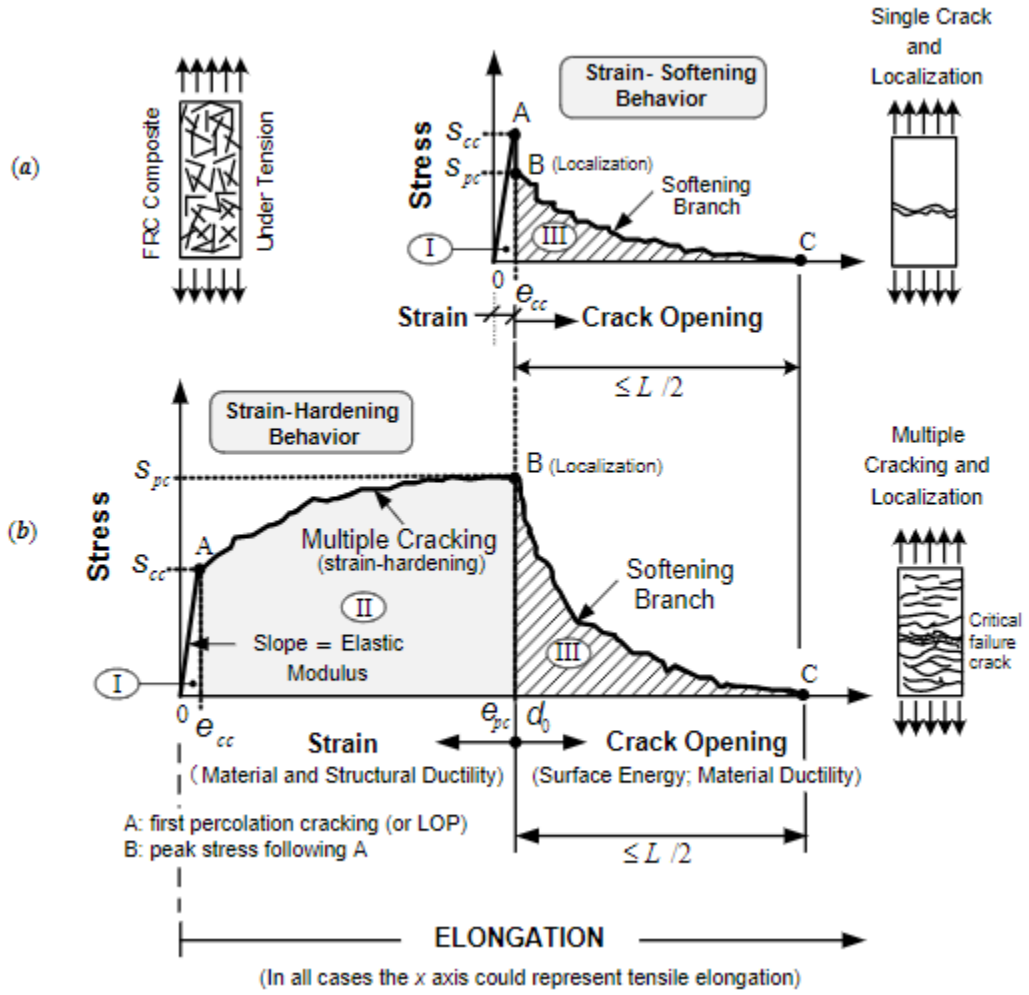

Figure 1.2 Typical stress-strain or stress-elongation curve in tension up to complete separation. (a)Conventional strain softening FRC composite. (b) Strain-hardening FRC composite (also often termed HPFRC composite) (Naaman, 2018).

1.1.3 VecTor2

VecTor2 is a nonlinear finite element analysis (NLFELA) program that has been tailored for reinforced concrete. Developed at the University of Toronto in 1990 to allow for modelling of concrete elements subjected to shear and plane stress, the basis of the program was initially the Modified Compression Field Theory (MCFT) (Vecchio & Collins, 1986). The MCFT modelled the occurrence of cracks as smeared within concrete elements and able to freely rotate co-axially with the principal direction of the compressive field within concrete elements with the analysis carried out based on an incremental total load and iterative secant stiffness approach. Building on the to the MCFT a new model, the Disturbed Stress Field Model (DSFM) (Vecchio, 2000), was implemented in VecTor2 which allowed for calculation of crack-slip in concrete elements and improved the orientation of stress and strain fields that were found to lag each other in certain instances. In addition to the MCFT and DSFM, VecTor2 has constantly been revised and updated, now having an extensive library of constitutive models for secondary phenomena ranging from dilation to dowel action and hysteretic responses. Many constitutive models have options which take into considerations the effects of FRC particularly in the inclusion of an FRC tension response.

1.2 Scope and Research Objectives

The primary objective of the research is to be able to accurately model the incorporation of ECC in reinforced concrete (RC) and SMA-steel hybrid shear walls. This will be achieved by investigating the ability of custom and built-in models available in the VecTor2 to accurately predict the behaviour of ECC at a small scale. In parallel a modelling approach will be developed to predict the response of RC and SMA-steel hybrid shear walls more accurately. Results from the small scale testing will then be incorporated into modelling an ECC repair of RC and SMA-steel hybrid shear walls. The following are more specific objectives undertaken to achieve this work:

1.2.1 Small Scale Modelling of ECC

- Testing of ECC cylinders and flexural prisms to determine compressive and flexural properties of ECC. The specific ECC tested has been reported on previously by Soto (2020). The objective of this testing is to have accurate inputs for models within VecTor2 as well as provide experimental data that can be used to assess performance of models.
- Investigate built-in and user defined constitutive models that impact the response of unreinforced ECC at small scale within VecTor2. This work will also help identify to

shortcomings and possible avenues for improvement within built-in fibre reinforced concrete (FRC) models which were initially created to capture behaviour of steel-fibre reinforced concretes.

1.2.2 Large Scale Modelling of ECC

- Develop a modelling approach which can accurately predict the load and displacement response of RC and SMA-steel hybrid previously tested by Morcos (2021).
- Apply lessons learned from small scale testing to the modelling approach mentioned above in order to capture the repairs caried out by Soto-Rojas (2020) used of ECC.

1.3 Research Novelty

Literature on the performance of seismic resisting structures utilizing both SMAs and ECCs is quite limited with only four experimental projects of their kind available to the authors knowledge, including work by Soto-Rojas (2020). Additionally, investigations into the use of ECC in VecTor2 often lack a detailed methodology, typically only going so far as stating the values from tensile tests that were input in a user defined model. This approach of using a user defined model, although beneficial in terms of brevity and ability to provide acceptable responses, can make the modelling process difficult and unclear to those looking to use the software for modeling of ECC. Use of a user defined model also assumes that modellers have accurate experimental tension data, an assumption that may not be realistic if a structure is modelled years into its service life. In contrast built-in FRC models only require inputs about the plastic fibres which can easily be found online but the applicability and accuracy of these models when applied to ECC is not well document. The novelty in this research is providing a more detailed analysis of the current ability of VecTor2 and the various constitutive models within to accurately model ECC. Modelling of a SMA-steel hybrid structure repaired with ECC is also relatively novel with only Soto-Rojas & Palermo (2020) having done so to the authors knowledge. Part of the modelling approach consists of applying a percent reduction in cross sectional area to account for damage incurred during strain gauge instillation which to the authors knowledge is a new consideration for the walls examined.

1.4 Thesis Layout

The thesis is divided into seven chapters. Chapter 1 serves as an introduction of the material that will be covered in the thesis and provides readers with a background understanding of the materials

being modeled. Chapter 2 is a literature review presenting the state-of-the-art work that has previously been conducted into the incorporation of SMA in seismic force resisting elements and recent testing of ECC materials and attempts to model their compressive and tensile behaviour. Having presented the two materials individually, literature on the combined use of ECC and SMA in structural elements is provided. Chapter 3 documents the experimental testing of small scale ECC specimens undertaken to determine material properties inputs necessary for FEA modelling. This testing also provides load-displacement data which can be used to assess the performance of different constitutive models. Chapter 4 examines how to best model unreinforced ECC flexural prisms in VecTor2 to understand the capabilities of different constitutive models using results from Chapter 3 to quantify the accuracy. A comparative analysis of available compression and tension constitutive models for ECC materials was undertaken. The formulation of built-in FRC models and their implantation within VecTor2 was also discussed to provide context for the differences in the responses they provide. Chapter 5 is focused on the creation of a modelling approach which can be applied to RC and SMA-steel hybrid shear walls with and without ECC. The first set of walls and models does not consider ECC to allow for a baseline model before examining the incorporation of ECC in a second set of models. Experimental data was used to examine the validity modelling choices made. Chapter 6 documents attempt to recreate the ECC mix which had been the basis of Chapters 3-5. Multiple trials are undertaken with a discussion on what caused issues throughout all trials presented. Chapter 7 is the conclusion of the thesis summarizing the main findings as well as proposing future work that could be conducted based on the findings.

2 Literature Review

The following literature review is broken into three main sections: the first section aims to provide an overview of research conducted into seismic resilient structures with a focus on SE-SMA and particularly Nitinol. The second section focuses on the state-of-the-art work that has been conducted into the experimental testing and numerical modelling of ECC. The third section presents literature that has looked into the use of both ECC and SMA in the same shear walls.

2.1 Use of SE-SMA in Seismic Resilient Structures

The field of seismic resilience has great breadth in different approaches researched but for the sake of this thesis the literature of interest will consist of research into use of SMA as a reinforcing material within reinforced concrete (RC) structural members. Literature is grouped based on the type of structural member which is incorporating the SMA and is the focus of the publication; shear walls, the focus of this thesis, and other structural members consisting of columns, beams, and beam-column connections. Additionally, research into non-Nitinol SMA is presented separately since these Nitinol alternatives are relatively new in the time frame of SMAs.

2.1.1 Shear Walls

2.1.1.1 SMA Tension Brace for Retrofitting Concrete Shear Walls (W. L. Cortés-Puentes & Palermo, 2017)

This work was the first of two complementary papers by Cortes-Puentes and Palermo which investigated the use of a novel tension-only Nitinol SMA brace as a retrofit for pre-1970's squat shear wall. The pre-1970's squat shear wall which would be examined was dimensioned to be 6000 mm long by 6000 mm high by 300 mm and designed according to 1965 standards for a west coast structure. The full-sized hypothetical wall was then scaled to a third of the original size for practicality of experimental testing resulting in an experimental wall measuring 2000 mm by 2000 mm by 100 mm. The proportions for the braces, which consisted of either an SE-SMA or reinforcing steel link connected to hollow structural steel sections through the use of mechanical screw couplers, were determined using the capacity spectrum of the wall. Three sets of SMA braces, which utilized a SMA link approximately 1/12 the total length of the brace, and two sets of steel braces were constructed and tested in uniaxial tension to understand their response for modelling in VecTor2. One of the main issues found during testing was that SMA braces would

fail prematurely at the location of the coupler due to the sharp end bolts necessary to connect the SMA link to the steel sections. This was remedied by reducing the cross sectional of the link at its midspan. An initial FEA carried out using VecTor2 found that both the steel and SMA brace increased lateral capacity and ductility when compared to the retrofitted wall, with SMA braces providing 50% displacement recover at ultimate load.

2.1.1.2 Seismic Retrofit of Concrete Shear Walls With SMA Tension Braces (W. L. Cortés-Puentes & Palermo, 2018)

To corroborate the numerical results from the previous paper, the authors designed and built four scaled-down shear squat walls, using two different reinforcement layouts such that two walls would fail due to sliding shear while the remaining two would be controlled by diagonal tension cracking. Each set of walls would contain one control wall and one retrofitted with the SMA braces tested in the previous paper. All walls were tested under reverse cyclic loading applied by an actuator 1600mm from the wall base with the loading stages using FEMA 461 guidelines. The loading frame is shown below in Figure 2.1. From the results, the SMA braces were shown to increase the lateral strength, ductility, and energy dissipation while decreasing residual drift, strength degradation, and stiffness degradation.

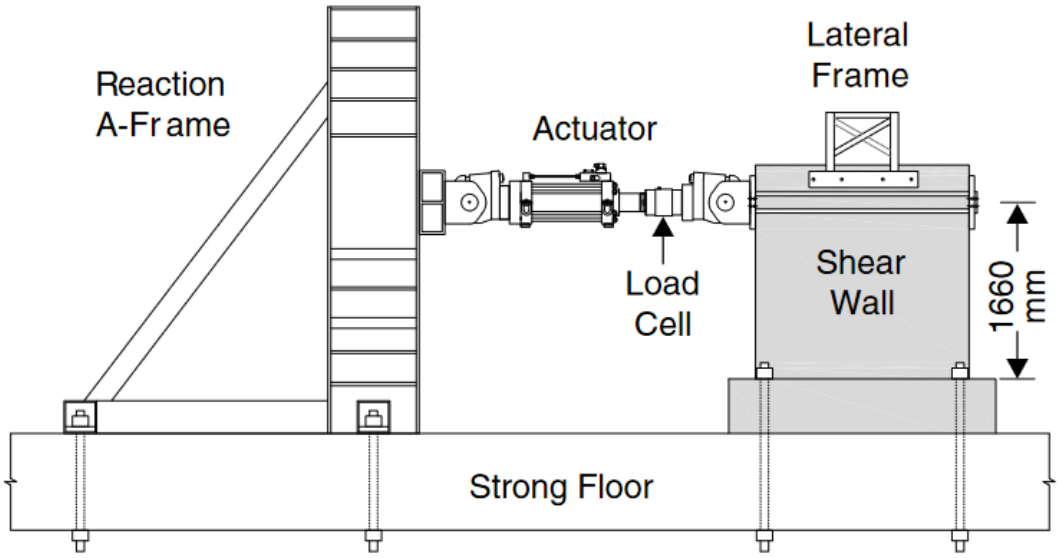

Figure 2.1 Experimental loading frame for shear squat walls (W. L. Cortés-Puentes & Palermo, 2018).

2.1.1.3 *Behaviour and Modelling of Hybrid SMA-Steel Reinforced Concrete Slender Shear Wall (Abdulridha & Palermo, 2017)*

Abdulridhaa and Palermo focused on the experimental testing and numerical modeling of a novel slender shear wall with hybrid NiTi SE-SMA-steel reinforcement in the critical section. The slender shear wall measured 2200 mm high by 1000 mm in length and 150 mm thick with a large base foundation and loading cap as shown in Figure 2.2.

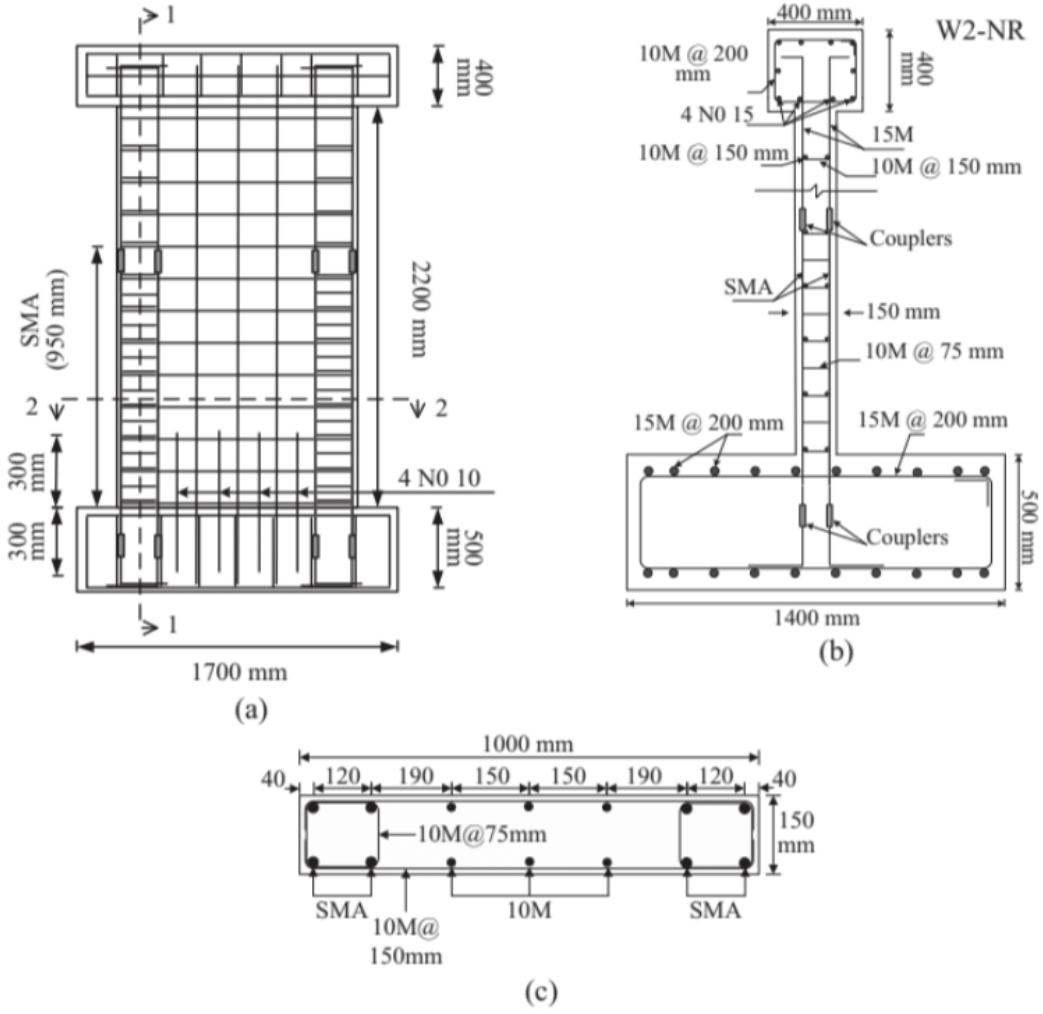

Figure 2.2 Reinforcement Details for the SMA-steel hybrid shear wall: (a) Elevation View; (b) Section 1-1; and (c) Section 2-2 (Abdulridha & Palermo, 2017).

A control slender shear wall using traditional deformed reinforcing steel was designed to meet the CSA A23 Design of Concrete code from the time of testing. The companion slender shear wall, an SMA-steel hybrid, was designed and constructed following the same procedure as the

control since there were, and still to the date at the time of writing, no provisions for SMA. SE-SMA bars replaced tradition reinforcement in the plastic hinge region of the boundary elements and were chosen to have a similar tensile force resistance as the longitudinal reinforcement they replaced. These SE-SMA bars measured 1200 mm long and extended from 250 mm below the base of the wall until the were coupled 950 mm above the base using mechanical couplers similar to those used by Cortés-Puentes & Palermo (2017, 2018). These couplers initially caused slipping issues which were fixed by using an arrangement of 18 screws, shown in Figure 2.3, instead of the standard 6 screws. Both walls were tested in reverse cyclic load by applying a transfer load via a displacement-controlled actuator with no axial load. The loading program followed ATC-24. Experimental results were also compared to analytical results from FEAs developed in VecTor2. The testing showed that although the steel wall provided greater strength and ductility, the SMA wall did provide better re-centering capabilities. It should be noted that a reason for the larger ductility of the steel wall was largely due to ductility being defined using methodology by Park (1989), where ductility is a ratio between the ultimate and yield displacement of a structure, and the SMA wall having a significantly larger yield displacement. The numerical studies showed good alignment with the steel wall but required changing of bound to better capture the reverse cyclic behaviour of the SMA wall, demonstrating the need for proper understanding of bond.

Figure 2.3:Mechanical screw coupler after modifications to solve premature failure and slipping (Abdulridha & Palermo, 2017).

2.1.1.4 Cyclic Loading Testing of Repaired SMA and Steel Reinforced Concrete Shear Walls (L. Cortés-Puentes et al., 2018)

The tested walls from Abdulridha & Palermo (2017) were taken and repaired by the authors to investigate the feasibility of repairing SMA walls. Repair of ruptured reinforcement consisted of removing damaged sections which were replaced with new sections through the use of screw lock

mechanical couplers. In the steel wall, RW1-SR, all longitudinal steel reinforcement needed to be replaced by sections measuring 600 mm in the boundary regions and 500 mm in the web. In the SMA wall, RW2-NR, it was necessary to replace both SMA and steel longitudinal reinforcement. Replacement of steel longitudinal reinforcement in the web consisted of a 540 mm section while instead of being replaced with new sections, SMA bars were shortened to a height of 450 mm above the base of the wall from their original length of 900 mm. This method of reducing the length of the SMA instead of replacing it was more economical and allowed for insight into the reusability of SMA. In both walls the damaged starter bars were removed completely without any replacement and concrete replacement consisted of using a self consolidating concrete (SCC). The repaired reinforcement layouts can be seen Figure 2.4.

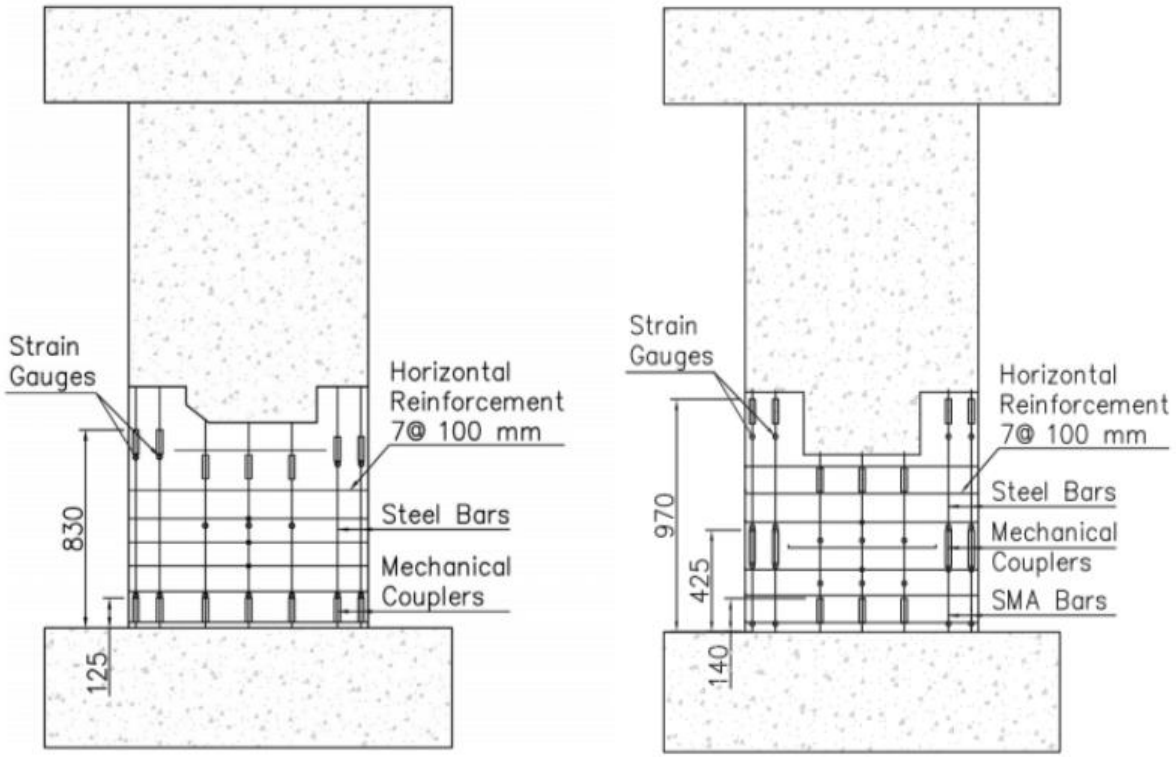

a) b)

Figure 2.4 Repaired reinforcement layouts for a) RW1-SR and b) RW2-NR (L. Cortés-Puentes et al., 2018).

Prior to testing of the repaired walls, the removed portions of SMA bars were tested under reverse cycle loading to re-examine the material properties after having undergone testing in a structure. It was found that there was sufficient strength and super-elasticity retention although the

stress at both upper and lower plateaus had been reduced slightly which could impact the cyclic behaviour. Repaired walls were tested using the same loading protocol as their original construction counterparts. It was found that the cracking in the SMA wall was localized at the elevation corresponding to where the coupler and SMA bars meet while the steel wall demonstrated more distributed cracking through the plastic hinge. Repaired walls showed similar strengths and stiffnesses with the yield stiffness of the repaired SMA wall being slightly increased due to the shortened length of SMA and higher compressive strength of SCC leading to increased stiffness in the plastic hinge. Drift capacity was found to be reduced in both cases due to rupture of reinforcement in the proximity to couplers. The reduction of the SMA bars was found to not have significant impact on the recentering capabilities of the wall with a residual strain recover of 80% at 2% drift. Additionally, the SMA wall maintained a symmetrical response indicative of proper recentering as opposed to the ratcheting seen in steel walls.

2.1.1.5 SMA-Reinforced Concrete Shear Walls Subjected to Reverse Cyclic Loading (Morcos & Palermo, 2019)

Morcos and Palermo provide the results of an experimental study of a control RC slender shear wall and a RC shear wall utilizing NiTi SE-SMA bars in the boundary plastic hinge regions. Both walls were dimensioned following the work by Abdulridha & Palermo (2017) . A notable difference was that SMA bars were fabricated to have a headed end to allow for coupling using a specialized headed mechanical coupler shown below in Figure 2.5 instead of the mechanical screw couplers used in other research discussed. This specialized coupler avoided premature failure or slip common with the screw couplers. Additionally, unlike Abdulridhaa's walls, both walls tested by Morcos lacked stater bars along the base of the wall and decreased the width of the foundation and cap beam from 1700 mm to 1600 mm. The wall dimensions and reinforcement layout of the walls is presented in Figure 2.6. There is complimentary work that consisted of initial modelling done in VecTor2 which provided predicted yield values for both walls needed when determining the target displacements for loading cycles (Morcos & Palermo, 2018).

Figure 2.5: Headed mechanical coupler used with headed bars fabricated by supplier (Morcos & Palermo, 2018).

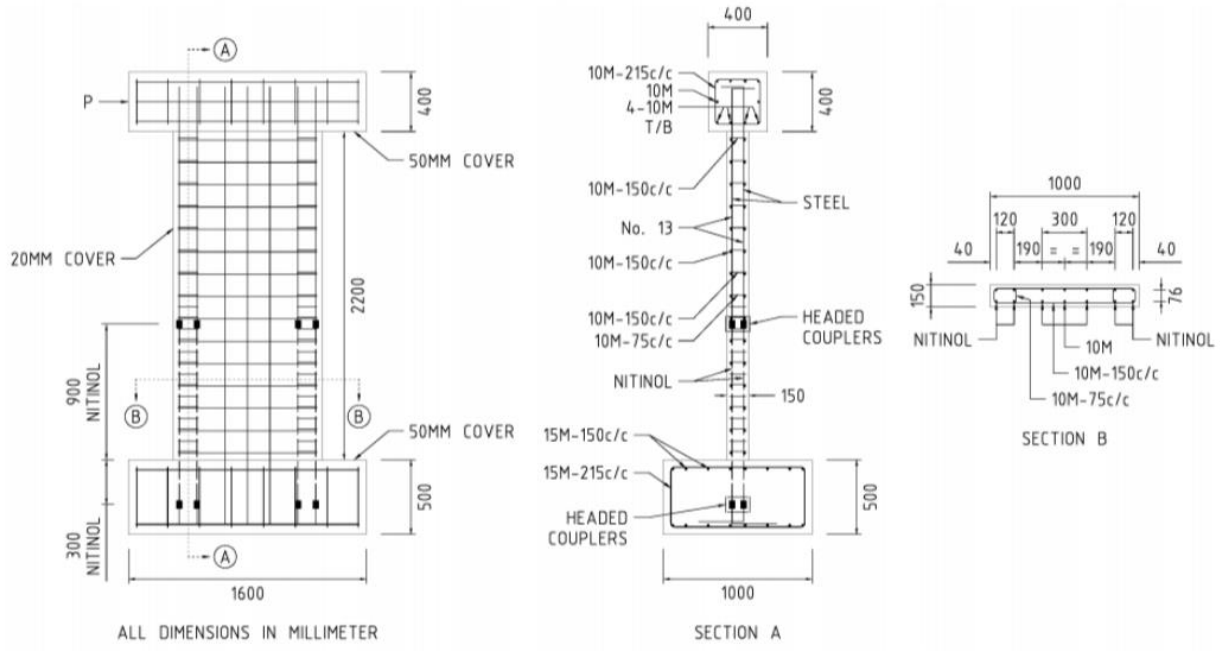

Figure 2.6 Wall dimensions and reinforcement layout of SMA shear wall (Morcos & Palermo, 2018).

Testing involved applying reverse cyclic load by a displacement-controlled actuator through the cap beam. The loading cycles were based on a combination of FEMA 461 and ATC 24 guidelines using drift ratios starting at 0.05% increasing to 0.1% and then incrementing by 0.1% until a drift of 0.5% was achieved. After this point loading increased by 0.5% until testing was terminated after a cycle at 5% drift ratio was achieved. The experimental results showed the RC wall experienced extensive cracking and crushing of concrete at the toes of the wall while the SMA wall had two predominant horizontal cracks at the base and 300 mmm above the base. Despite these cracks SMA displayed superior self centering at 2.5% drift by recovering 66% of the drift experience compared to 26% drift recovery of the control wall. Additionally, when unloaded from

a 2.5% drift the SMA wall, excluding the two predominate crack, had crack widths of 0.08 mm compared to steel wall which saw crack widths of 3 mm.

2.1.1.6 Seismic Performance Analysis of High-Rise RC Shear Walls Reinforced with Superelastic Shape Memory Alloys (Maciel et al., 2019)

Maciel and Palermo presented an FEA model in VecTor2 of a 10 storey-high rise shear wall originally designed as a traditional ductile RC slender shear wall and then modified to utilize NiTi SE-SMA in the boundary regions of the plastic hinge. Both walls were designed based on the current CSA code of the time and assuming the site of the building was in Vancouver. For comparison's sake, the same reinforcement detailing found in the plastic hinge region of the control steel reinforced wall was used beyond the plastic hinge in both models despite the code allowing for a reduction in reinforcement. Both walls had an applied axial load ratio of 0.69% ($P/A_g f'_c$) in order to account for gravity loading due to self-weight of the tributary areas supported by the wall. A lateral reverse cyclic displacement was applied at the top of the wall and was incremented by multiples of the yield displacement. The models revealed that both walls could meet code specifications of a lateral top drift ratio of 2.5% without a significant reduction in load. However, whereas larger drift ratios saw the residual drift of the RC wall increase up to 3% the SMA wall only experienced residual drifts below 0.25%. Additionally, the SMA wall maintained a recovery of 97% while the RC wall only recovered 34.5%. This suggests that the SMA wall can provide similar strength resistance as an RC wall while also providing better recentering and damage reduction characteristics.

2.1.1.7 Seismic Performance of Concrete Core Walls Reinforced with Shape Memory Alloy Bars (Abraik et al., 2020)

Abraik et al. numerically modeled a U-shaped core shear wall found in a hypothetical Vancouver building that utilizes SE-SMA in order to reduce seismic damage. The authors used a wide column model and OpenSees to model a previously experimentally tested U-shape RC core in order to corroborate the analytical results. Having successfully corroborated their model with the experimental results the authors then designed a hypothetical wall for a 9-storey building with a storey height of 3.4 m. The wall had a thickness of 400 mm with flanges and the web measuring 3000 mm and 6600 mm long respectively. An axial load corresponding to 6.6% of the core's capacity was assumed to be acting and a torsional eccentricity of 10% was also assumed when

detailing the reinforcement. The plastic hinge length for SMA bars was determined using an equation developed for the core wall used for validation. After calculating the structural period for both the RC and SMA core walls assuming either a 5%, 10%, and 20% torsional eccentricity the authors selected 6 appropriate ground motion histories. The final non-linear seismic analysis was carried out by taking the motions to be acting uniaxially in either the E-W or N-S directions or biaxially by acting in both the E-W and N-S directions at once. It was found that SMA core walls experience lower floor accelerations which would result in less damage to non-structural elements. Although the lateral envelope for all eccentricities did not differ between steel and SMA core walls, SMA walls demonstrated on average a 36% reduced residual drift with this reduction being less significant at higher eccentricities. The SMA core wall showed a wide range of reductions in wall rotation ranging between 6-58%.

2.1.1.8 Shape-Memory Niti Alloy Rebars in Flexural-Controlled Large-Scale Reinforced Concrete Walls: Experimental Investigation on Self-Centring and Damage Limitation (Almeida et al., 2020)

Walls similar to those by Morcos and Abdulridhaa were investigated by the authors under axial and reverse-cyclic lateral load. Two walls measuring 2000 mm high by 1200 mm long and 200 mm thick (compared to 2200 mm x 1000 mm x 150 mm of walls by Morcos and Abdulridhaa) were constructed with one serving as a traditional RC shear wall and the second utilizing NiTi SE-SMA bars measuring 500 mm long (compared to 1200 mm of Morcos and Abdulridhaa) in the boundary elements of the plastic hinge regions. The SMA sections were attached to the steel reinforcement using screw couplers similar to other described in this report, however instead of adding more lines of screws as was done by others to prevent slippage (Abdulridha & Palermo, 2017; W. L. Cortés-Puentes & Palermo, 2017, 2018) the authors used a combination of epoxy injection into the coupler and welding the SMA bar to the coupler itself. A total axial force of 350 kN was applied corresponding to 7.3% of the axial capacity while a transverse reverse-cyclic displacement control load was applied through the cap beam based on increments of drift ratio, described in two thesis written by authors in French (Herrezeel & Rigot, 2019; Wyckmans & Steinmetz, 2019), although a figure of the overall cycle history is provided in Figure 2.7. The authors also discuss numerical models used to predict the behaviour of the walls prior to testing but found that ductility and failure of the numerical analysis did not align well with the experimental RC wall due to cone failure in the wall foundation resulting in a premature inelastic

failure during testing. The SMA wall demonstrated a 75% recover of lateral displacement up to failure keeping residual drift below 0.5%. The authors also investigated the vertical elongation of the wall and saw that the SMA wall provided reductions of 50%.

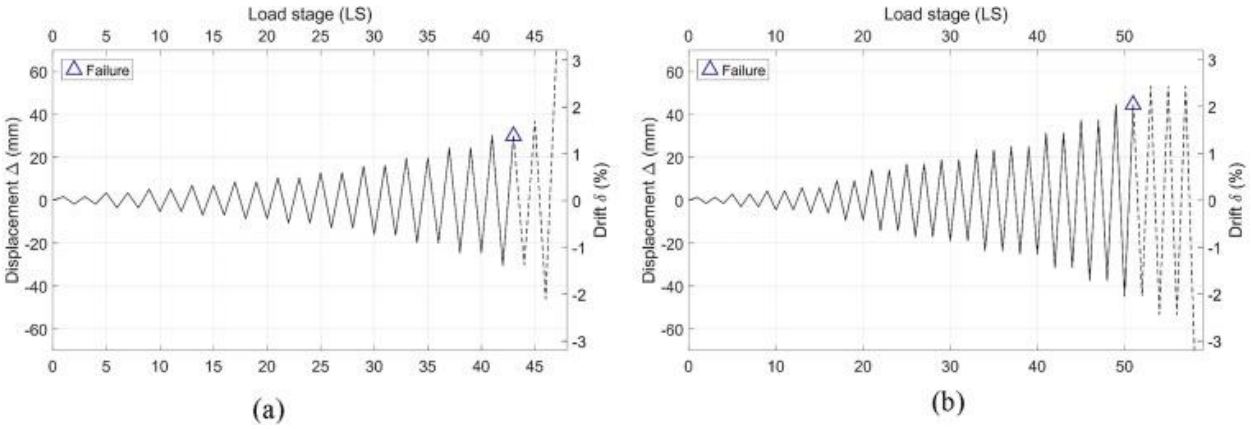

Figure 2.7 Loading protocol applied to the (a) RC wall, and (b) hybrid SMA-steel wall (Almeida et al., 2020).

This work was further expanded on in two complimentary papers examining the effect SMA had on strain development and plastic hinge of the slender shear walls (R. Hoult & de Almeida, 2022) and residual displacement (R. D. Hoult & de Almeida, 2022). It was shown that strain in the SMA-steel hybrid wall was concentrated along the base of the wall where a predominate crack had formed while the conventional wall had more traditional strain development along the height of the wall. Authors also examined the plastic hinge length and found that the hybrid wall exhibited an equivalent plastic hinge length that was near constant throughout the loading program and equal in the length of the SMA bar. Wanting to investigate the impact of SMA's on the residual displacements, which are often used as the limit for structural stability after seismic event, VecTor 2 was used to allow for investigation of wall properties beyond what was available experimentally. The parametric study using VecTor2 consisted of 42 modelled walls varying the parameters of height, wall length, axial load ratio, and longitudinal refinement ratio in the web and boundary regions. Similar to experimental testing it was found that curvature in the wall was concentrated along the wall base and that the plastic hinge could be taken as the length of the bars themselves as long as it is limited to half the wall length. Additionally, for the most part, the walls modelled consistently achieved drift levels of at least 2.5% before failing with the residual drift on average remaining below the permissible limit of 0.005 rad up to the 2% drift cycles.

2.1.2 Beams, Columns, and Beam Column Joints

2.1.2.1 Seismic Performance of Concrete Columns Reinforced with Hybrid Shape Memory Alloy (SMA) and Fiber Reinforced Polymer (FRP) Bars (Muntasir Billah & Shahria Alam, 2012)

The authors examine the impact of using SE-SMA and FRCP bars in the plastic region of a RC column through a numerical analysis software. The 450 mm by 450 mm square column measured 2732 mm high and was calculated to have a plastic hinge region measuring 468mm. Four columns were considered; a control consisting of all traditional steel reinforcement, one using SMA in the hinge and traditional steel in the remain section, a third with SMA in the plastic hinge and FRP bars in the remain portion, and finally a column with FRP in the plastic hinge and traditional steel in the remaining portion. A mechanical coupler similar to those used by (Abdulridha & Palermo, 2017), and Cortés-Puentes & Palermo (2017, 2018) was used to couple the steel and SMA together while a mechanical-adhesive coupler was used to couple any bar to the FRP bars. All couplings were tested on their own to allow for adequate modeling in SeismoStruct. The models were validated using experimental data from a 3/4th scale beam column joint tested by Nehdi et al., 2010) where SMA was used and coupled to GFRP bars. After validating their models, the authors tested the four columns under historical seismic ground records. Use of SMA allowed for up to 87% reduction in residual drift while SMA in the plastic hinge and steel could dissipate significant amounts of energy (although SMA with steel did not provide as large hysteresis loops as SMA with FRP).

2.1.2.2 Experimental Investigation on the Seismic Behavior of Beam-Column Joints Reinforced with Superelastic Shape Memory Alloys (Youssef et al., 2008)

Noting how beam column joints are typically the weakest structural element in RC frame resisting moment structures which rely on yielding of steel reinforcement to dissipate energy (resulting in permanent deformation) the authors propose using SE-SMAs, specifically NiTi. The thought process being that the superelasticity would allow for joints to recover any incurred drift during seismic events reducing the extent of damage and need for replacement. To investigate this approach two beam column joints were constructed; one reinforced with only steel and a second which replaced steel in the plastic hinge with SE-SMA. The beam column joints were designed as a ¾ scale version of an interior joint located at the 6th storey in a hypothetical 8-storey Vancouver

structure. A mechanical screw coupler was used to join the SMA in the plastic region to the adjacent steel bars outside of the region. Although the coupler initially had three screws for each end inserted into it, modifications were made for 9 screws to be used on the SMA bars to ensure full yielding of the SMA without slip. Based on CSA design standards of the time and governing load cases, the beam column joint specimens were tested with an applied axial load of 350 kN to the column section. A reverse cyclic load was applied to tip of the beam in two stages. First a load control stage consisting of two cycles at 10% of the predicted yield, two cycles at cracking load, and two cycles at the yield load were carried out. After these cycles displacement control was used to increment cycles by multiples of the yield displacement with two repetitions of each cycle. The results demonstrated that the SMA column joint has significant reduction in residual displacement while also reducing strain in the transverse reinforcement when compared to steel, as well as moving the plastic hinge away from the face of the column (as was observed in the steel control beam column joint) to a distance of half the beam depth. Due to the reduced modulus of elasticity of SMA the overall stiffness of the joint was reduced and resulted in larger rotations of the beam and dissipated less energy at a given drift ratio when compared to the control, caused by pinching of hysteresis loops due to self-centering behaviour. The authors would go on to use this work to validate an analytical model that would later be used to model beam column joints in a hypothetical building (Alam et al., 2012).

2.1.2.3 Seismic Overstrength and Ductility of Concrete Buildings Reinforced with Superelastic Shape Memory Alloy Rebar (Alam et al., 2012)

Informed by the previous work of Youssef et al. (2008) the authors investigated the applicability of overstrength, R_o, and ductility factor, R_d, provided for RC structures in the NBCC to hypothetical NiTi SE-SMA and NiTi SE-SMA-steel hybrid structure. The authors went on to model three moment resisting frames structures varying in number of stories (3, 6, and 8 stories) that utilize the same general floor layout and are designed to withstand seismic conditions in Vancouver. Each structure was also varied in reinforcement used as either 1) all steel, 2) all SMA, or 3) steel with SMA used only in plastic hinge regions. All models were created and analyzed in SeismoStruct. The primary analysis consisted of monotonic pushover tests to determine R_o and ductility. A secondary dynamic loading analysis was conducted using 10 ground motions. It was found that R_o for an SMA frame is similar to that provided by the code for a steel RC structure, with the maximum difference being 8%. However, the ductility of the walls varies more

significantly with the SMA structure providing at least 15% less ductility compared to the steel structure with the SMA-steel hybrid structure showing between 8% and 18%. Based on the dynamic loading it was found that the SMA structure provided greater base shear and drift capacity demand rotation up to 6 stories at which point they are effectively the same. The SMA-steel hybrid frame provides a capacity between that of the SMA frame and the steel frame. The steel frame is shown to provide reduced inter-storey and roof drift in an 8-storey building which is likely due to the lower stiffness of SMA resulting in larger displacements to reach yielding. Overall, the authors conclude that SMA-steel hybrid RC frames may outperform steel RC frames due to their larger capacity demand ratio while still being more economically feasible compared to a completely SMA RC frame.

2.1.2.4 Experimental Study on Concrete Beams Reinforced with Pseudoelastic Ni-Ti Continuous Rectangular Spiral Reinforcement Failing in Shear (Mas et al., 2016)

The authors present a novel continuous rectangular spiral reinforcement made from NiTi SE-SMA which is used in the shear critical section of a beam. The continuous rectangular spiral has been shown to be more financially and material efficient while allowing for easier fabrication of beams. U-bolt saddle clamps were used to connect the terminating leg of the spiral to the adjacent ordinary stirrup to ensure proper anchorage of the spiral reinforcement. The beams measured 80 mm wide by 200 mm high and measured 1260 mm between supports. The loading of the beam consisted of three-point bending under monotonic or cyclic loading, in intervals of 2 mm, with a shear span of 520 mm. Eight beams were cast and varied between having no shear reinforcement, traditional steel stirrups, NiTi spiral stirrups with a pitch of 130 mm, and NiTi spiral stirrups with a pitch of 65 mm. Experimental results showed an increased strength and ductility provided by the NiTi spiral with increased crack width at ultimate failure. By allowing the substantial load increase after development of the critical crack the authors surmise that other shear resisting mechanisms are enhanced, primarily dowel action, arch effect, and shear transferred by stirrups. Such behaviour could be utilized in seismic resisting joints to avoid sliding shear failure at the column joint interface.

2.1.2.5 Joint Performance in Concrete Beam-Column Connections Reinforced Using SMA Smart Material (Oudah & El-Hacha, 2017)

The authors of this paper wanted to examine joint performance and anchorage when NiTi SE-SMA bars are used in a beam column joint. The joint considered was based on the experimental beam column joint tested by Oudah (2014) in a PhD thesis, which will only be briefly covered due to its length. The original joint assembly was scaled down by 20% for use in this work with only the column being present and measuring 300 mm x 400 mm x 900 mm. The experimental setup involved a pull-out test of an anchored reinforcement bar which in a full beam-column joint would go into the beam. The SMA bars used were 610 mm long and anchored using a mechanical screw coupler like the work of Abdulridhaa and Palermo and Cortes-Puentes and Palermo, however it had a head at the end to assist with anchorage. Detailing of reinforcement as well as orientation of anchors are shown below in Figure 2.8. The specimens tested varied in the vertical reinforcement into the joint (NiTi SMA or steel), spacing of stirrups, and in the case of the SMA specimens the orientation of the coupling and the embedment depth. All specimens were tested using a cyclic loading program that pulled the vertical reinforcement upward. The experimental results had SMA specimens underperforming compared to steel specimens due to premature fracture or slipping in the coupler. The authors then investigated and tested four different modifications to the coupler settling on the solution of adding two more rows of screws into the coupler, similar to the approach employed by in Abdulridha & Palermo (2017) and Cortés-Puentes & Palermo, 2017, 2018). Having fixed the coupler issue the authors then employed an analytical method to determine the slip behaviour of the vertical reinforcement which they combined with a struct and tie model to predict the moment curvature response of all specimens tested. These analytical predictions were validated by the authors based on a comparison of experimental and analytical result for the steel specimens. Based on their predictions the authors suggest that the optimal detailing for SMA bars anchored using the modified coupler consist of having the bar placed at a depth of 84% of the column width and that the anchor head be facing the top fiber of the column. This detailing is believed to allow for a stiffer response post cracking and lower the curvature at ultimate displacement.

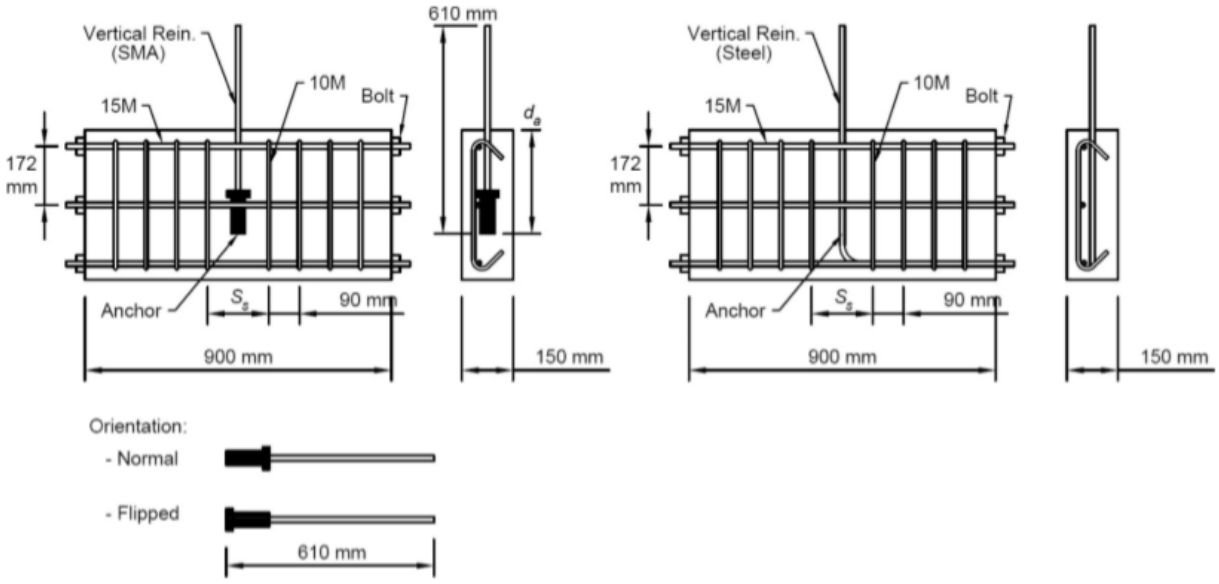

Figure 2.8: Column beam joints with reinforcement detailing and orientation of mechanical couplers used to anchor SMA bars (Oudah & El-Hacha, 2017).

2.1.2.6 Ductility of High-Performance Concrete and Very-High-Performance Concrete Elements with Ni-Ti Reinforcements (Pereiro-Barceló et al., 2018)

Pereiro-Barceló̱a et al. performed testing of semi-column connections in order to understand the behaviour of RC supports that uses either high performance concrete (HPC) or ultra-high-performance concrete (UHPC)[1] with NiTi SE-SMA in the critical section of the support. The experimental specimens were rectangular columns measuring 260 mm by 150 mm and were 3000 mm long with a span of 1500mm on each side of the stub which was included to simulate other structural elements connecting into a column. The detailing of the specimens can be found below in Figure 2.9, including placement of the NiTi bar which measured 750 mm long and used a shear screw coupler to be splice to the steel rebar. The specimens would be loaded axially while a transverse load was applied to the stub. Specimens varied by concrete material used, HPC or UHPC, as well as tie spacing, and relative axial force in relation to the total axial force resistance of the section. The loading program had the axial load held constant while a reverse cyclic transverse displacement-controlled load was applied in increments of 1% drift ratios with three repetitions at each drift ratio.

[1] Note that the authors use the term very-high-performance concrete (VHPC) which is defined as having a compressive strength between 100 and 150 MPa

The results of the experimental test were then used to calibrate an OpenSees analytical model developed by the authors. Having validated the analytical models, the authors then varied parameters such as the relative normal force, tie spacing, concrete strength, and length of SMA used to further extrapolate results not possible from the experimental specimens. From the experimental and analytical results, the authors suggest that the best combination for a building's lifecycle would be the use of UHPC with SMA as it provides reduced damage compared to HPC. Additionally, they emphasize that NiTi bars used must span the full plastic hinge. From their experimental results they also found that the displacement ductility was greater in HPC specimens but in general was lowered by increasing relative axial force and tie separations. It appeared that stiffness degradation was consistent across materials and tie spacings but did decrease due to increased relative axial load. Finally, based on the analytical extrapolations, they found that ductility increased with greater lengths of SMA used and increased with longitudinal reinforcement ratio and concrete strength.

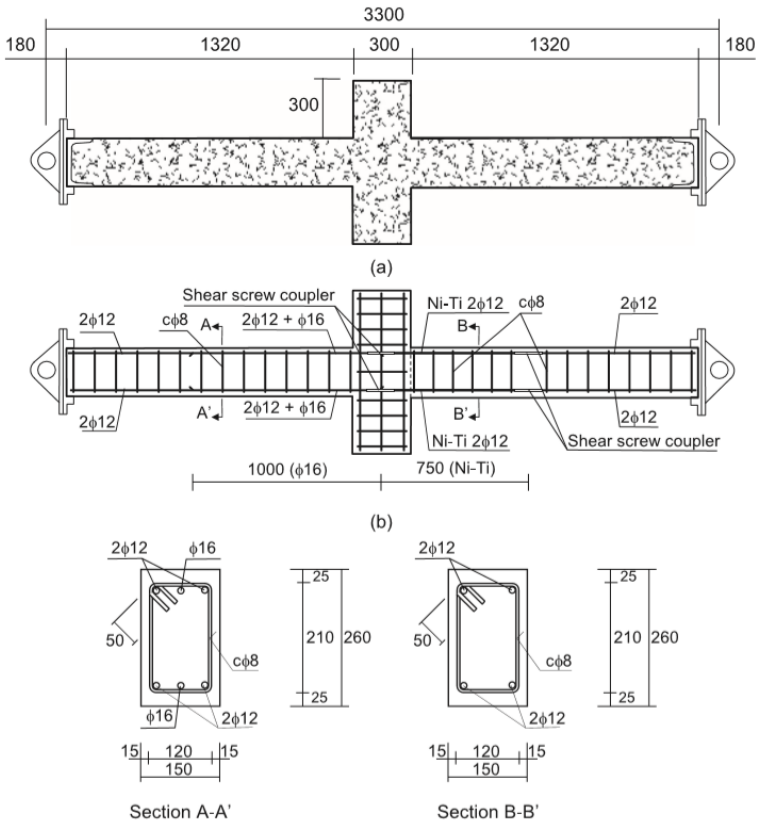

Figure 2.9: Beam column specimen dimensions and detailing (Pereiro-Barceló et al., 2018).

2.1.2.7 Seismic Performance of Shape Memory Alloy Reinforced Concrete Moment Frames Under Sequential Seismic Hazard (Abraik, 2020)

Providing a summary of research on SMA up to the time of the paper's writing, the author identifies the issue that SMA continues to be significantly more expensive than traditional steel resulting in the consistent recommendation amongst experts that it be used in plastic hinge regions. Since the plastic regions of beams in a moment resisting frame experience different amounts of deformation based on their location, and thus SMA would have different degrees of impact, the author's objective is to better understand the optimal joint locations in a structure to which SMA reinforcements should be applied. Since creating a full-scale frame structure would be impractical the authors model four buildings with varying numbers of story levels (3, 5, 7, and 9) under four cases which assume either: 1) the whole structure only uses steel reinforcement at all joints, 2) SMA reinforcement is used in joints throughout the entire building, 3) SMA reinforcement is used for joints in the middle stories, or 4) SMA reinforcement is used for joints in the bottom stories. The models were then subject to ground motions from 10 seismic events. It was found that the use of SMA in lower stories provided similar recentering capabilities to a structure using SMA throughout. Fragility comparisons of the structures were also carried out and it was found that the SMA use in lower stories could increase the fundamental period of a structure thereby reducing damage to high story levels. The authors estimate that the use of lower story SMA implementation could reduce costs by two-thirds without any notable sacrifice to self entering capabilities.

2.1.2.8 Seismic Collapse Safety and Response Modification Factor of Concrete Frame Buildings Reinforced with Superelastic Shape Memory Alloy (SMA) Rebar (Siddiquee et al., 2021)

Research into the use of SE-SMAs was noticed by authors to focus primarily on controlling residual drift but little work looked at the impact SMA in the plastic regions of columns and beams have on the collapse safety of a building. Part of this lack of research was due to little definition of what collapse safety entails in existing codes. To investigate this the researchers designed buildings varying the number of story levels as either 3, 6, or 8 stories corresponding to a low, medium, and high-rise building. Each of these buildings was then modeled as having 1) steel reinforcement only, 2) SMA reinforcement in the plastic hinge of the ground floor columns, 3) SMA reinforcement in the plastic hinge region of beams, and 4) SMA reinforcement in both column and beam plastic hinge reasons. All building structures were modeled in SeismoStruct

assuming a storey height of 3 m and 5 bays spaced 5 m apart. Based on push over analysis 20 ground motion histories were chosen and applied for incremental dynamic analysis. The analyses were used by authors to define and calculate a Collapse Margin Ratio (CMR), an indicator of the probability a building would collapse. For the low- and high-rise building use of SMA increase this CMR while for mid-rise building use of SMA decreases the CMR. Ductility, based on a ratio of ultimate to yield displacement of the structure, for the SMA buildings was lower but this is an expected result due to the lower stiffness of SMA requiring larger displacements to reach yielding.

2.1.3 Non-NiTi SE-SMA for Seismic Resilient Structures

2.1.3.1 Strengthening of RC Beams by Iron-Based Shape Memory Alloy Bars Embedded in a Shotcrete Layer (Shahverdi et al., 2016)

The primary focus of the authors is the application of the shape memory effect of an iron based SMA to a beam using shotcrete to externally bond the SMA before providing a prestressing force. Although this literature review is focused on super-elastic SMAs this paper is of interest as it outlines a method by which the researchers and EMPA, their employer, have created ribbed bars of the iron based SMA. If this fabrication process is also applicable to super-elastic iron based SMAs, there would be improvement in the bond strength that is often a concern with current NiTi SE-SMA bars.

2.1.3.2 Probabilistic Seismic Risk Assessment of Concrete Bridge Piers Reinforced with Different Types of Shape Memory Alloys (Billah & Alam, 2018)

The authors of the paper look to apply previous performance-based design guidelines they had developed to perform a probabilistic seismic risk assessment following the Pacific Earthquake Engineering Research (PEER) Centre PBEE methodology for 5 RC bridge columns, measuring 1 m in diameter and 5 m high, utilizing SMA materials. All SMA elements were limited to the plastic hinge to maximize cost efficiency and were detailed such that they provided an equivalent axial force resistance as the steel found throughout the rest of the column. This resulted in each column having 28 SMA bars varying in diameter from 22.5mm to 30 mm. The five SE-SMA materials considered can be found below in Table 2.1 and are based on previous research carried out by others into the mechanical properties of the selected SMAs.

Table 2.1 Material properties of SE-SMAs used in the numerical modeling (Billah & Alam, 2018).

Alloy	E (GPa)	ε_s (%)	f_y (MPa)	f_{P1} (MPa)	f_{T1} (MPa)	f_{T2} (MPa)
$NiTi_{45}$	62.5	6	401	510	370	130
$NiTi_{45}$	68	8	435	535	335	170
FeNCATB	46.9	13.5	750	1200	300	200
CuAlMn	28	9	210	275	200	150
FeMnAlNi	98.4	6.13	320	442.5	210.8	122

SeismoStruct was used by the authors to model the columns with the assumption that the piers be restricted from rotating at the top boundary and have a slip and rotation spring to approximate the interaction between the modeled piers and a foundation. There was no indication that an axial load was applied in the model to account for the dead load imposed by a bridge superstructure. Peak ground acceleration and spectral acceleration were chosen based on the seismic hazard of Vancouver and used to inform the selection of 30 ground motion records. The common parameters for the probabilistic seismic design were discussed by the authors who settled on using maximum and residual drift as engineering design parameters and PGA as the intensity demand. The results of the analysis through linear regression demonstrated that FeNCATB provided the best results for residual drift, likely due to its high recovery strain, and along with CuAlMn which provided greater maximum drift capacity. After creating fragility and seismic hazard curves for each of the RC columns the researchers conclude that FeNCATB outperformed all other SMAs due to its higher recovery strain but that all SMAs tested would incur lower annual costs and be less susceptible to damage compared to their RC counterparts.

2.1.3.3 Experimental Research on Resilient Performances of Fe-Based SMA-Reinforced Concrete Shear Walls (Yan et al., 2018)

The authors of the paper experimentally test 4 slender shear walls that utilize Fe SE-SMA reinforcement as the longitudinal bars in the boundary regions. The walls varied in the bar diameter of Fe SE-SMA used and spacing of ties. Two control walls consisting of only steel reinforcement were also constructed with all walls being scaled to 1/3 of a typical storey height and measuring

1000 mm high by 600 mm long by 140 mm thick. Walls were subject to a constant axial load of 500 kN corresponding to 0.4% of their axial capacity and a reverse cyclic lateral force. There is no information given regarding the loading cycles beyond that it is force controlled until yield at which point it becomes displacement controlled. The authors propose a new metric for quantifying the seismic resilience of the structure, termed equilibrium resilient factor, which is a ratio of the residual force at the zero-displacement position to the ultimate force experienced by the wall. Using this metric, the researchers found an increase in the resilience factor of up to 21% when using Fe SE-SMAs compared to steel. There is no comparison of the residual drift, ultimate drift, ductility ratio, or definition of a peak or ultimate load (the latter two are difficult to precisely determine due to the quality of the graphs presented but may be determined using an image editing tool). The results for all walls are presented below in Figure 2.10. Note that the naming convention was based on SMA and GJ indicating the type of reinforcement bar in the boundary region; Fe SE-SMA or steel respectively. The first number indicates the bar dimeter in mm and the second number indicates the spacing of shear stirrups.

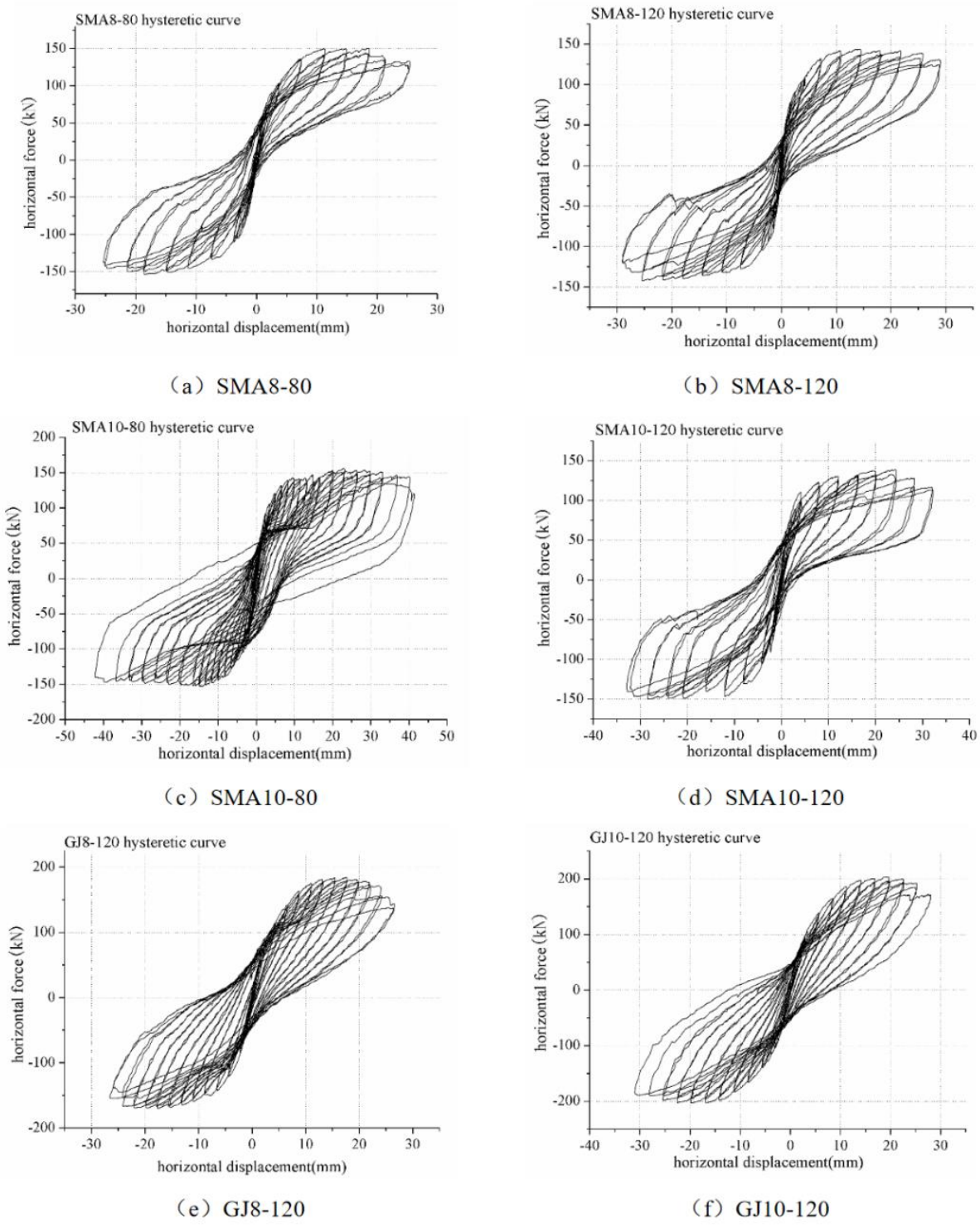

Figure 2.10: Load displacement response of Fe SE-SMA and Steel tested specimens (Yan et al., 2018).

2.2 Recent Work into the Material Characterization and Modelling of ECC

Modern Fibre Reinforced Concretes (FRC) have been around in some form as far back as 1963 based on research into the history of FRCs done by Naaman (2018). For this reason, the works covered in this literature review, for the most part, are limited to work done in the last five years. Such work often consists of both material property characterization and numerical modelling/model formulation making it difficult to categorize and is simply presented in chronological order.

2.2.1 Mechanical Behaviour of a Polyvinyl Alcohol Fibre Reinforced Engineered Cementitious Composite (PVA-ECC) Using Local Ingredients (Meng, Huang, et al., 2017)

Noting the environmental impacts of requiring large amounts of micro silica sands, the authors examine using local sand that are larger grain but may still be able to provide a stain response compatible with reinforcing steel. The testing procedure is very thoroughly explained and consisted of compression testing of cylinders, tensile coupon tests, and flexural beam tests. Based on results the authors caried out a statistical analysis to provide average, upper, and lower bounds for values. These values were then used to model the flexural specimens in ABAQUS using a polyline compression curve and trilinear tensile curve with a concrete damage plasticity model. The authors note that when using tensile coupons, the tensile properties are thought to be over estimated as the dimensions of the specimen confine distribution of fibres into 2D parallel layers as opposed to a more dispersed 3D distribution that would be expected in flexural specimens. To compensate for this a ratio is used to scale values from direct tension tests to more appropriate conservative values. Modeling demonstrated that use of the scaled values provided agreeable results for the experimental responses.

2.2.2 Flexural and Shear Behaviours of Plain and Reinforced Polyvinyl Alcohol-Engineered Cementitious Composite Beams (Meng, Lee, et al., 2017)

Building on their previous work the authors investigated how use of ECC could improve the shear capacity of beams compared to RC counterparts. This was done using 10 beam specimens measuring 2200 mm x 200 mm x 100 mm in four-point bending. The mix proportions and material properties of the ECC used, which were made more environmentally conscious by use of local sands as opposed to micro silica sand, were presented as shown in Table 2.2 . It was found that use of ECC could reduce the amount of shear stirrups required. Failure of the RC beam saw significant

crushing and spalling of concrete in the compression zone while ECC beams had localized stress around a predominate crack which led to flexural failure with reinforcement bars rupturing. Additionally, there was less slip of longitudinal bars in ECC beams suggesting an increased bond between reinforcement and concreting material with the use of ECC.

Table 2.2 Mix design of PVA-ECC with all quantities expressed as a ratio of mass (Meng, Lee, et al., 2017).

Cement	Fly Ash	Sand/binder	Water/binder	High-Range Water Reducer	Fibre (vol.%)
1.0	1.2	0.36	0.3	0.01	2.2

2.2.3 Behaviors of Steel-Reinforced ECC Columns Under Eccentric Compression (Yuan et al., 2018)

The authors look at how eccentric axial loading affects the performance of ECC-steel reinforced columns. This is done by using two different eccentricities, three different diameters of longitudinal reinforcement and a concrete control. It was observed that significant spalling happened in RC columns while no spalling occurred in ECC columns. The crack width of ECC seemed to plateau at 60 micrometers while RC columns crack width increased linearly to a maximum of 2 mm. The authors developed a sectional analysis model to accurately model the experimental results with 10%.

2.2.4 Bond Behavior of Steel Bar Embedded in Engineered Cementitious Composites Under Pullout Load (Deng et al., 2018)

The authors investigated the effect different strengths and fibre contents of ECC had on the bond strength of smooth and deformed bars. Additional parameters considered were bar diameter and cover thickness. It was found that for smooth bars, ECC significantly improved bond strength although pull out was still observed. High ECC strengths and fibre contents were also shown to improve the bond strength of bars due to tension stiffening and confinement provided by fibres respectively. The paper clearly outlines the approach used for the testing and methodology as well as how they developed their formulations of bond slip.

2.2.5 Bond behavior of deformed bar embedded in Engineered Cementitious Composites under cyclic loading (Deng et al., 2019)

A continuation of their previous work the authors now investigated the bond behaviour between deformed bars and different ECC mixes under cyclic loading using similar methods as before. It was demonstrated that the cyclic loading significantly reduced bond strength of the ECC materials. Compressive strength of ECC had a beneficial impact on bond strength, energy dissipation, and degree of degradation while flexural toughness could have a slight impact on bond strength and concrete cover was able to reduce degradation as well. The authors proposed an equation for cyclic bond strength that considers compressive strength, flexural toughness, cover thickness, and anchorage length, it should be noted this modification only has impact for the maximum bond strength.

2.2.6 Investigation of Interface Shear Properties and Mechanical Model Between ECC and Concrete (J. Tian et al., 2019)

The authors, noting that ECC has become a method for repairing deteriorated concretes, investigated the shear slip behaviour between ECC and concrete. Specimens varied between three ECC concrete strengths, two types of PVA fibres, two application methods (cast in place and sprayed on), and degree of roughness of interface. It was found that only roughness affected failure type. The shear load-slip curves were nearly linear up to maximum values followed by a sharp decrease and no variable seemed to change the response significantly. Traditional casting provided higher interface shear strength compared to spraying while ECC strength and roughness also improved shear interface response. Fibre type was found to have had a negligible effect. The authors used results to provide equations that could adequately predict the shear load-slip curves.

2.2.7 A Modified Cyclic Constitutive Model for Engineered Cementitious Composites (X. Li et al., 2019)

The authors propose a new constitutive model for the cyclic loading of ECC in tension and compression. This model builds on work by Han et al. (2003), Hung & Li (2013), and Gencturk & Elnashai (2013). The proposed model, shown in Figure 2.11, uses 5 key points (3 in tension 2 in compression) and 12 constants to define hysteresis and degradation. The 12 constants were calibrated based on material scale testing of a single ECC mix. To gauge the validity of the calibrated constants the final model was implemented into OpenSees and compared against

experimental results from 6 different ECC mixes that vary in material properties as well as a very small-scale bending specimen. These experimental comparisons demonstrated that the numerical model and experimental values differed by most 6%.

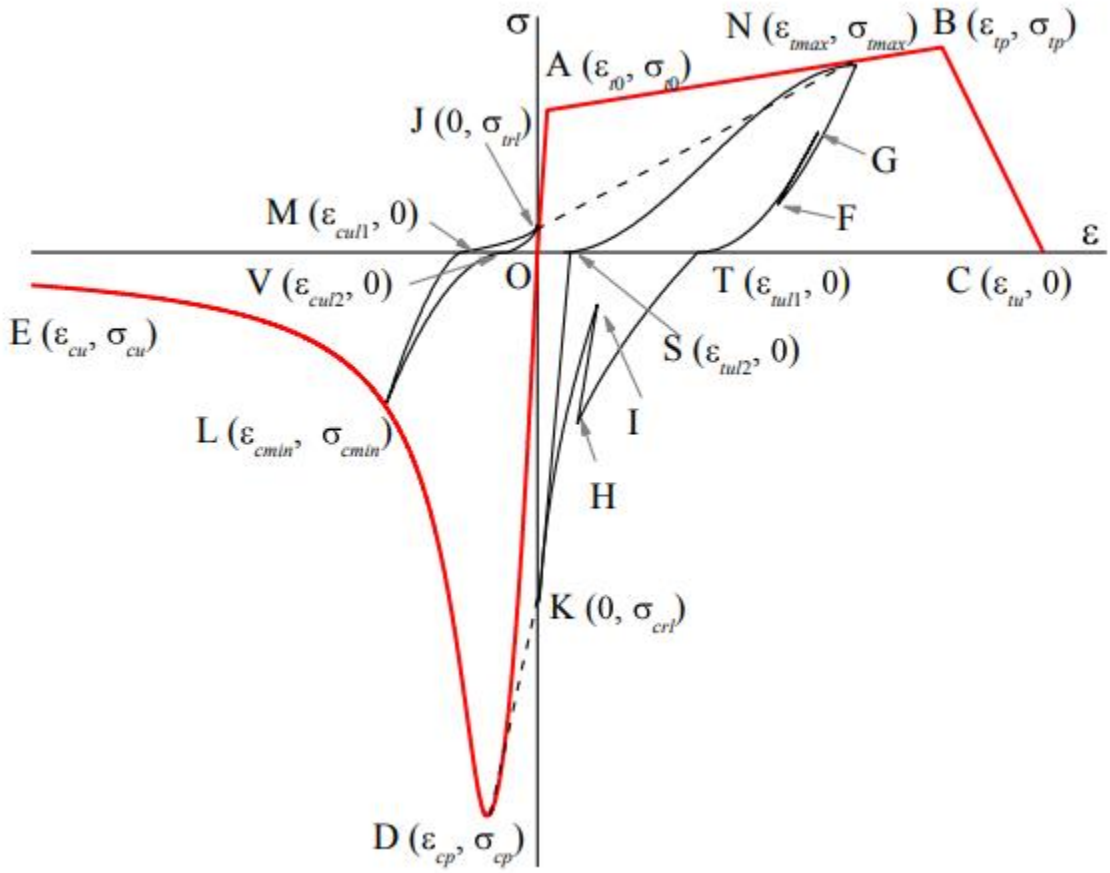

Figure 2.11 Proposed cyclic tension and compression response of ECC (X. Li et al., 2019).

2.2.8 Fiber-hinge Modeling of Engineered Cementitious Composite Flexural Members Under Large Deformations (Tariq et al., 2019)

The authors looked to investigate the effect ECC has on the rupturing strain of reinforcement noting that structural elements with ECC as a concreting material tend to have crack localization resulting in reinforcement rupture. They propose the use of a fiber-based lumped-plasticity model, shown in Figure 2.12, implemented in Opensees and validated against a database of 18 small scale ECC beams with varying reinforcement ratios and geometries which were restrained as a cantilever and underwent reverse cyclic. The rational of a fiber-based lumped-plasticity model is that damage accumulation and inelastic behaviour is confined to the plastic hinge. With this consideration it is

more efficient to only model the plastic hinge as inelastic while the remainder of the model can be assumed to act elastic cutting down on the computational requirements. The paper is quite thorough in laying out the procedure used to determine and calibrate both material property parameters such as the tension softening section of an ECC material as well as modifications required to formulate the plastic hinge, an assumed spring coefficient to adjust for initial stiffness, and material degradation factors for steel. The final models were able to predict experimental data with 9% error across multiple metrics such as strength, energy dissipation, and ultimate displacement. The authors concluded that the model has trouble at low reinforcement ratios and that ECC unlike conventional concrete has improved ductility with greater reinforcement ratios.

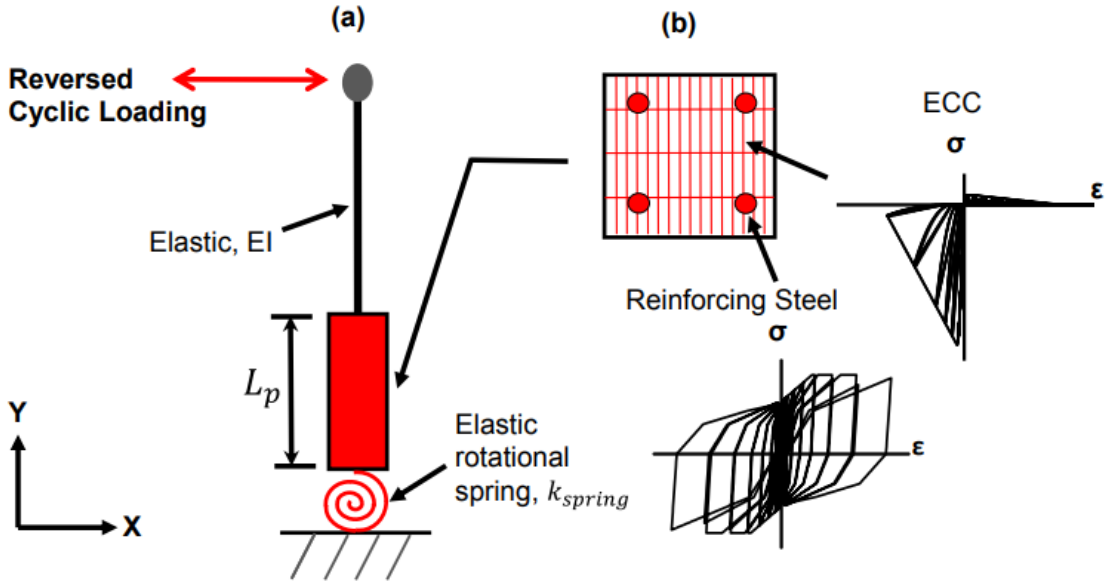

Figure 2.12 (a) The proposed fibre hinged lumped plasticity with a rotational spring and (b) inelastic fibre section (Tariq et al., 2019).

2.2.9 Performance-Based Design of All-Grade Strain Hardening Cementitious Composites with Compressive Strengths From 40 Mpa to 120 Mpa (L. Li et al., 2019)

The authors investigated how fibre content affected the performance of polyethylene (PE)-ECCs ranging in compressive strength from 40-120 MPa. The fibres used were different types of PE fibres ranging in length from 12-18mm. Testing included compression testing of cylinders, uniaxial tension tests, and single fibre pull out test. The authors used several of their experimental results to formulate equations for calculating tensile strength and strain based on fibre parameters. Higher fibre reinforcement ratios resulted in high peak strengths with the same w/b ratio. With

increasing strength there was a decrease in the strain capacity. Crack width and crack spacing of ECC specimens varied with fibre reinforcement index and compressive strength.

2.2.10 Compressive Performance of All-Grade Engineered Cementitious Composites: Experiment and Theoretical Model (Ding et al., 2020)

Building on previous work by Li et al. (2019) into the tensile response of ECC using high density PE fibres the authors now wanted to understand the compressive behaviour of ECC ranging in strengths between 43 and 115 MPa. They proposed equations for Youngs Modulus and peak compressive strain based on compressive stress through regression of the experimental results. It was found that compressive strength of ECC has little effect on Poisson's ratio, which averaged 0.237. It was also found that unlike normal concrete the Possion's ratio of ECC stays stables until close to 90% of the peak load. The authors examined four previous constitutive models but only models by Wang and a modified Carriera and Chu model could accurately predict both the pre and post peak slopes. The modified Carriera and Chu would be easier to implement into FEA models since it does not require individual calibrated values. The authors proposed equations, but these equations are found to have issues when applied to PVA based ECC from other works of literature.

2.2.11 Seismic Behavior of Composite Columns with Steel Reinforced ECC Permanent Formwork and Infilled Concrete (Pan et al., 2020)

The paper investigated performance of novel columns which used a permanent ECC formwork exterior infilled with normal concrete. This was done using seven scaled columns with a cross section measuring 300 mm x 300 mm while varying shear-span ratios and transverse reinforcement ratios. One column served as a control while the remaining six were the columns utilizing ECC, termed RECC/C. Additional numerical modelling was done in Openseeas using Nonlinear Beam-Column elements and ECC01 material model. The results of the experimental testing showed that use of ECC resulted in more ductile behaviour with cracks appearing finer in width and larger ultimate displacement capacities. The numerical modeling appeared to provide acceptable results and the parametric study demonstrated that increasing ECC strength and strain resulted in more ductile behaviour. Another key finding was that thickness of the ECC layer was important in determining the increase in ductility when compared to RC.

2.2.12 Numerical Modelling of Engineered Cementitious Composites-Concrete Encased Steel Composite Columns (Khan et al., 2020)

The authors investigated the use of ECC in novel concrete encased steel composite columns. This work also consisted of numerical modelling with the creation of an FEM model in ABAQUS which was then validated against small scale columns measuring 160mm x 160mm. The authors present in detail the constitutive models used, particularly how a tri-linear curve was used for axial tension in conjunction with a concrete damaged plasticity (CPD) model. The finalized models were shown to provide accurate results below 10% error. Their parametric study demonstrated that increasing the strength of ECC was not as effective as increasing the strength of confined concrete.

2.2.13 Peridynamic Modeling of Engineered Cementitious Composite with Fiber Effects (Cheng et al., 2021)

The authors outline the use of peridynamics (PD) models as opposed to FEM for the modelling of ECC. Presented in this paper is a detailed background of attempts to model ECC as well as the theory behind PD models. The program in which the PD model was implemented was not mentioned however when compared against experimental data the cracking pattern was found to preform accurately.

2.2.14 Interfacial Bond–Slip Behavior Between H-Shaped Steel and Engineered Cementitious Composites (ECCs) (L. min Tian et al., 2021)

The paper looks at modelling of a novel H-shaped steel ECC enclosed column. The authors focused on the factors that could impact the bond strength between the H-shape steel and ECC such as ECC strength, embedment length of steel, thickness of ECC cover and volumetric stirrup ratio. Once they had sufficient data and relationships for bong strength a model was constructed in ABAQUS. The ECC was defined using a bilinear ascending branch and an exponential decay for the descending branch following GB 50010 code for design. Also presented are the mix designs used and other material properties, with tensile properties being from a direct tension test. The FEM model was further applied to two ECC flexural beams that demonstrated aggregable results.

2.2.15 Numerical Simulation of Shear-Critical Engineered Cementitious Composites Structural Members Using a New Two-Dimensional Fixed Crack Constitutive Model (Fan et al., 2021)

The authors outline an in depth ECC smear crack model they propose which was developed in ABAQUS 2017. The study in particular focuses on creating a model suited for shear critical structural elements and on ECC that makes use of PVA fibres. For the curve of the compressive response the authors outline equations which only require the compressive strength of the concrete as an input parameter. Building upon the unconfined curve the authors also modify models proposed by Legeron and Paultre and incorporate fibre volume in their formulation of peak compressive strain. The tensile curve is formulated based on four parameters, the peak tensile strength (f_t), tensile cracking load (f_{tcr}), peak tensile strain (ε_t), and the slope of the softening branch (n_t). The authors due note that some stress and strain values can be calculated based on the following relationships: $\varepsilon_{tcr}= f_{tcr}/E_c$, $f_{tcr}=0.8f_t$, and n_t being 0.5-2% of the elastic modules suggesting rough results could be obtained by simply using/knowing f_t and ε_t. Further details are provided regarding the unloading paths when hysteretic behaviour occurs during cyclic and reverse cyclic loading as well as shear transfer. The validated models were tested against 19 coupling beams and 6 shear walls with agreement between simulated and experimental results. Typically, the initial stiffness was higher and certain specimens showed faster degradation, but the peak values were consistently accurate.

2.3 Use of SE-SMA and ECC as Novel Hybrid Structures

2.3.1 Shake-Table Studies of a Four-Span Bridge Model with Advanced Materials (Cruz Noguez & Saiidi, 2012)

Cruz and Saiidi examine the use of smart materials in the plastic hinge region of columns in a four-span bridge. The bridge itself was a quarter scaled model of the RC bridge discussed (Nelson, 2007). This resulted in a bridge 32626 mm long, 2388 mm wide with three sets of two column bents measuring 304.8mm in diameter. The three sets consisted of either replacing the plastic hinge with an elastomeric pad and a PT steel tendon, traditional RC columns that integrate a PT steel tendon, and a pair of columns where the plastic hinge is replaced with ECC and an equivalent number of NiTi SE-SMA bars replacing deformed rebar in this region. Concrete blocks and lead weights were added to the structure to replicate deadload on the structure. OpenSees was used to

determine the optimal arrangement of bents as well as predict the ultimate displacement of each bent in a monotonic push over analysis. Loading was applied using the shake tables based on modified transverse and longitudinal motions from the 1994 Northridge earthquake for 7 runs (although only transverse motion was used for the last two runs to avoid drastic failure). SMA columns were found to minimize residual drift as well as reduce overall damage, in part due to the ductility of the ECC. It was demonstrated that the use of SMA and ECC would allow for the bridge to remain in service after the maximum earthquake. Additionally, the numerical analysis predicted that the SMA bent would be least critical.

2.3.2 Advanced Materials for Control of Post-Earthquake Damage in Bridges (Shrestha et al., 2015)

Shrestha et al. built on the work of the previous paper by Cruz and Saiidi by creating a numerical model in OpenSees of the four-span bridge. An initial analysis was run with the same geometry and placement of the three different bents to validate the model constructed. Once validated the model was altered into five bridges of the same geometry but instead of having three different bents, had all bents in a single bridge consisted of identical reinforcing. The five bridges consisted of a control bridge entirely of RC and four bridges where the plastic region of the bents was altered using either an elastomeric rubber, post tensioning, NiTi SE-SMA bars with ECC, or CuAlMn SE-SMA bars with ECC. 10 near-fault ground movement histories from around the world were applied to the models. It was found that both SMA bents provided superior responses with residual drift consistently falling below the 1% threshold used to define if a bridge would be serviceable after an earthquake. For comparison the RC control bridge was found to exceed the 1% residual drift limit for all records while the bridges employing post tensioning and elastomeric rubber only stayed within the 1% limit for certain records.

2.3.3 Optimal Design of Bridge Columns Constructed with Engineered Cementitious Composites and Cu-Al-Mn Superelastic Alloys (Hosseini et al., 2019)

The authors undertook a parametric numerical study to see the effects of ECC quality, number of Cu-Al-Mn SMA bars, and section type on the performance of bridge columns. To perform this numerical study the authors used a 3D model in Atena providing detailed explanation of the models and values used. The results demonstrated that increases in tension performance of ECC did not have significant effects on results when looking at lateral strength, residual deformation, and

energy dispersion. The largest increase in performance was seen when SMA bars made up 65% of the reinforcement area.

2.3.4 Seismic Design of Three Damage-Resistant Reinforced Concrete Shear Walls Detailed with Self-Centering Reinforcement (Tolou Kian & Cruz-Noguez, 2020)

The authors investigated the design parameter required for seismic design of novel walls. Current seismic standards such as FEMA as well as design principles are based on traditional RC shear walls while the use of novel reinforcing and concreting materials is not well understood. To address this the authors constructed four walls with one being a control RC wall (CW) and the remaining three using novel reinforcements, PT steel (PT), GFRP bars (GFRP), and SMA bars (SMA) and FRCCs as concreting materials; either SFRC or ECC. All walls had a shear span of 2005 mm, a width of 1000 mm, and a thickness of 150 mm with reinforcement layouts shown in Figure 2.13. The authors compared walls by examining parameters including stiffness, inelastic rotational capacity, plastic hinge length, and self centering moment. Based on the results the authors also discussed the implication on design parameters for self-centering walls. They found that SMA had the highest inelastic rotational capacity but also required that the longitudinal steel reinforcement be 200 mm from the boundary to avoid localized high stresses. Similar to R. Hoult & de Almeida (2022) it was found that curvature of the SMA wall remained constant along the 500 mm length of SMA bars suggesting that the plastic hinge for design can be taken as the bar length.

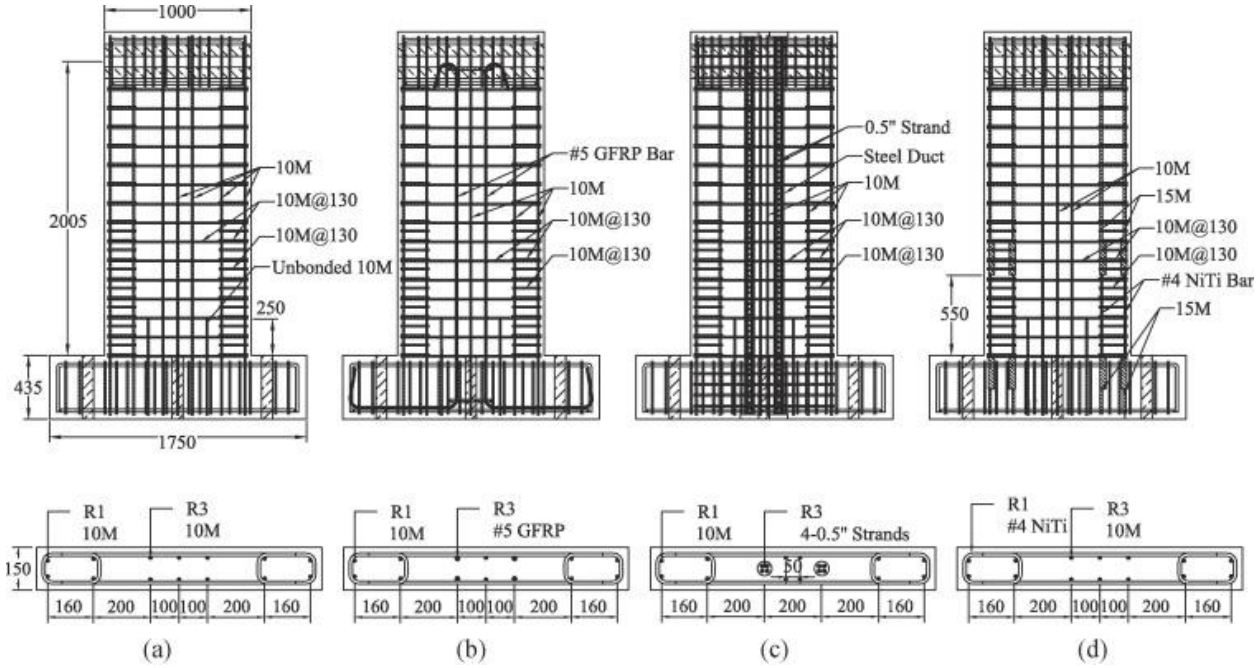

Figure 2.13 Reinforcement detailing of (a) CW, (b) GFRP-ECC, (c) PT-SFRC, (d) SMA-SFRC (Tolou Kian & Cruz-Noguez, 2020).

2.3.5 Seismic Performance of SMA/ECC Concrete Shear Wall with Self-Centering and Self-Repairing (Kang et al., 2021)

Kang et al. undertook a testing program looking at the performance of four shear walls under reverse cyclic loading using SMA and ECC. The four walls consisted of a control RC wall (R-C), a wall with SMA in the plastic hinge of the boundary region (SMA-C), a wall using steel reinforcement and ECC in the plastic hinge (R-ECC), and a wall with SMA in the plastic hinge of the boundary region and ECC as the concreting material (SMA-ECC). Although the paper is brief the reinforcement layout for the SMA-ECC wall shown in Figure 2.14 was included and the remaining walls likely followed the same reinforcement design with SMA replaced for steel in walls R-C and R-ECC. All walls were reverse cyclically loaded according to the Chinese Specification of Testing Methods for Earthquake Resistant Building (JGJ101-2015). Examining the hysteretic response of the walls demonstrated the superior ductility of walls utilizing SMA. Wall SMA-ECC was also found to reach larger displacements than the SMA-C wall suggesting that the ECC further improved ductility. Additionally, the SMA walls had a consistent recovery capacity ranging from 84-90% after yielding of the structure while steel walls see a linear decrease in recovery capacity.

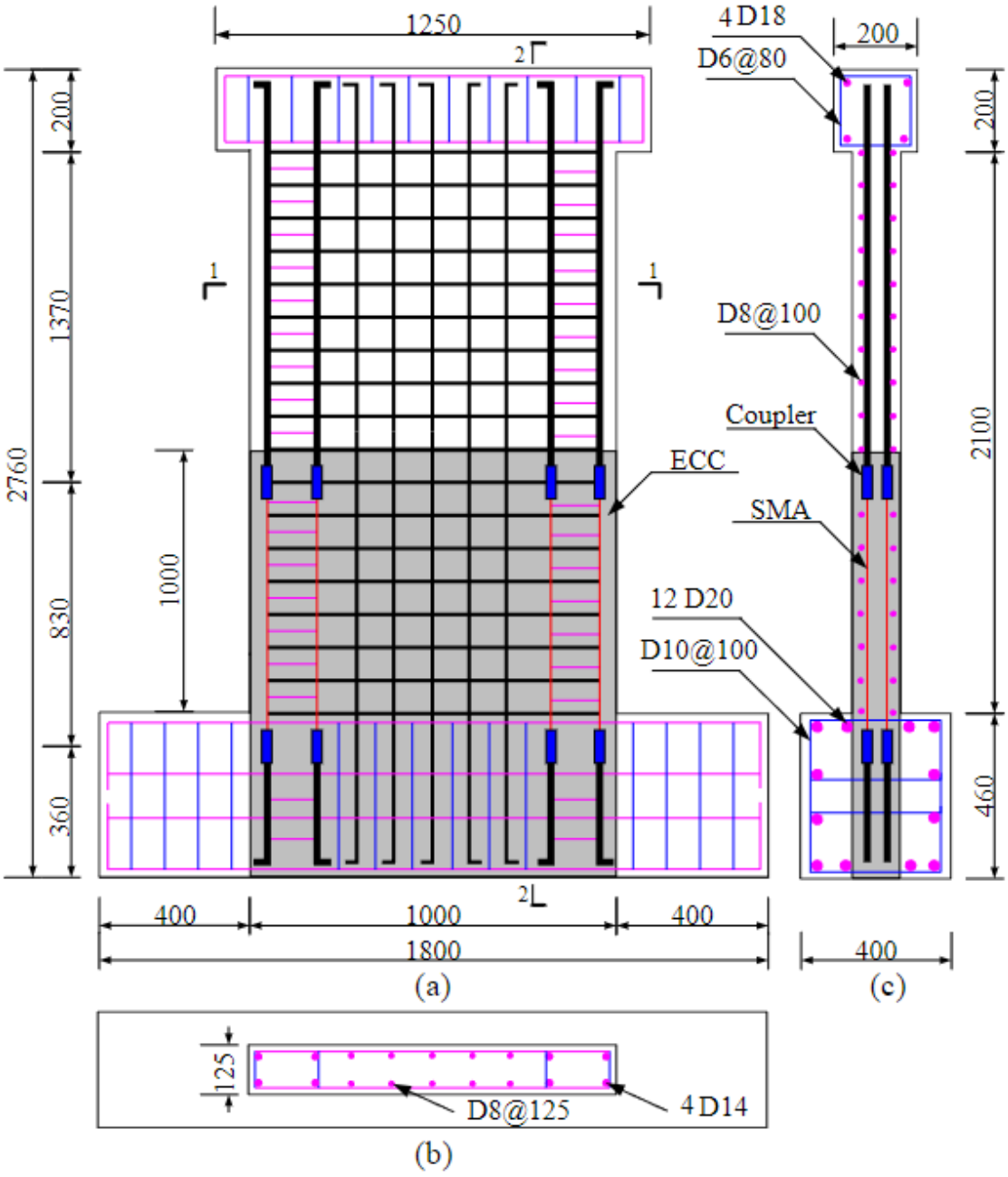

Figure 2.14 Reinforcement details of SMA-ECC:(a) elevation view, (b) section 1-1, and (c) section 2-2 (Kang et al., 2021).

2.3.6 Modelling Of Engineered Cementitious Composite-Repaired Superelastic-Shape Memory Alloy Reinforced Shear Walls (M. Soto-Rojas & Palermo, 2020)

The work presented by Soto-Rojas & Palermo documents the experimental procedure by which the shear walls tested in Morcos & Palermo (2019) were repaired and retested. The repair work

consisted of removal of damaged concrete from a depth of 60 mm below the base of the wall to an elevation of 1020 mm. Steel longitudinal reinforcement was then removed and replaced with new 10M deformed steel sections measuring 500 mm in length and coupled to existing reinforcement with mechanical screw lock couplers. Unlike the walls repaired in L. Cortés-Puentes et al. (2018) the SMA reinforcement in boundary regions did not have to be shortened or replaced as there were no visible signs that the bars had not undergone permanent deformation or buckling. To address sliding that had been observed by Morcos & Palermo (2019) four starter bars were installed between existing longitudinal reinforcement by drilling 300 mm into the foundation and extended 300 mm above the base of the wall. The reinforcement layouts of the two repaired walls are shown in Figure 2.15 and Figure 2.16. Looking to increase the ductility of the walls the damaged concrete was replaced with an ECC. Preliminary modelling of the repaired walls was carried out in VecTor2 making use of the user defined "Custom Input" model for tension softening to represent the tensile response of ECC.

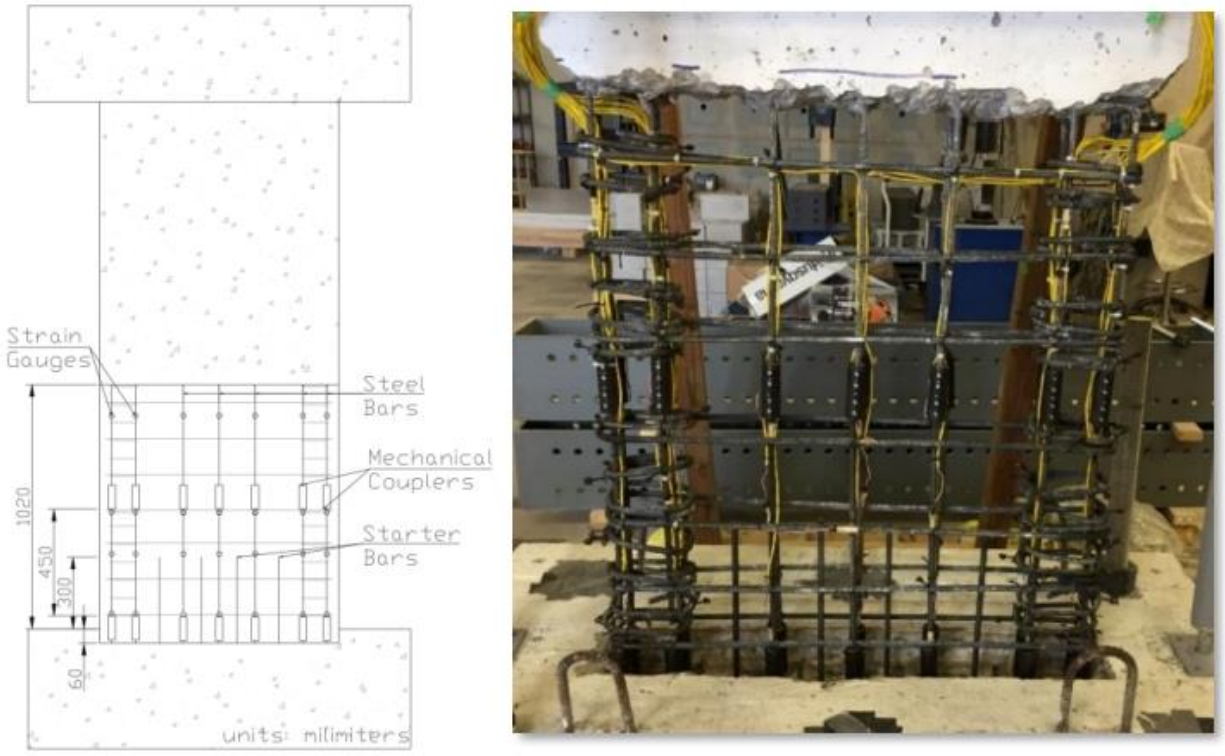

Figure 2.15 Reinforcement layout of steel wall (RSWS) (M. Soto-Rojas & Palermo, 2020).

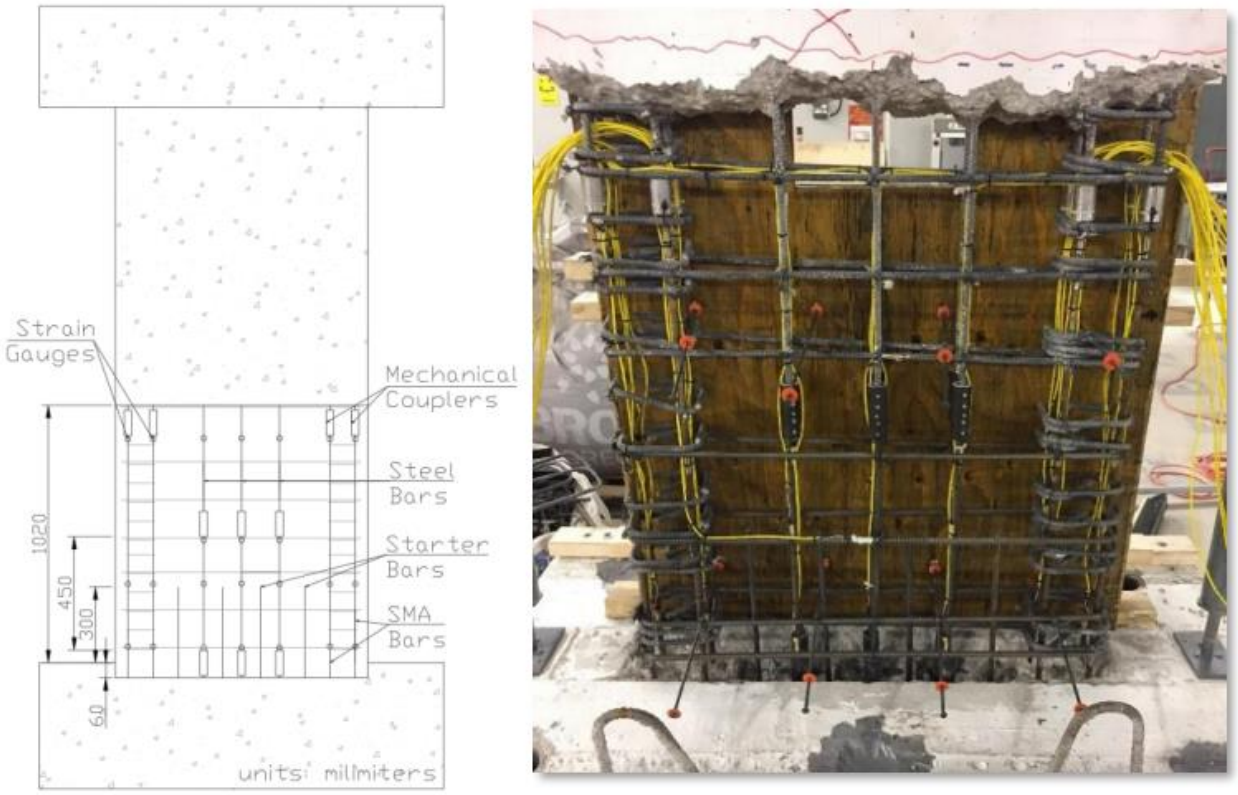

Figure 2.16 Reinforcement layout of SMA-steel wall (RSWN) (M. Soto-Rojas & Palermo, 2020).

3 Experimental Program and Testing of ECC

3.1 Introduction

Following the completion of his MASc thesis, Soto-Rojas (2020) had left ECC specimens which had not been tested and could be used for future work. These specimens included four flexural prisms measuring 75 mm x 75 mm x 280 mm (height x depth x length), four flexural prisms measuring 75 mm x 75 mm x 500 mm, four cylinders measuring 100 mm x 200 mm (diameter x height), and a cylinder measuring 75 mm x 150 mm. All specimens came from mixes which Soto used to repair the slender shear walls outlined in his thesis. While casting the ECC required for repairs it was necessary that three 75 litre batches be made for each wall as the industrial pan-type mixer concrete mixer could not produce a single batch large enough for a single wall. Based on the marking of the specimens it was determined that half of the flexural prisms had come from batches used in each of the two walls, while only one cylinder came from a batch used in the SMA-Steel hybrid (ECC-RSWN) wall and the other four cylinders came from batches used in the Steel control (ECC-RSWS) wall. The mix design for the ECC tested is shown below in Table 3.1 and is based on what was reported by Soto.

Table 3.1 Soto-Rojas (2020) mix proportions for Engineered Cementous Composites (ECC).

PVA Fibres (kg)		**Cement (kg)**	**Fly Ash (kg)**	**Silica Fume (kg)**	**Slag (kg)**	**Sand (kg)**	**Water (kg)**	**Superplasticizer (kg)**	**Volume (L)**
∅=0.1 mm	**∅=0.04 mm**								
0.94	0.94	30	50	8.25	3.38	33.83	23.33	0.75	75

∅ = fibre diameter

3.2 Compression Testing of ECC Cylinders

The day prior to compression testing cylinders were put into a cylinder grinder to make sure the ends were level and plane with each other. After grinding was completed, four measurements for diameter and two measurements for height were taken per cylinder with larger cylinders having average measurements of 102 mm x 199 mm (standard deviations of 1.7 mm and 1.1 mm) while

the small cylinder had average measurements of 76.88 mm x 147.5 mm (standard deviations of 0.73 mm and 0.5 mm). At the time of testing, it had been 324 days since casting for ECC-RSWN specimens and 331 days since casting for ECC-RSWS specimens.

Previous testing by Soto-Rojas of cylinders from the same ECC mixes at 151 and 152 days had resulted in compression strengths of 63.5 MPa. ASTM C1856/C1856M (2017), which is intended for Ultra-High Performance Steel Fibre Reinforced Concrete (UHP-SFRC), was followed since the compressive strength of the cylinders would only increase over time. Based on this standard, cylinders were loaded at a constant stress rate of 1+/-0.05 MPa/sec in a Pilot Controls compression testing machine. The compressive strengths of all cylinders are presented in Table 3.2 and show consistency with an average compressive strength of 70 MPa and a standard deviation of 2.28 MPa.

Table 3.2 Compressive strength of ECC cylinders.

Batch	**Cylinder Size (diameter x height)**	**Compressive Strength f_c (MPa)**
ECC-RSWN	102.9 mm x 198.5 mm	67.08
ECC-RSWS	76.9 mm x 147.5 mm	68.96
ECC-RSWS	101.9 mm x 200.5 mm	73.98
ECC-RSWS	101.4 mm x 199 mm	69.53
ECC-RSWS	101.8 mm x 198 mm	70.61
28 days (M. A. Soto-Rojas, 2020)		47.57
151/152 days (M. A. Soto-Rojas, 2020)		63.5

3.3 Flexural Testing of ECC Prisms

3.3.1 Testing Protocol

Prisms were tested in four-point bending following ASTM C1856 (2017) using an MTS universal testing machine under a constant displacement rate of 0.005 mm/sec which is an alteration from the original displacement rate of 0.05 mm/sec stated in the standard. The alteration in the loading rate is to allow for better observation of the ductile behaviour of the prisms inline with work conducted by Eshghi (2019), Saikali (2019), and Soto-Rojas (2020). It should also be noted that although ASTM C1856 is UHP-SFRC it has been applied by Soto-Rojas (2020) to calculate flexural strength (σ_f) or Modulus of Rupture (MOR) of ECC. Calculation of these properties will be discussed later in the chapter. Two sizes of prisms are used to ensure there is no significant difference in flexural strength due to different shear span-to-depth ratios with smaller prisms having a ratio of 1 while the larger prisms have a ratio of 2.

3.3.2 Loading Setup

The loading and support distances for the different sized prisms are shown below in Figure 3.1. Load was applied using two rollers held at a fix distance which had freedom to tilt in the out of plane direction to ensure full contact across the width of the beams. Supports consisted of a semi-circular metal contact point which can tilt in the out of plane direction with no rotation about any other axes and a roller which was free to rotate. To ensure the flexural prisms were centered in the out of plane direction markings were applied to the supports before each test to indicate where the edges of the prisms should sit. The prisms themselves were marked as well to ensure both supports and loading points were being applied at proper locations. Additional marks were made on the prisms to ensure the jig used to measure displacement was centered.

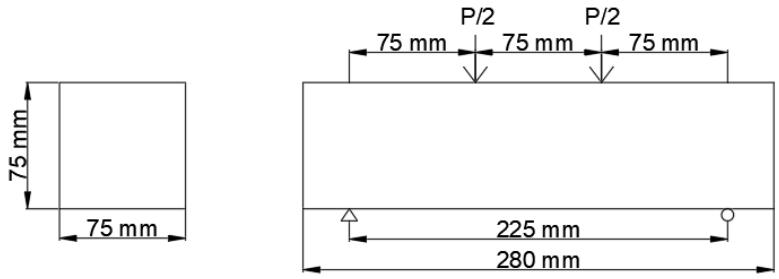

a)

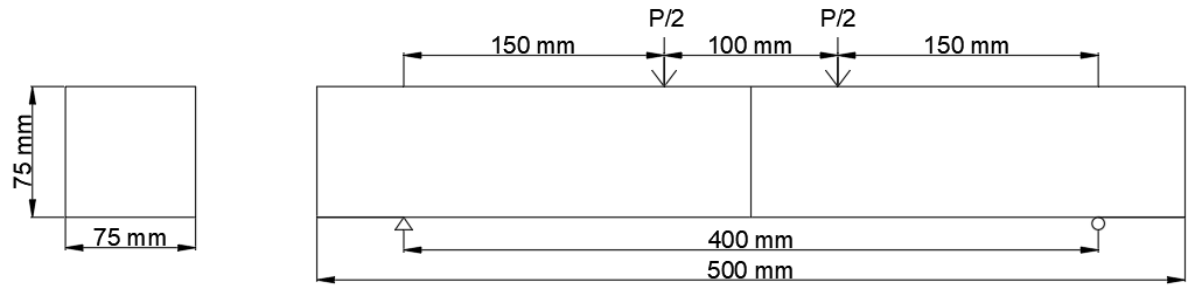

b)

Figure 3.1 dimensions of loading points and supports for prisms measuring a) 280 mm in length and b) 500 mm in length.

The jig, shown in Figure 3.2, consisted of two U shaped frames made from extruded aluminum which were placed at the same distance from the midspan as the supports and connected on each side with a single straight extruded aluminum piece. Each U-shaped frame was held in place using adjustable feet which could be raised or lowered by turning the threaded rod which attached them to the frame. Two feet contacted the top side of the prism while one foot on each side contacted the prism at the centre height. Each frame was ensured to be level before the connecting extruded aluminum piece was attached on each side. To ensure that the frames could rotate with the beam, each connecting aluminum piece had one end attached as a pin to one U frame while the other side was slotted to ensure it sat freely on the remaining U frame without restrain. A Linear Variable Differential Transformer (LVDT) with a stroke of 10 mm and sensitivity of 0.001 mm was attached to each connecting extruded aluminum piece at the midspan which also corresponded to the midspan of the prisms. To measure the midspan displacement a bracket, made from sheet steel, was attached to the top prisms at the midspan using hot glue. The LVTDs would contact the flanges of the bracket, allowing measurement of midspan displacement relative to the center of the prism at the supports.

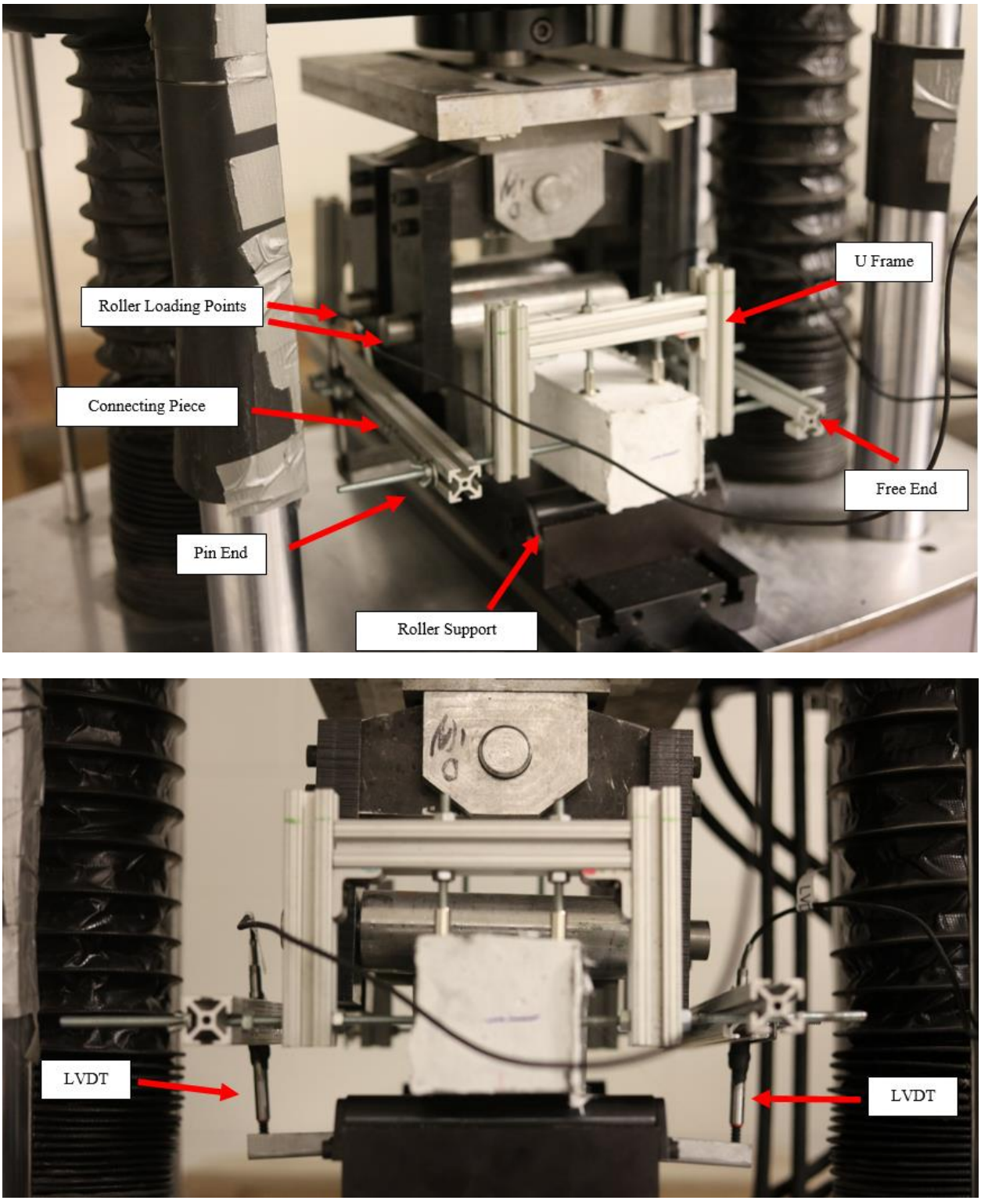

Figure 3.2 Loading and jig setup of prisms in flexure.

3.3.3 Results

The load-midspan displacement response of all flexural tests are presented in Figure 3.3 with the midspan displacement being the average of the readings from the two LVDTs. The initial stiffness, load at first crack, displacement at first crack, peak load and displacement at peak load are summarized in Table 3.3. Tests of the same size prisms are presented on the same graph along with load-midspan displacement data obtained from testing by Soto-Rojas (2020) to demonstrate the similarity between responses. It should be noted that data provided by Soto-Rojas came from testing which was done at 28 days after the ECC prisms were cast. Across both the 280 mm and 500 mm long prims, there is a stiff initial response with a drop occurring when crack formation began. The occurrence of this first crack corresponds to approximately 75% and 65% of the peak load for the 280 mm and 500 mm long prims respectively. After a slight drop in load capacity, fibres bridge the crack before strain hardening occurs with more fibres being exposed as the crack width increases before reaching a peak load. After the peak load there is gradual decent as localization of the predominant crack reduces the uncracked cross section thereby reducing the moment resistance of the prims. The presence of the descending slope demonstrates the ability of fibres to provide residual strength after cracking compared to normal concrete which would have a sudden failure following the peak load.

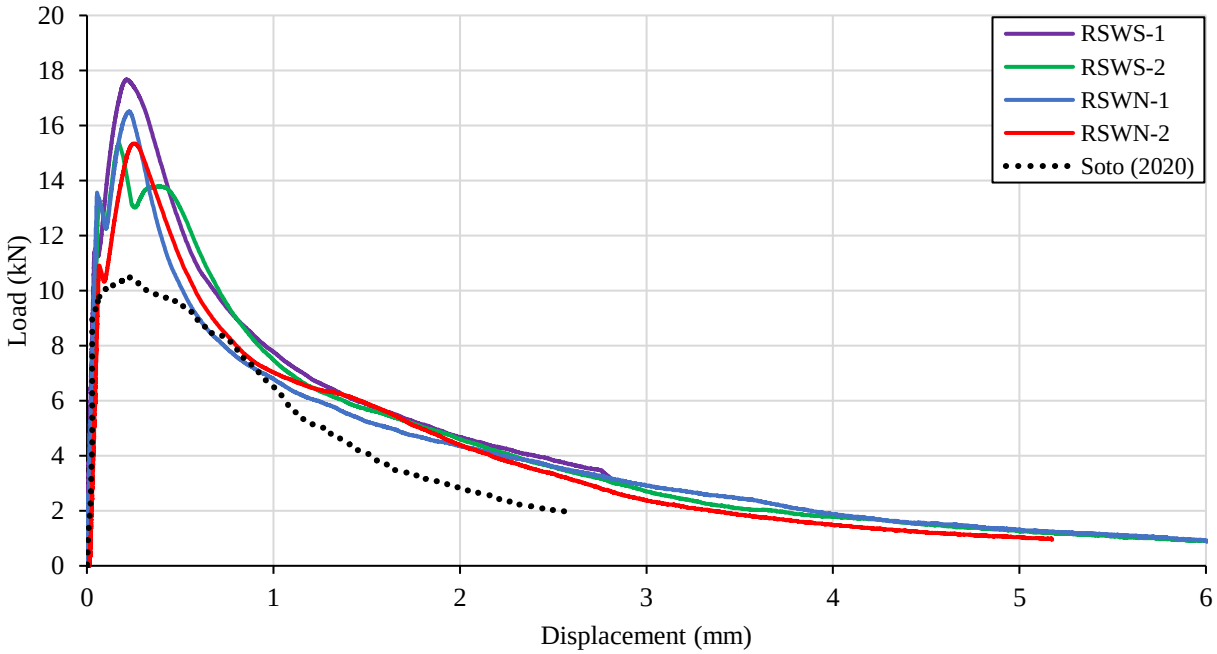

a)

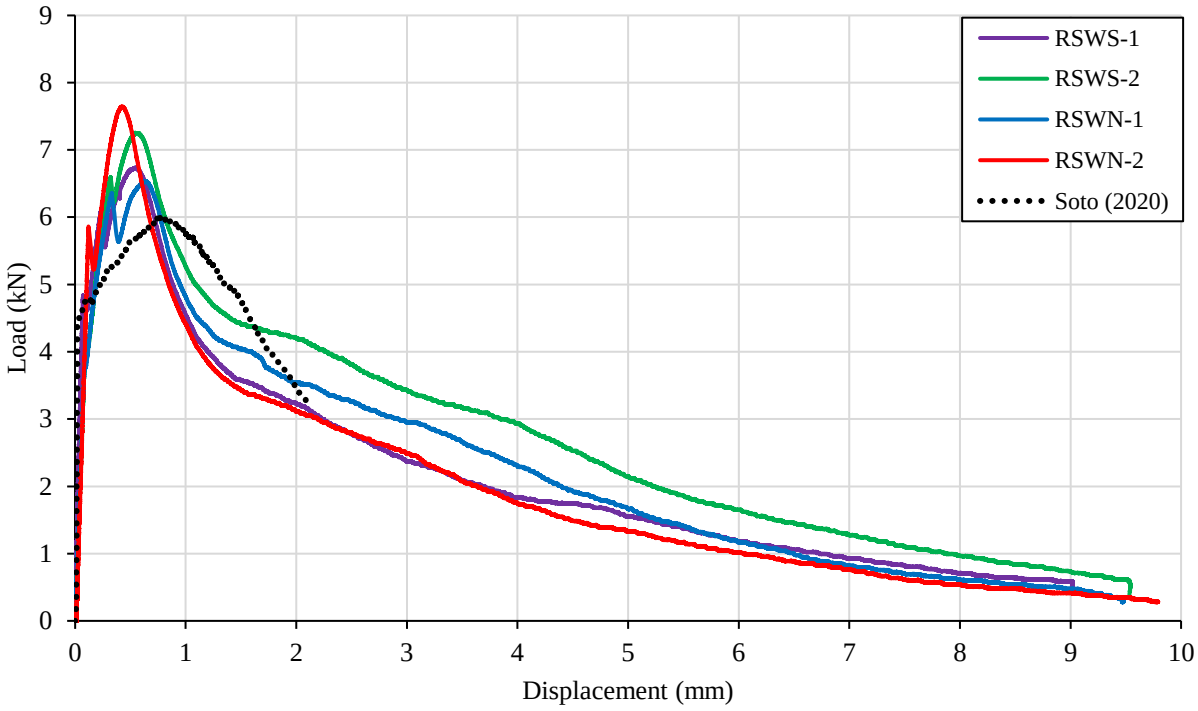

b)

Figure 3.3 Load-Midspan Displacement of a) 280 mm long prisms and b) 500 mm long prisms.

Table 3.3 Response of ECC prisms.

Prism (length-wall-#)	Stiffness (kN/mm)	Load at First Crack (kN)	Displacement at First Crack (mm)	Peak Load (kN)	Displacement at Peak Load (mm)
280-RSWS-1	261.49	11.47	0.047	17.66	0.215
280-RSWS-2	227.57	13.28	0.058	15.34	0.170
280-RSWN-1	252.13	13.56	0.054	16.50	0.223
280-RSWN-2	223.03	10.85	0.049	15.34	0.233
280 Average (STD)	241.06 (16.18)	12.29 (1.16)	0.052 (0.004)	16.21 (0.96)	0.210 (0.024)
500-RSWS-1	53.77	4.81	0.090	6.74	0.560
500-RSWS-2	43.22	4.16	0.096	7.25	0.542
500-RSWN-1	42.79	3.76	0.088	6.54	0.627
500-RSWN-2	53.58	5.86	0.109	7.64	0.421
500 Average (STD)	48.34 (5.34)	4.65 (0.79)	0.096 (0.008)	7.04 (0.43)	0.538 (0.074)
280 (M. A. Soto-Rojas 2020)	319.00	9.07	0.028	10.50	0.219
500 (M. A. Soto-Rojas 2020)	189.91	4.42	0.023	6.02	0.769

Flexural strength is calculated assuming a linear distribution of stress across the full depth of the prism based on Equation 3.1 and the fact that the width and depth of all prisms are equal:

$$\sigma_{flexure} = \frac{My}{I} = \frac{6M}{bh^2} = \frac{6M}{h^3} \quad [3\text{-}1]$$

Where:

$\sigma_{flexure}$= Flexural Strength or MOR (MPa)

M = Moment at peak load (Nmm)

b = Width of the prisms (mm)

d = Depth of the prisms (mm)

It should be noted that this is not a true flexural strength as Equation 3.1 assumes the full cross section of the prism is uncracked. When the peak load is reached during testing the crack would have propagated reducing the uncrack depth of the prism. Despite this simplification it does serve a useful metric to compare the response of prisms tested for this thesis and those tested by Soto-Rojas (2020) with flexural strengths listed in Table 3.4. Prisms tested for this thesis had an average flexural strength of 8.08 MPa and a standard deviation of 0.75 MPa while the two prisms tested by Soto-Rojas (2020) at 28 days after curing had an average flexural strength of 6.01 MPa and a standard deviation of 0.41 MPa.

Table 3.4 Flexural strength of ECC prisms.

Prism (length-wall-#)	$\sigma_{flexure}$ (MPa)
280-RSWS-1	9.42
280-RSWS-2	8.18
280-RSWN-1	8.80
280-RSWN-2	8.18
280 (M. A. Soto-Rojas, 2020)	5.60
500-RSWS-1	7.19
500-RSWS-2	7.74
500-RSWN-1	6.97
500-RSWN-2	8.16
500 (M. A. Soto-Rojas, 2020)	6.42

From both the overall load-displacement responses and the material properties of the prisms, it is evident that the material has changed significant between when it was first tested by Soto-Rojas (2020) at 28 days and the most recent testing at 324/331 days. Considering that the compressive strength had increased by 47% it is likely that the bond strength between the concrete matrix and PVA fibres has also been affected. The cracking exhibited by prisms after loading, both those tested by Soto-Rojas (2020) and for the thesis, are shown in Figures 3.4 and 3.5. Prisms tested by Soto-Rojas (2020) at 28 days demonstrate the typical multiple cracks that are indicative of ductile ECC, however the most recent prisms have only one predominate crack with at most a second hairline crack. This behaviour suggests that the ECC, having aged significantly since 28 days, now had a matrix-PVA bond strength that required a force larger than the tensile resistance provided by the PVA fibres, resulting in fibres being more likely to yield and rupture than to slip from the matrix surrounding them. Although this still provides a fibre bridging effect and increased

ductility compared to normal concrete it could have adverse effects to the damage resilience that have been an important benefit of ECC in structures.

a)

b)

c)

d)

e)

Figure 3.4 Cracking pattern of 280 mm prisms: a) Soto-Rojas (2020) b) RSWS-1, c) RSWS-2, d) RSWN-1, and e) RSWN-2.

a)

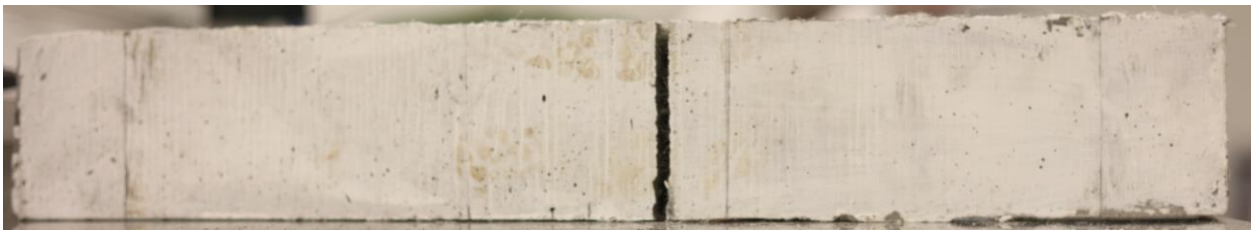

b)

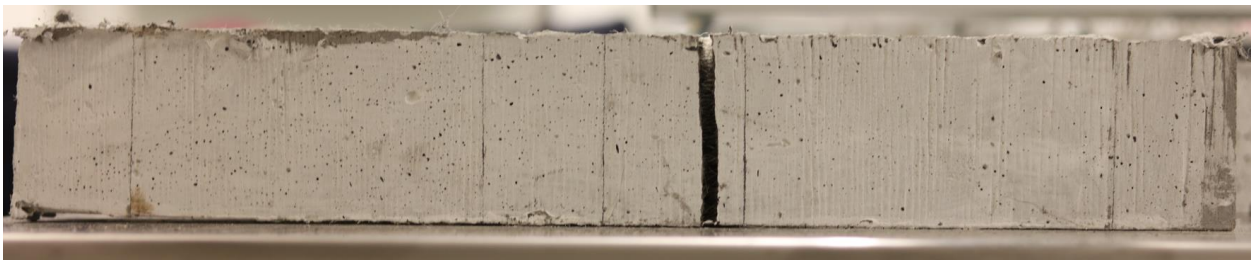

c)

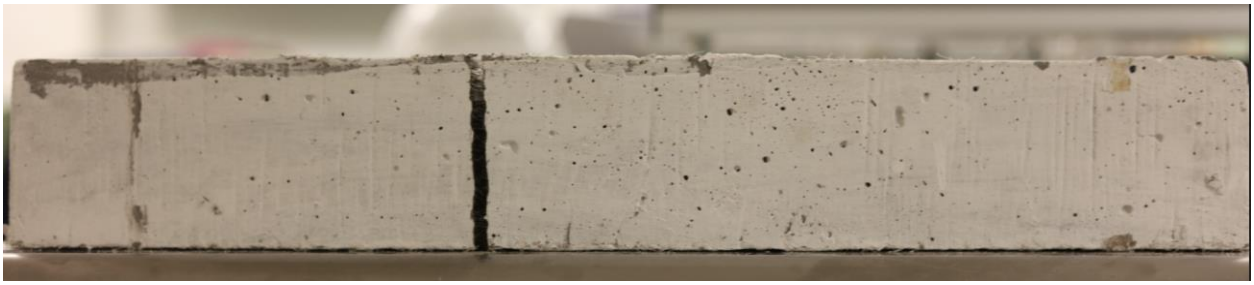

d)

e)

Figure 3.5 Cracking pattern of 500 mm prisms: a) Soto-Rojas (2020), b) RSWS-1, c) RSWS-2, d) RSWN-1, and e) RSWN-2.

4 Numerical Modelling of ECC Prisms

4.1 Introduction

The material characterization of ECC flexural prims allows for the ability to corroborate numerical models in programs such as VecTor2 to the experimental results. This chapter will examine the current capabilities of VecTor2 to accurately model small scale unreinforced ECC specimens. Unreinforced small-scale specimens should provide a more controlled baseline to assess the modelling capabilities of VecTor2 since the lack of any other materials or reinforcement would ideally highlight the key constitutive models needed to properly predict the flexural behavior of ECC. Previous research into modelling of ECC and ECC reinforced structures typically has either small scale models consisting solely of ECC, such as tension coupons or compression specimens, or larger scale structures including reinforcement. Tension and compression specimens can demonstrate the accuracy of stress strain response constitutive models while modelling of larger structural elements where reinforcement and other materials are present highlight the interaction between different element types. In either case it is difficult to directly conclude if the flexural behavior of ECC is accurately captured.

The ECC mix considered in this chapter was described and characterized in Chapter 3. Modelling of this mix had been previously carried out by Soto-Rojas (2020) using the 28-day testing data. Based on the experimental testing of flexural prisms conducted for this thesis, the flexural behavior of the ECC present in the repaired walls at the time of experimental testing likely differed from what had been captured and modelled at 28 days. In an effort to better understand the behavior at the time of testing additional modelling of flexural prisms was undertaken.

There are other FEA modelling software in addition to VecTor2 available to academics and consultants that allow for the modelling and response prediction of reinforced concrete structures. These include, but are not limited to, Atena, Opensees, SeismoStruct, and Abaqus. VecTor2 was chosen for this research due to it robust library of built-in constitutive models which are supported by thorough documentation, in the form of a free-to-access user manual, that explains the theory and formulations behind different models and provides suggestions for best practice Wong et al. (20013). Many of the software noted require that users define their own material response and, while this can allow for very precise recreations of material behaviors, this approach can be daunting for consultants in industry who need to understand the response of the structure they are

modelling. Additionally, this detailed approach often requires large amounts of material properties obtained from specimen testing, something which can become more difficult later into a structures service life. VecTor2, on the other hand, can use limited inputs from basic material properties to produce accurate predictions allowing for greater ease of use. The applicability of VecTor2 has been shown accurate in real world applications particularly in the investigation of structure damage, failures, and repair strategies (VecTor Analysis Group, 2019). Furthermore, VecTor2 is widely used in research and has shown that is can satisfactorily model the response of various structural elements including shear walls.

4.2 Constitutive Models

The default constitutive models for concrete and steel in VecTor2 are shown below in Table 4.1. When modelling the prisms only the Concrete Constitutive Models have an effect since these prisms lacked any steel reinforcement. Note, that although the tension stiffening constitutive model is listed under concrete models it can have a significant effect on reinforced concrete elements. Tension stiffening allows for the concrete in close vicinity to steel reinforcement to retain residual tensile strength after cracking when it would otherwise provide no tensile strength if unreinforced and will be discussed more in Chapter 5. Full details on different constitutive models can be found in the VecTor2 user manual (Wong et al., 2013) but for the purposes of this work the impact of the compression and FRC tension models are most crucial.

Table 4.1 Default Constitutive Models in VecTor2.

Concrete Constitutive Models			
Compression Pre-Peak	Hognestad (Parabola)	**Dilation**	Variable - Isotropic
Compression Post-Peak	Modified Park-Kent	**Cracking Criterion**	Mohr-Coulomb (Stress)
Compression Softening	Vecchio 1992	**Crack Stress Calc**	Basic (DSFM/MCFT)
Tension Stiffening	Modified Bentz 2005	**Crack Width Calc**	Agg/2.5 Max Agg.
Tension Softening	Nonlinear (Hordijik)	**Crack Slip Calc**	Walvern
FRC Tension	SDEM-Monotonic	**Creep and Relaxation**	Not Considered
Steel Constitutive Models			
Hysteric Response	Bauschinger Effect (Seckin)	**Buckling**	Modified Dhakal-Maeka
Dowel Action	Tassios (Crack Slip)	**Concrete Bond**	Eligehuasen

4.2.1 Compression Pre-Peak and Post Peak

The ECC examined presents both a high compressive strength and, due to fibres, would likely have an altered post peak descending branch. Although compression will not have as large an impact on the flexural behaviour of the prisms as the tension softening and FRC tension, it is of use to understand the differences these compression models have on the stress strain response since they will be required for accurate modelling of slender shear walls in Chapter 5. The manual does provide formulations and recommendations for when models are appropriate, for example highlighting that Hognestad and Popovics are applicable for normal strength concretes, but in general the overall differences in stress-strain responses are difficult to visualize and comprehend abstractly. A single 50 mm by 50 mm element, shown in Figure 4.1, was defined in FormWorks, the preprocessor program for VecTor2, to demonstrate these differences. The element has force applied via two-unit support displacements on one face of the element while the opposite side of the element had a pin and roller support. Displacement was applied monotonically in increments of 0.001 mm. The concrete material was defined to have a cylinder compressive strength of 62.92

MPa while the maximum aggregate size and density were defined as 0.3 mm and 1900 kg/m^3 respectively. The straight polyethylene fibre reference type was selected for modelling of the ECC prisms since there is no PVA fibre reference. The fibre properties for the two different PVA fibres used are as follows and are based on manufacturer specifications; PVA fibre 1 had a fibre volume fraction of 1%, a fibre length of 12 mm, a fibre diameter of 0.1 mm, and fibre tensile strength of 1200 MPa while PVA fibre 2 had a fibre volume fraction of 1%, a fibre length of 12 mm, a fibre diameter of 0.4 mm, and fibre tensile strength of 1560 MPa.

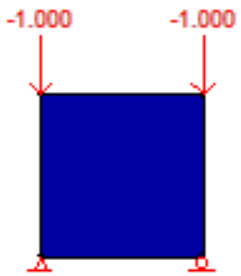

Figure 4.1 Compression element.

The first set of constitutive models considered were the Compression Pre-Peak models, specifically Hognestad, Popovics (NSC), Popovics (HSC), Hoskikuma, Smith-Young, and Lee et al (FRC). All other constitutive models remained constant as shown in Table 4.1. The compressive stress-strain responses are shown in Figure 4.2 while the peak strain values and stiffness of the different models are summarised in Table 4.2. It is evident that all the non-default options for the pre-peak behavior of concrete greatly increase the stiffness of the ascending branch with the only outlier being Lee et al. 2011 (FRC) whose constative model reduces the stiffness of the compression response. This reduced stiffness is beneficial to the overall ductility of the ECC and is chosen as the pre-peak constitutive model going forward for any ECC element. Additional points of interest are that the Hoshikuma and Popovics (NSC) models present nearly the same stress-strain response and that Smith-Young formulation results in a greater initial stiffness for the ascending branch while having the same peak strain value as the two previous models. It should also be noted that the Lee et al (FRC) model modifies the default value used by VecTor2 for the Modulus of Elasticity to $3320\sqrt{f'_c}+6900$ in the presence of smeared fibres.

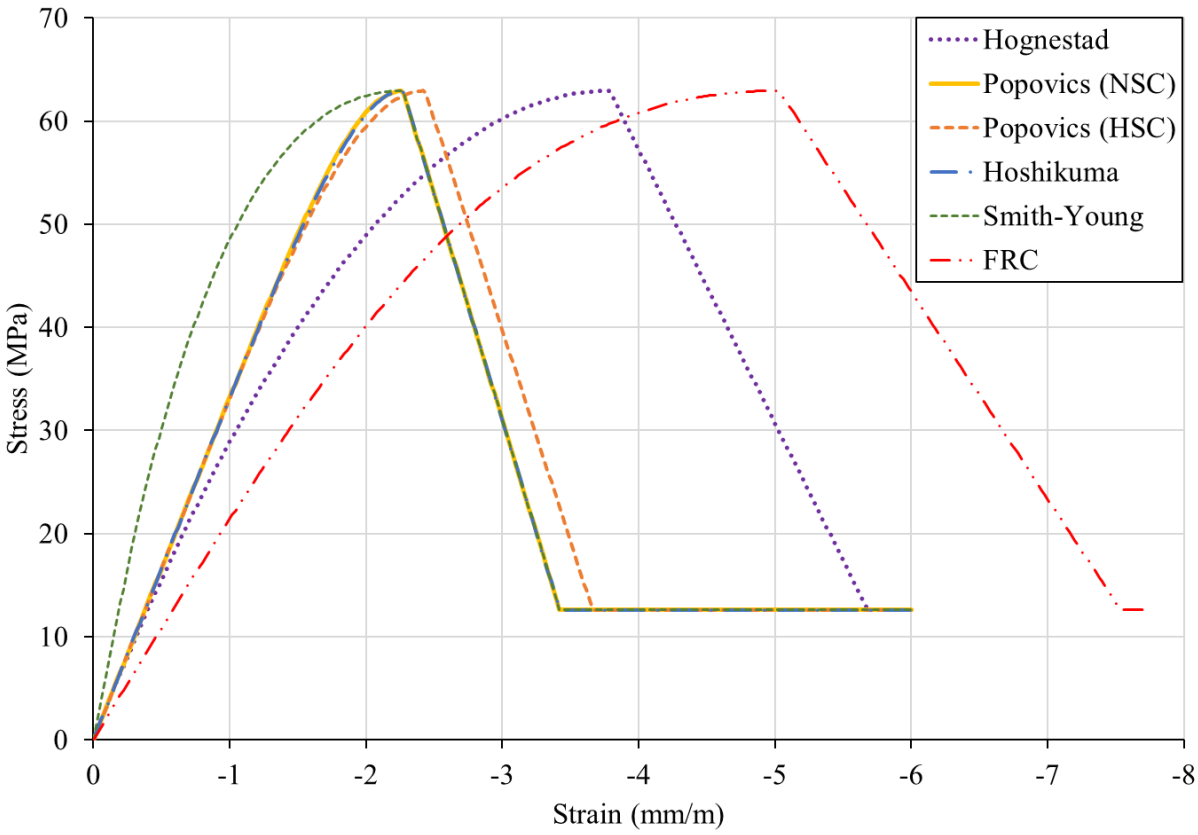

Figure 4.2 Stress-strain response with varied compression pre-peak models.

Table 4.2 Properties of compression pre peak for different constitutive models.

Constitutive Model	Peak Strain (mm/m)	Peak Secant Stiffness (MPa)
Hognestad	-3.78	16651
Popovics (NSC)	-2.26	27850
Popovics (HSC)	-2.42	26008
Hoshikuma	-2.24	28098
Smith-Young	-2.26	27850
FRC	-5.02	12538

VecTor2 provides more options for the compression post-peak model, however some can be applied more freely than others. This is because some post-peak models can simply be chosen in combination with any of the compression pre-peak constitutive models while others can only be implemented in conjunction with the compression pre-peak model of the same name. The models that can be used independently consist of the Modified Park-Kent, Popovics/Mander, Hoshikuma et al, Montoya (2003), and Saenz/Spacone models. The Hognestad, Popovics (NSC), Popovics (HSC), Smith-Young, and Lee et al (FRC) models can only be used for compression post-peak by selecting the "Base Curve" option when their pre-peak counterpart is also defined. All the compression post-peak models that can be independently defined were modelled such that all other constitutive models were left as default. The stress-strain responses of these models are shown below in Figure 4.3. The modified Park-Kent and Hoshikuma et al models consider the descending branch as a sharp linear decent while Saenz/Spacone and Popovics/Mander follow more parabolic and exponential responses. It should be noted that in VecTor2 these four models will maintain a residual strength capacity equal to $0.2f'_c$. All four responses also incorporate factors in their formulation to account for confinement due to reinforcement which would alter the stiffness slope of the descending branches improving the ductility.

The remaining models are difficult to compare directly since the compression pre-peak models do not stay constant. As such the stress-strain responses of models using the Popovics (NSC), Popovics (HSC), Smith-Young, and Lee et al 2011 (FRC) compression post-peak are shown in Figure 4.4, Figure 4.5, Figure 4.6, and Figure 4.7 respectively. Each figure contains the response of a model using all default inputs with the Modified Park-Kent chosen for post-peak compression, the particular compression pre-peak model with Modified Park-Kent post-peak, and the full base curve. The most notable point is that all models seem to incorporate the residual strength capacity equal of $0.2f'_c$ which is not stated in the User Manual and should be kept in mind. Popovics (NSC), Smith-Young, and Lee et al (FRC) all provide improvements in the ductility of the post peak response while Popovics (HSC) does not provide significant deviation from the default Modified Park Kent model. The Hognestad and Montoya 2003 post-peak responses were not presented as the stress strain response was identical to the Popovic/Mander response from Figure 4.3, the cause of which cannot be determined without examining the code implantation of VecTor2.

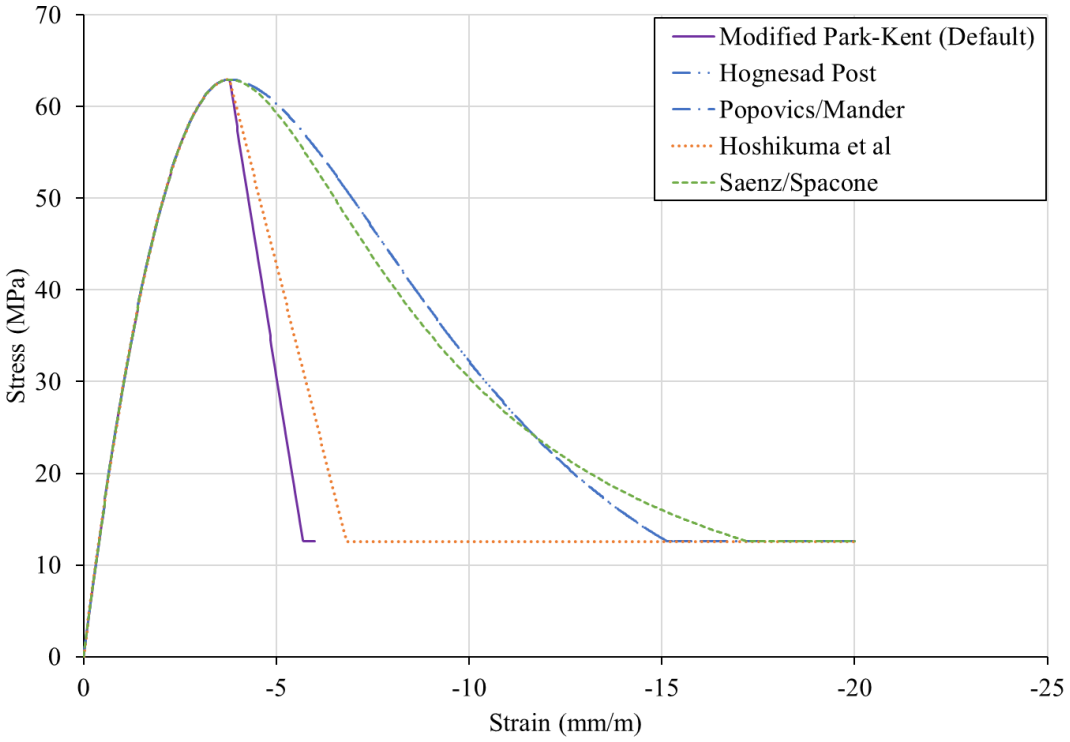

Figure 4.3 Post-peak stress strain response of independent models.

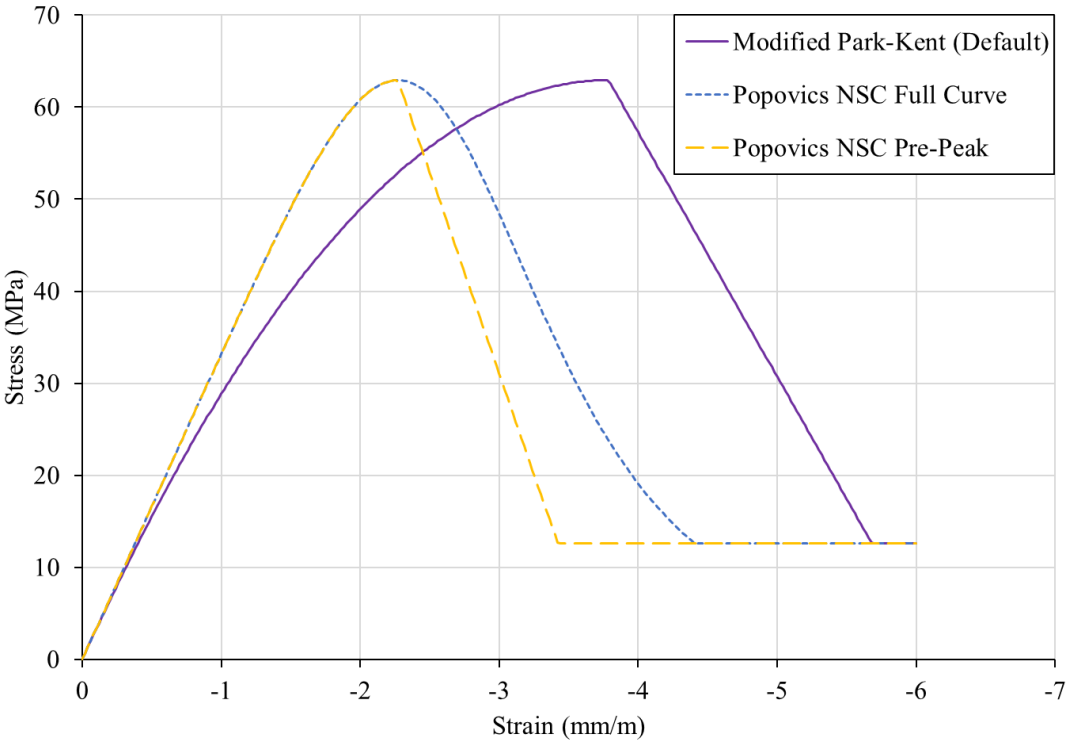

Figure 4.4 Post-peak stress-strain response of Popovics (NSC).

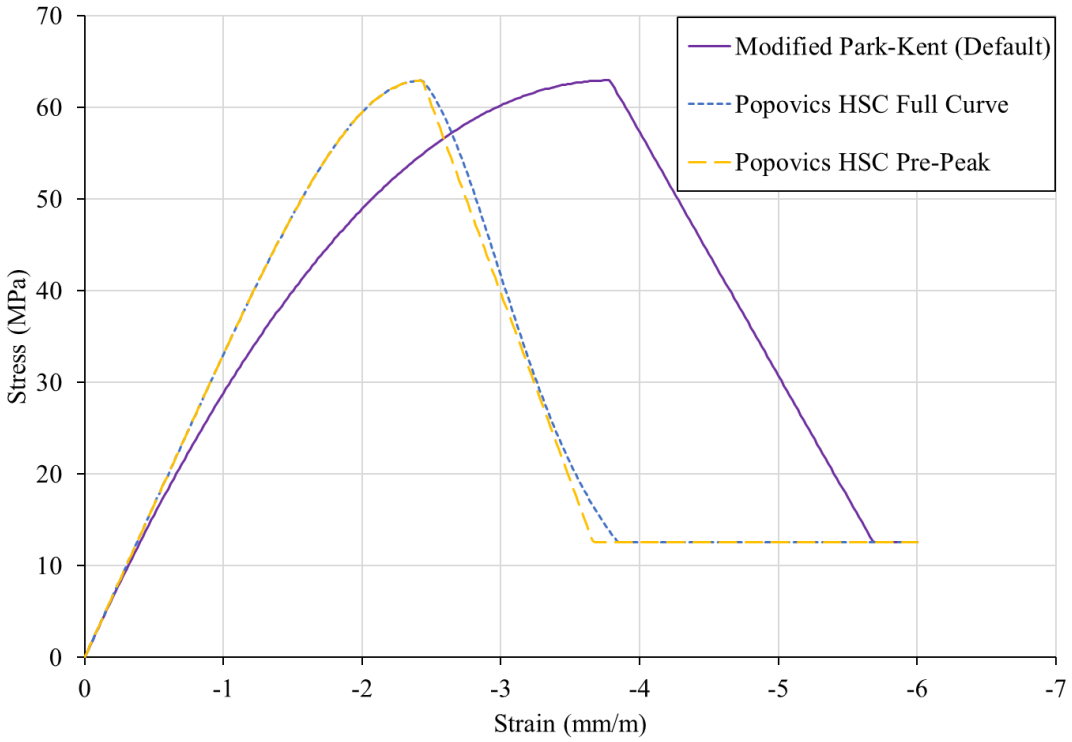

Figure 4.5 Post-peak stress-strain response of Popovics (HSC).

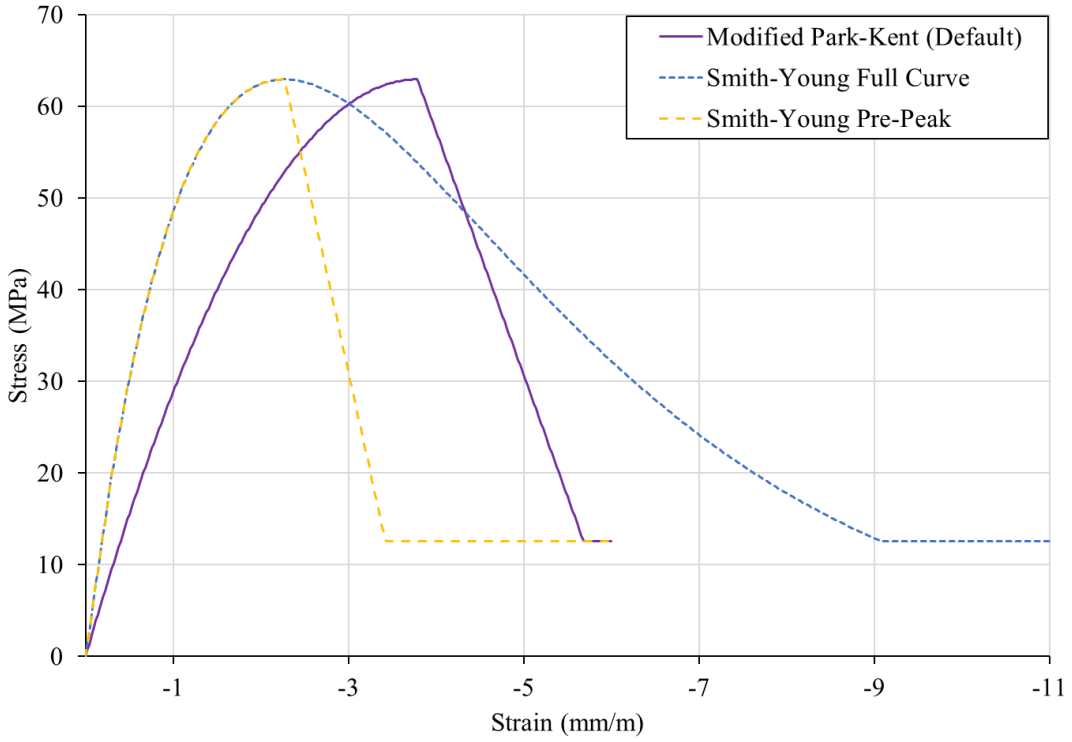

Figure 4.6 Post-peak stress-strain response of Smith-Young.

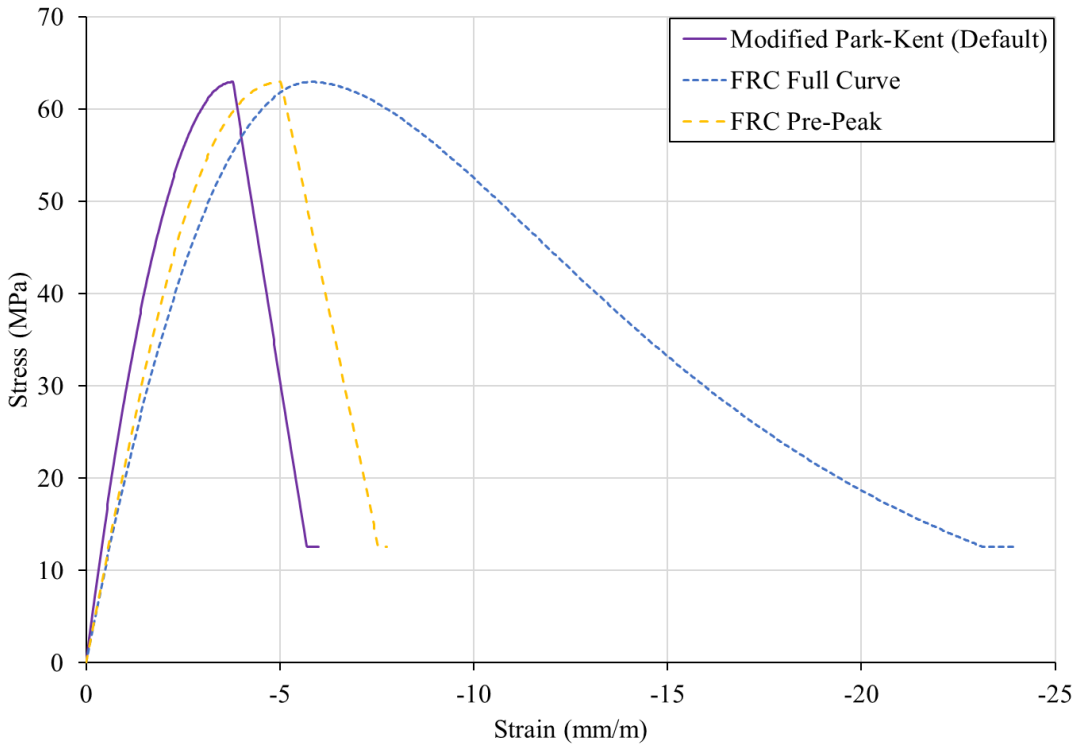

Figure 4.7 Post-peak stress-strain response of Lee et al. 2011 (FRC).

To provide quantitative comparison the ultimate strain, taken as the strain at which $0.2f'_c$ was reached, the ultimate strain with respect to the peak, and the secant stiffness of the descending branch are listed in Table 4.3. The ultimate strain with respect to the peak was taken as the difference between the ultimate strain and either the peak strain from the Hognestad pre-peak response, for models that could be implemented independently, or the peak from the corresponding pre-peak constitutive model, for models that can only be used as an extension of the base curve. The large variance in both ultimate strains and stiffness of the descending branch highlight the importance of selecting the proper post peak behaviour. Similarly, to the compression pre-peak constitutive model, the Lee et al (FRC) post-peak model will be implemented in any models that incorporate ECC going forward to ensure a ductile response and be reflective of the damage resiliency ECC can provide in compression zones.

Table 4.3 Properties of compression post-peak for different constitutive models.

Constitutive Model	Ultimate Strain (mm/m)	Ultimate Strain w/r to Peak (mm/m)	Descending Branch Stiffness (MPa)
Hognestad	-15.14	-11.36	4432
Modified Park-Kent	-5.7	-1.92	26225
Popovic/Mander	-15.14	-11.36	4432
Saenz/Spacone	-17.22	-13.44	3746
Hoshikuma et al	-6.82	-3.04	16563
Popovics (NSC)	-4.42	-2.16	23311
Popovics (HSC)	-3.86	-1.44	34967
Smith-Young	-9.08	-6.82	7383
FRC	-23.14	-18.12	2779

4.2.2 FRC Tension Theory and Formulation

VecTor2 currently contains six built-in options for constitutive models of FRC tension responses: SDEM monotonic or cyclic, DEM, VEM, UVEM, SDEM-UHPFRC, and FIB Model Code 2010. If one of the models are selected, then VecTor2 will calculate the tensile stress due to fibres in the concrete at a given strain and compare this value to the stress calculated from the tension response of the concrete dictated by the Tension Softening models, the larger of which is then used by VecTor2. A summary of the different FRC tension models including the factors considered in their formulation as well as their implementation is provided below. FIB Model Code 2010 is not summarized as it requires inputs from experimental data which is not available for the ECC material that was tested for this thesis.

4.2.2.1 Variable Engagement Model (Voo & Foster, 2003)

The VEM considered fibre distribution, the effect of randomized fibre angles, and damage degradation. For their approach Voo and Foster only considered hooked end and crimped fibres; other models discussed would build on this by considering straight fibres. The tensile stress provided by a fibre was calculated to be as follows:

$$\sigma = K_f K_d \alpha_f \rho_f \tau_b \quad [4\text{-}1]$$

Where

K_f is the fibre orientation factor

K_d is the damage or fibre efficiency factor

α_f is the aspect ratio of a fibre (l_f/d_f)

ρ_f is the volumetric ratio of the fibre content ($V_f \; in \; VecTor2$)

τ_b is the mean shear stress between the concrete matrix and the fibre

K_d is explained by the authors to be a measure of the damage cause by fibre pull out in a region $l_a/2$ way from the crack. They posit that as the volume of fibres increases then the damage factor should decrease due to the proximity of more fibres. The issue of fibres clumping during mixing would also impact this parameter. The authors suggest that given quality materials and proper mixing practice this coefficient can be taken as 1 which is what is implemented in VecTor2.

The simplest use of this equation is when fibres are not considered to rupture in which case K_f is defined as

$$K_f = \frac{\tan^{-1}\left(\frac{w}{\alpha}\right)}{\pi}\left(1 - \frac{2w}{l_f}\right)^2 \quad [4\text{-}2]$$

Where

w is the width of the crack

α is recommended to be $3.5d_f$

When fibre fracture is considered, it is necessary to introduce integration to satisfy force equilibrium of the fibres:

$$K_f = \frac{4}{\pi {l_f}^2} \int_0^{\theta_{crit}} \{max(l_{a,crit} - w, 0)\}^2 \, d\theta \quad [4\text{-}3]$$

Where

$$l_{a,crit} = min\left(\frac{l_c}{2} + w_e, \frac{l_f}{2}\right) \quad [4\text{-}4]$$

$$\theta_{crit} = \tan^{-1}\left(\frac{w}{\alpha}\right) \quad [4\text{-}5]$$

$l_{a,crit}$ is the critical embedment length for fracture to occur

l_c is critical fibre length

$$l_c = \frac{d_f}{2}\frac{\sigma_{fu}}{\tau_b} \quad [4\text{-}6]$$

Voo and Foster also considered fibre bending but this was not incorporated into VecTor2 and as such is not described. When VEM was implemented in VecTor2 the following relation was given for τ_b:

$$\tau_b = \begin{cases} 2.5{f'}_t \ for\ concrete\ with\ hooked-end\ fibres \\ 2.0{f'}_t \ for\ concrete\ with\ straight\ fibres \\ 1.2{f'}_t \ for\ mortar\ with\ hooked-end\ fibres \\ 1.0{f'}_t \ for\ mortar\ with\ straight\ fibres \end{cases}$$

VecTor2 classifies a material as concrete, or mortar based on the maximum aggregate size input in the material properties. Materials with an aggregate size of 2mm or larger are classified as concrete while those below 2mm are considered mortar.

4.2.2.2 Unified Variable Engagement Model (Htut T.N.S. & Foster, 2010)

Htut and Foster looked to improve the VEM model by unifying two different methods of deriving VEM that had been explored, termed the VEMI and VEMII models. The later model used a lumped model which although more physically accurate was more intensive compared to uniformed bond models. The unified model also considered straight fibres by treating them as hooked fibres where the hooked ends had a length of 0. The results of their unified model were the following calculations:

$$\sigma = K_f K_d \alpha_f \rho_f \tau_{b,ave} \quad [4\text{-}7]$$

$$K_f = \frac{1}{2}\left(\frac{a+b}{\pi}\right)\left(1-\frac{2w}{l_f}\right)^2 \quad [4\text{-}8]$$

$$\tau_{b,ave} = \tau_{b.0} + 0.0625{\gamma_{crit}}^3 \quad [4\text{-}9]$$

$$\gamma_{crit} = \frac{2\gamma_{max}}{\pi}\tan^{-1}{}^3\sqrt{\frac{w}{\alpha l_f}} \quad [4\text{-}10]$$

$$\gamma_{max} = |\emptyset| + \frac{\pi}{2}\left(\frac{\pi}{2} \le \gamma_{max} \le \pi\right) \quad [4\text{-}11]$$

$$a = \min\left[\gamma_{crit}, \frac{\pi}{2} - |\emptyset|\right] \quad [4\text{-}12]$$

$$b = \gamma_{crit} \quad [4\text{-}13]$$

Where

$\tau_{b,ave}$ is the average bond contribution from all engaged fibres

$\tau_{b.0}$ is the bond stress of a fibre when the bending angle is 0

γ_{crit} is the maximum bending angle of a fibre

4.2.2.3 Diverse Embedment Model (Lee et al., 2011a)

The DEM considered both frictional bond, which is the dominate force in straight fibres, and anchorage effects, which provide additional benefits to hooked fibres. This required consideration of two theoretical cases for the pullout behaviours of a single fibre; that the fibre has either one or two ends embedded in a concrete matrix. For the case where a straight fibre has only one end embedded in concrete Lee et al proved that slip along the length of the fibre is nearly constant and that the interaction can be considered as a rigid body translation thus neglecting any elastic strain displacement. When considering a straight fibre embedded on both ends it was shown that the slip at peak bond strength could be twice as great as that in the single embedded end case. Having satisfied conditions for straight fibres, the calculations were extended to consider the anchorage effects due to hooked fibres. The average fibre stress was derived as

$$\sigma_{f,cr} = \frac{4\tau_{short}(l_a - s_{short})}{d_f} + \frac{4P_{eh,short}}{\pi {d_f}^2} \quad [4\text{-}13]$$

Where

$\sigma_{f,cr}$ is the stress of a fibre at cracking (MPa)

τ_{short} is the frictional bond strength of the short fibre end

l_a is the fibre embedment length at the short end

s_{short} is the slip due to the shorter embedment length at cracking

$P_{eh,short}$ is the mechanical anchorage force due to embedment of the short fibre end

Equation 4.13 can be applied to both straight and hooked end fibres by removing the second term if the fibres in question are straight. For simplicity the calculations presented above had assumed a fibre normal to the crack surface. To consider the randomly distributed nature of fibre alignments not normal to the crack face and fibre embedment length a general equation for the average stress in a fibre was derived as:

$$\sigma_{f,cr,avg} = \frac{1}{\frac{l_f}{2}} \int_0^{\frac{l_f}{2}} \sigma_{f,cr,\theta}\,(l_a) dl_a \qquad [4\text{-}14]$$

Where

$\sigma_{f,cr,avg}$ is the average stress of a fibre at a crack considering random fibre orientations and embedment lengths

l_f is the fibre length

$\sigma_{f,cr,\theta}$ is the fibre stress as a cracked averaged through a various θ for the given length of l_a

The final consideration given was how to incorporate a factor to reflect the impact element dimensions have on the orientation of fibres. This fibre orientation factor is denoted as α_f, not to be confused with the aspect ratio in VEM, and requires integration based on the shape of the element considered. For a rectangular element the tensile stress can then be calculated as:

$$f_f = \frac{1}{A_c} \int_{A_c} \alpha_{f,3D}(y,z) V_f \sigma_{f,cr,avg}(y,z) dA_c \qquad [4\text{-}15]$$

The numerical model was then verified against 20 SFRC specimens from three independent studies that covered a range of straight and hooked end fibres (Lee et al., 2011b). It was shown that the model provided reasonable responses when observing tensile stress vs crack width. The

experimental results did highlight that the size of the specimen could provide significant variance in results.

When implemented in VecTor2 the fibre orientation factor is calculated:

$$\alpha_f = \begin{cases} -0.05\left(\frac{h}{l_f}\right)^{2.8} + 0.64 & for \ \frac{h}{l_f} \leq 1 \\ 0.087\left(\frac{l_f}{h}\right)^{1.12} + 0.5 & for \ \frac{h}{l_f} > 1 \end{cases}$$

4.2.2.4 Simplified Diverse Embedment Model (Lee et al., 2013)

The Diverse Embedment Model by Lee et al. (2011a) had been proven to work well; however, it did require a double integration, Equation 4.15, which can be both numerically intensive and difficult to incorporate into existing models such as DSFM and programs like VecTor2. The need for the double integration arises from the compatibility checks required when calculating the crack width as a summation of slip from both embedded lengths. To achieve the simplification Lee et al. (2013) made the assumption that the crack width is equal to the slip on the short, embedded length of the fibre. Two coefficients are introduced for the straight fibre and hooked fibre cases, β_f and β_{eh} respectively, to ensure this assumption does not overestimate the tensile strength contribution of fibres. The tensile force due to frictional bond is calculated as:

$$f_{st} = \alpha_f V_f \sigma_{f,cr,st} = \alpha_f V_f K_{st} \tau_{f,max} \frac{l_f}{d_f}\left(1 - \frac{2w_{cr}}{l_f}\right)^2 \quad [4\text{-}16]$$

$$where \ K_{st} = \begin{cases} \frac{\beta_f}{3}\frac{w_{cr}}{s_f} & for \ w_{cr} < s_f \\ 1 - \sqrt{\frac{s_f}{w_{cr}}} + \frac{\beta_f}{3}\sqrt{\frac{s_f}{w_{cr}}} & for \ w_{cr} \geq s_f \end{cases}$$

Where

K_{st} is frictional bond factor

$\tau_{f,max}$ is the frictional bond strength

w_{cr} is the width of the crack

β_f is taken as 0.67 in Lee et al (2013) and 0.6 when implanted in VecTor2 (Wong et al., 2002b)

The tensile force due to mechanical anchorage is defined as

$$f_{eh} = \alpha_f V_f \sigma_{f,cr,eh} = \alpha_f V_f K_{st} \tau_{eh,max} \frac{2(l_i - 2w_{cr})}{d_f} \quad [4\text{-}17]$$

$$where\ K_{eh} = \begin{cases} \frac{2}{3}\frac{w_{cr}}{s_{eh}} - \frac{1}{5}\left(\frac{w_{cr}}{s_{eh}}\right)^2 & for\ w_{cr} < s_{eh} \\ 1 + \left(\frac{7\beta_{eh}}{15} - 1\right)\sqrt{\frac{s_f}{w_{cr}}} - \frac{2\left(\sqrt{w_{cr}} - \sqrt{s_{eh}}\right)^2}{l_f - l_i} & for\ s_{eh} \le w_{cr} < \frac{l_f - l_i}{2} \\ \left(\frac{l_i - 2w_{cr}}{2l_i - l_f}\right)^2 K_{eh,i} & for\ \frac{l_f - l_i}{2} \le w_{cr} < \frac{l_i}{2} \end{cases}$$

Where

K_{eh} is mechanical anchorage factor

$K_{eh,i}$ is K_{eh} at $w_{cr} = \frac{l_f - l_i}{2}$

$\tau_{f,max}$ is pull out strength due to mechanical anchorage

l_i is distance between mechanical anchorages (hooks) for hooked end fibres

The total tensile strength provided by fibres is then either f_{st} if using straight fibres or f_{st}+f_{eh} if using hooked fibres. The SDEM was compared to DEM and found to provided similar stress-crack width response despite less intensive calculations. SDEM was further compared to experimental data consisting of SFRC tension and flexural responses. Additional work was done to implement a cyclic response of the SDEM in VecTor2. The backbone curve of the cyclic model follows the above-described formulations but also includes calculations for unloading and reloading stiffnesses based on the maximum crack width (Wong et al., 2013).

4.2.2.5 UHPFRC SDEM (Franssen et al., 2021)

Franssen et al wanted to extend the capabilities of SDEM model, which had initially been verified against traditional FRC, to Ultra High-Performance Fibre Reinforced Concrete (UHPFRC). The main change implemented was to the value of $\tau_{f,max}$ which in the SDEM model was limited to $0.396\sqrt{f'_c}$ and $0.429\sqrt{f'_c}$. Franssen et al instead proposed $\tau_{f,max}$= $0.75\sqrt{f'_c}$ to account for the strong bond UHPFRC can have with fibres. The tensile strength of the concrete matrix was also

increased to $0.6\sqrt{f'_c}$ and new calculations for crack spacing to be more reflective of UHPFRC which in turn affect the strain calculations used in VecTor2. These suggestion modifications showed agreement with experimental data.

4.2.3 FRC Tension Model Implementation

To demonstrate the differences between the models, the same single element described in Section 4.2.1 was used except that the support displacement loads were changed to a negative unit to apply pure tension. All constitutive models were kept default except for the compression pre and post-peak, which both used Lee et al 2011 (FRC), while FRC Tension was varied. The stress-strain responses are shown below in Figure 4.8.

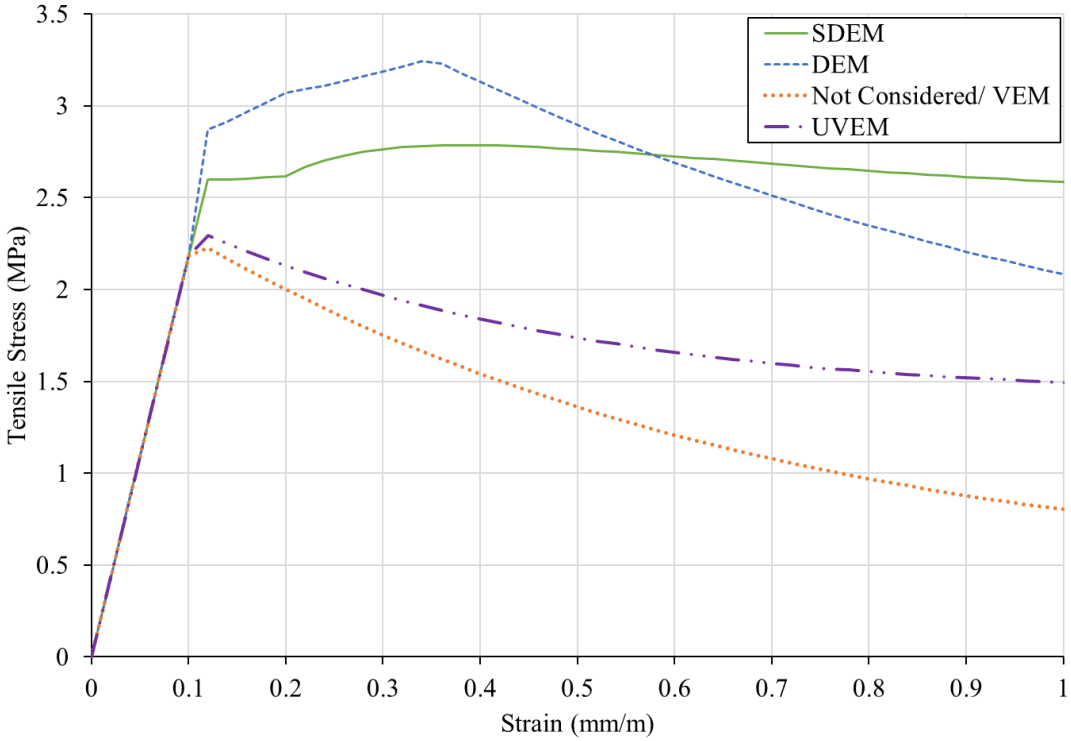

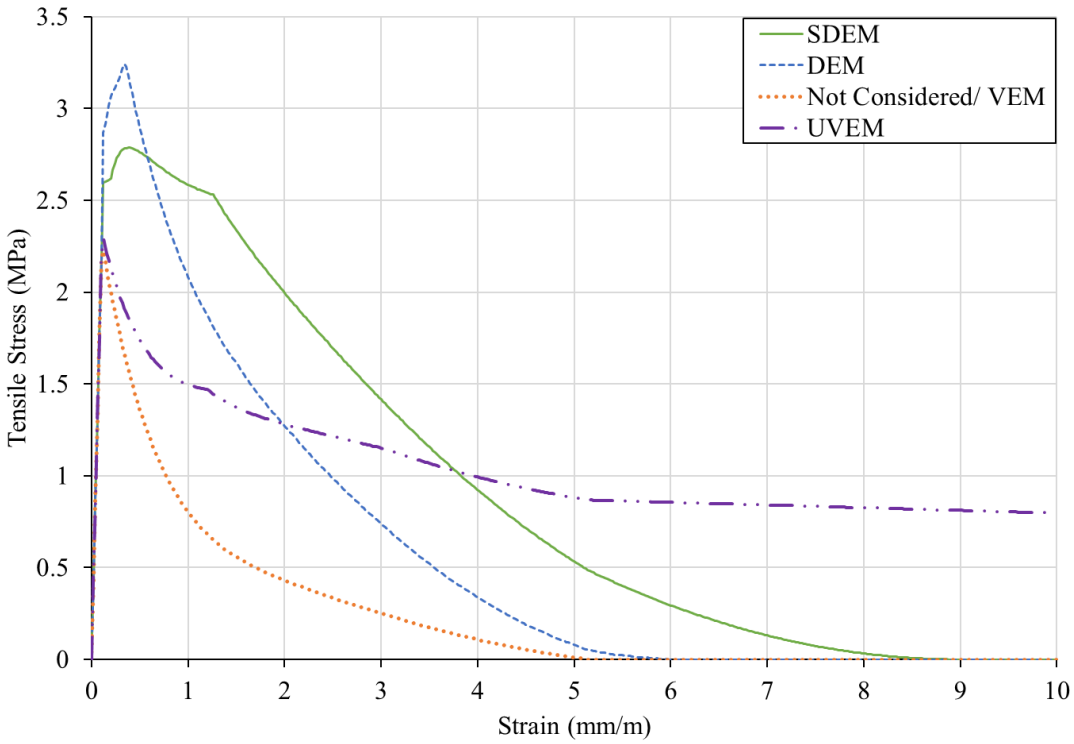

Figure 4.8 Tensile stress-strain response of different FRC tension models.

The cracking stress, cracking strain, peak stress, peak strain, and ultimate strain of each FRC tension response are provided in Table 4.4. The first thing to note is that when FRC tension is not considered it provides the same response as when VEM is specified as the FRC tension model. This highlights a limitation of VEM for modeling ECC. ECCs have a maximum aggregate size less than 1mm and use straight fibres; the combination of these two factors based on the formulation of VEM in Section 4.2.2. results in a maximum bond strength of $1.0f'_t$. This limited bond strength will result in a response identical to that of normal concrete. Use of UVEM does not appear to provide significant improvement to the ultimate tensile strength of the ECC but does greatly increase the residual strength capacity far beyond any other model. DEM provides a significantly larger peak strength, but this comes at a more brittle post peak behaviour while SDEM despite providing a more conservative value for the peak stress allows for the formation of a more gradual initial descending branch and greater ultimate strain which would be considered more ductile.

Table 4.4 Properties of tensile response.

FRC Tension Model	Cracking Stress (MPa)	Cracking Strain (mm/m)	Peak Stress (MPa)	Peak Strain (mm/m)	Ultimate Strain (mm/m)
Not Considered/ VEM	2.225	0.12	2.225	0.12	5.14
UVEM	2.292	0.12	2.292	0.12	117.26
DEM	2.869	0.12	3.242	0.34	5.98
SDEM	2.598	0.12	2.786	0.38	8.88
SDEM UHPFRC	3.92	0.12	9.863	3.68	NA

The response of a single element implementing the SDEM UHPFRC FRC tension model is shown in Figure 4.9 with the SDEM response for reference. The increased cracking load is reflective of the change in the default calculation for the bond strength. Overall, the tensile strength is far above what any other FRC tension model can provide and for the purposes of ECC would be a grave overestimate based on reported tensile values found during the literature review.

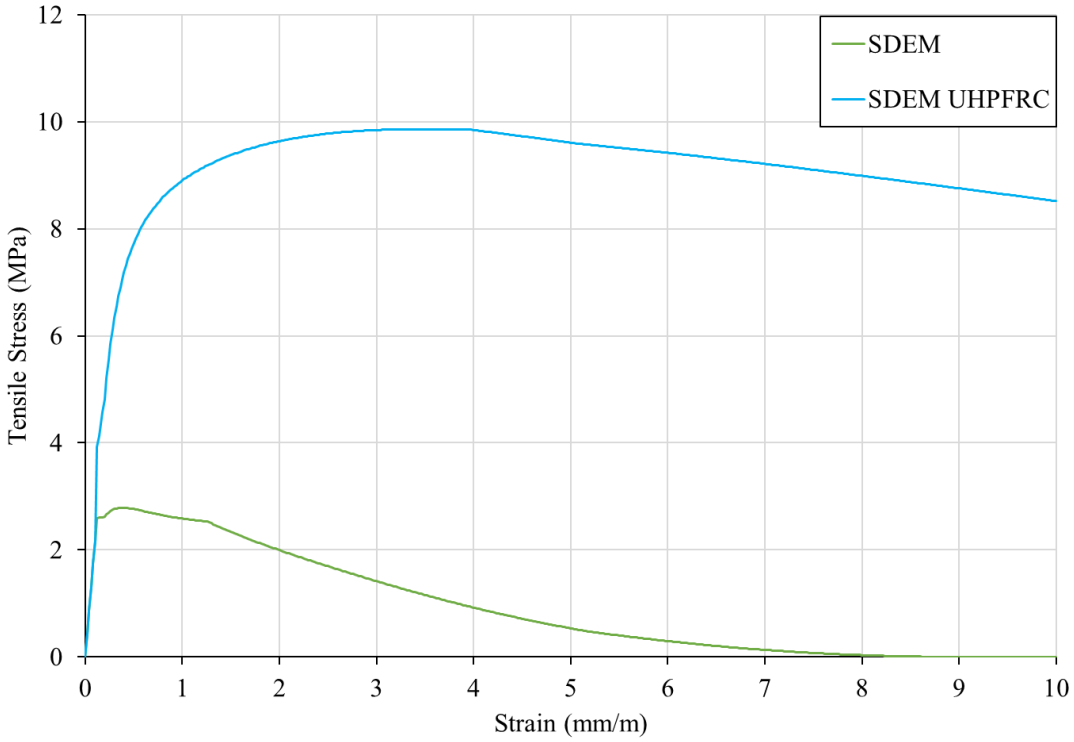

Figure 4.9 Comparison of stress-strain response due to SDEM and SDEM UHPFRC.

4.3 FEA Prism Modelling in VecTor2

Modelling of unreinforced flexural prisms does not use all of VecTor2's capabilities and functions. For this reason, only what is required to create the models (such as Mesh Discretization, Material Properties, and Constitutive Models) will be discussed and outlined in this chapter while a more detailed discussion will be conducted in the following chapter.

4.3.1 Prism Mesh Definition and Discretization

Models in VecTor 2 are first defined and created in the FormWorks preprocessing program. Within FormWorks it is necessary to define the structure geometry and the mesh size that will determine the nodal points. Regions are used to define the geometry of different sections in the structure, the "Regions" panel is shown in Figure 4.10 and can be brought up by selecting the "Define Mesh and Structures" in the top ribbon.

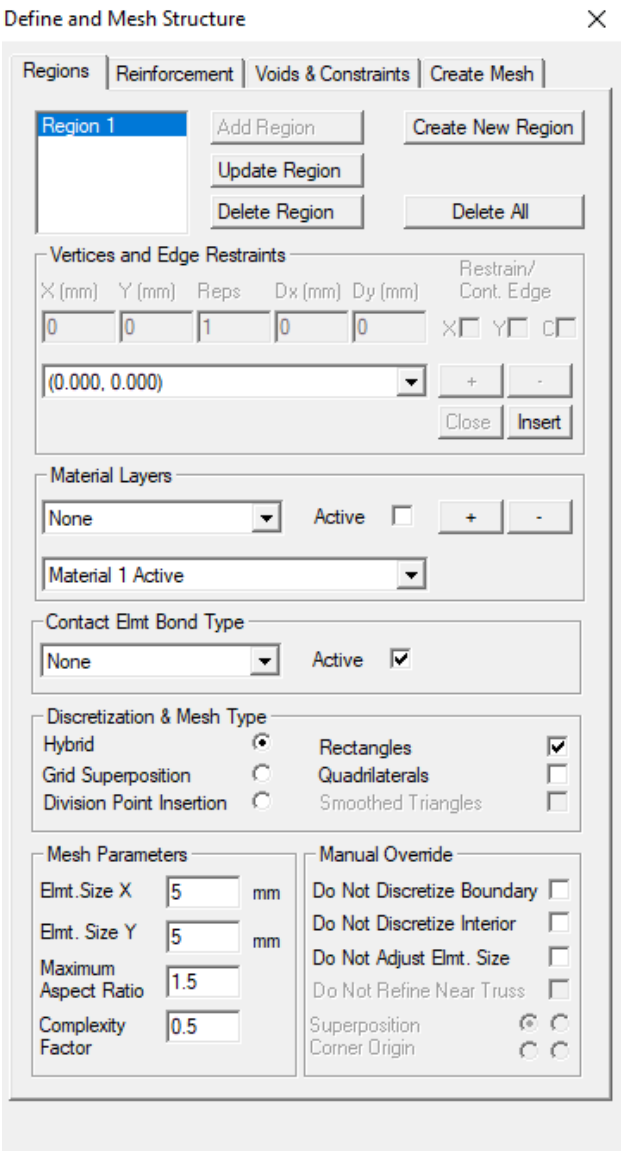

Figure 4.10 Regions panel.

The 2-D models of the flexural prims are single rectangles which only requires a single region with a hybrid discretization and a rectangular mesh type. Best practice, as outlined by Palermo & Vecchio (2007) is to define the mesh size of elements such that there are at least 14-20 elements in the smallest dimension. In the case of both the 280 mm and 500 mm long prims the smallest dimension would be the height of 75 mm which is divisible into 15 elements with a size of 5mm. The final element size used was 5 mm by 5mm for both prisms which maintained an ideal aspect ratio of 1. Based on having an element size measuring 5mm x 5mm it was necessary to increase the length of the 280 mm prims to 285 mm in Formworks to ensure that the 75mm spacing

between loading points and nodal restrains was reflective of test conditions. Loading was applied through two support displacements while restraints consisted of one pin and one roller. The prism models for the 280 mm and 500 mm long prims are shown in Figure 4.11.a) and b) respectively.

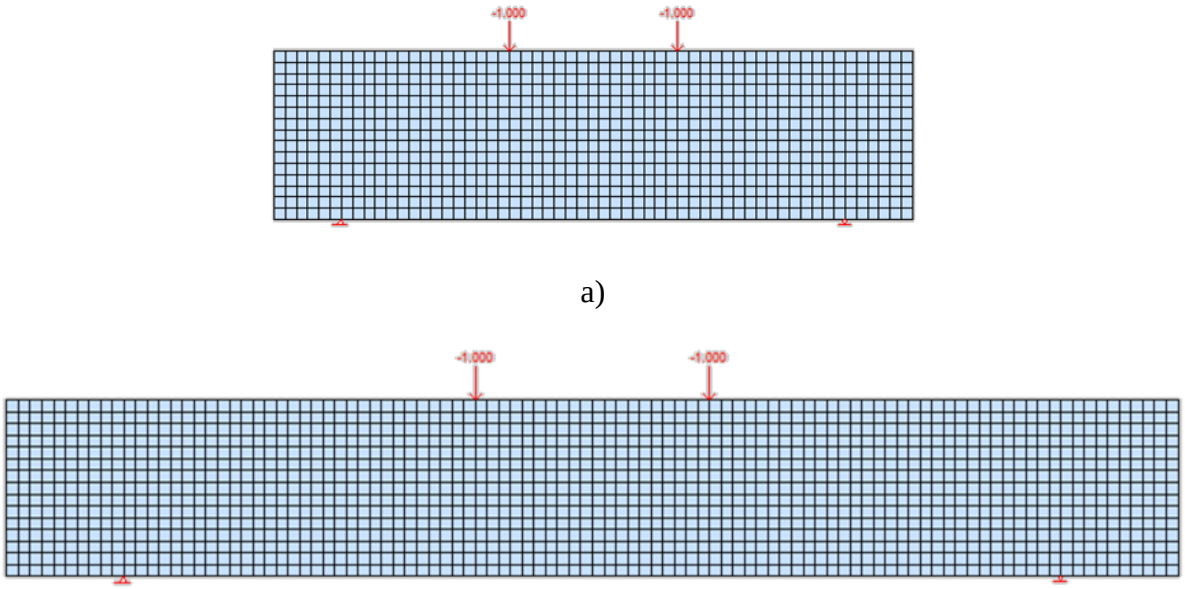

a)

b)

Figure 4.11 FEA models for: a) 280 mm and b) 500 mm prisms.

4.3.2 Prism Material Definition

The ECC material was defined in the Define Material Properties panel shown in Figure 4.12. ECC can be defined in VecTor2 as a Reinforced Concrete. The cylinder compressive strength was defined as 70 MPa (the average of compressive strength of cylinders tested in Chapter 3) for all prisms while the maximum aggregate size and density were defined as 0.3 mm and 1900 kg/m^3 respectively. The fibres found in ECC can be defined as a "Fibre Reinforcement" in the smeared reinforcement properties on the right side of the panel. Currently, VecTor2 only includes Steel – Hooked, Steel – Straight, Polypropylene – Straight, and Polypropylene – Hooked as options for the types of fibre that can be included. VecTor2 includes inputs for fibre volume fraction V_f, fibre length L_f, fibre diameter D_f, fibre tensile strength F_u, fibre bond strength T_u, and residual flexural strength. Residual flexural strengths are used only if the FIB Model Code 2010 option is selected for the FRC Tension constitutive model. The remaining inputs are all necessary except for fibre

bond strength which if left blank will be assigned a default value based on the fibre type and FRC Tension model chosen by the user. The PVA fibres were defined the same as in Section 4.2.1.

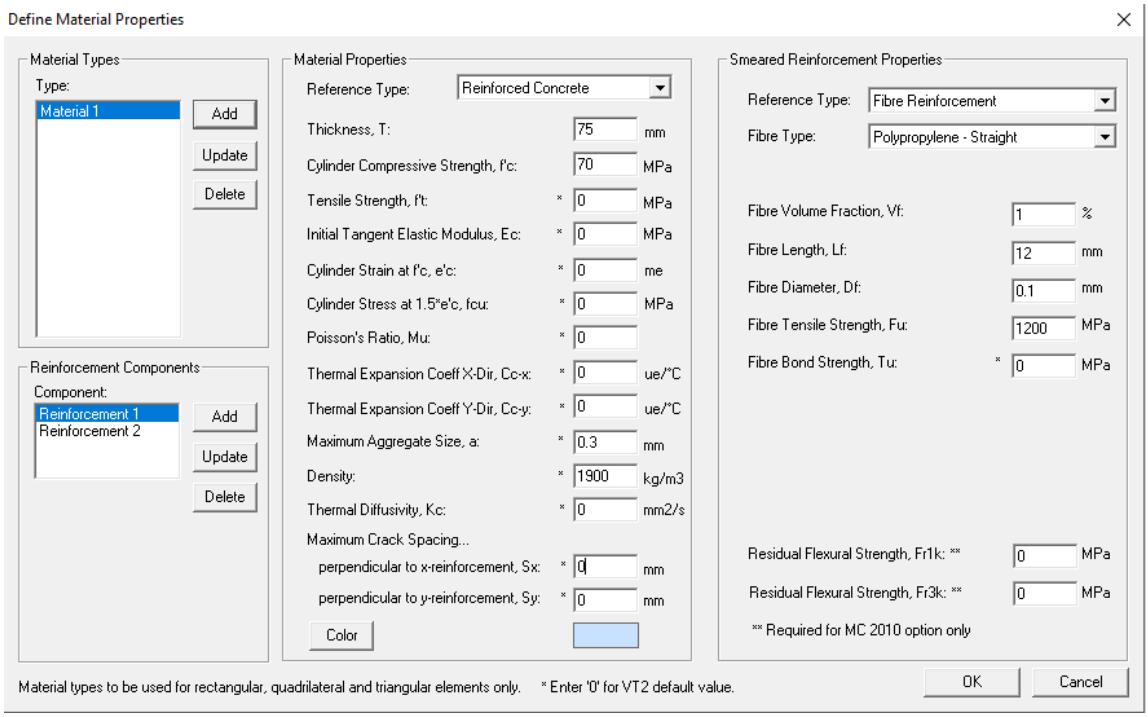

Figure 4.12 Define Material Properties panel for ECC.

Constitutive models were left as default where possible, the exceptions being compression pre-peak, compression post peak, and FRC tension which were chosen as Lee et al 2011 (FRC) for both compression models and varied for the FRC tension. Load was applied monotonically in 0.05mm increments by two support displacements spaced as outlined in the experimental procedure for flexural testing from Chapter 3.

4.3.3 Results of FEA Modelling of Prims with Built in Models

The load-midspan displacement results of the 280 mm and 500 mm prisms are shown below in Figure 4.13 while the peak load and midspan displacement are presented in Table 4.5. It is important to note that like the tension responses presented in Section 4.2.3 the VEM response is identical to a response which does not consider FRC tension. Across both the 280 mm and 500 mm prisms it is clear that the only built in FRC tension model that provides a gradual reduction in load carry capacity is the UVEM with all remaining models having a sudden drop in load following the peak of their response. The DEM and SDEM are able to more accurately predict the peak load capacity of the prims while they vary between a slightly better to far worse ability to predict the

displacement at peak load. The SDEM model consistently provides the greatest overestimation of displacement at peak load with an 83.3% and 106.7% error for the 280 mm and 500 mm prims respectively. The UVEM model provides a minimal increase in the load carry capacity imparted by the PVA fibres compared to the VEM. The overall response of the FEA models is not satisfactory since a user is forced to choose between selecting a model that can predict the load capacity or better represent the gradual load loss due to propagation of cracking.

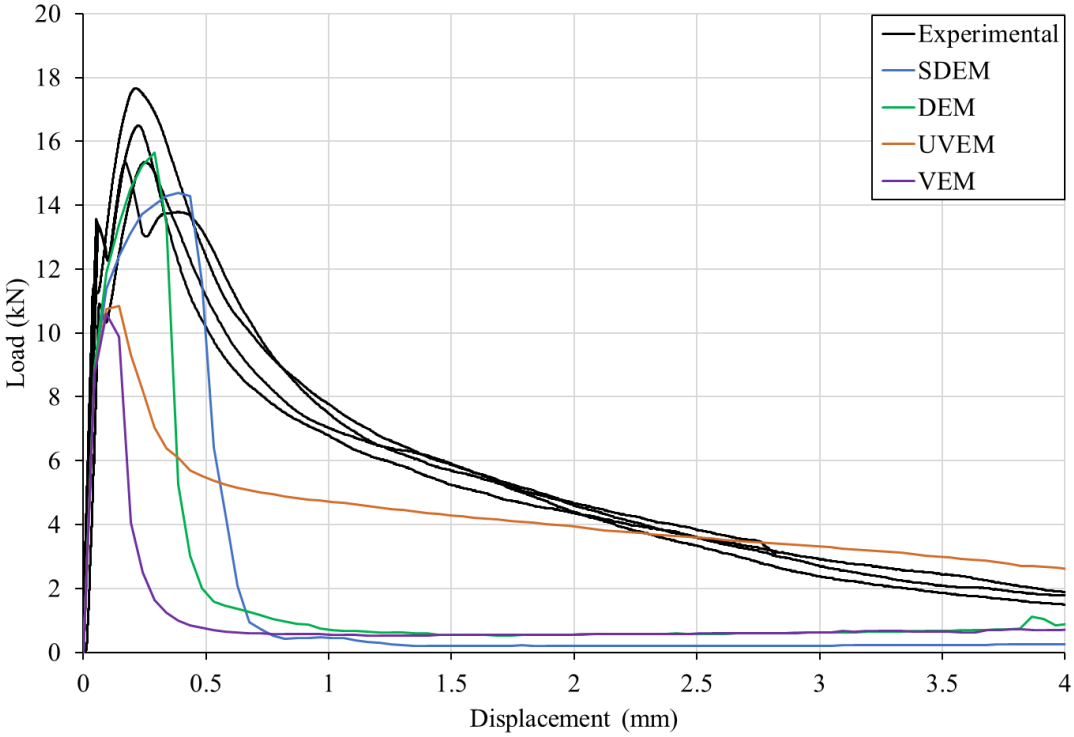

a)

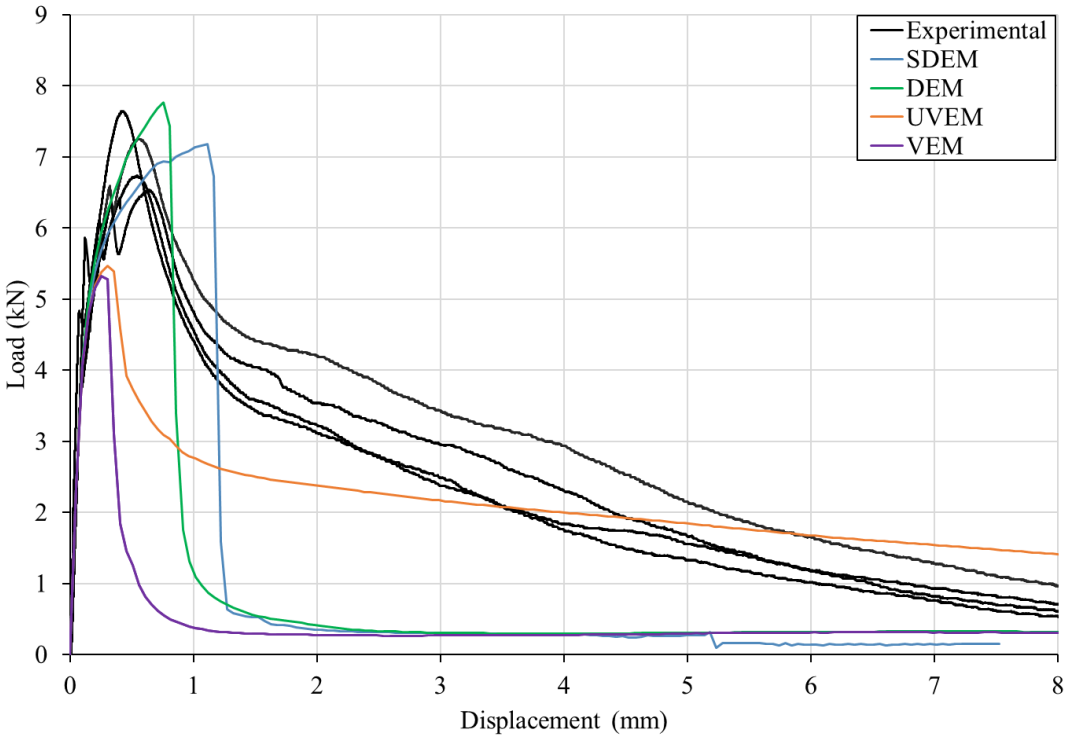

b)

Figure 4.13 Load-Midspan displacement response of FEA models and experimental data for: a)280 mm long and b) 500 mm long prisms.

Table 4.5 Peak values for prism models.

Response	Peak Load (kN) (% Error)	Displacement at Peak Load (mm) (% Error)
280 Experimental Average	16.21	0.210
280 VEM	10.60 (-34.6)	0.095 (-54.8)
280 UVEM	10.85 (-33.1)	0.144 (-31.4)
280 DEM	15.66 (-3.4)	0.289 (37.6)
280 SDEM	14.39 (-11.2)	0.386 (83.8)
500 Experimental Average	7.04	0.538
500 VEM	5.32 (-24.4)	0.251 (-53.3)
500 UVEM	5.46 (-22.4)	0.302 (-43.9)
500 DEM	7.76 (10.2)	0.756 (40.5)
500 SDEM	7.18 (2)	1.112 (106.7)

4.3.4 User Defined Custom Tension Stiffening Constitutive Model

The models covered so far have been built in models due to their plug and play nature which only require that a user input the smeared properties of the fibres used, parameters that are easily found and typically known when ordering fibres from a supplier. The alternative to using a built-in model is to make use of the "Custom Input (Stain Based)" option available as a Tension Softening model based on data from tensile testing, often in the form of tension coupons, or through inverse analysis of flexural prisms. This model, shown in Figure 4.14, allows the user to define up to four points which the program will use to linearly interpolate any stress value based on the computed element strains. A "Custom Input (Crack Based)" model is also available and functions the same except instead of inputting strain values the user defines crack widths in mm which the program converts

based on the formation $w = 1000 * \frac{\varepsilon_{c1}}{s_{cr1}}$ where w is the crack width, ε_{c1} is the strain, and s_{cr1} is the crack spacing. It is important to note that since this is intended to provide a softening response VecTor2 will calculate the initial response until cracking assuming a linear elastic behaviour. The strain is based on the f'_t and Elastic Modulus of the RC material and VecTor2 will override any defined points located before the cracking strain.

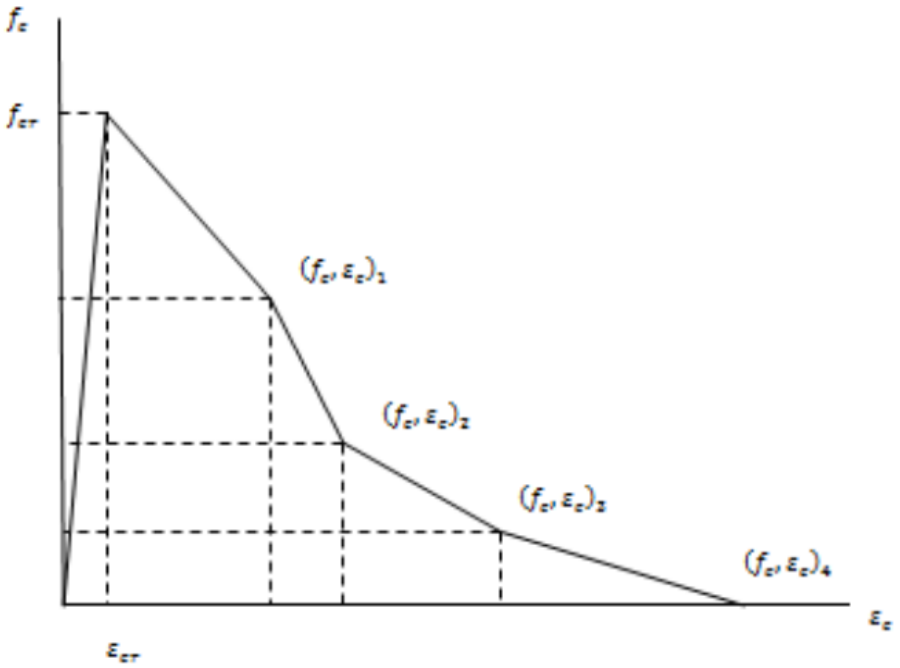

Figure 4.14 Stress-strain response based on Custom Input Wong et al. (2013).

The Custom input model has been used to model SFRC in VecTor2 by Saikali (2019), Yang et al. (2020), Tolou-Kian (2020), and Zhang (2020). The methods used varied with Saikali and Yang et al performing inverse analysis of prisms following Annex 8.1 of CSA-S6, Kian using inverse analysis of prisms following FIB (2013), and Zhang using both inverse analysis of prisms and direction tension tests. Custom inputs were also applied in the modeling of ECC by Soto-Rojas (2020) and Tolou-Kian (2020). When used on ECC the two methodologies applied where either taking a trilinear response from direct tension coupon tests (Kian) or an interactive curve fitting approach using experimental flexural prisms (Soto-Rojas). The experimental data available for the ECC material in this thesis only consists of flexural prisms which limits the use of inverse analysis techniques originally developed for SFRC. It would be of interest to see how applicable the inputs used by Soto-Rojas and Kian are in predicting the experimental flexural responses presented

earlier. The ECC materials of Soto-Rojas and Kian are similar when considering the basic inputs required for their modelling in VecTor2 using built in models; compressive strength, fibre content, and fibre material properties. Although specifics of Kian's ECC mix design are sparse it is know that the " ECC [is] made of PVA (polyvinyl alcohol) with a length of 12 mm, a minimum aspect ratio of 300, and a minimum tensile strength of 1000 MPa" (2020) and had a fibre volume fraction of 2% while Soto-Rojas used the same volume fraction, fibre type, length, had fibres with tensile strengths of 1200 and 1560, and aspect ratios of 120 and 300.

Soto-Rojas' custom inputs consisted of the following four points pt.1(mε,MPa)= (50,4) pt.2 = (100,6), pt.3 = (200,6), and pt.4 (300, 1) while that of Tolou-Kian's consisted of a trilinear curve using three points estimated to be pt.1=(1,3.1), pt. 2 = (8.5,3), and pt.3 = (16,0). The reason Kian's input points were estimated is due to the fact that they are never stated but simply shown as the idealized curve in Figure 4.15. The two custom input models, despite trying to define similar materials, are vastly different with the entirety of Tolou-Kian's response occurring before the first point in Soto-Rojas' which may hint at the different challenges faced when curve fitting to a prism as compared to a tension coupon of ECC. The 280 mm FEA model outlined earlier in this chapter were used with constitutive models left as default where possible except for compression pre and post-peak, Lee et al 2011 (FRC) was chosen for both, tension stiffening which was switched to Custom Input (Strain based), and FRC tension which was not considered. The results of the different input models are shown in Figure 4.16.

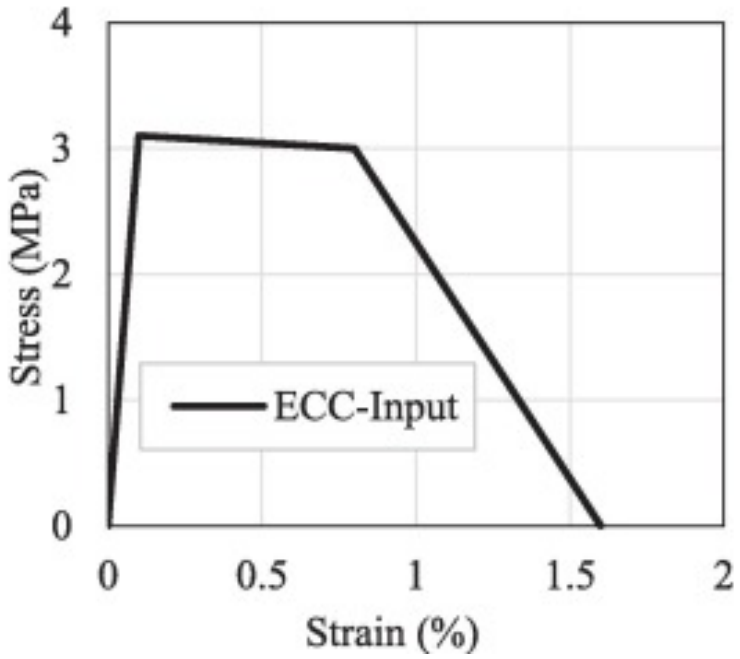

Figure 4.15 Tension stiffening input for VecTor2 (Tolou-Kian & Cruz-Noguez, 2022).

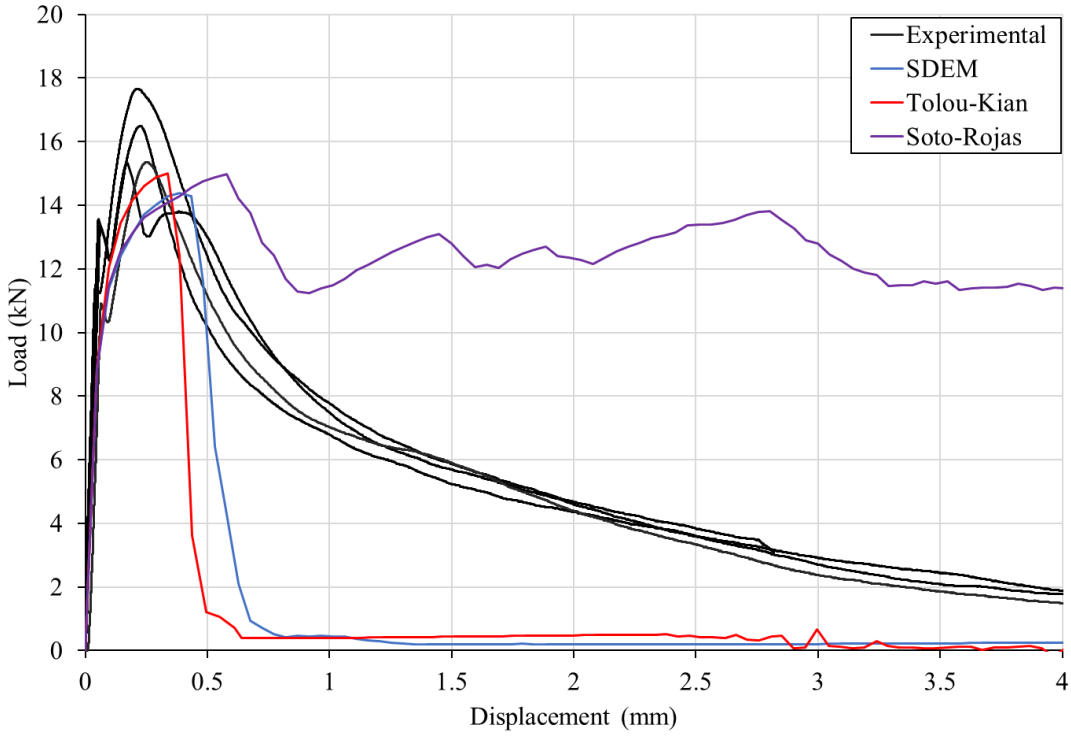

Figure 4.16 Load displacement response of 280 mm prism using Custom Input tension models.

Despite Soto-Rojas' input model having a peak stress value twice that of Tolou-Kian, the peak load capacities of the FEA prisms are nearly identical. Tolou-Kian's input model provides a

similar response to the SDEM FRC tension model with a notable drop in load capacity following the peak while Soto-Rojas' model has the opposite effect, greatly overestimating the residual load carried by the prims following the peak. This vast overestimation is likely due to the large strain value, 20%, required to attain post peak slopes. As far as the author can tell, Tolou-Kian's model was never verified against small-scale prisms and was simply put into a larger shear wall model and compared to experimental test data from the wall. Soto-Rojas' model on the other hand was not verified against any direct tension test to see if it maybe overcompensating the physical limitation of the material. Additionally, Soto-Rojas' model was implemented an earlier version of VecTor2 than what was used in the modelling work of this thesis. The overestimation of the prism's ductility may be the result of compensating for a calculation which was present in the older version's code but has been alerted in the newer version.

When examining Tolou-Kian's work it appears that the intent was to produce the stress strain response in Figure 4.15. It was mentioned before that the Custom Input tension softening option only governs the stress-strains response after strains exceed the tensile cracking strain calculated by VecTor2. This may cause some deviation from Tolou-Kian's, or any users, idealized ascending branch. To examine this possibility the single element FEA model from Section 4.2.3 was used once again with modifications made to reflect how Tolou-Kian described the approach used for modelling ECC in VecTor2. This included using Hognestad and Park et al as the compression pre and post-peak modes respectively and changing the material properties of the ECC so that f'_c is 38 MPa, strain at peak compressive strength is 2 mε, and initial Tangent Elastic Modulus is 12000 MPa (Tolou-Kian, 2020). The result of this modified tension element is shown in Figure 4.17. Although the strain of the second point seems to have been slightly overestimated the peak point and failure point were properly chosen. As suspected, the input values did not seem to account for the initial linearly elastic ascending branch that governs until VecTor2's cracking point are reached. This is not a major shortcoming as it likely did not significantly impact the overall response of the shear walls modelled with the material. This difference could lead to an initial over stiffening of an FEA response during displacement cycles prior to yielding. This over stiffening may become significant in cases where the input Elastic Modulus for compression and tensile test differ.

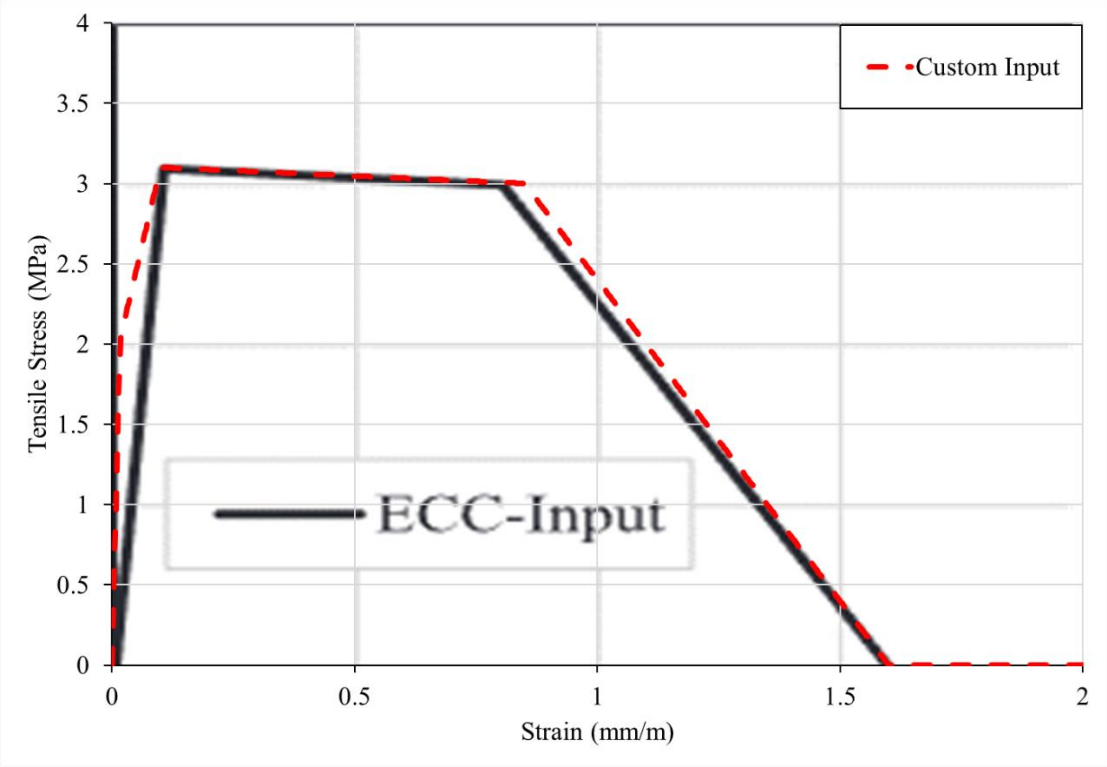

Figure 4.17 Tolou-Kian's idealized and actual tensile response (Tolou-Kian & Cruz-Noguez, 2022).

4.3.5 Influence of Aggregate Size and Crack Spacing on Prism Modelling

The FRC tension models have been compared and shown to have varying levels of inaccuracy when trying to model ECC materials. Part of this inaccuracy may be due to differences between typical concrete input values which differ from ECC and can cause issues in the formulation used by FRC tension models and other constitutive models. One such shortcoming was already highlighted in the fact that the bond strength assumed by the VEM model is based on if a material is considered concrete or mortar and when implemented into VecTor2 a mortar is defined as any material with a max aggregate size less than 2 mm. The result is that any ECC will be considered a mortar due to its max aggregate size being below the 2 mm limit. In their analysis of VecTor2's ability to model UHPFRC Zhang (2020) investigated the impact of aggregate size and crack spacing parameters on the response of modelled shear panels. These two parameters are still relevant in the consideration of ECC since it demonstrates similar characteristics to UHPFRC such as smaller max aggregate size and finer crack spacing.

The influence of crack spacing was compared between the default value if no user input is specified, a crack spacing of 75 mm which corresponds to both the height and depth of the prism, a spacing of $2l_f$ which was suggested based on Zhang (2020), and a crack spacing of $0.75l_f$. The responses are shown in Figure 4.18. The main effect of the input crack spacings was a greater residual load capacity of the prism. Additionally, all input crack spacings did provide slight improvements the peak load, while a crack spacing of $2l_f$ and h allowed for a slight delay in the sudden drop in load. Neither of these increases are significant enough to warrant altering the inputs.

The maximum aggregate sizes considered were the actual max aggregate of 0.3 mm, 1mm, 2mm (which represents the limit of what is considered mortar or concrete), 10 mm, 14 mm (which is the aggregate size of the normal concrete used in Chapter 5), and the default value if no user input is provided. The responses are shown in Figure 4.19. The peak load of the response is demonstrated to increase with larger aggregates inline with the fact that a larger aggregate size would allow for greater aggregate interlock and increase the ability for the concrete to carry stress along cracks. For aggregate sizes above 2mm it is clear that the bond strength has increased due to the material's reclassification as concrete allowing for substantially greater loads and a larger displacement at peak. When using the SDEM this increase in displacement is not representative of the actual experimental response resulting in the aggregate size of ECC remaining 0.3 mm in future models.

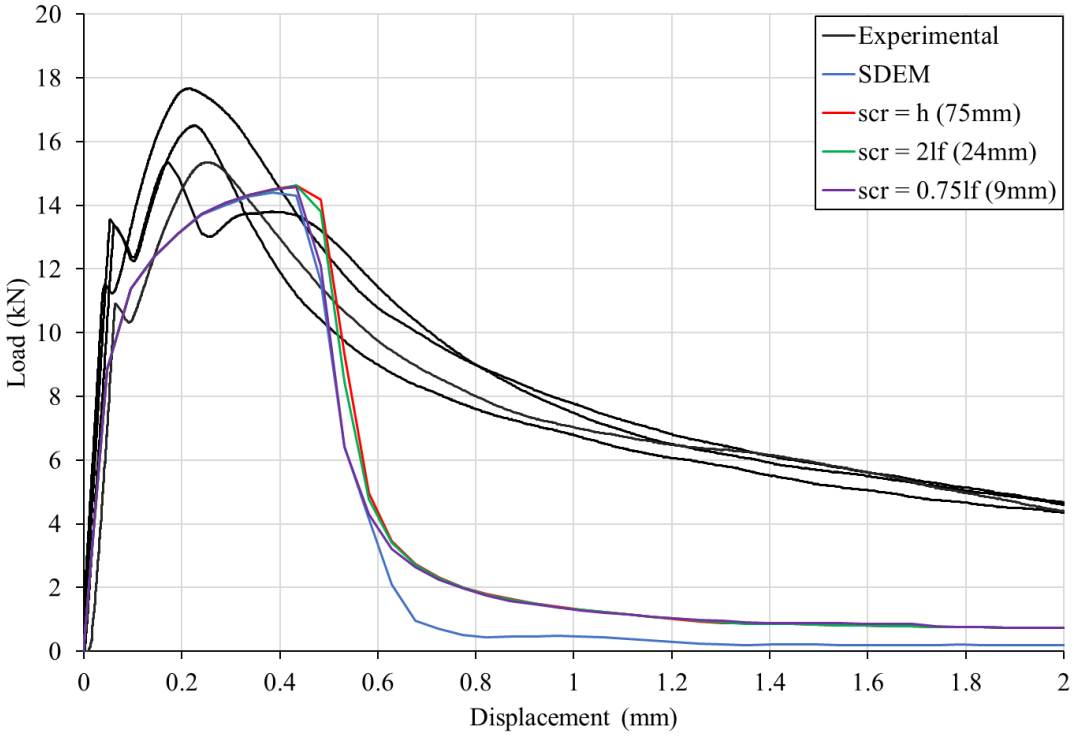

Figure 4.18 Influence of crack spacing on 280 mm prism response.

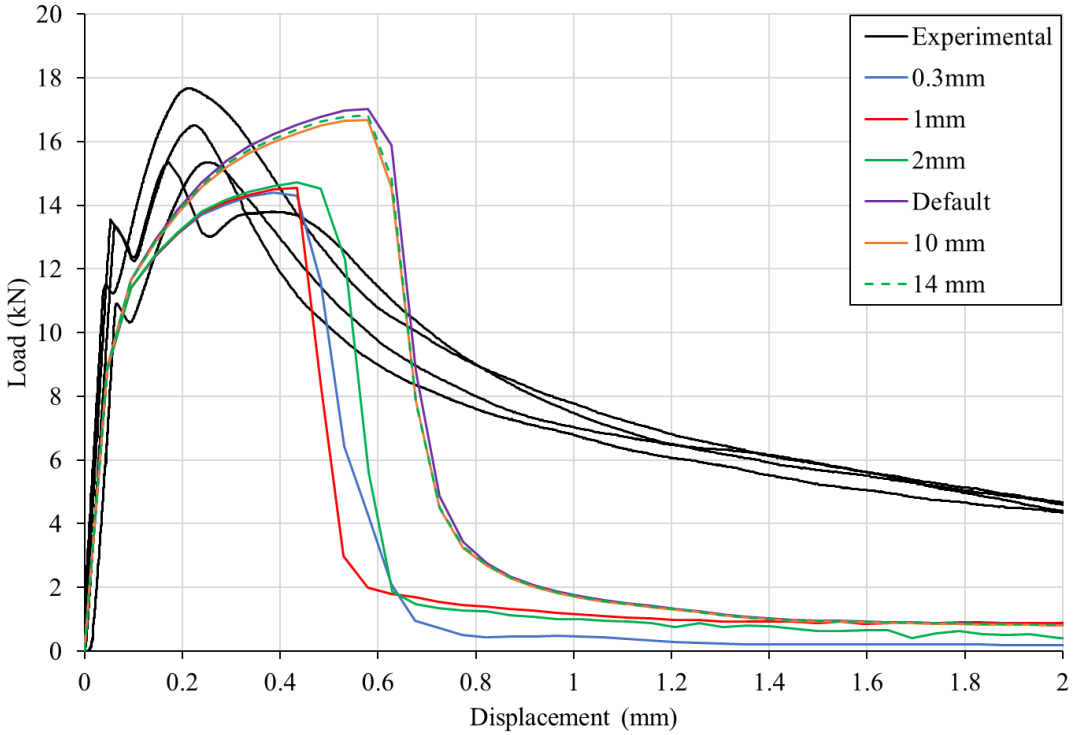

Figure 4.19 Influence of max aggregate size on 280 mm prism response.

5 Numerical Modelling of SMA-ECC Shear Walls

5.1 Introduction

This chapter focuses on the creation and refinement of numerical models in VecTor2 which can accurately predict the response of both traditionally reinforced and hybrid SMA-steel reinforced slender shear walls. The numerical work presented will be compared against the experimental testing conducted by Morcos and Sato-Rojas allowing for a single modelling methodology to be applied to both studies. The work conducted by Morcos consisted of traditionally reinforced and hybrid SMA-steel reinforced slender shear walls which used normal strength concrete (NC) as the concreting material throughout. Once the model outputs were refined to an acceptable level of agreement with experimental data they would then serve as the starting point for modelling of Soto-Rojas' walls. Soto-Rojas' work took Morcos' damaged walls and repaired them by removing and replacing the damaged reinforcement in the plastic hinge as well as replacing the NC concrete in the plastic hinge with Engineered Cementitious Composites (ECC).

5.2 Morco's Slender Shear Walls

The slender shear walls constructed by Morcos consisted of one traditionally reinforced wall, denoted SWS, which served as a control and a second wall where longitudinal reinforcement in the boundary regions was replaced with SMA bars of a similar diameter, denoted SWN. The dimensions of both walls were identical, measuring 2200 mm high, 1000 mm long, and 150 mm wide for an overall aspect ratio of 2.2. Walls also consisted of a foundation block measuring 500 mm deep, 1600 mm long, and 1000 mm wide which allowed for the wall to be anchored into the strong floor for testing while a cap beam measuring 400 mm high, 400 mm wide, and 1600 mm long allowed for connection of the actuator. Wall dimensions and reinforcement layout are shown for the SWN wall below in Figure 5.1. The SWS wall had the same geometry and reinforcement layout with the only difference being that the Headed Couplers and Nitinol are not present.

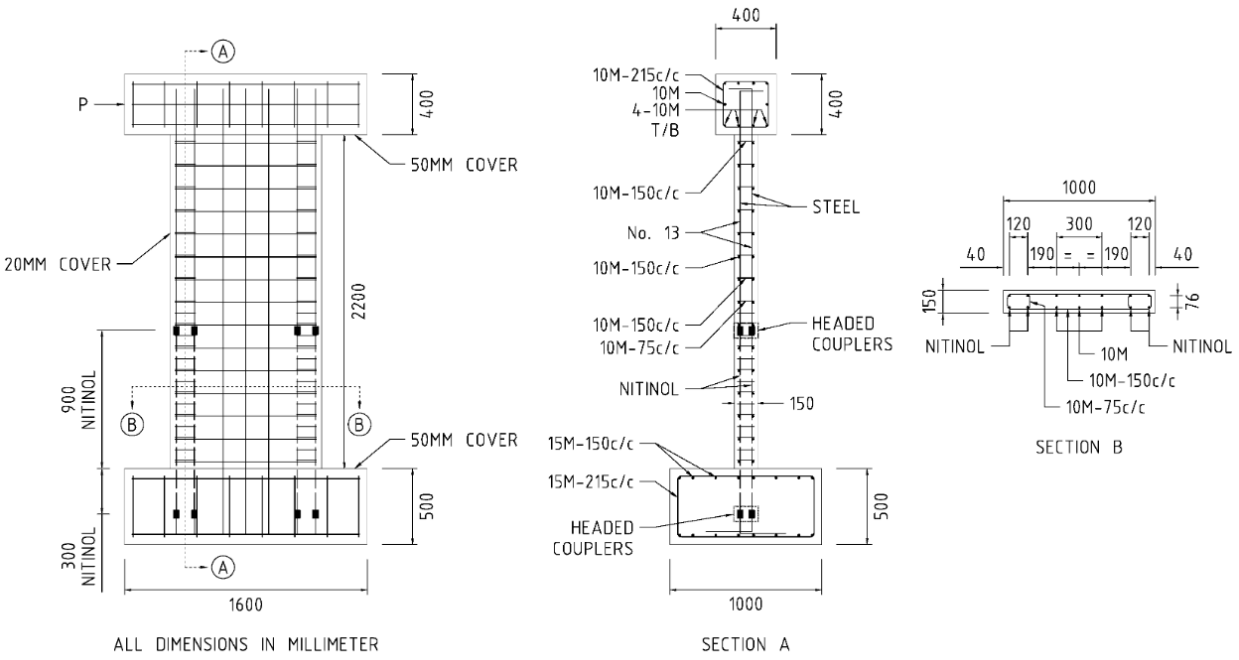

Figure 5.1 SWN wall dimensions and reinforcement layout with vertical (SECTION A) and horizontal (SECTION B) cross-sections (Morcos & Palermo, 2018).

Both walls had 10M rebar shear reinforcement spaced at 150 mm along the height of the wall with additional 10M rebar buckling reinforcement in the boundary regions with a spacing of 75mm from the base of the wall to a height of 1100 mm. Longitudinal reinforcement consisted of two curtains with three 10M bars in the web of the wall and four bars in each boundary. SWS utilized 10M rebar for the boundary longitudinal reinforcement while SWN utilized a combination of SMA and traditional reinforcement in the boundary. To optimize the inherent cost associated with the use of SMAs, 12.7 mm diameter SMA bars were used only in the plastic hinge, this meant SMA bars would span between 300 mm below the foundation to a height of 900 mm above the foundation block. SMA and rebar in the boundary region of the SWN wall were headed at their ends to allow for use of the mechanical coupler shown in Figure 5.2. The use of these specialty couplers eliminated slipping which was reported across several experimental programs when SMA and rebar was coupled using traditional screw couplers. #13 rebar was used in the boundary region of SWN to accommodate the 12.7 mm diameter of the SMA bars and allow for proper confining force in the coupler.

Figure 5.2 Headed #13 rebar (left) and SMA (right) with mechanical coupler (Morcos & Palermo, 2018).

5.3 Modelling of Morcos' Walls

Modelling of the walls described was previously done by Morcos & Palermo (2018) as part of a conference paper as well part of a MASc thesis (Morcos, 2021). These models were created in an older version of VecTor2 than what is currently available and were developed separately from the repaired wall models presented in work done by Soto-Rojas (2020) and Soto-Rojas & Palermo (2020). Since both Morcos and Soto-Rojas utilized the same base walls, it would be ideal to have a set of models constructed with a consistent methodology and approach in mind. These models would allow for a better demonstration of the impact variations in constitutive models, material properties, and modeling choices can have on structural response of slender shear walls.

5.3.1 Mesh Discretization

When creating the mesh for the wall, all regions used a hybrid discretization type and rectangular elements. This was chosen since all points can be defined in the global reference frame of an x and y axis and the structure is rectangular in shape. These two factors remove the need for quadrilateral and triangular elements which would be required when a structure has angles that are not 90 degrees. Detailed explanation of the differences between different element types (rectangular, triangular, and quadrilateral) and discretization types (hybrid, grid superposition, and division point insertion) can be found in the VecTor2 user manual. To assist in mesh definition, the wall was conceptualized as having six specific region types based on the differing reinforcement ratios found in parts of the wall. The six regions are the foundation block, cap beam, unconfined cover, web, boundary (top), and plastic hinge boundary (bottom) regions and shown below in Figure 5.3.

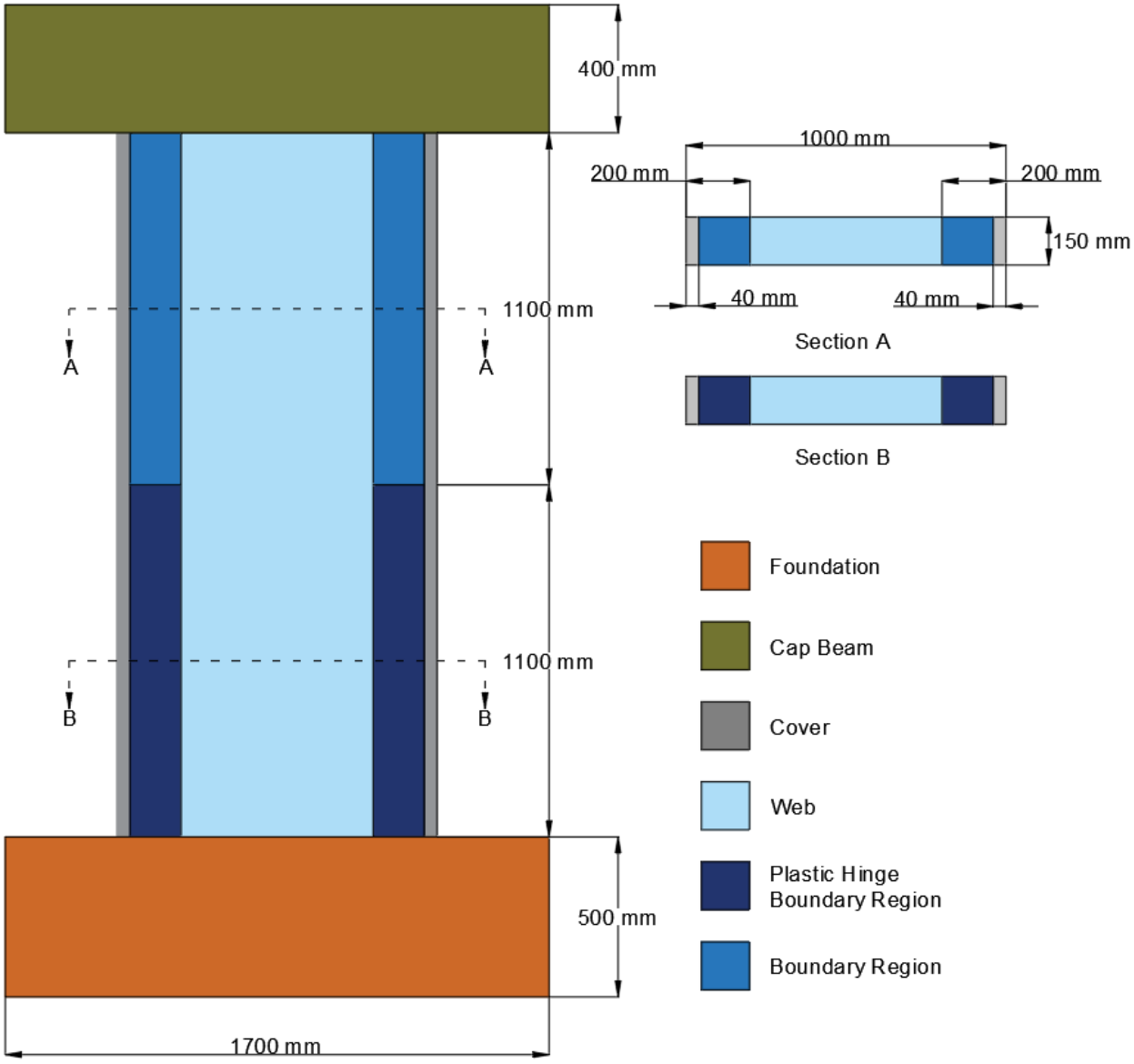

Figure 5.3 Mesh regions for shear walls.

The regions were created to maximize the number of elements which have an aspect ratio of 1. A larger aspect ratio can increase the likelihood an element becomes a source of instability in the model, anything less than an aspect ratio of 1.5 is generally seen as acceptable (Palermo & Vecchio, 2007). The ideal element size based on the geometry of the wall and reinforcement spacing is 50 mm by 50 mm as this would result in 20 elements across the shortest dimension of the wall, its length, with 14-16 elements in the shortest direction considered sufficient for a finely defined mesh (Palermo & Vecchio, 2007). All elements were ensured to measure 50 mm in the y-

direction, however, the size of elements in the x-direction varies as shown below in Figure 5.4 to accommodate measurements such as the 120 mm spacing between longitudinal bars in the boundary regions and the clear cover. In the web sections, elements measured 50 mm in the x direction. In the boundary regions elements measured either 40 mm (aspect ratio=1.25) or 60 mm (aspect ratio=1.2) in the x direction to accommodate for the 120 mm spacing between longitudinal reinforcement found here. The unreinforced cover region has elements measuring 40 mm (aspect ratio=1.25) in the x direction. The outer portions of the foundation and cap beam regions consisted of elements measuring 100 mm in the x direction (aspect ratio=2). The use of an aspect ratio of 2 was acceptable in these regions since they are highly reinforced and not critical to the failure mode of the walls allowing for a reduced number of nodes.

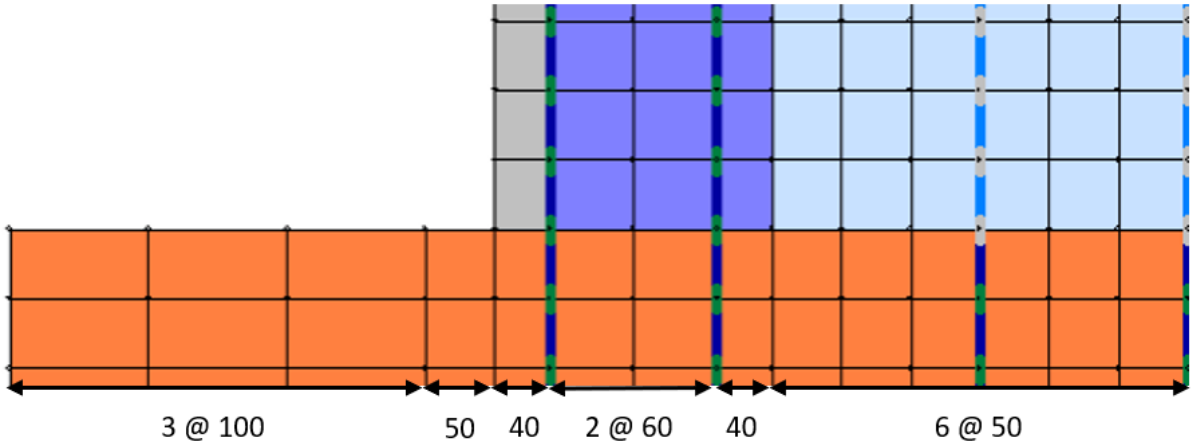

Figure 5.4 Final mesh sizing of elements in different regions.

When defining the regions in Formworks using the hybrid discretization type there may be instances where triangular elements are inserted as the program tries to satisfy both the size parameters and maximum aspect ratio the user has input. If triangular elements do occur, it is best to try remeshing after changing the complexity factor input and maximum aspect ratio. It should be noted that the models presented have a foundation block and cap beam measuring 1700 mm in length despite both Morcos and Soto-Rojas having a foundation and cap beam length of 1600 mm. This was done to allow for easier comparison of results, if needed at a later time, to work done by Abdulridha and Palermo (2017) whose walls did consist of a foundation and cap beam measuring 1700 mm. Such a small difference should not cause any issues, since the function of these sections is to maintain rigidity while transferring loads from the setup and actuator to the wall.

5.3.2 Truss Reinforcement Definition

The best practice for modeling and definition of steel reinforcement is to model the principal longitudinal steel reinforcement as discrete elements while any other steel reinforcement be modeled as smeared, this includes stirrups and ties. Details about smear reinforcement will be provided in Section 5.3.3. Discrete reinforcement elements can easily be defined using the reinforcement panel shown in Figure 5.5.

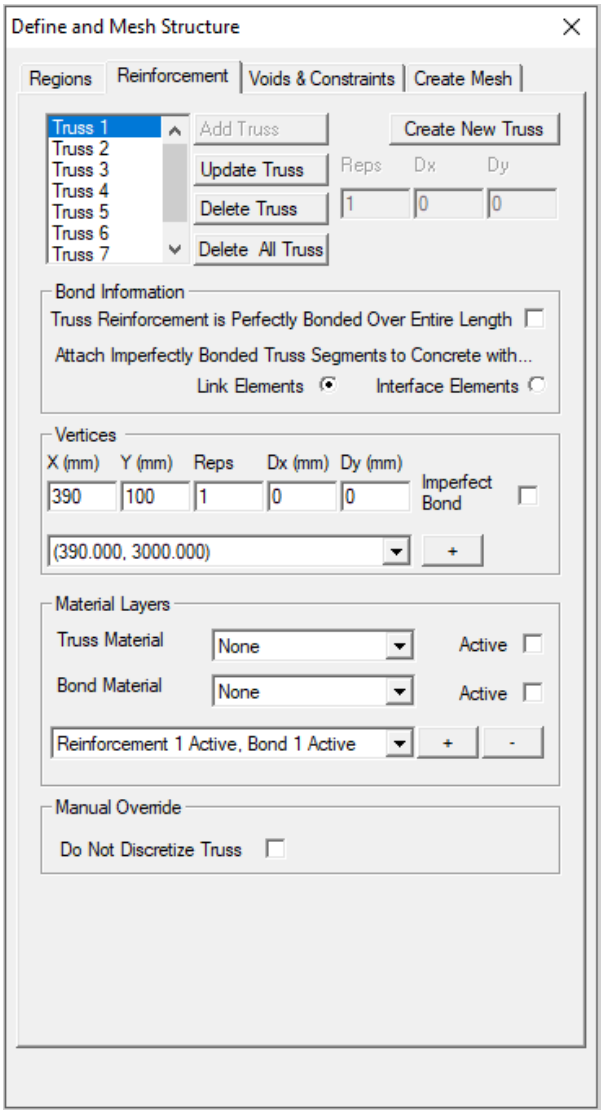

Figure 5.5 Reinforcement panel.

The simplest type of reinforcement is a perfectly bonded bar along the full length in which case only two vertices, the start and end of the bar, need be defined. If bond models are going to be used along some length of the bar it necessary to ensure that the "Truss Reinforcement is

Perfectly Bonded Over the Entire Length" box is not selected before any vertices are defined. If a vertex is defined while this box is active, then every node of the truss reinforcement element will be taken as perfectly bonded. Truss elements that have been created can only be altered in terms of the truss material and bond materials selected and their state as either inactive or active, the definition of a node as perfectly or imperfectly bonded cannot be changed. If the bond box is unclicked, then each time a vertex is input it can be defined as either perfectly or imperfectly bonded based on selection of the "Imperfect Bond" option. The use of bond is an important consideration in the walls being modeled since the SMA reinforcement bars found in the SWN wall have a smooth surface. The smooth surface of SMA results in a decrease of bond strength between the bar and surrounding concreting material compared to the bond between traditional deformed steel bars. The specific details of the bond models used will be defined in the Section 5.3.5.

Although an entire truss reinforcement bar can be defined as imperfectly bonded this is not advisable in the context of the slender shear walls being modeled. Having the entire reinforcement imperfectly bonded can lead to instability and premature failure of the models. Instead, it is best practice to have a perfectly bonded reinforcement truss element in the foundation, where bars have been hooked leading to sufficient confinement by the surrounding concrete, and define subsequent nodes as needed. To keep models consistent all longitudinal bars were defined as having imperfect bond extending from 350 mm below the foundation to 950 mm above the foundation to correspond to the length of the SMA bars and couplers. The vertices that are used to define reinforcing bars can impact the size of elements FormWorks creates for the overall mesh. For example, if the elements size in a region is 50 mm by 50 mm but there are truss nodes spaced 30 mm apart within the same region, FormWorks will resolve the conflicting values by discretizing the mesh to a smaller size or inserting triangular elements which are not ideal.

5.3.3 Reinforced Concrete Material Properties Definition

When creating a model in FormWorks it is important to consider the types of materials that will need to be defined. The material definition button can be found in the top ribbon in FormWorks with the material definition panel is shown in Figure 5.6. The user can select between reinforced concrete, structural steel, masonry, timber, bearing, void, concrete-special, and fixed orthotropic.

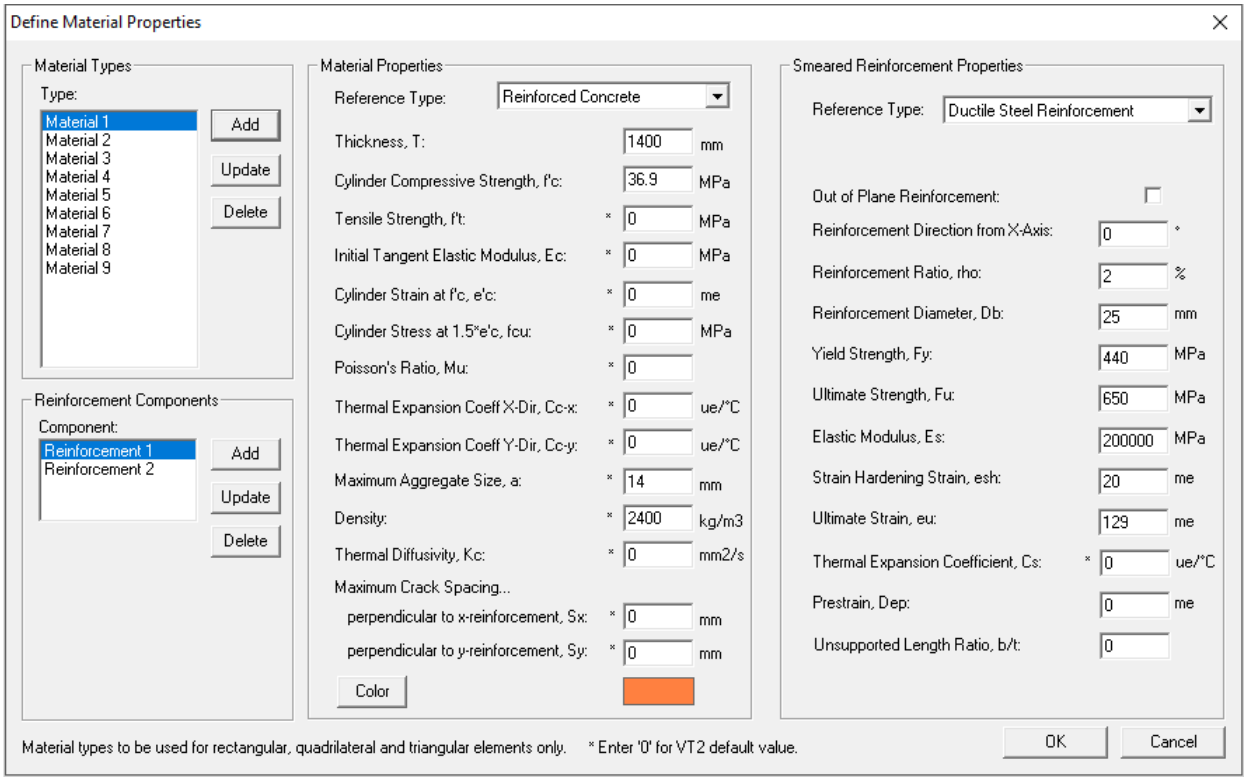

Figure 5.6 Define Material Properties panel.

For the purposes of the shear walls being modeled only the reinforced concrete material is used and described in detail. When defining reinforced concrete in FormWorks the only material properties that need to be define are the thickness of the concrete and its compressive strength. If any property besides thickness and compressive strength is left as “0”, VecTor2 will use a default value as shown below in Table 5.1.

Table 5.1 Default reinforced concrete values.

Material Property	Default Value
Tensile Strength, f'_t (MPa)	$0.33\sqrt{f'_c}$
Elastic Modulus, E_c (MPa)	$3320\sqrt{f'_c}$+6900
Strain at f'_c, ε_o ($\times 10^{-3}$)	$1.8 + 0.0075 f'_c \, v$
Poisson's Ratio, v_o	0.15
Thermal expansion Coefficient, C_c (/^{o}C)	10×10^{-6}
Maximum Aggregate Size, a (mm)	20
Density (kg/m^3)	2400
Thermal Diffusivity, K_c (mm^2/s)	1.2
Max. Crack Spacing, S_x (mm)	1000
Max. Crack Spacing, S_y (mm)	1000

When defining a reinforced concrete material in FormWorks, steel reinforcement can be included as smear reinforcement on the right side of the definition window. Defining steel reinforcement as smeared instead of discrete truss elements allows for greater computational efficiency by eliminating additional elements in favor of accounting for steel in the stiffness matrix of the reinforced concrete element itself. The direction of the smeared reinforcement can vary between 0^o and 90^o with respect to the x-axis with the additional option to define out of plane smear reinforcement by checking the "Out of Plane Reinforcement" box which will input a value of 361^o. The reinforcement ratio, rho, is taken as the ratio between the area of the reinforcement and the total area of the concrete material based on reinforcement spacing. For the purposes of the models constructed the reinforcement ratios were as follows:

Web Region

$$\rho_x = \frac{area\ of\ 2\ 10M\ legs}{150\ mm\ spacing * concrete\ thickness}$$
$$= \frac{2 * 100\ mm^2}{150\ mm * 150\ \ mm}$$
$$= 0.88\%$$

Plastic Hinge Boundary (bottom)

$$\rho_x = \frac{area\ of\ 2\ 10M\ legs}{150\ mm\ spacing * concrete\ thickness} + \frac{area\ of\ 2\ 10M\ legs}{75\ mm\ spacing * concrete\ thickness}$$
$$= \frac{2 * 100\ mm^2}{75\ mm * 150\ mm} + \frac{2 * 100\ mm^2}{150\ mm * 150\ mm}$$
$$= 2.67\%$$

$$\rho_z = \frac{area\ of\ 2\ 10M\ legs}{75\ mm\ spacing * width\ of\ concrete}$$
$$= \frac{2 * 100\ mm^2}{75\ mm * 160\ \ mm}$$
$$= 1.67\%$$

Boundary (top)

$$\rho_x = \frac{area\ of\ 4\ 10M\ legs}{150\ mm\ spacing *\ area\ of\ concrete}$$
$$= \frac{4 * 100\ mm^2}{150(spacing) * 150\ (concrete\ thickness)}$$
$$= 1.78\%$$

$$\rho_z = \frac{area\ of\ 2\ 10M\ legs\ spaced\ 150\ mm}{150\ mm\ spacing *\ area\ of\ concrete}$$
$$= \frac{2 * 100\ mm^2}{150\ mm * 160\ \ mm}$$
$$= 0.83\%$$

The cap beam and foundation block regions were given arbitrary rho values of 2% and 1% in the x and y-directions respectively to ensure that they remained stiff. The cap beam was defined to have an additional smeared reinforcement component in the z-axis consisting of 1% rho. The

material properties for the concrete and smeared reinforcement are summarized below in Table 5.2, Table 5.3, and Table 5.4. Any material properties not listed were left as default. Honeycombing had occurred during casting of the SWS wall which required a small portion measuring 200 mm wide with a height of 150 mm to be removed from the boundary region and replaced with SCC. The amount removed only went 35 mm into the wall from each side but for the sake of simplicity in the model for the SWS wall it was assumed that SCC would be defined as being the entire thickness of the wall.

Table 5.2 Smeared reinforcement properties of different regions.

Region	ρ_x	ρ_y	ρ_z
foundation block	2	1	NA
cap beam	2	1	1
unconfined cover	NA	NA	NA
web	0.88	NA	NA
boundary (top)	1.78	NA	0.83
plastic hinge boundary (bottom)	2.67	NA	1.67

Table 5.3 Concrete material properties.

Wall	f'_c (MPa)	Maximum Aggregate Size (mm)	Density (kg/m^3)
SWS	47.2	14	2400
SWS -SCC	57.3	8	2400
SWN	36.9	14	2400

Table 5.4 Smeared reinforcement properties.

Wall	Reinforcement	D_b (mm)	F_y (MPa)	F_u (MPa)	E_s (GPa)	ε_{sh} (mε)	ε_u (mε)
SWS	10M	11.3	428	558	197	23	174
SWN	10M	11.3	435	564	186.2	21	158

5.3.4 Reinforcement Properties Definition

FormWorks allows users to define multiple types of discrete reinforcement, the Define Reinforcement Properties panel is shown below in Figure 5.7. For the SWN and SWS walls two types of reinforcement are used in the models: ductile steel reinforcement for the longitudinal rebar and couplers and Shape Memory Alloy (Type 2) for the SE-SMA bars. FormWorks accounts for buckling behavior through the use of the Unsupported Length Ratio, b/t, parameter. b/t is not considered unless the user manually inputs a value themselves due to the nature of buckling being dependent on the configuration of reinforcement in an element. Calculation of b/t is based on equations proposed by Dhakal & Maekawa (2002). Previous modelling work by Morcos and Soto-Rojas had not considered buckling parameters. The occurrence of deformed reinforcement buckling during their experimental testing of both the new construction and repaired walls prompted the inclusion of buckling in the models presented to incorporate properties of past walls more accurately. The specific material properties used for the discrete longitudinal reinforcement are presented in Table 5.5. Yield and ultimate strength for the couplers and SMA used in the SWN wall were taken from values reported by Morcos (2021). The elastic modulus, strain hardening, and ultimate strain values were selected to ensure that the coupler would be sufficiently stiff not to undergo any yielding or failure.

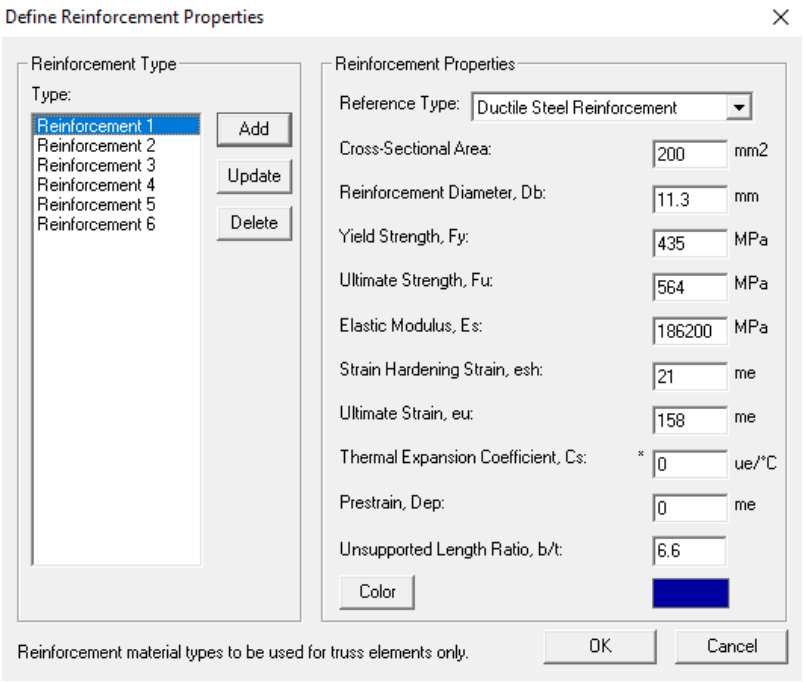

Figure 5.7 Define reinforcement properties panel.

Table 5.5 Material properties for discrete longitudinal reinforcement.

Wall	Reinforcement	A (mm^2)	D_b (mm)	F_y (MPa)	F_u (MPa)	E_s (GPa)	ε_{sh} (mε)	ε_u (mε)	b/t
SWS	10M[1] Rebar	200	11.3	428	558	197	23	174	13.2
	10M[2] Rebar	200	11.3	428	558	197	23	174	6.6
SWN	10M[1] Rebar	200	11.3	435	564	186.2	21	158	13.2
	10M[2] Rebar	200	11.3	435	564	186.2	21	158	6.6
	#13 Rebar	253.35	12.7	463	627	202.6	16	165	0
	Coupler	962	35	690	795	200	40	350	0
	SMA	252	12.7	338	1034	42	50	160	6.6

[1] indicates reinforcement used in the web and boundary regions above the plastic hinge

[2] indicates reinforcement used in heavily reinforced sections (foundation, cap beam, and plastic hinge boundary regions)

Work by Morcos (2021) had also included material testing of 10M and #13 rebar, however the values obtained lead to overestimation of load capacity when input into VecTor2 models, which will be discussed in Section 5.3.8.2. To investigate if the testing had provided higher strengths than what was experienced, additional material testing was conducted on surplus material which had been ordered but not used in the construction of the shear walls. The 10M from the SWS, 10M from SWN, and #13 from SWN all came from different suppliers and had been labelled and kept in storage. Testing of the surplus material was done in an MTS universal testing machine (UTM) which allowed for the application of a twostep loading protocol in line with ASTM E8/E8M standards (ASTM, 2021). Testing of each material was conducted in triplicate with strain being measured using a 50 mm extensometer which was attached at the midpoint of the specimens while the UTM moved at a constant strain rate of 0.015 mm/mm/min until strain hardening occurred at which point strain rate was increased to 0.05 mm/mm/min until failure. The stress-strain responses are shown below in Figure 5.8, Figure 5.9, and Figure 5.10.

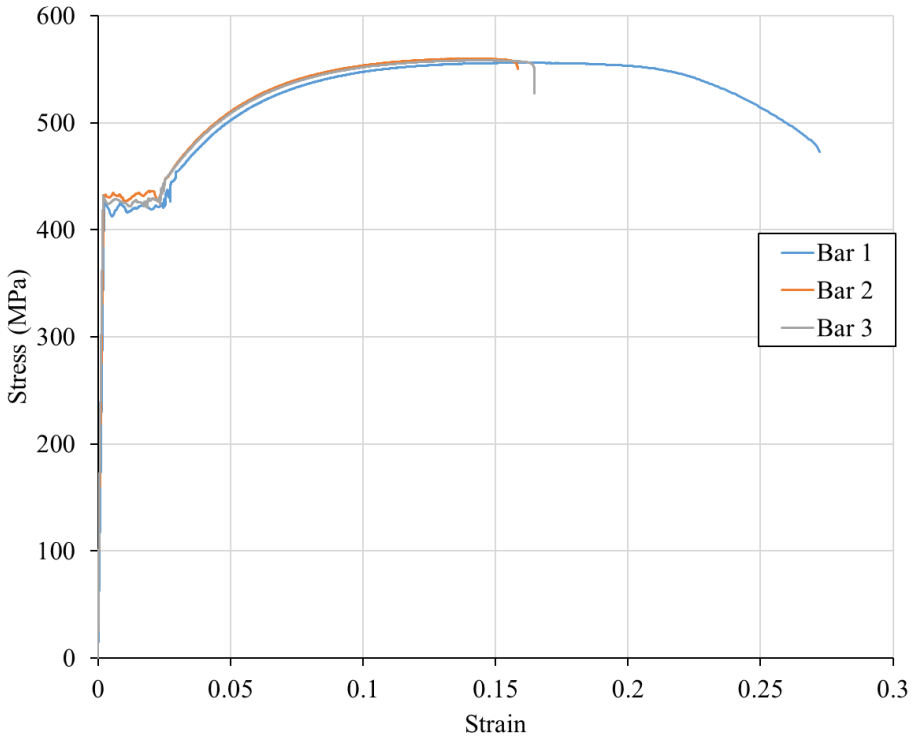

Figure 5.8 Stress-strain response of 10M from SWS.

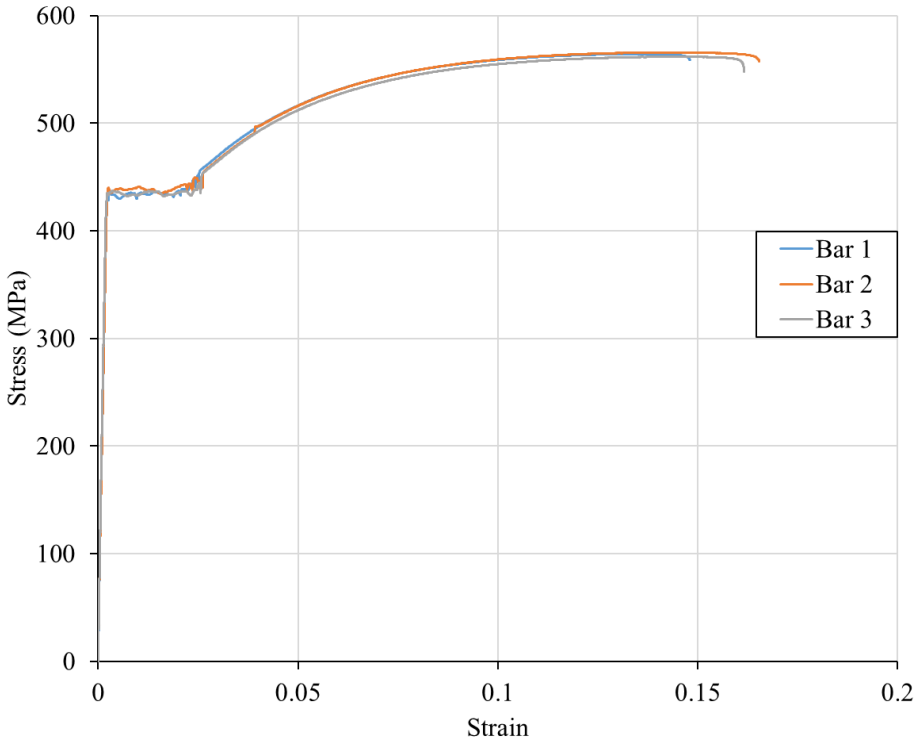

Figure 5.9 Stress-strain response of 10M from SWN.

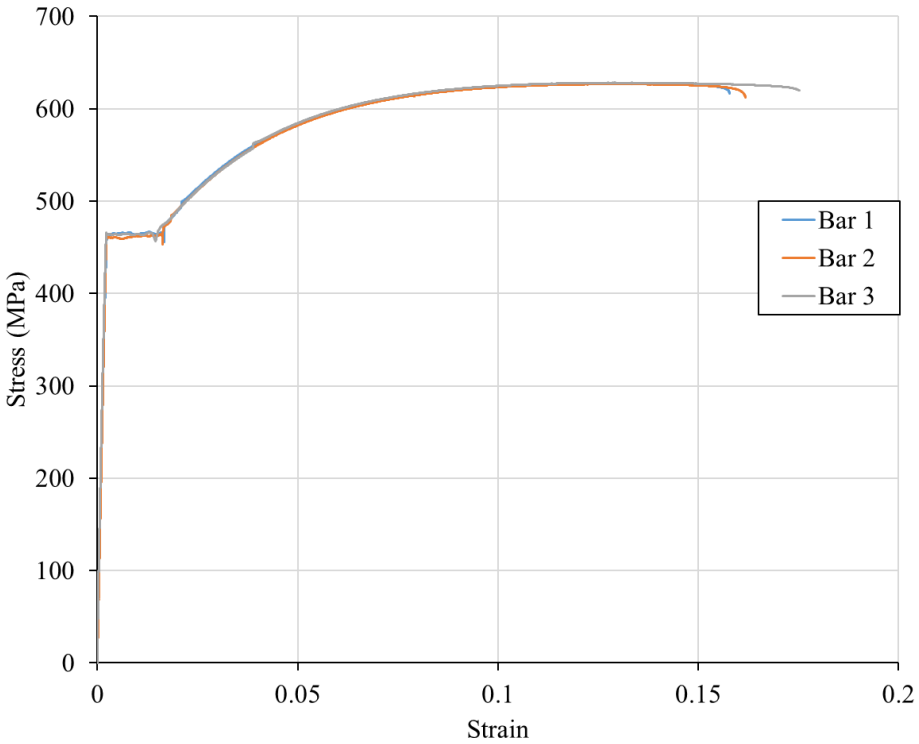

Figure 5.10 Stress-strain response of #13 from SWN.

The updated testing provided lower stress values for both yield and ultimate tensile strength compared to values reported by Morcos. The most likely cause for the discrepancy in testing shown here and by Morcos is thought to be based on when the UTM was zeroed in the testing setup. The UTM, as shown in Figure 5.11, secures a specimen by clamping it with two grips on the top and bottom. When these grips are engaged, they can also apply a compressive force to the specimen which will not be captured in data if the load is zeroed after a specimen has been secured at both ends. During the most recent testing it was ensured that the load was zeroed after the specimen had been secured on one end and before the second end was secured. It is likely that when testing was done by Morcos on the same UTM the load was zeroed after the second end of the grip was closed. Based on the recent testing this compressive preloading force could result in compressive stresses as high as 41.59 MPa, which would be considered as additional tensile strength if the UTM is zeroed only after both ends are secured.

Figure 5.11 UTM setup with rebar and extensometer at beginning of tension test.

Additional errors could have come from how the average diameter used in Morcos' calculations was obtained. Bars were first weighed and then had an area reduced for the application of the strain gauge and reweighed. The weight lost was then converted into an average reduction in area based on the length of the reduced area and the density of steel. An overestimate of reduced average would lead to larger stress values than what was actual values.

5.3.5 Bond Definition

When describing how to define reinforcement truss elements in Section 5.3.2 the use of bond was briefly mentioned. During creation of a model in FormWorks all discrete reinforcement elements can be modeled most simply as perfectly bonded in which case the truss elements and the reinforced concrete material elements share common nodes and undergo the same displacements. The use of bond allows for truss elements to be connected to reinforced concrete elements by link or contact elements. These link or contact elements pair the nodes of a reinforcing truss element to the nodes of the adjacent reinforced concrete element. Prior to slipping both the reinforced concrete and reinforcement truss nodes will have the same co-ordinates/displacements but act independently once slipping occurs. Since the SMA bars used in wall SWN have a smooth finish unlike the rougher and ribbed exterior of deformed bars it is important that a bond model be implemented to capture the effects lower bond strength and slip of the SMA bars can have on the overall behavior of the walls. The Define Bond Properties panel is shown below in Figure 5.12.

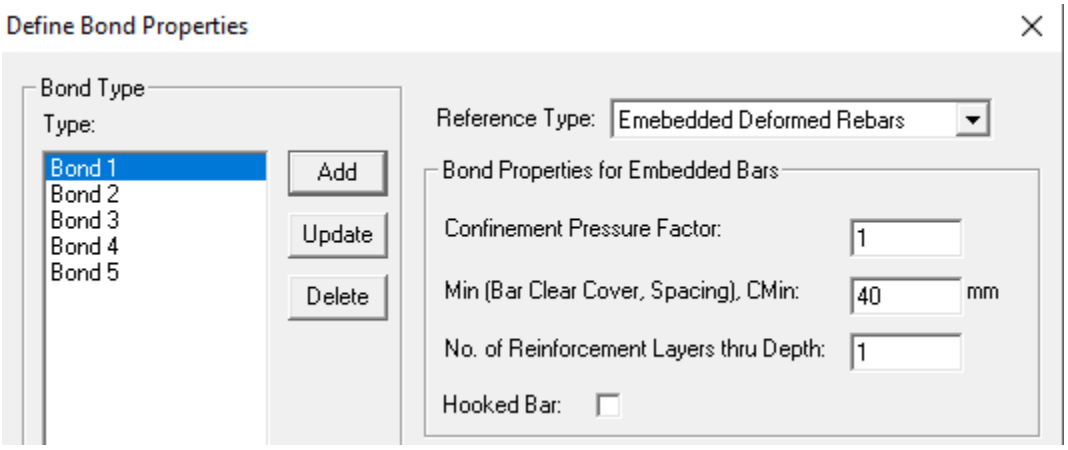

Figure 5.12 Define Bond Properties panel.

VecTor2 allows for the bond definition of multiple types of embedded and externally attached reinforcement elements but only the reference types of "Embedded Deformed Rebars" and "Embedded Smooth Rebars" were used to model the deformed steel and SMA bars

respectively. It should be noted that there is the option to define a custom bond-slip relationship through the section of the "Embedded Bars-Custom Input" option but for the present work this was not considered as it is very case specific requiring the input of three stress-slip points and the ideal use of any FEA model requires the least number of custom inputs from the user. When using either the "Embedded Deformed Rebars" or "Embedded Smooth Rebars" reference type it is still necessary to input the Confinement Pressure Factor (β), the minimum of either the bar spacing or clear cover (C_{min}), and the number of reinforcement layers thru the depth. Confinement Pressure Factor can be any value between 0 and 1 based on the expected confinement pressure in MPa, σ, exerted on the reinforced element and the following equation where:

$$\beta = \frac{\sigma}{7.5}$$

A factor of 0 corresponds to unconfined pullout failure while a factor of 1 corresponds to a fully confined pullout failure. The number of reinforcement layers thru the depth refers to the number of adjacent reinforcement layers in the x or y-direction that are represented by a single truss element which the bond will be applied. The layers do not refer to how many bars of rebar a single truss element represents if they are spaced into the z axis. When modelling the SWN and SWS walls all bond types were defined to have a C_{min} of 40 mm and the number of reinforcement layer through depth was 1. For bond of reinforcement in the web a Confinement Pressure Factor of 0.5 was used while reinforcement found anywhere else used a bond with a Confinement Pressure Factor of 1. All bond models are summarized in Table 5.6.

Table 5.6 Bond model properties.

Bond Model	β	C_{min}	# Layers Through Depth	Walls Utilized
Embedded Deformed Rebar	1	40	1	SWS/SWN in boundary regions or foundation
Embedded Deformed Rebar	0.5	40	1	SWS/SWN in web
Embedded Smooth Rebar	1	40	1	SWN for SMA

5.3.6 Initial Wall Models

The initial wall models were constructed as described above and are shown below in Figure 5.13 and Figure 5.14. All elements in the wall were given a gravity load of 2400 kg/m^3 and a unit support displacement acting in the positive (right) x-direction was applied at the mid height of the cap beam to represent the lateral load applied by the actuator during experimental testing. How loads are applied can vary between modelers and can have significant impact on the behavior of the wall. The support displacement was applied at a single node to ensure that the rotation of wall and cap beam was not restricted as the actuator had a seated head allowing for unrestricted rotation during tests. Support displacements work by restricting the displacement of the node they act upon to the value defined in the loading data. If the support displacement had been applied to multiple nodes, a portion of the cap beam face would always remain perpendicular to the direction of loading inducing additional stresses and strains. Having the support displacement applied at the centroid of the cap beam would be inaccurate since it does not reflect the fact that the load was only applied to the wall at the face of the cap beam through the actuator head. The only nodal restraints applied to both walls were fully pinned supports along the foundation of wall. A total of 9 pinned supports were used and split into three groups of three to reflect the three threaded rods that were used to anchor the walls to the strong floor during testing. The use of three nodes per threaded rod was to ensure that there would not be local failure of single element. The groups were spaced roughly 600 mm apart as this was the spacing between the threaded rods.

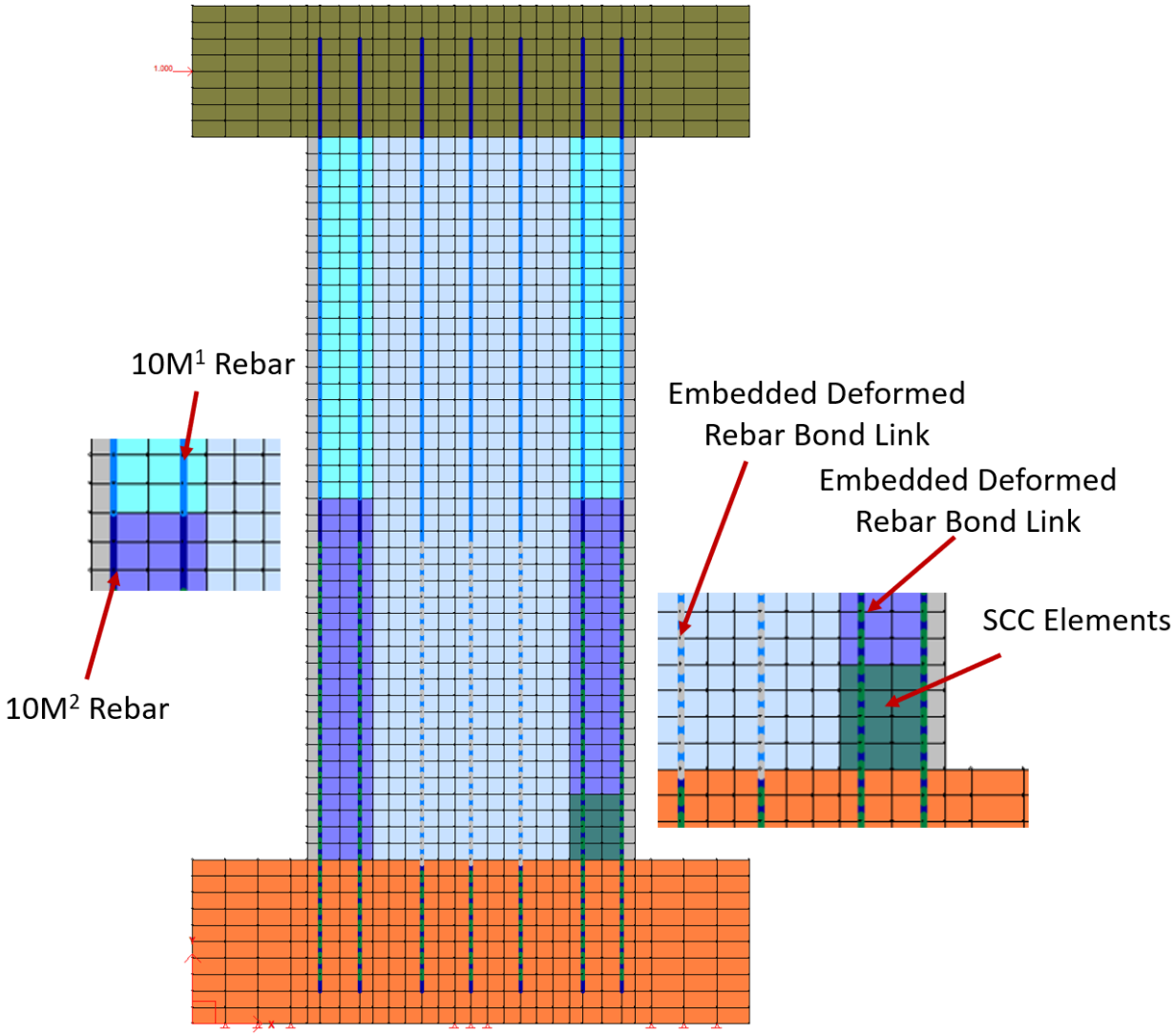

Figure 5.13 Initial FormWorks model of SWS.

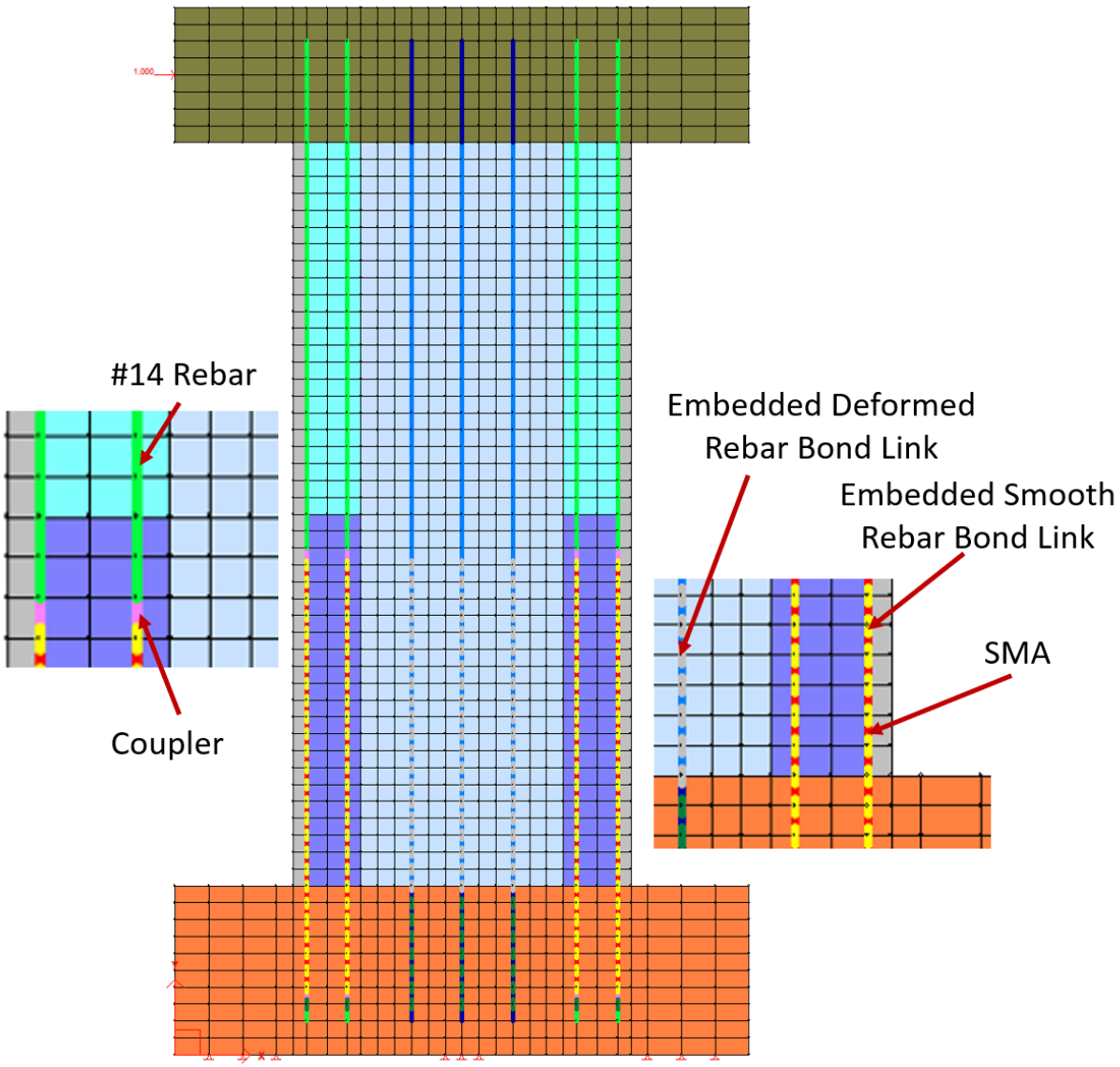

Figure 5.14 Initial FormWorks model of SWN.

5.3.7 Constitutive Models

The constitutive models used for both the SWS and SWN wall models are shown below in Table 5.7. All models except the hysteretic response were kept default since the concrete and steel reinforcement utilized in the wall are typical. The SCC in SWS is higher strength than what is typically considered normal strength concrete but due to the limited number of elements it occupies, it does not justify changing the model which would be applied to all concrete elements. The hysteretic response model accounts for the internal damage that accumulates in concrete which is repeatedly loaded and unloaded. This damage is presented as plastic strains which cause the reloading branches of the concrete stress-strain response to be offset from the “back-bone” curve.

The default hysteretic response is the nonlinear with plastic offsets. The Palermo 2002 model builds on the default model by further defining partial unloading and reloading as well as better representing the modified shape of the reloading curve due to damage degradation.

Table 5.7 Constitutive models used in preliminary analysis.

Concrete Constitutive Models

Compression Pre-Peak	Hognestad (Parabola)	**Dilation**	Variable - Isotropic
Compression Post-Peak	Modified Park-Kent	**Cracking Criterion**	Mohr-Coulomb (Stress)
Compression Softening	Vecchio 1992	**Crack Stress Calc**	Basic (DSFM/MCFT)
Tension Stiffening	Modified Bentz 2005	**Crack Width Calc**	Agg/2.5 Max Agg.
Tension Softening	Nonlinear (Hordijik)	**Crack Slip Calc**	Walvern
FRC Tension	SDEM-Monotonic	**Creep and Relaxation**	Not Considered
Hysteretic Response*		Palermo 2002 (w /decay)	

Steel Constitutive Models

Hysteric Response	Bauschinger Effect (Seckin)	**Buckling**	Modified Dhakal-Maeka
Dowel Action	Tassios (Crack Slip)	**Concrete Bond**	Eligehuasen

* indicates non-default model choice

5.3.8 Parametric Study

When modelling slender shear walls in VecTor2 the modeller is tasked with having to make decisions which can vary from user to user. To ensure that that certain choices made in the procedure for the modelling of Morcos' and Soto-Rojas' have legitimacy a parametric study was conducted on three key features of the models; the impact of displacement step size used, the impact of the chosen mesh size, and the impact of the updated steel properties discussed in Section 5.3.4. Although the modelling of all walls preformed in this work will mainly be done in a reverse-

cyclic manner reflective of the experimental data, the parametric models will be loaded monotonically as it is a less computationally intensive while still allowing for comparison to the envelope response of the experimental tests.

5.3.8.1 Impact of Displacement Increment Size

Displacement increment size can vary greatly depending on the final expected displacement, the desired sensitivity of the response, and in the case of reverse-cyclic loading based on the desired displacement cycles and the incremental increase between cycles. Larger displacement increments are beneficial in that they allow for faster model response turn around due to requiring less load steps to reach the same target displacement as smaller increments. This does come at the cost of losing sensitivity of the response and more sudden failures if calculated strains suddenly exceed failure properties of materials. The use of smaller increments while providing greater sensitivity does require more computation and can lead to responses with more noise as the models redistribute strains between elements more frequently, especially when bond models are present. The chosen displacement increment sizes were 0.5mm, 1mm, 2mm, and 5mm, with responses for walls SWS and SWN shown below in Figure 5.15 and Figure 5.16 respectively.

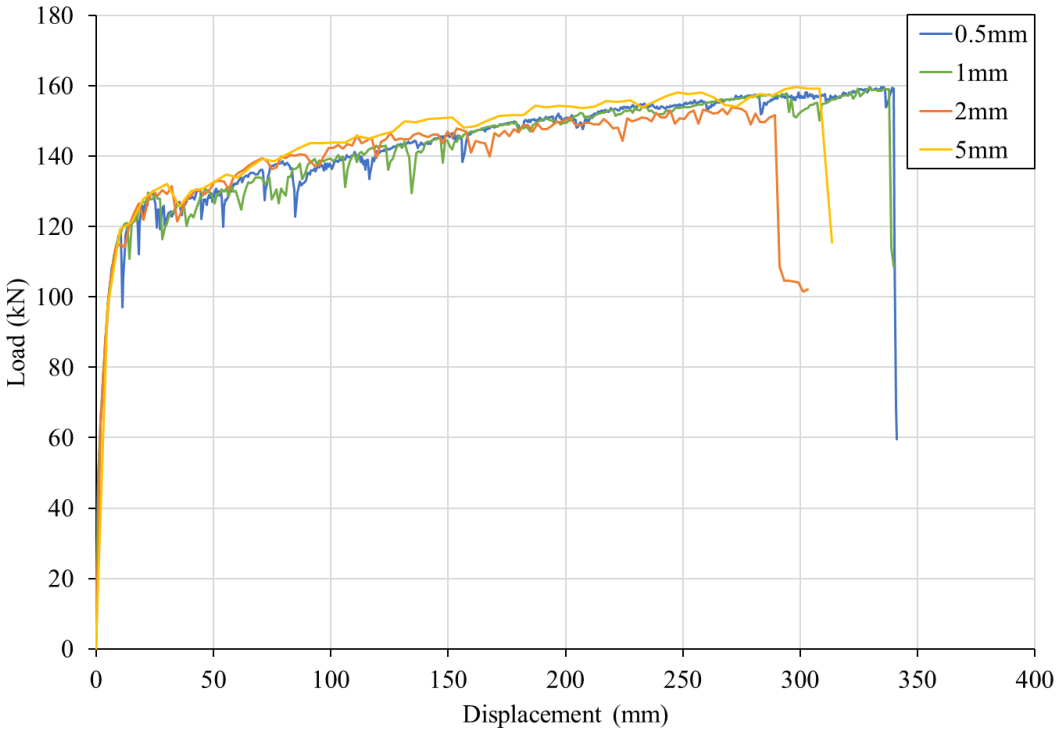

Figure 5.15 Load-displacement response of SWS with different load increments.

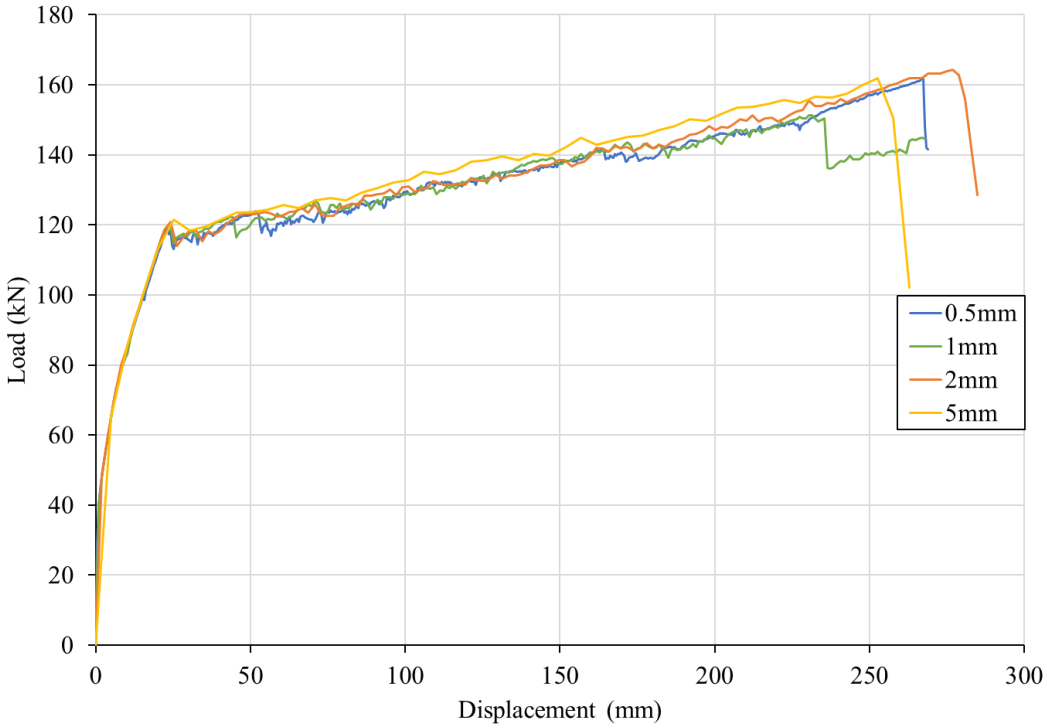

Figure 5.16 Load-displacement response of SWN with different load increments.

When examining the responses, failure was based on the methodology proposed by Park (1989) and consisted of either a sudden drop corresponding to a failure of material element i.e. fracture of reinforcement or substantial degradation of concrete, or a gradual drop below 80% of the peak load. For all increments across both walls, failure was consistent as rupture of deformed steel reinforcement (in the boundary region for SWS and in the web for SWN) which is inline with failure modes found by Morcos (2021). The 1mm increment load for SWN, Figure 5.16, was a slight outlier with the rupture of rebar not occurring at the first drop in load but at the second. The analysis demonstrates that all increment sizes preformed similarly except for the ultimate displacement which is to be expected. The largest increment considered, 5mm demonstrated the smoothest response and provides an upper bound for the load capacity. All increments provide similar initial response with small variation being caused by the transition from uncracked to cracked concrete. The prevalent noise in smaller increment levels was due to the use of bond models which cause small drops in load as link elements cause redistribution of strains within the model from one step to the other. For the remaining parametric models an increment step of 1 mm was used as the models were found to have an acceptable runtime without significant loss of sensitivity.

5.3.8.2 Impact of Updated Steel Properties

The models presented in this work utilize material properties for steel reinforcement which differ from previous modelling done by Morcos (2021) and used by Soto-Rojas & Palermo (2020) as discussed in Section 5.3.4. The main reason these new values are being considered is the overestimation of peak load capacity by previous models compared to the experimental results, summarized in Table 5.8. Two models were run to investigate the impact of the new material properties on the monotonic response of the walls. One model utilized the reinforcement properties from Morcos (2021) while the other used the material properties presented earlier in the thesis. The load-displacement responses of each model were compared against the response envelope from experimental testing are shown in Figure 5.17 and Figure 5.18. The experimental envelope for SWS was the average value of the positive and negative displacements while for SWN the positive and negative values were shown as individual envelopes due to the differences in the response. The change in properties do not have a significant impact on the monotonic response of SWS with load values often converging for most of the response. When using updated properties for steel reinforcement in SWN there was up to an 8.7% reduction in the load capacity compared to load at similar displacements using Morcos' values. Based on this the updated properties will be used as input values in all remaining models.

Table 5.8 Numerical and experimental peak load capacities for SWS and SWN.

Response	**SWS**		**SWN**	
	Peak +	**Peak -**	**Peak +**	**Peak -**
Experimental Load (kN)*	125	111	116	121
Numerical Load (kN)*	138	128	147	147
Error (%)	10.4	15.3	26.7	21.5

*Indicates data from Morcos (2021)

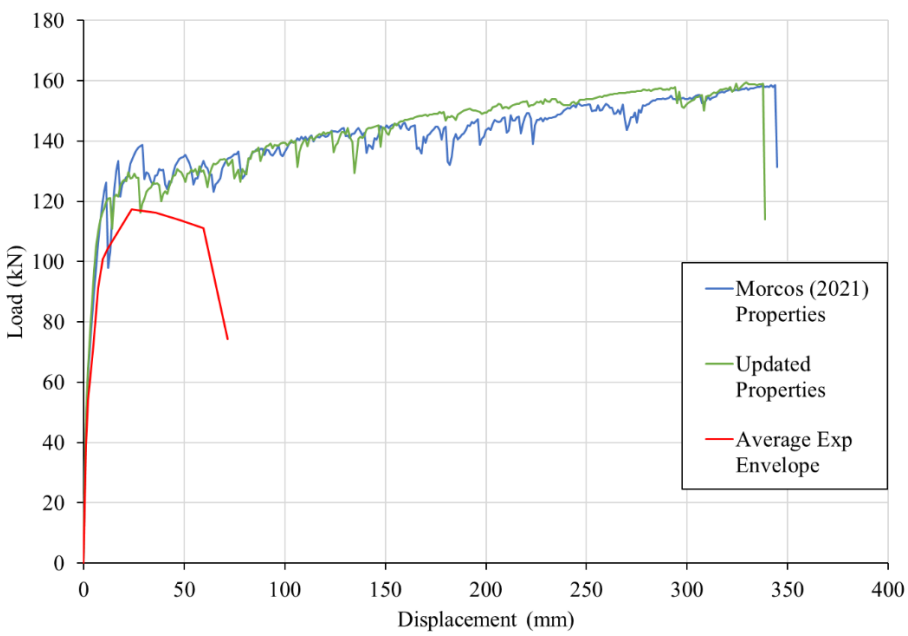

Figure 5.17 Load-displacement response based on different material properties for SWS.

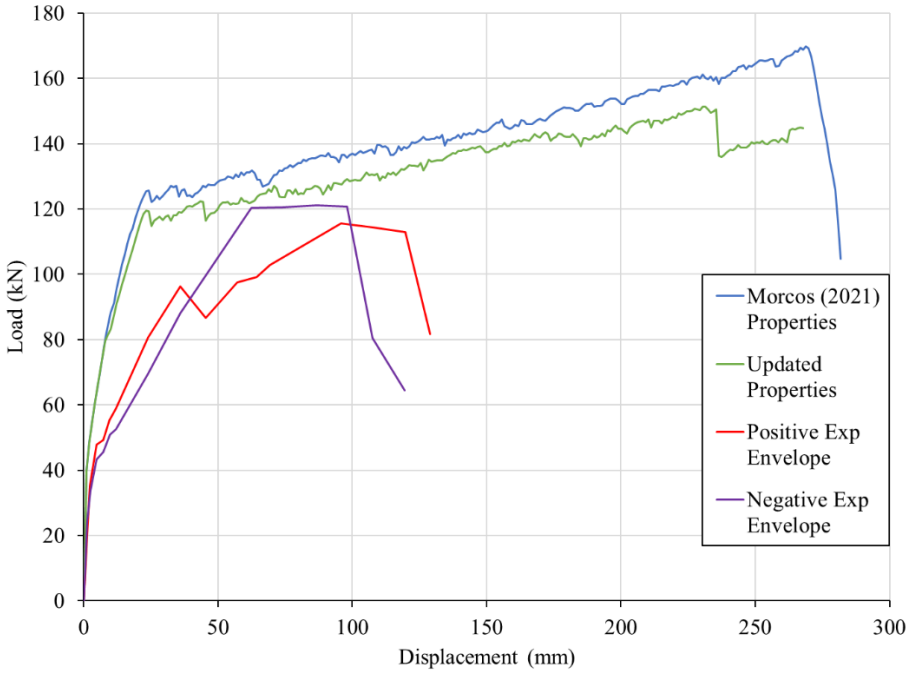

Figure 5.18 Load-displacement response based on different material properties for SWN.

It is important to note that although monotonic FEA responses provide overestimates in both load and displacement compared to experimental results from reverse cyclic loading, this is to be expected due to the nature of the two types of loading. Reverse cyclic loading will reduce

both the strength and ductility capacity of a structure due to the cycles causing continued material degradation captured by the hysteretic response.

5.3.8.3 Impact of Mesh Size on Model Performance

In Section 5.3.1 it was stated a mesh size of 50 mm x 50 mm was ideal for modelling but in reality, the ideal mesh size could vary from modeller to modeller. To gain a better understanding of the impact different mesh sizes can have on the performance and response of the models two additional mesh sizes were considered: a mesh measuring 25 mm x 25 mm and a mesh measuring 75 mm x 50 mm representing finer and coarser mesh comparisons respectively. Although the 25 mm x 25 mm mesh size keeps the same aspect ratio of 1 there were no other mesh sizes larger than 25 mm aside from 50 mm that could maintain a aspect ratio of 1 while allowing for both the proper 150 mm spacing on longitudinal bars in the x direction and maintaining key points that were multiples of 100 mm in the y direction, such as the end of the plastic hinge region at 1100 mm. The 75mm x 50 mm mesh in the web was able to maintain a 1.5 aspect ratio while maintain the appropriate spacings. The load-displacement responses are shown Figure 5.19 and Figure 5.20. The initial stiffness of all response across SWS and SWN are similar as are the load prediction until the premature failure of the 25mm discretization models. In the SWS model the 25mm mesh fails at a displacement of 186 mm compared to 388 mm for the remaining two meshes while in the SWN model the 25 mm mesh fails at 117 mm compared to 268 mm and 260 mm for the 50 mm and 75 mm mesh. The reason for such a large discrepancy is likely due to the fact that at smaller mesh sizes small round off in the calculated strains are more magnified and can cause earlier localized failure of the reinforcement, the primary failure mode of all models shown. Based on the results its appears that a 50 mm x 50 mm mesh size is sufficient for the purposes of this study with coarser meshes providing similar results with the finer mesh, while maintain the same aspect ratio, providing issues with premature failure.

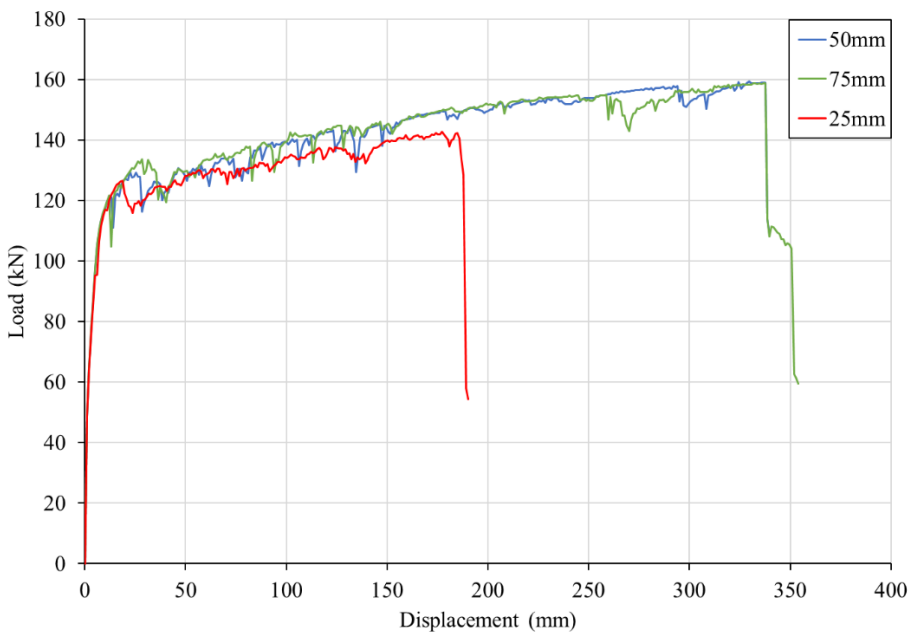

Figure 5.19 Load-displacement response of different mesh discretization sizes for SWS.

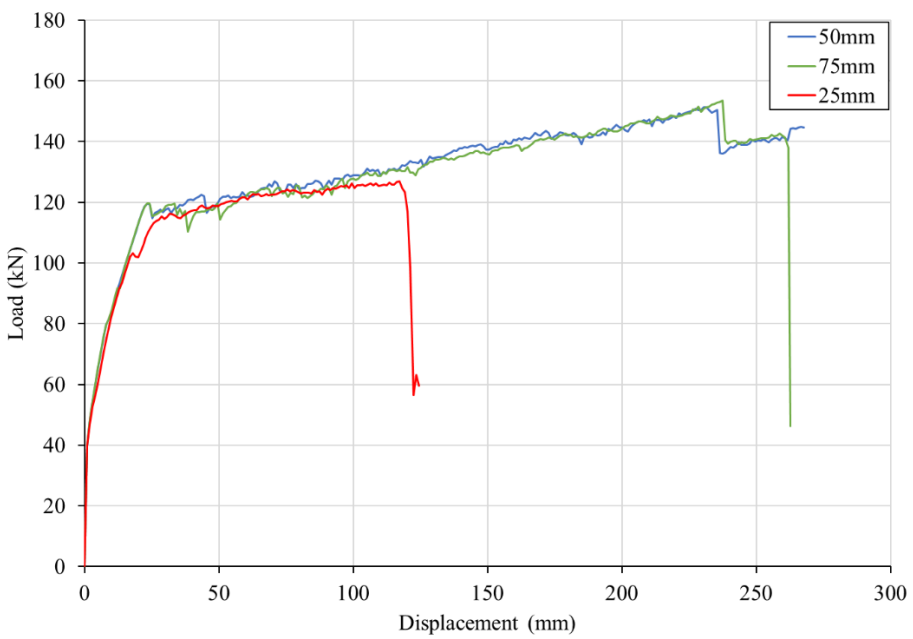

Figure 5.20 Load-displacement response of different mesh discretization sizes for SWN.

5.3.9 Reverse Cyclic Load

The models discussed up to this point were now subjected to reverse cyclic loading based on the experimental loading protocol outlined by Morcos (2021). The loading protocol for SWS and SWN were similar but not identical. Experimental loading for both walls was based on a

combination of FEMA 461 (FEMA, 2007) and ATC 24 (ATC, 1992) guidelines and involved using drift ratios starting at 0.05% before increasing to 0.1% and then incrementing by 0.1% until a drift of 0.5% was achieved (Morcos, 2021). After this point loading cycles were increased by 0.5% drift until testing was terminated. For SWS each drift ratio was run for a total of three cycles up to and including 1% drift at which point all remaining drift ratios only consisted of 2 cycles. For SWN each drift ratio was run for a total of three cycles up to and including 2% drift at which point all remaining drift ratios only consisted of 2 cycles. The loading procedure for the models is summarized in Table 5.9. The displacement increments were decided based on being a common factor for a set of load cycle displacements as well as to ensure that the number of steps in a give cycle never exceeded 200 until past 5%. All displacement increments used were similar to those in the parametric study, Section 5.3.8.1, which had shown reasonable consistency. To run a reverse cyclic analysis in VecTor2 the number of repetitions for each cycle and cyclic increment factor must be input and stay consistent for the entirety of the run. Changing either the load step increment, cyclic increment, or number of repetitions requires the model to be stopped and new inputs to be defined. Wall SWS was run in four sets consisting of cycle numbers 1-2,3-6,7, and 8-15 while SWN was run in sets consisting of cycle numbers 1-2,3-7,8-10, and 10-15.

Table 5.9 Reverse-cyclic loading parameters for VecTor2 models.

Cycle #	Drift (%)	Final Displacement	Repetitions		Load Step Increment (mm)	Cyclic Increment (mm)
			SWS	SWN		
1	0.05	1.2	3	3	1.2	
2	0.1	2.4	3	3	1.2	1.2
3	0.2	4.8	3	3	2.4	2.4
4	0.3	7.2	3	3	2.4	2.4
5	0.4	9.6	3	3	2.4	2.4
6	0.5	12	3	3	2.4	2.4
7	1	24	3	3	6	12
8	1.5	36	2	3	6	12
9	2	48	2	3	6	12
10	2.5	60	2	2	6	12
11	3	72	2	2	6	12
12	3.5	84	2	2	6	12
13	4	96	2	2	6	12
14	4.5	108	2	2	6	12
15	5	120	2	2	6	12

5.3.10 Initial Reverse Cyclic Modelling

Models for SWS and SWN were run based on the definitions presented previously with load applied based on the reverse cyclic loading protocol outlined in the previous section. The load-displacement responses of the walls are shown against experimental data from Morcos (2021) in Figure 5.21 and Figure 5.22.

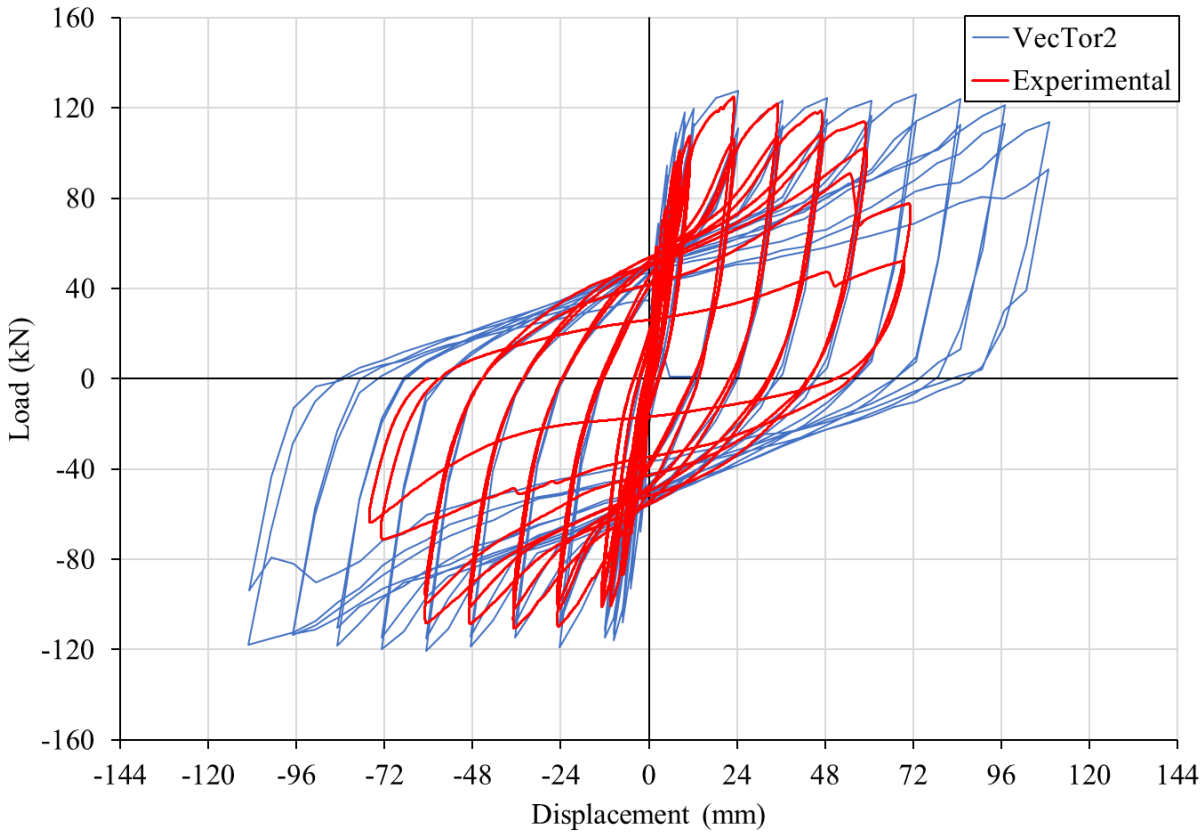

Figure 5.21 Load-displacement response of SWS-Initial reverse cyclic response.

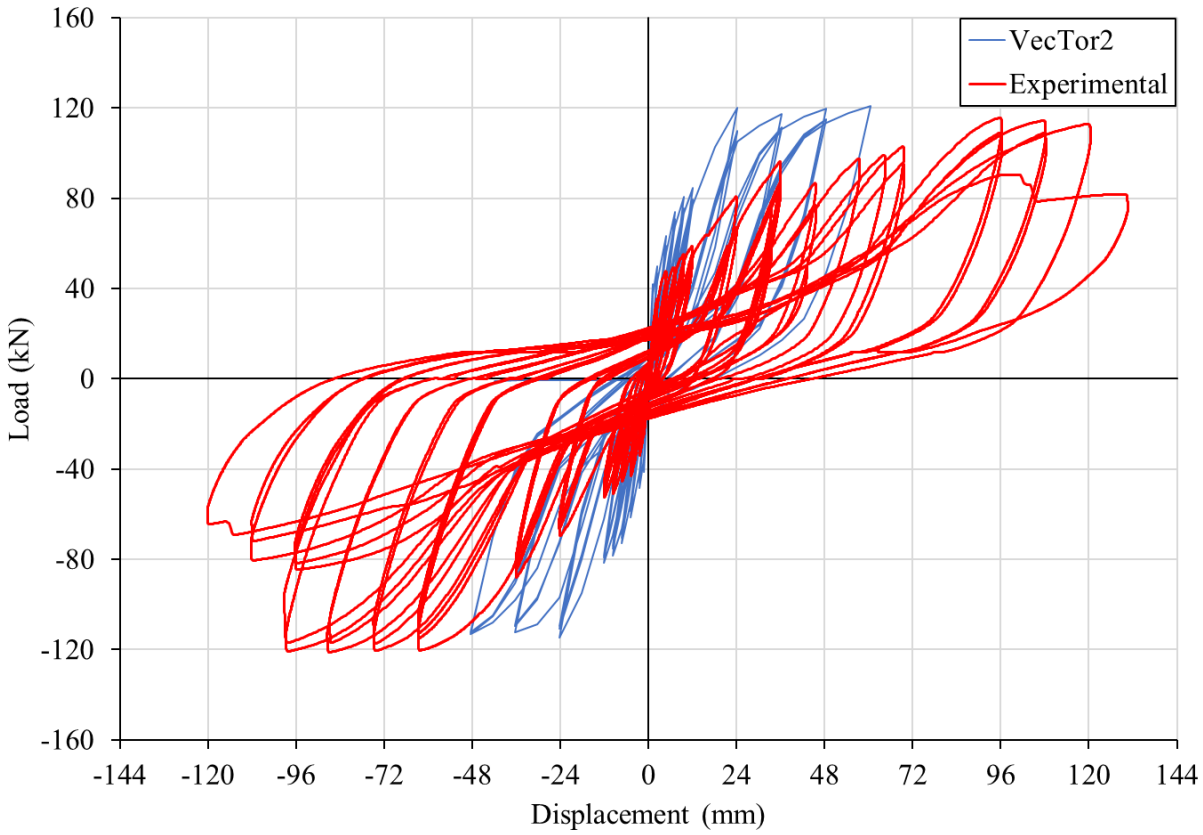

Figure 5.22 Load-displacement response of SWN-Initial reverse cyclic response.

The responses of both the SWN and SWS models provide improved load capacity predictions compared to the previous modelling presented in Morcos (2021) with SWN predicting a maximum load of 127.7 kN and 120.5 kN in the positive and negative directions, compared to the experimental peak loads of 125 kN and 111 kN respectively. Likewise, the SWS models provide similar load improvements with numerical data predicting peak loads of 121 kN and 114.8 kN to the experimental peaks of 116 kN and 121 kN. The ability for the initial models to capture the displacement of the experimental walls is lacking with SWS greatly overestimating the ductility of the wall, predicting failure during the 108 mm load cycle compared to the experimental failure at the 60 mm cycle. SWN models inversely greatly underestimate the ductility wall with a sliding failure occurring after the 60 mm cycle compared to the experimental failure only being reached after the 120 mm and 96 mm cycles in the positive and negative directions. The cause for the early failure of the SWN model was failure of transverse shear reinforcement in the boundary region along the base of the wall which is a completely different failure mode than the rupturing of steel reinforcement bars in the web observed by Morcos (2021). During experimental testing the

foundation block of the wall may be considered to provided additional confinement and stiffening to the portion of the web directly adjacent due to the large quantity of concrete. To better reflect this the first ro0077 of elements in the wall, measuring 50 mm in height, were defined to have twice the rho value than normal. The web elements in the first row were defined to have ρ_x = 1.78% while the boundary elements were defined to have ρ_x = 5.33% and ρ_z = 3.33%. This change was implemented into both the SWS and SWN models, shown in Figure 5.23, to ensure consistency between both walls and avoid overcompensating to force a result in one wall. The load-displacement responses of the walls are shown in Figure 5.24 and Figure 5.25.

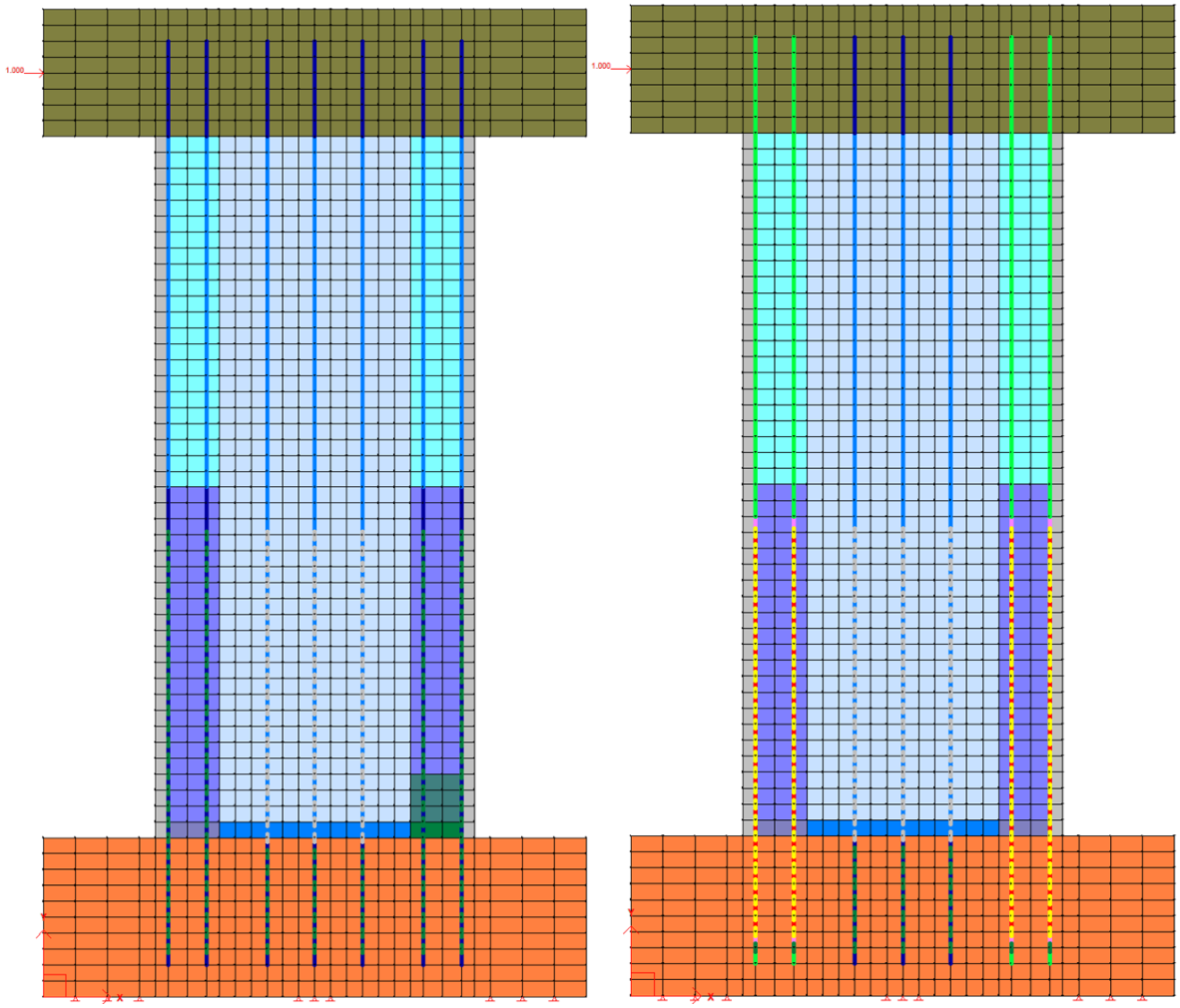

a) b)

Figure 5.23 Updated FEA models considering increased confinement reinforcement for a) SWS and b) SWN.

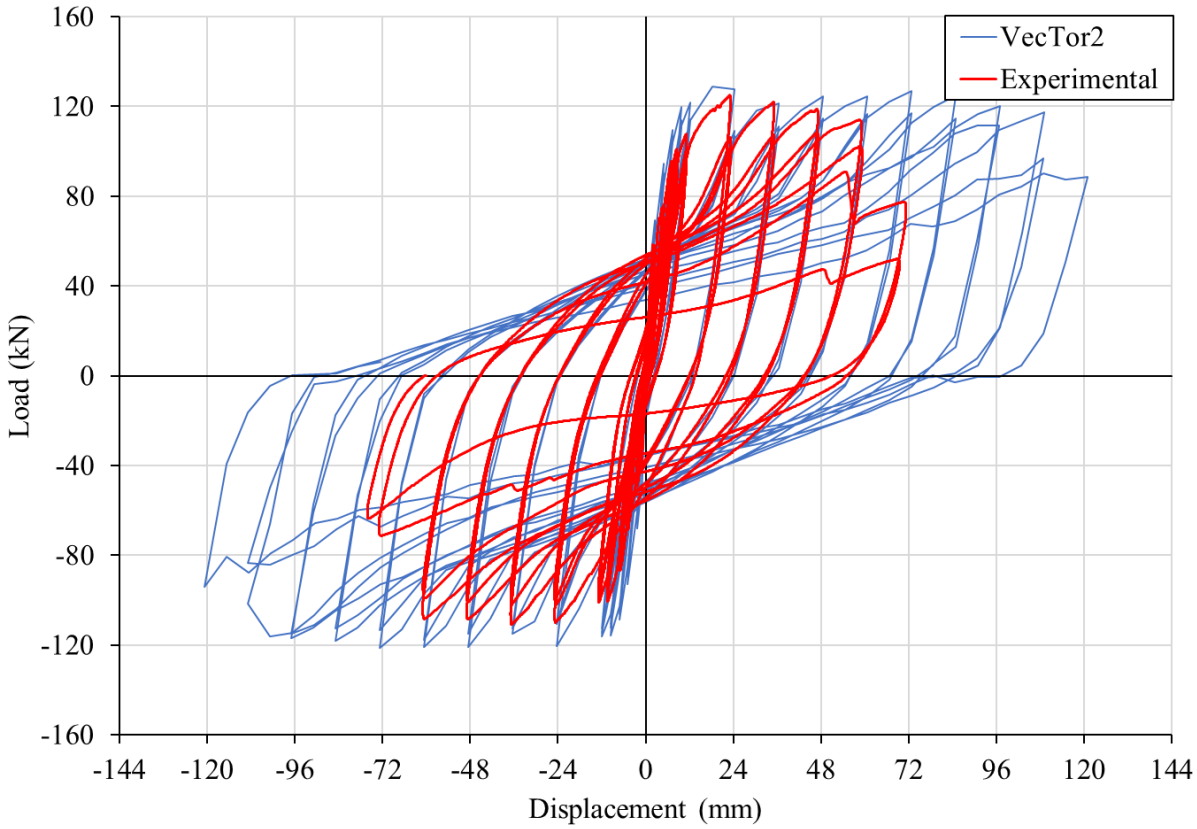

Figure 5.24 Load-displacement response of SWS-Increased Base Confinement.

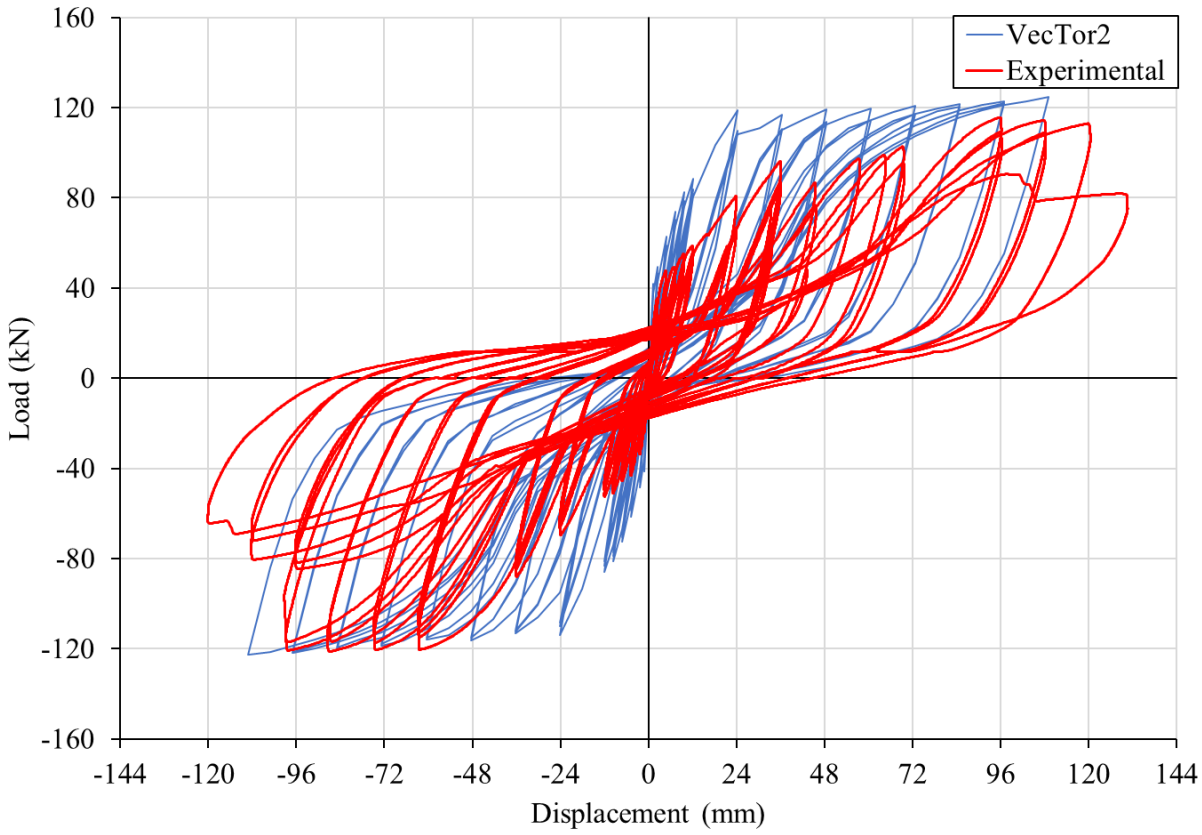

Figure 5.25 Load-displacement response of SWN-Increased Base Confinement.

Increasing reinforcement ratios of the elements along the base of walls appears to have the intended affect with the response of the updated SWS model being nearly identical to that of the base SWS model in peak load and only achieving one further displacement cycle which demonstrate signs of material degradation before failure by reinforcement fracture. The updated SWN model allowed for greater ductility almost matching the experimental results which saw the wall sustaining cycles of 120 mm in the positive direction and 96 mm in the negative direction compared to numerical data which now had the wall failing after the 108 mm cycle. The improved SWN model also allowed for a more symmetrical response with the peak loads in the positive and negative direction increasing to 124.9 kN and 122.8 kN respectively. The failure was also seen to change to a sliding failure along a major crack which occurred 200 mm above the base. This failure mode is reasonable due to similarity in crack patterns, shown in Figure 5.26, between the numerical model and experimental wall leading up to failure. In the numerical model the location of sliding is highly dependant on small differences in strains at the location of cracks at the base and 200 mm above.

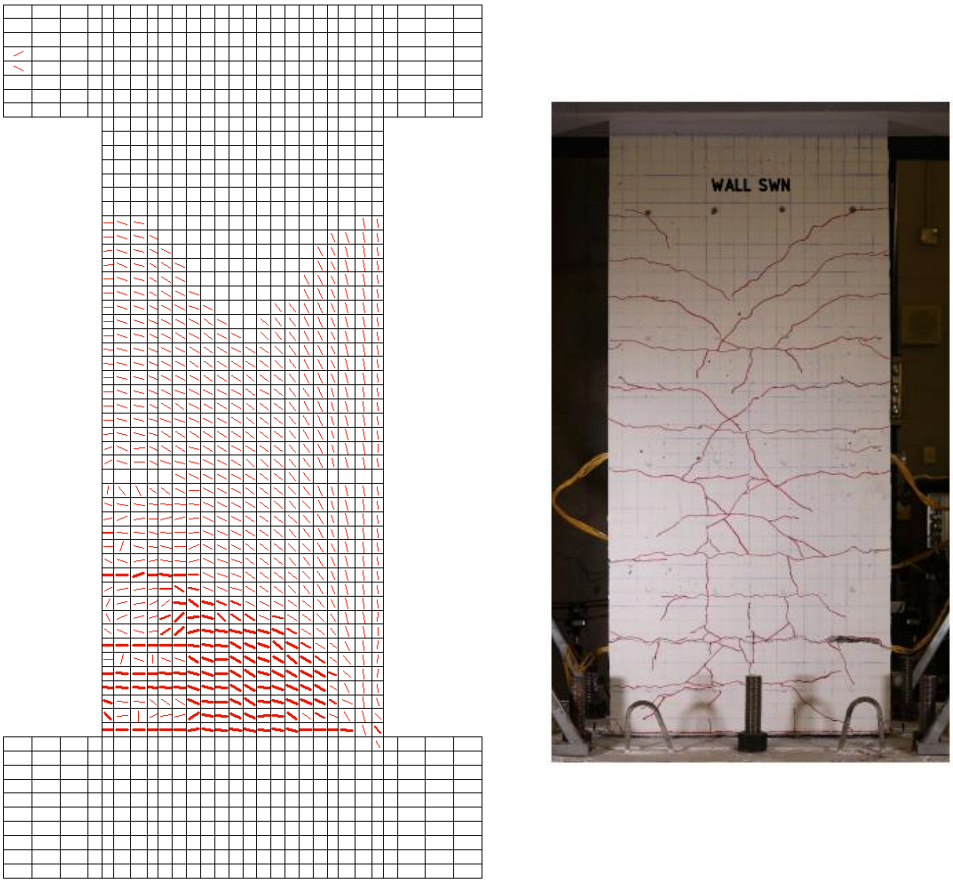

a) b)

Figure 5.26 Cracking pattern at peak load from a) VecTor2 and b) experimental testing (Morcos, 2021).

5.3.11 Reverse Cyclic Modelling Accounting for Reduced Reinforcement Bar Area

The inclusion of an increased reinforcement ratio along the wall base was beneficial to the SWN model but the model for SWS still seemed to be significantly overestimating the ductility of the wall prompting consideration into what other options could be implemented to reduce the ultimate displacement. When considering possible options, it was preferable that the reason for the change was reflective of some physical quality of the wall as opposed to simply using an arbitrary model or modification that provides a better response. To this end it was noticed that in the observations made by Morcos post-testing, the rupture location of reinforcement seemed to be in the vicinity of strain gauges as shown in Figure 5.27 and Figure 5.28. When installing strain gauges, the ribs of the deformed bars had to be filled down to create a smooth flat surface onto which the strain gauges could be attached. Although care was taken not to take off anymore material than necessary the

cross-sectional area and in turn force capacity of the bar will be slightly decreased which can lead to localized straining at the reduced area and premature failure.

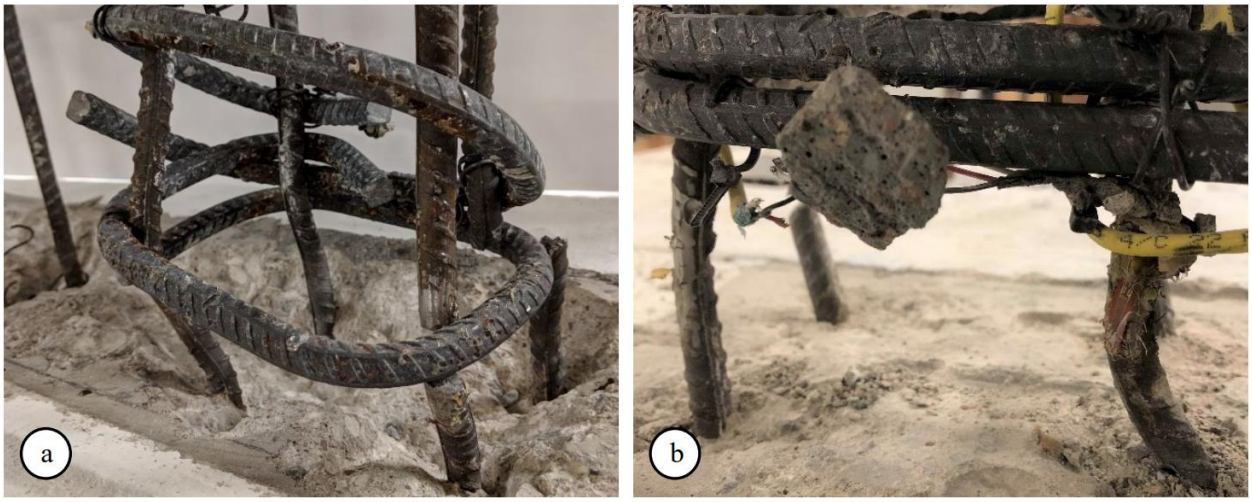

Figure 5.27 Buckled and ruptured longitudinal reinforcement at the base of Wall SWS-R: a) right boundary and b) left boundary (Morcos, 2021).

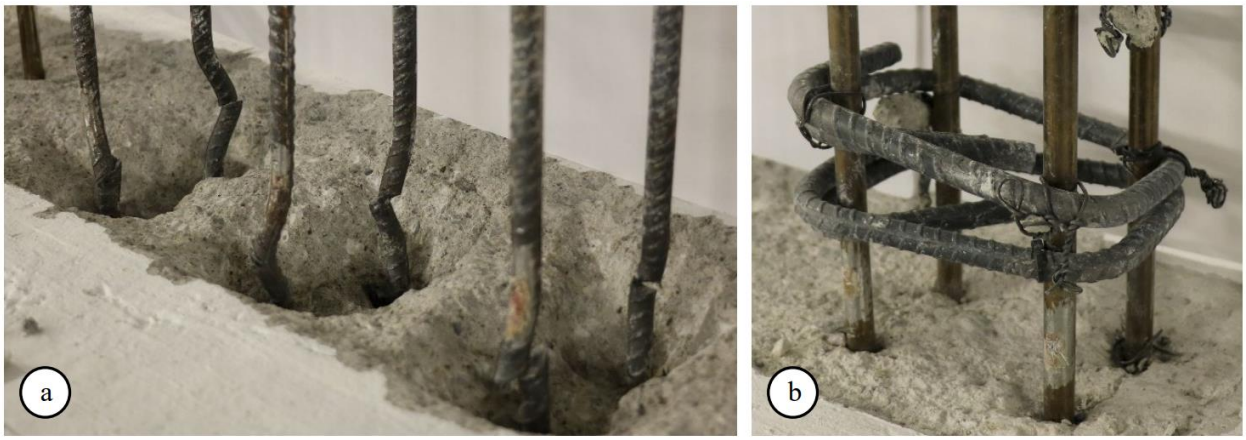

Figure 5.28 Buckled and ruptured longitudinal reinforcement at the base of Wall SWS-R: a) web and b) right boundary (Morcos, 2021).

To reflect this reduction in area it was decided that the improved SWS and SWN models, referred to with a V2 suffix in the remainder of the chapter, would be altered such that steel reinforcement bars would have a 50 mm long section, a single element, defined to have a reduced area reflective of having been filled down for strain gauging. SMA reinforcement bars were not altered since their smooth surface meant that strain gauges could be attached directly onto the bar without having to reduce the cross section. This reduced cross section element would be at the base of the wall. Based on diagrams outlining the strain gauge installation locations it was

determined that in the boundary region steel reinforcement on the front and back curtain were strain gauged while in the web only one curtain of steel reinforcement was strain gauged. This resulted in having in having the area of web bars reduced by a percent of only a single bar. When defining these elements with reduced cross section it was necessary to ensure that the bar diameter was also adjusted to reflect the new area since bar diameter is used by VecTor2 in multiple calculations. This work considered three different reductions in bar cross-sectional area: 5% reduced area, 10% reduced area, and 15% reduced area. The input parameters that are changed for the elements corresponding to the strain gauge locations for different walls are shown in Table 5.10

Table 5.10 Reinforcement properties for steel rebar with reduced area.

Reduction in Area (%)	**Steel Bars in Boundary Region**		**Steel Bars in Web Region**	
	Cross-Sectional Area (mm^2)	Reinforcement Diameter, D_b (mm)	Cros-Sectional Area (mm^2)	Reinforcement Diameter, D_b (mm)
5	190	11	195	11.1
10	180	10.7	190	11
15	170	10.4	185	10.8

5.3.11.1 5% Reduction in Steel Reinforcement Cross Sectional Area

The first reduction that was attempted was 5% on each bar with a strain gauge, the load displacement responses of SWS-V2 and SWN-V2 are shown in Figure 5.29 and Figure 5.30. The response of SWS-V2 with 5% area reduction shows a slight decrease in ductility, not being able to complete a single 108 mm displacement cycle before the exterior bar in the boundary region ruptures right at the base. This suggests that the reduction of area is having the intended effect, although it will be necessary to increase the reduction to see greater reduction in ductility. The response of SWN-V2 appears to provide more ductility with the 5% reduction being able to complete a single 144 mm displacement cycle before sliding failure occurs compared to the SWN-V2 model with no reduction from section 5.3.10 which could only complete up to the 108 mm

cycle. There does appear to be more slip in the SMA bars which could be causing other discrepancies leading to a higher ductility, but no specific process can be singled out for this occurrence and highlights the difficulty incorporation of more novel materials like SMA can have in FEA programs.

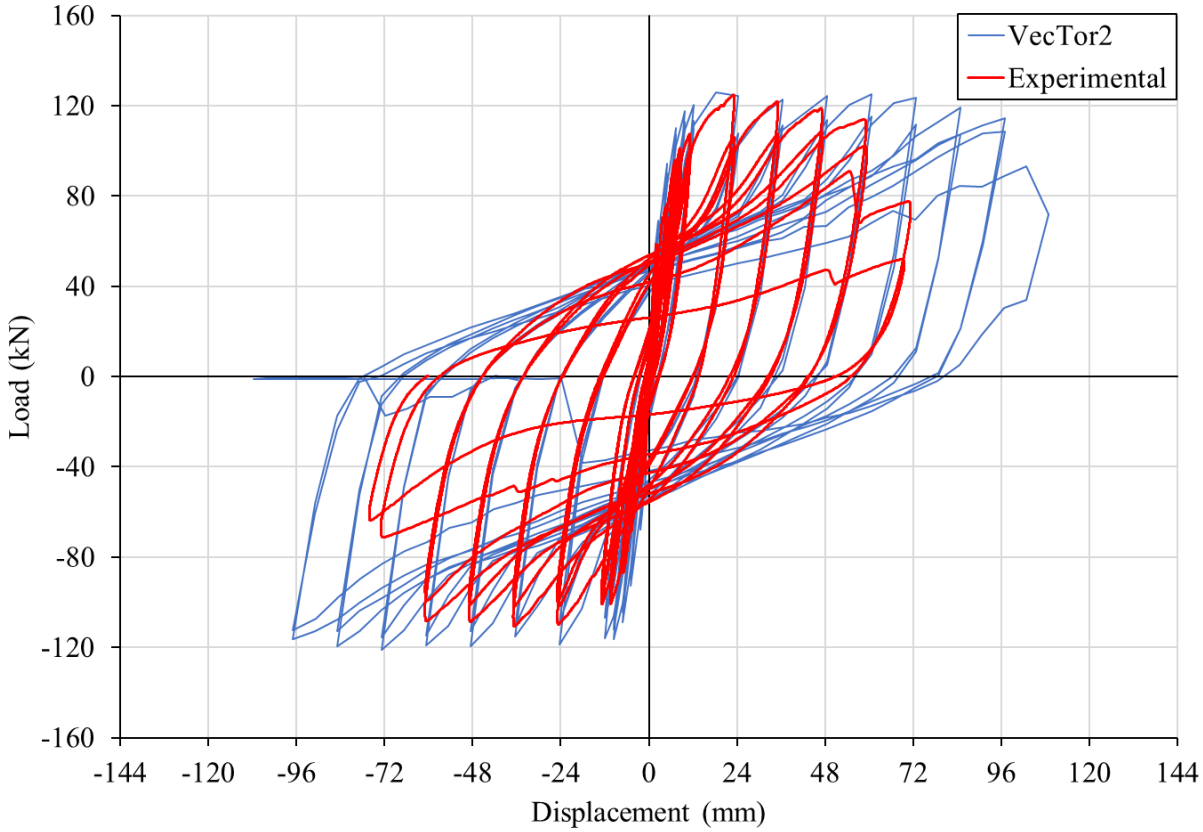

Figure 5.29 Load-displacement response of SWS-V2 5% reduced bar area.

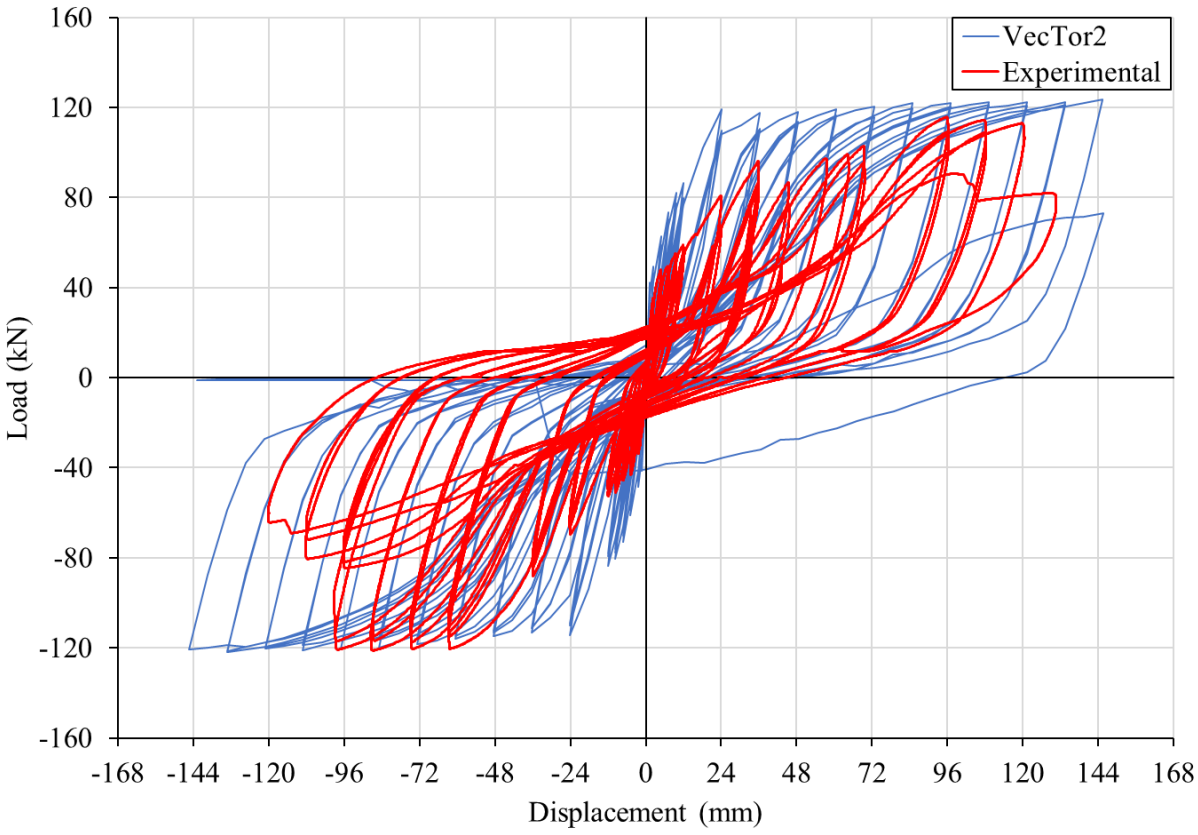

Figure 5.30 Load-displacement response of SWN-V2 5% reduced bar area.

5.3.11.2 10% Reduction in Steel Reinforcement Cross Sectional Area

Progressing from 5% reduction in area, the next step was decided to be doubled with the corresponding load-displacement for a 10% reduction in cross-sectional area for SWS-V2 and SWN-V2 being presented in Figure 5.31 and Figure 5.32. The further reduction does not have significant effects on SWS-V2 which maintains similar ductility and failure consisting of rupture of an external bar in the boundary region. There does appear to be less load reduction in cycles leading up to failure with the 10% reduced area model achieving 122.4 kN and 114.5 kN in the positive and negative loading directions at the 96 mm displacement cycle while the 5% reduced area model achieved 108 kN and 116 kN at the same cycles. The SWN-V2 model with 10% area reduction presents similarly to the 5% counterpart except it now fails on the first 144 mm cycle as opposed to the second and the failure mode has changed from sliding to rupture of the exterior web steel reinforcement.

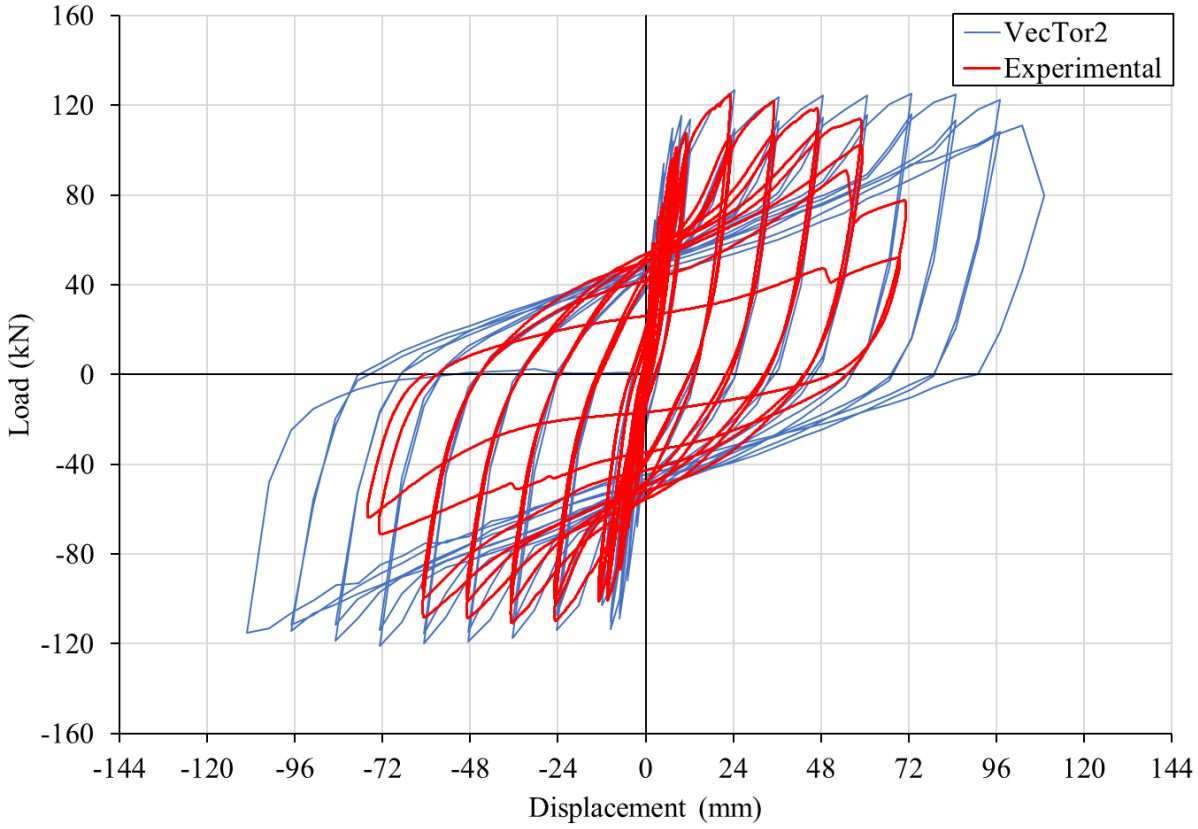

Figure 5.31 Load-displacement response of SWS-V2 10% reduced bar area.

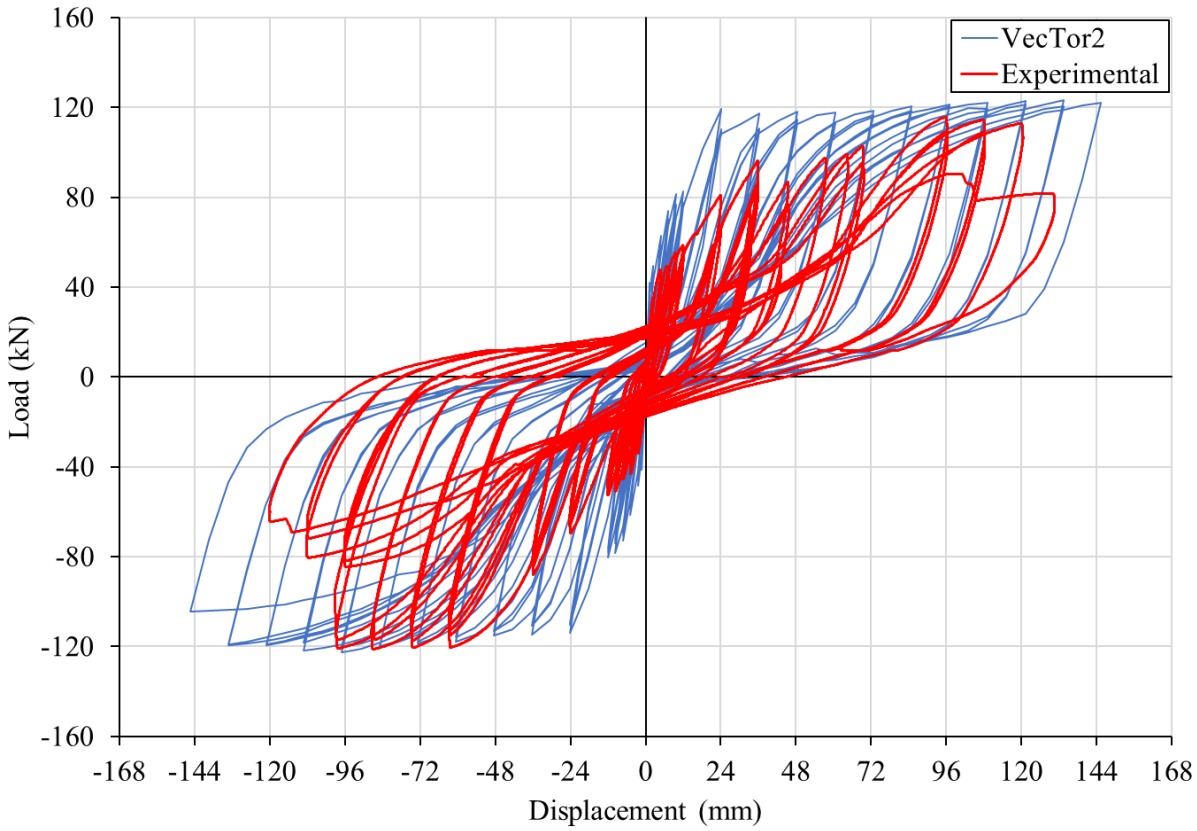

Figure 5.32 Load-displacement response of SWN-V2 10% reduced bar area.

5.3.11.3 15% Reduction in Steel Reinforcement Cross Sectional Area

Increasing the reduction in area once more by a factor of 5% the load-displacement response of SWS-V2 and SWN-V2 with a 15% reduction in steel reinforcement cross-sectional are presented in Figure 5.33 and Figure 5.34. Across both the SWS-V2 and SWN-V2 response it appears that the reduction has now gone too far resulting a very premature failure with SWS-V2 failing during the 36 mm displacement cycle while SWN-V2 fails at the 48 mm displacement. SWS-V2 maintains the same failure mode of steel reinforcement fracturing at the boundary region while SWN-V2 reverts to a sliding failure along the base of the wall.

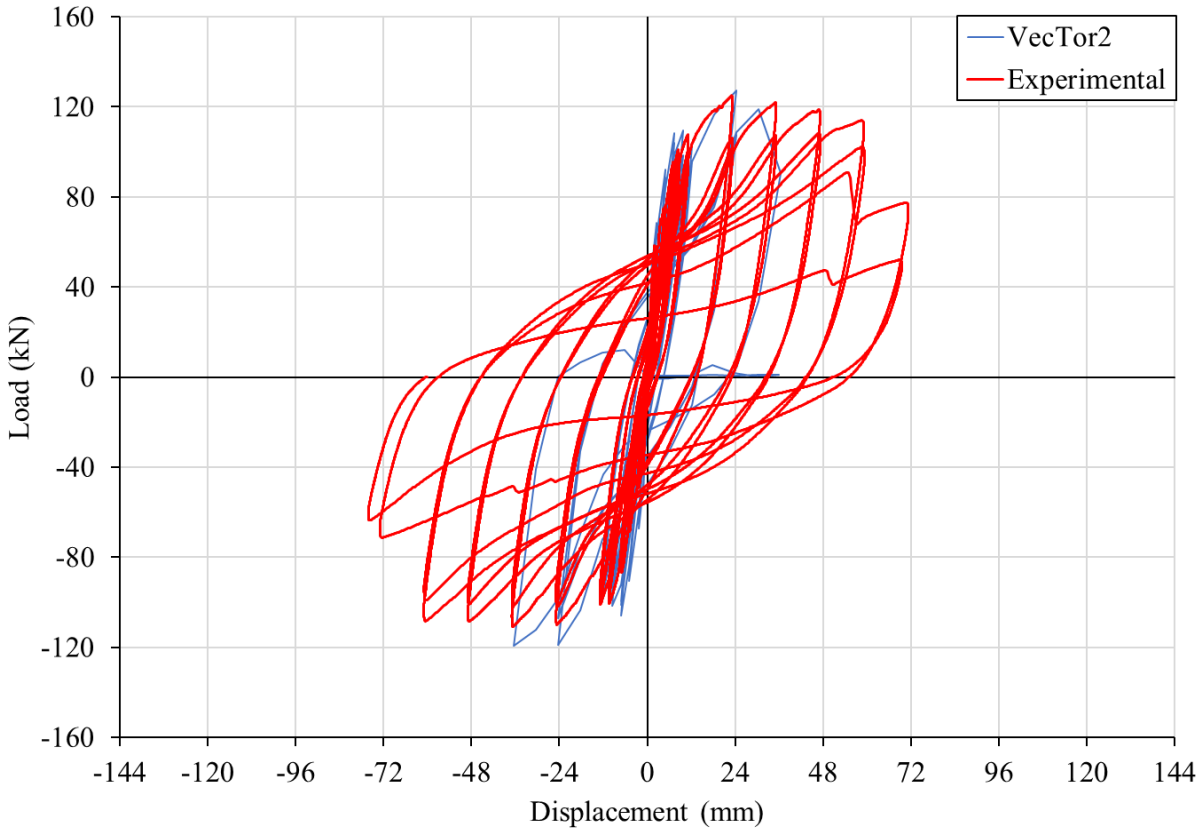

Figure 5.33 Load-displacement response of SWS-Increased Base Confinement 15% reduced bar area.

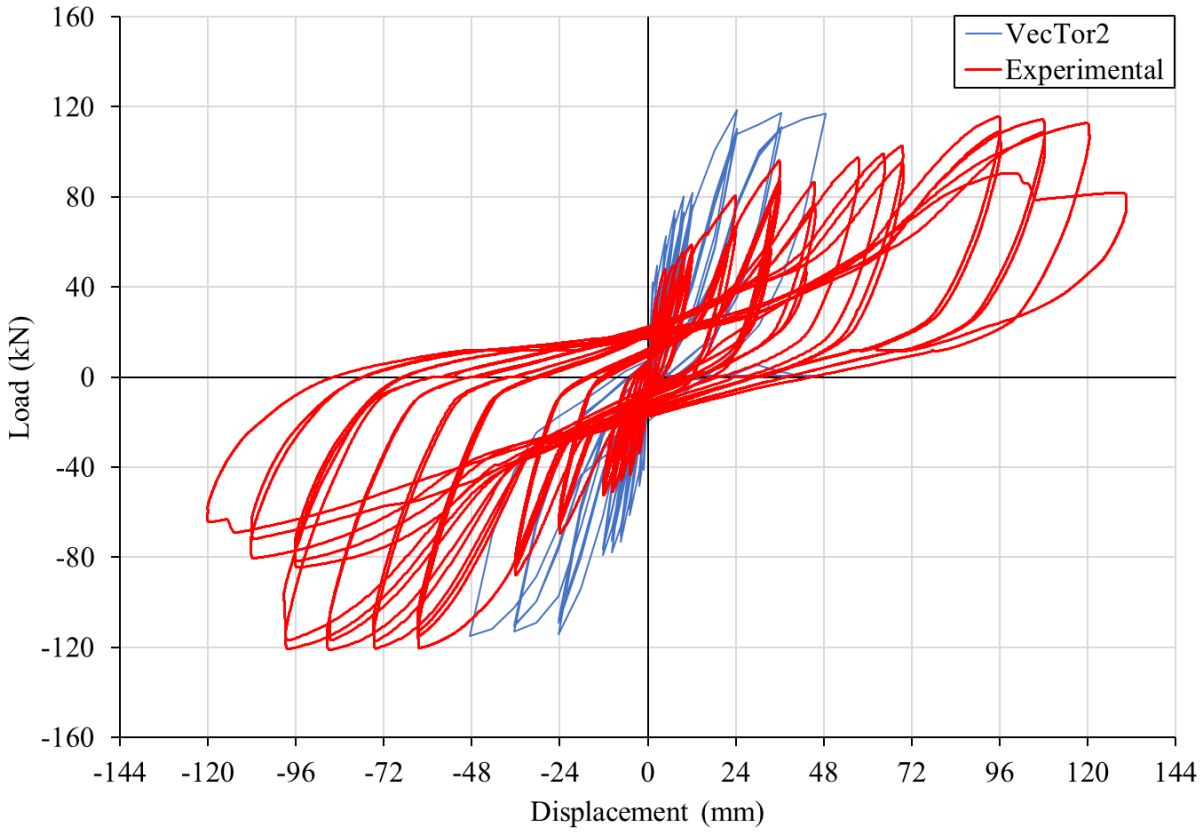

Figure 5.34 Load-displacement response of SWN-Increased Base Confinement 15% reduced bar area.

5.3.12 Reverse Cyclic Modelling Accounting for Local Fracture of Bars

When reinforced concrete is subjected to tension, the tensile strain that develops in the reinforcing bars does not act uniformly along the entire length in the direction of application. Instead, it often localizes in the area around cracks since the bars in these areas can more freely deform and undergo straining compared to sections that are still confined by uncracked concrete. This phenomenon is termed tension stiffening and is one of the constitutive models that is incorporated into VecTor2 with several options available. The tension model that has been used until this point was the default model of Modified Bentz 2005 which is able to consider reinforcement ratios and bond properties in the calculation of tension stiffening. This model does not however directly impact the rupture strain of steel which can be an issue when significant strain localization takes place. Zhang (2020) addresses this by proposing a simplified equation which predicts the reduced rupture strain of reinforcement based on properties of the reinforcement and the surrounding concrete. The

simplified equation is presented below and has been incorporated in VecTor2 as the Modified Bentz 2005 with local fracture:

$$\frac{\varepsilon_{rupt,embed}}{\varepsilon_{rupt,bar}} = FAC = \frac{7}{5} + 213 * 10^{-6} * d_b \frac{f_u - f_y}{f'_t}$$

$$\frac{1}{3} \leq FAC \leq 1.0$$

$$\varepsilon_{rupt,embed} = \varepsilon_{rupt,bar} * FAC$$

Where

$\varepsilon_{rupt,embed}$ is the modified rupture strain of reinforcement embedded in concrete

$\varepsilon_{rupt,bar}$ is the rupture strain of bare reinforcement

In the case of SWS and SWN using the material properties of the 10M rebar and tensile strength of concrete calculated by VecTor2, the rupture strains of reinforcement crossing cracks are reduced to 41.8% and 43.5% of their original stain capacity for SWS and SWN respectively. This reduction in rupture strain could provide the decrease in ductility allowing for results more similar to that of experimental data. The SWS-V2 and SWN-V3 wall models with 10% reduction in cross-sectional area were updated to have the Modified Bentz 2005 with local fracture as the constitutive model for tension stiffening while all other aspects were not altered in any way. The load displacement responses of these updated models are shown in Figure 5.33 and Figure 5.34.

The responses of both SWS-V2 and SWN-V2 demonstrate the impact the use of local fracture has on the ductility of the models. SWS-V2 with a 10% area reduction, which previously using Modified Bentz 2005 could complete the 96 mm displacement cycles, only completes a single cycle at 36 mm. SWN-V2 with a 10% area reduction and local fracture similarly has a reduced ductility, completing the 36 mm displacement cycle before a significant drop in load eventually leading failure. Both models had a fracture of the steel reinforcement along the base as the failure mechanics which is to be expected given the chosen tension stiffening model is significantly reducing the rupture strain of these reinforcement elements.

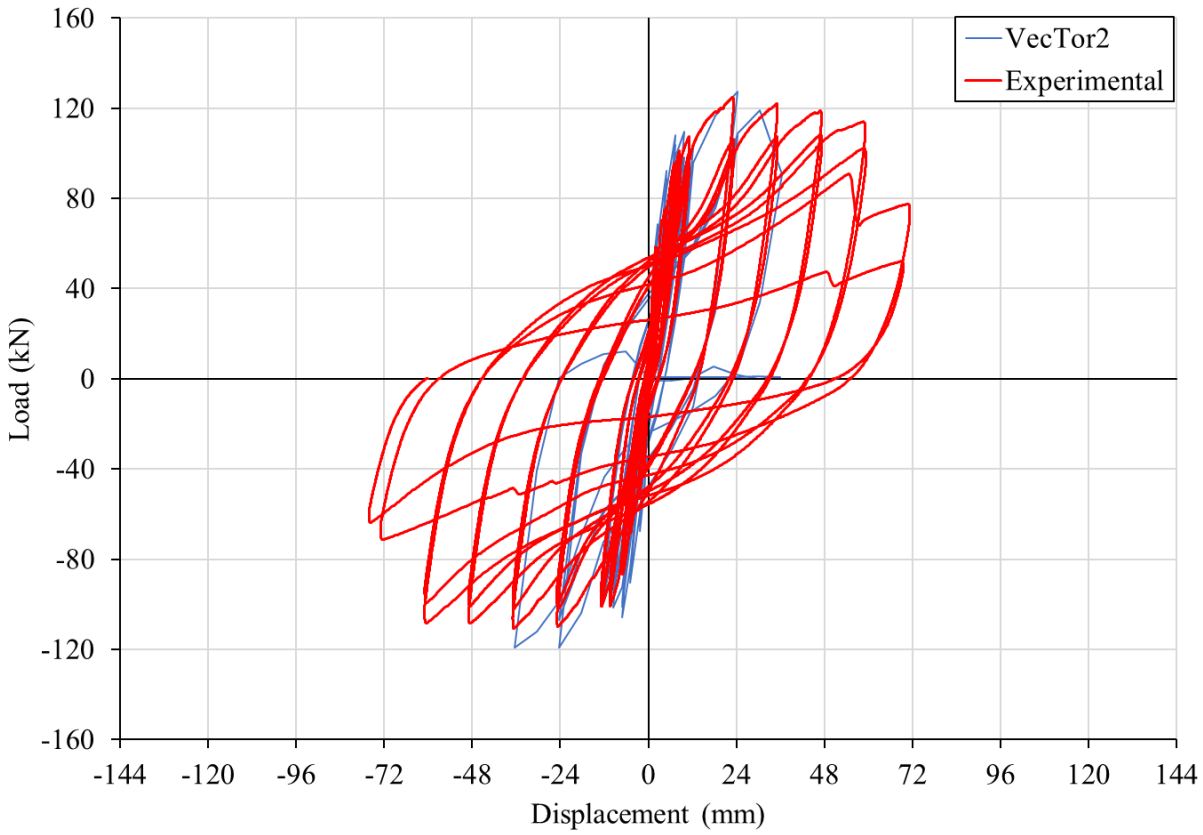

Figure 5.35 Load-displacement response of SWS-V2 10% reduced bar area with local fracture.

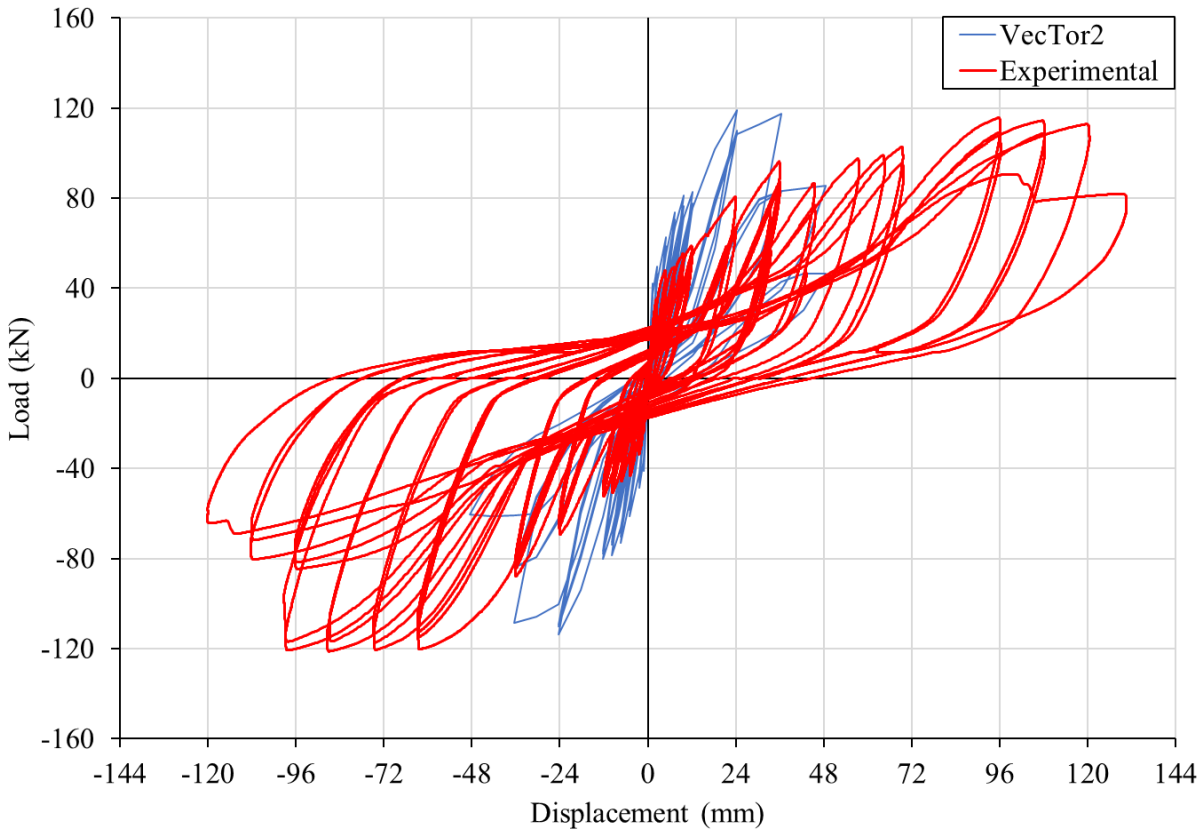

Figure 5.36 Load-displacement response of SWN-V2 10% reduced bar area with local fracture.

The combination of the reduced area with local fracture requires that a smaller reduction be used prompting SWS-V2 and SWN-V2 to be modelled once again with 5% reduction in area, with load-displacement responses in Figure 5.37 and Figure 5.38. This does provide greater ductility, SWS-V2 reaching up to the 48 mm displacement cycle and SWN-V2 reaching the 60 mm displacement cycle, but still leaves room for improvement as these displacements are still short of the experimental results. In both cases failure modes stayed consistent with exterior steel reinforcement rupturing along the base in both models, in the boundary region for SWS and in the web for SWN.

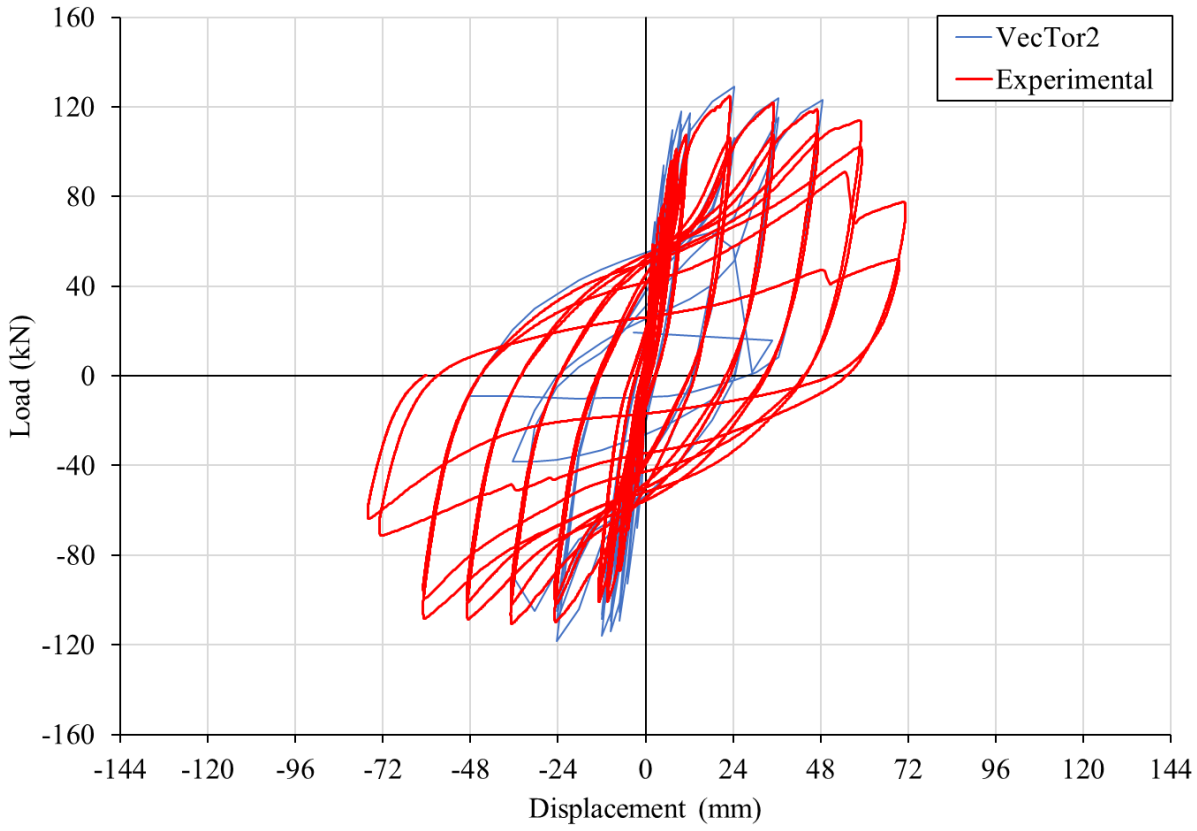

Figure 5.37 Load-displacement response of SWS-V2 5% reduced bar area with local fracture.

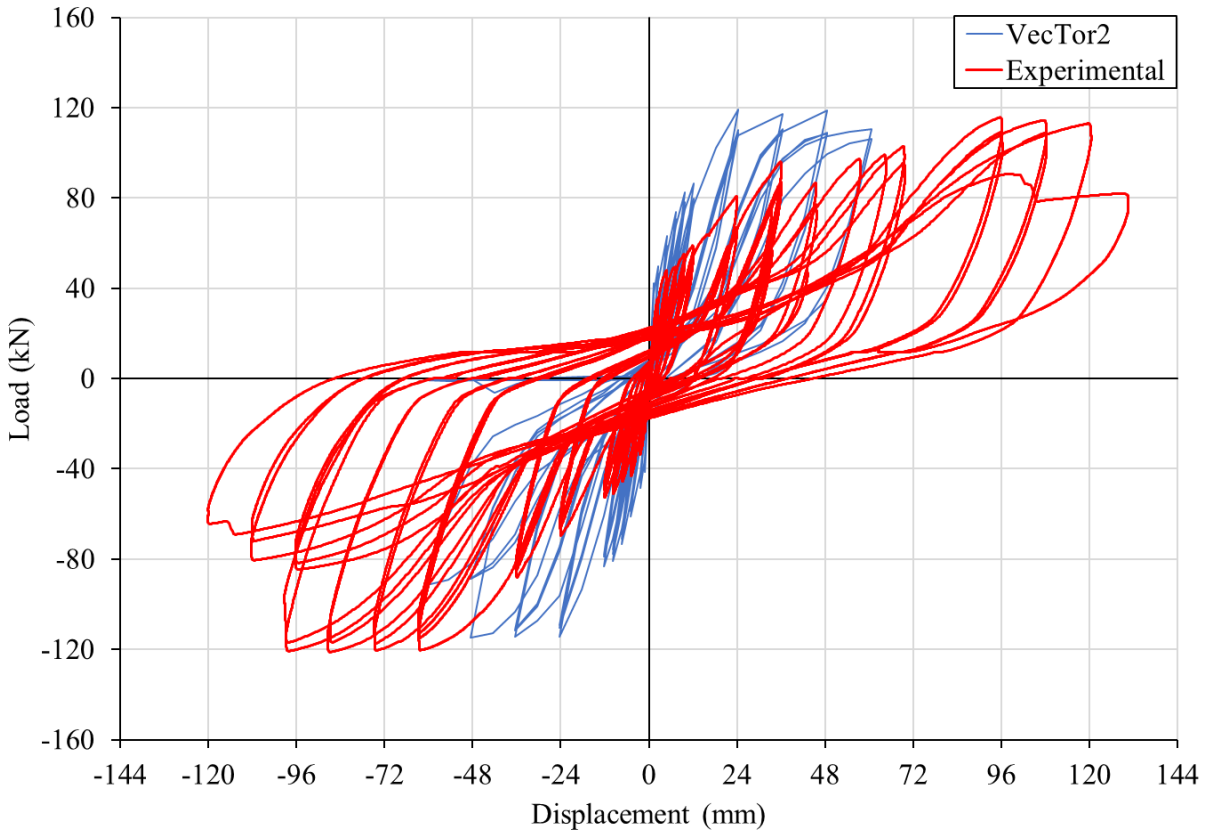

Figure 5.38 Load-displacement response of SWN-V2 5% reduced bar area with local fracture.

The final area reduction that was implemented in conjunction with use of the Modified Bentz 2005 with local fracture was a 3% reduction, with the load-displacement responses shown in Figure 5.39 and Figure 5.40. There is a significant increase in the ductility going from 5% to 3% reduction in area as SWS-V2 now fails on the second cycle at 84 mm displacement compared to the failure at 72 mm during experimental testing. SWN-V2 also provides appropriate failure displacements after the 108 mm displacement cycles compared to the experimental testing which saw the wall fail after 120 mm and 96 mm displacement cycles in the positive and negative direction respectively. While SWS-V2 maintains a failure mode of reinforcement rupture the SWN-V2 model reverts back to the failure mode of sliding at an elevation of 200 mm. Although further refinement of the models to a more specific reduction of area could allow for the SWS-V2 model to have a more accurate fracture and have SWN-V2 fail via reinforcement rupture the current V2-models with a 3% reduction on steel reinforcement area and use of Modified Bentz 2005 with local fracture is sufficient for the purposes of this work.

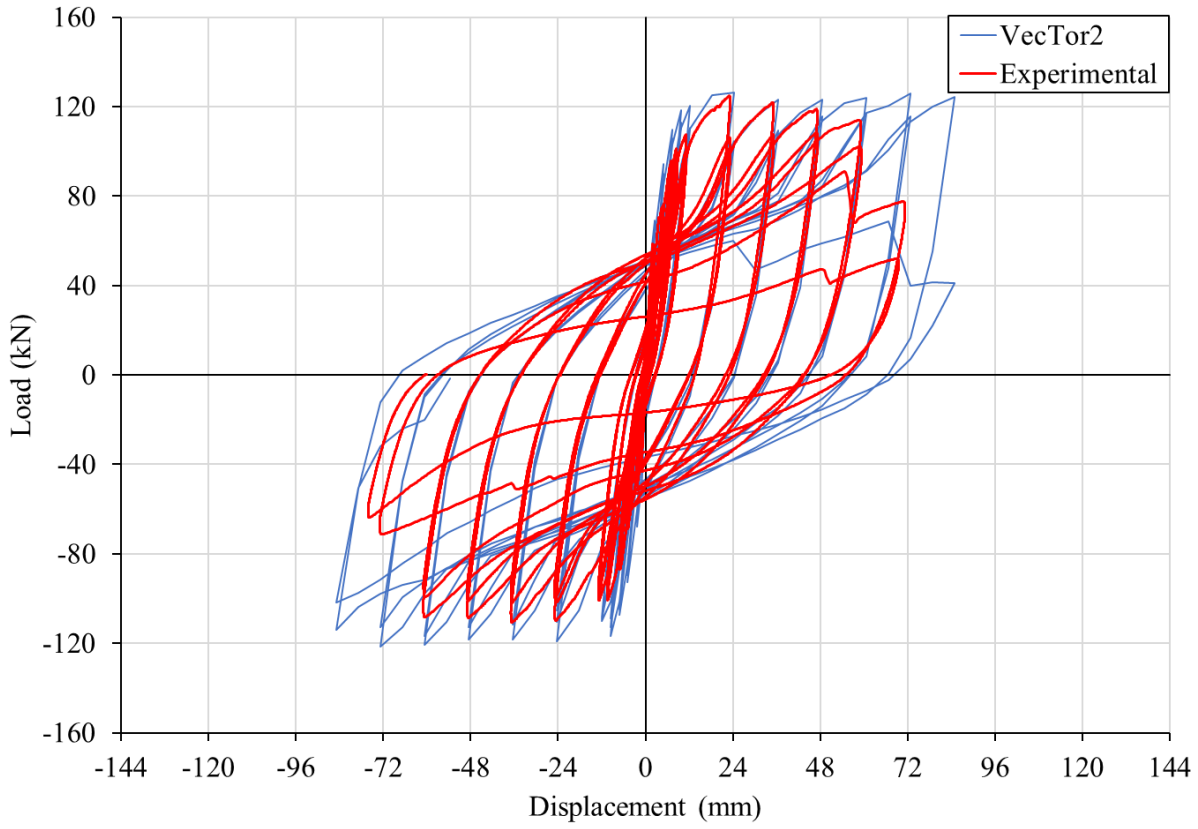

Figure 5.39 Load-displacement response of SWS-V2 3% reduced bar area with local fracture.

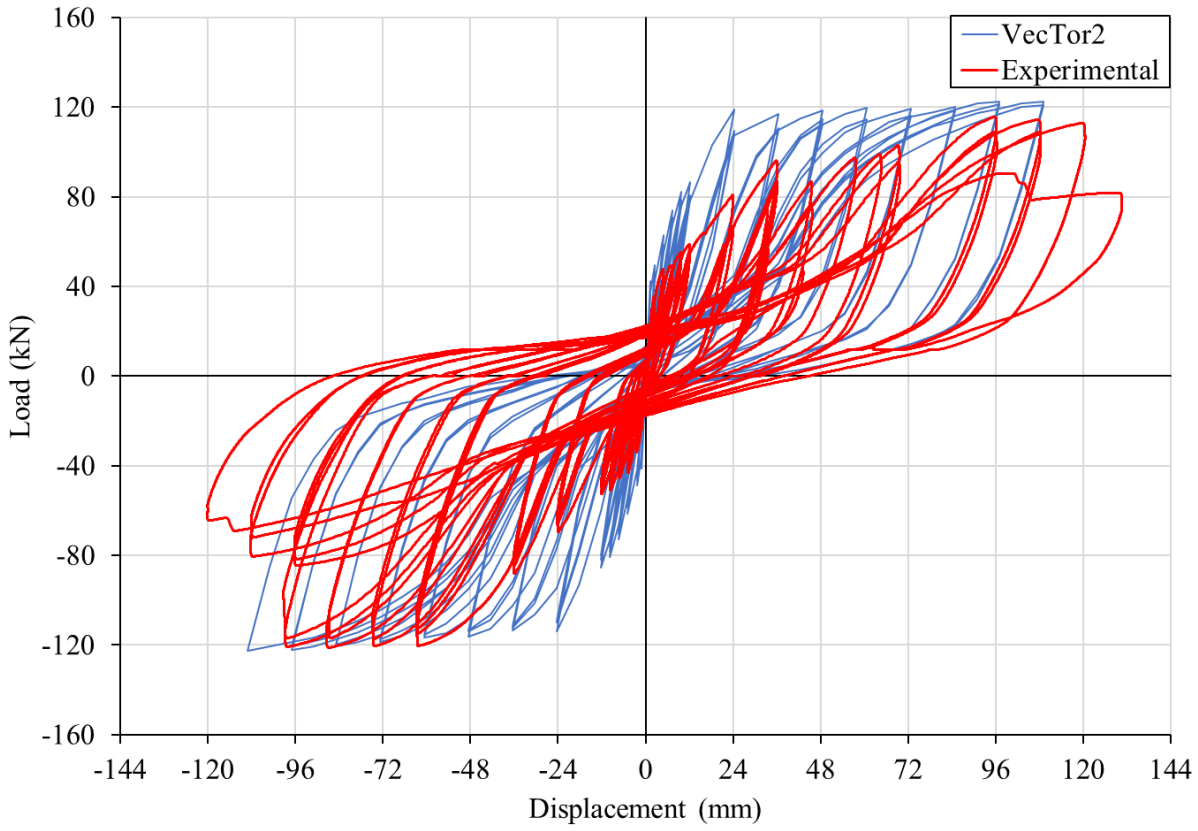

Figure 5.40 Load-displacement response of SWN-V2 3% reduced bar area with local fracture.

5.4 Soto-Rojas' Slender Shear Wall

Wanting to investigate the performance of repaired hybrid SMA-steel slender shear walls, Soto-Rojas applied a retrofitting methodology to the previously tested walls of Morcos, these repaired walls are denoted RSWS and RSWN in this work with the "R" prefix signifying repaired walls. Morcos' walls had seen extensive concrete crushing along the toes of the wall as well as rupturing of tradition steel reinforcement in the boundary and web regions for walls SWS and SWN respectively. This required that Soto-Rojas remove and replace damaged concreting material and ruptured reinforcement. Soto-Rojas defined the region that required repair starting from an elevation of 1020mm above the base of the wall until a depth of 60 mm into the foundation itself to allow for better bonding of the repaired concrete material to the surrounding existing concrete. Concrete was removed using a combination of normal hammering for large portions and a pneumatic hammer for more sensitive removal around reinforcement and couplers used in wall SWN. Any ruptured steel was cut at the base of the wall and at a height of 550 mm to allow for

replacement with new sections. The new and existing sections of reinforcement were coupled using 4-inch-long traditional mechanical-screw couplers. To try and prevent sliding that had occurred in testing of Morcos' walls it was determined that four starter bars would be installed in the wall, evenly spaced 150 mm apart between the existing longitudinal bar layout of Moroc's walls. The starter bars were fixed 300 mm into the foundation using Sika AnchorFix-300, a 2-step epoxy with, to bond the bars to the surrounding concrete in holes that had been drilled. The bars then extended 300 mm into the height of the wall. The repaired reinforcement layout for RSWS and RSWN are shown in Figure 5.41 and Figure 5.42.

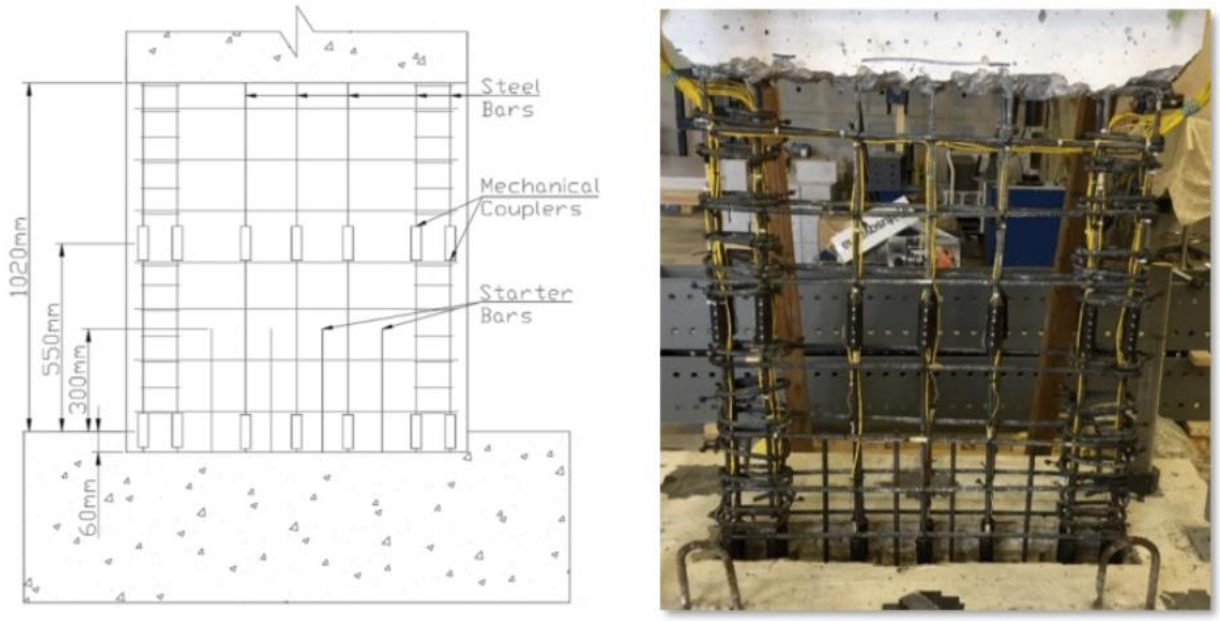

Figure 5.41 Repaired reinforcement layout and implementation for RSWS (Soto-Rojas & Palermo, 2020).

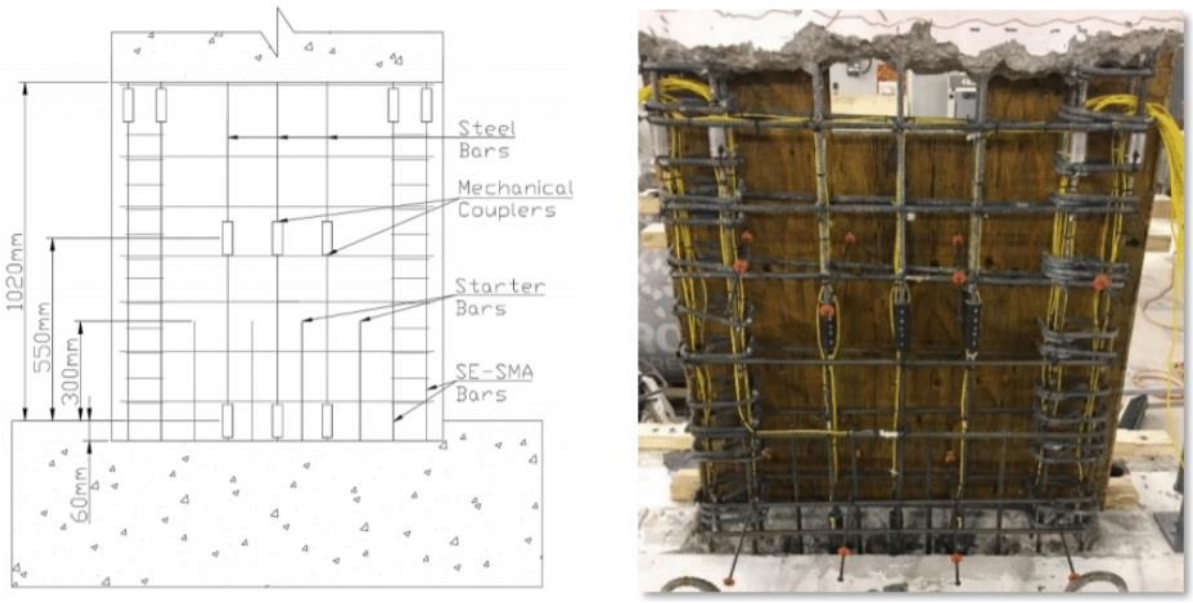

Figure 5.42 Repaired reinforcement layout and implementation for RSWN (Soto-Rojas & Palermo, 2020).

The damaged concrete was replaced with an ECC which has already been described in detail in Chapter 3. There were some deficiencies at the top of the repair region in RSWS that needed to be patched with SCC but this was not considered in modelling since it was deemed far enough from the base and end of starter bars, which were considered the critical areas of the wall.

5.5 Modelling of Soto-Rojas' Walls

Modelling of Soto-Rojas' shear walls was based on the models used throughout Section 5.3. The main issue that needed to be addressed was the introduction of the starter bars which would require changes to discretization and the mesh size. Similar to the approach used when modelling Morcos' walls the intent is for the model to be kept as simplistic as possible to be more approachable and intuitive to less experienced modellers. This results in trying to use as many default models as possible and keeping assumptions straightforward and reflective of the walls.

5.5.1 Mesh Discretization

The presence of the starter bars requires that the mesh size used in the web region be altered from the 50 mm by 50 mm elements in the previous models. Elements can still be defined as 50 mm in height since the starter bars end at 300 mm above the base of the wall. The width of elements is chosen to be 37.5 mm wide based on the 50 mm height and wanting to keep an aspect ratio of 1.5

or less while also accommodating the 75 mm spacing between starter bars and longitudinal bars. This new element width only increases the number of elements through the width of the wall by 4 and changes the aspect ratio from 1 to 1.33. The new variation of element width through the depth of the wall is shown in Figure 5.43.

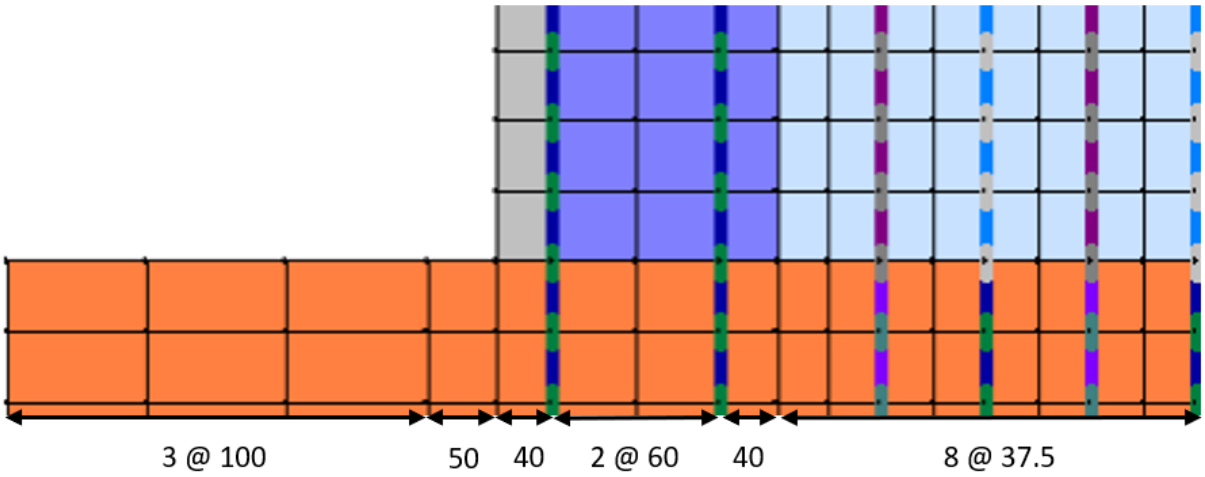

Figure 5.43 Final mesh sizing of elements in RSWS and RSWN walls.

The replacement of damaged concrete with ECC required that three new regions be considered when making the discretization of the wall: ECC cover, ECC web, and ECC plastic hinge boundary region (bottom). The ECC repairs were carried out from 60 mm below to 1020 mm above the base of the wall. For simplicity in the model, the ECC was only defined from the base of the wall to an elevation of 1000 mm due to the previously described element size limiting regions to be multiples of 50 mm. The width of the foundation being 1000 mm in the out of plane direction meant that the 150 mm thick section of ECC that went 60 mm into the foundation would not be the dominate material, thus the entirety of the foundation was left as the original concrete. The new conceptualization of ECC regions is shown in Figure 5.44.

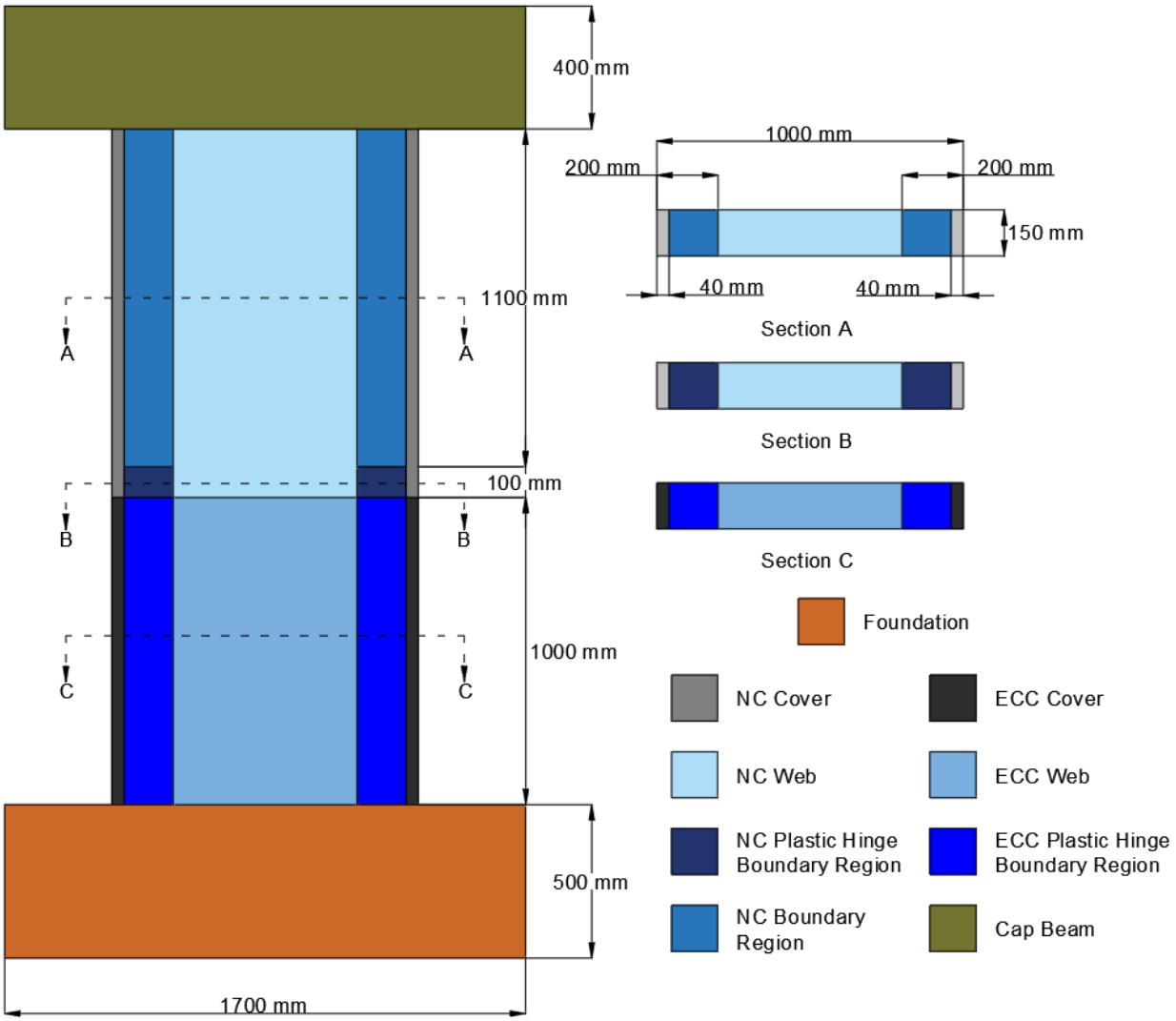

Figure 5.44 Region definition of walls repaired with ECC.

5.5.2 Parametric Study on Different Methods for Starter Bar Definition

The inclusion of the starter bars provides an additional complexity in modelling since these bars will not be able to develop their complete tensile strength along their whole length due their limited length and abrupt termination in the web. This development length is defined in CSA standard A23.3-14 Clause 12 based on the detailed equation:

$$l_d = 1.15 \frac{k_1 k_2 k_3 k_4}{(d_{cs} + K_{tr})} \frac{f_y}{\sqrt{f'_c}} A_b$$

$$where\ (d_{cs} + K_{tr}) \leq 2.5 d_b$$

$$K_{tr} = \frac{A_{tr} * f_{yt}}{10.5 * s * n}$$

Since the starter bars satisfy the requirement that clear cover and clear spacing are at least d_b (11.3mm) and $1.4d_b$ (15.82mm) respectively a simplified equation can be also used:

$$l_d = 0.45k_1k_2k_3k_4\frac{f_y}{\sqrt{f'_c}}d_b$$

Where

s is maximum centre-to-centre spacing of transverse reinforcement

A_{tr} is cross sectional area of all reinforcement that crosses the reinforcement at the plane of bond splitting and within spacing s

n is number of bars being developed along the potential plane of bond splitting

f_{yt} is the yield strength of transverse reinforcement

k_1 was taken as 1.0

k_2 was taken as 1.0 for uncoated reinforcement

k_3 was taken as 1.0 for normal density concrete

k_4 was taken as 0.8 for 20M and smaller bars

Using concrete properties from the original walls and the material properties of the starter bars as reported by Soto-Rojas (2020) these equations result in an l_d of 204 mm (detailed) and 255 mm (simplified) for SWS and 231 mm (detailed) and 288 mm (simplified) for SWN. Clause 12 does require that l_d be atleast 300 mm which would allow for a consistent and conservative l_d for both walls. When considering how to incorporate this development length within the models there are two potential options. The first is to represent the strength capabilities of the bar within the development length by giving each element a reduced area, for example if one were to define the bar element at the midpoint of the development length the bar would be assigned an area of 50% the total area. This method maintains the stiffness of the bar which would be impacted if the yield and ultimate strengths were reduced by 50% instead of area. The second option would be to simply define the bar as having an imperfect bond and letting VecTor2's formulations account for the development length through bond-slip mechanics. To examine how the two methods may impact the overall response the SWS and SWN models previously used for the parametric study in section 5.3.8 were updated to include starter bars with properties reported by Soto-Rojas (2020). In

addition to the two methods the original models without starter bars and a model assuming perfect bond were also included in the analysis with the load-displacement response shown in Figure 5.45 and Figure 5.46.

The inclusion of starter bars, no matter the method of their representation provides additional load capacity and stiffness particularly in the initial ascending portion of response for both SWS and SWN. All methods considered have the same failure mode of exterior steel reinforcement rupturing. Starter bars modeled with perfect bond tend to act as an upper limit for the load capacity of walls SWS and SWN while the method of using reduced area act as a lower bond. The use of imperfect bond varies between these upper and lower boundaries but tends to skew towards the reduced area model. Considering that there is not a significant difference between the imperfect model and reduced area method it was determined that for RSWS and RSWN wall models the starter bars would use an imperfect bond to account for development length. This approach is easier to implement while also being more user friendly and intuitive.

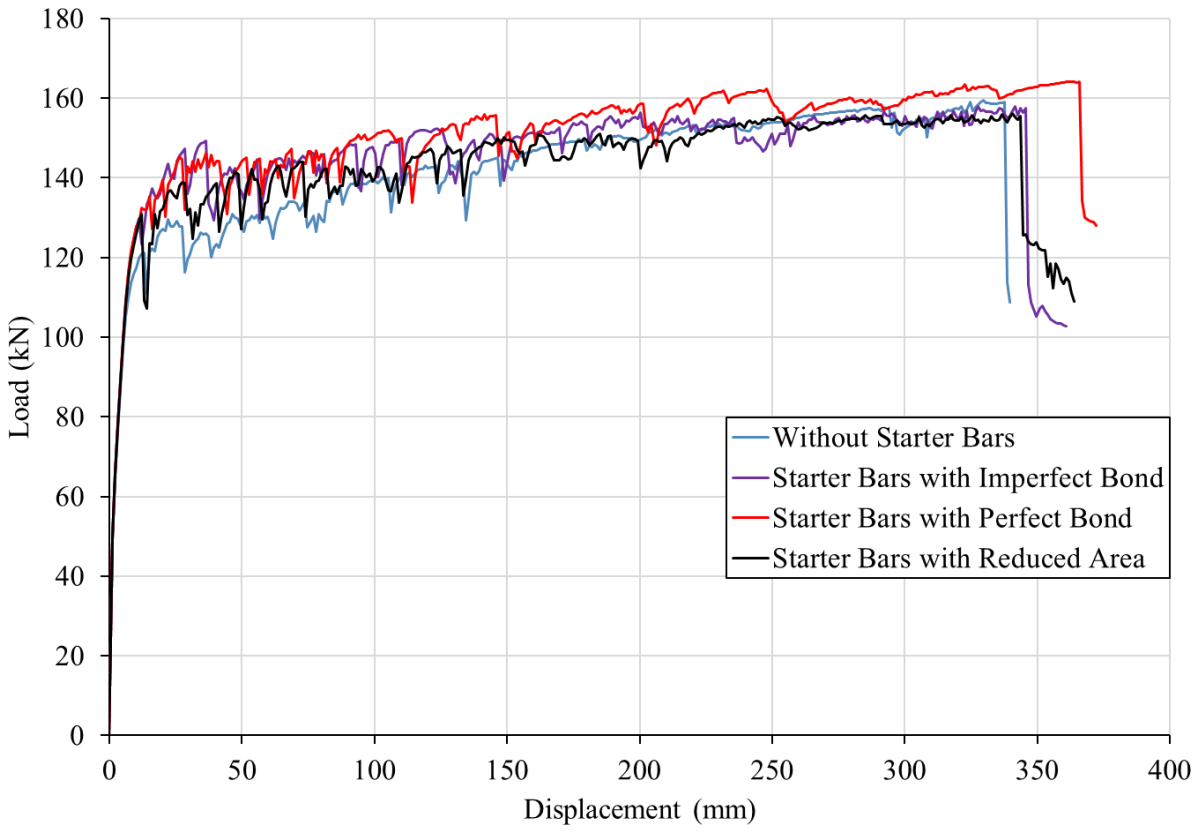

Figure 5.45 Impact of starter bars in SWS and different methods for their representation.

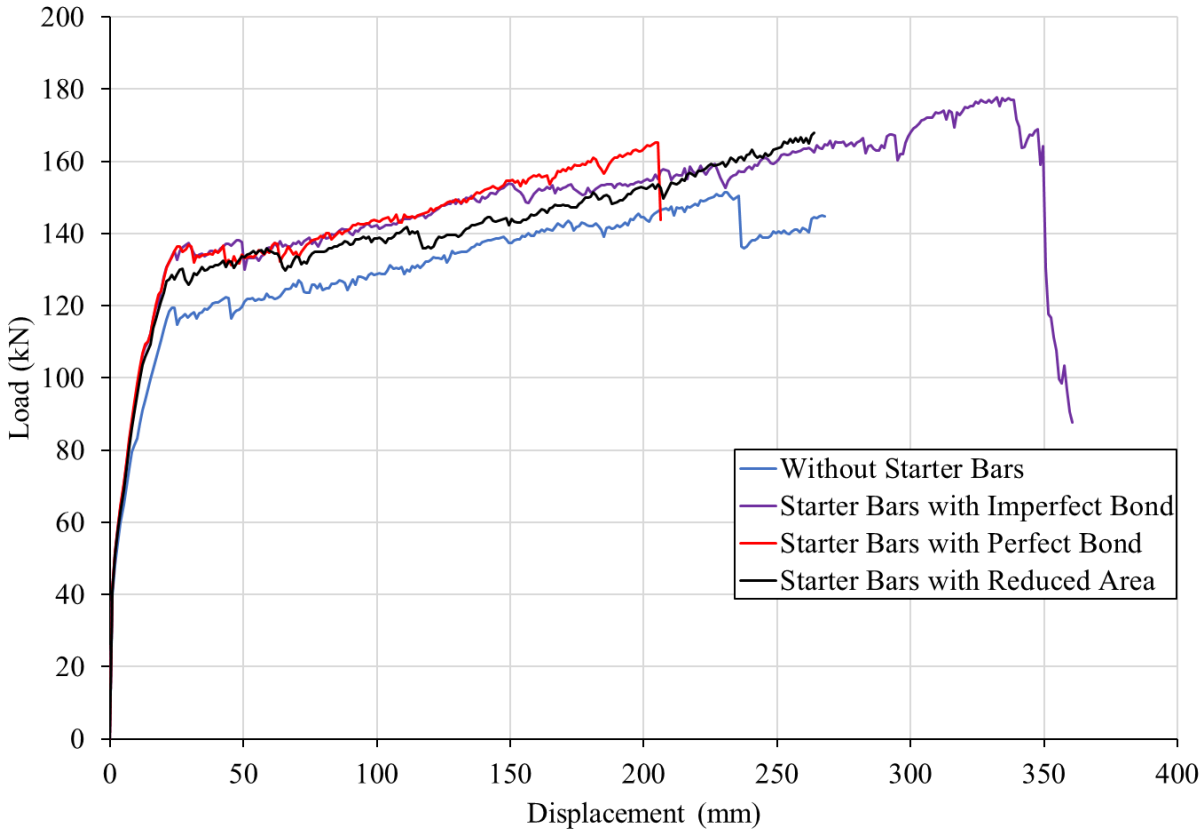

Figure 5.46 Impact of starter bars in SWN and different methods for their representation.

5.5.3 Material Properties Definition

The material properties for the different types of reinforced concrete, NC and ECC, used in RSWS and RSWN are shown in Table 5.11. NC that is not in the foundation or cap beam was further defined to have a tensile strength of 0.1 MPa as much of the original concrete in the wall itself had experienced some cracking during testing by Morcos and should not be considered to contribute significantly to the tensile capabilities of the wall. The choice of 0.1 MPa is to override the default value that VecTor2 would calculate had the input been left as 0 and note that VecTor2 cannot differentiate between the user inputting 0 to mean no tensile capability and to mean use the default calculation. ECC properties were based on compression testing Soto-Rojas (2020) had conducted on wall testing days.

Table 5.11 Concrete material properties.

Concrete	f'_c (MPa)	Maximum Aggregate Size (mm)	Density (kg/m^3)
RSWS-NC	47.2	14	2400
RSWS-ECC	64.03	0.3	1900
RSWN-NC	36.9	14	2400
RSWN-ECC	62.94	0.3	1900

The fibres in ECC concrete elements were modelled as smeared reinforcement using the "polyethylene fibre- straight" option. The fibre properties for the two different PVA fibres used are summarized in Table 5.12.

Table 5.12 Smeared fibre reinforcement properties.

Fibre Type	Volume Fraction (%)	Fibre Length, L_f (mm)	Fibre Diameter, D_f (mm)	Fibre Tensile Strength , F_u (MPa)
1	1	12	0.1	1200
2	1	12	0.04	1560

Smeared steel reinforcement definition was left the same as in Section 5.3.3. All discrete reinforcement was defined based on properties presented in Section 5.3.4 for pre-existing reinforcement and based on properties reported by Soto-Rojas (2020) for reinforcement material that was used in repairs. A full summary of input properties for all reinforcement materials is presented in Table 5.13.

Table 5.13 Discrete reinforcement properties.

Wall	Reinforcement	A (mm^2)	D_b (mm)	F_y (MPa)	F_u (MPa)	E_s (GPa)	ε_{sh} (mε)	ε_u (mε)	b/t
RSWS	10M[1] Rebar	200	11.3	428	558	197	23	174	13.2
	10M[2] Rebar	200	11.3	428	558	197	23	174	6.6
	New 10M[1] Rebar	200	11.3	430	537	175	23	262	13.2
	New 10M[2] Rebar	200	11.3	430	537	175	23	262	6.2
	10M Starter Bar	100	11.3	430	537	175	23	262	13.2
	Coupler	962	35	690	795	200	40	350	0
RSWN	10M[1] Rebar	200	11.3	435	564	186.2	21	158	13.2
	10M[2] Rebar	200	11.3	435	564	186.2	21	158	6.6
	New 10M Rebar	200	11.3	430	537	175	23	262	13.2
	10M Starter Bar	100	11.3	430	537	175	23	262	13.2
	#13 Rebar	253.35	12.7	463	627	202.6	16	165	0
	Coupler	962	35	690	795	200	40	350	0
	SMA	252	12.7	338	1034	42	50	160	6.6

[1] indicates reinforcement used in the web and boundary regions above the plastic hinge

[2] indicates reinforcement used in heavily reinforced sections (foundation, cap beam, and plastic hinge boundary regions)

The use of a 3% reduction in the area of reinforcement elements corresponding to locations of strain gauges was continued through into the RSWS and RSWN models. Due to the repair and replacement of certain bars the location of the strain gauges had to be adjusted to accommodate the use of couplers. The instillation locations of stain gauges in both experimental walls are shown in Figure 5.47.

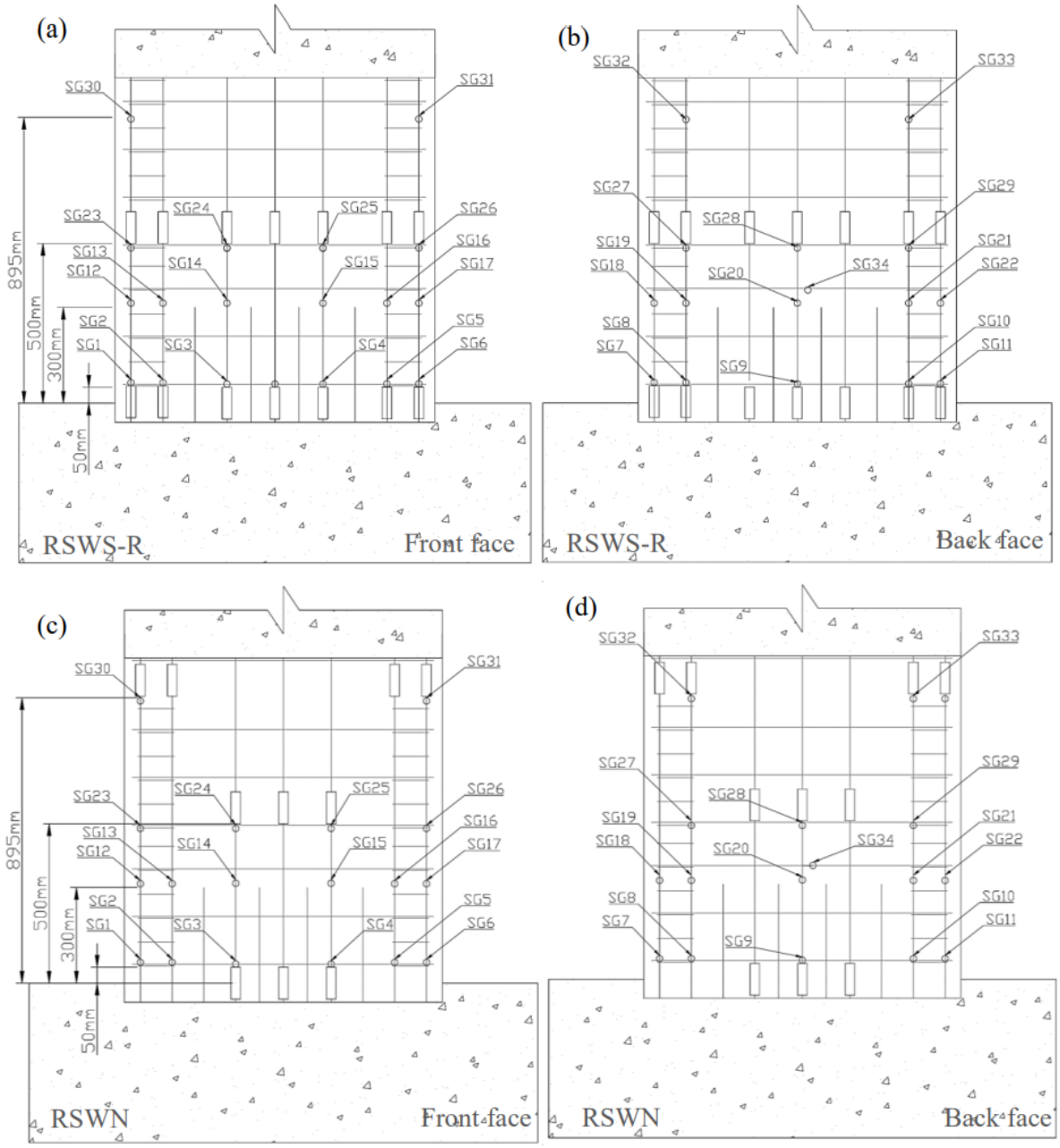

Figure 5.47 Strain gauge locations: (a) Wall RSWS-R (front); (b) Wall RSWS-R (back); (c) Wall RSWN (front); and (d) Wall RSWN (back) (M. A. Soto-Rojas, 2020).

The mechanical screw couplers used to couple replacement steel were modeled as two elements in length long, 100 mm in total, to reflect their reported length of 4 inches. The couplers in the foundation were modeled to have one element below the base and one above the base while the couplers in the wall were modeled as two elements starting at an elevation of 500 mm above the wall. This left strain gauges to be modeled as single elements directly above or below the coupler with the third strain gauge on each bar being placed at an element halfway between the couplers. Examining Figure 5.47 carefully it is clear that the replacement reinforcement in the web only has strain gauges on one curtain at heights of 50 mm, 300 mm and 500 mm while reinforcement in the boundary regions have strain gauges on all bars at elevations of 50 mm and 300 mm. The strain gauges attached to bars in the boundary region at a height of 500 mm however only do so on one curtain. The modified areas and diameters for bars with strain gauges are listed in Table 5.14. The element height above the wall stated in Table 5.14 is measured from the base of the wall to the lowest point of the element, meaning that the 250 mm element has the bottom two nodes at a height of 250 mm and top two nodes at a height of 300 mm.

Table 5.14 Reduced bar area and diameter at different locations coinciding with strain gauges.

Element Height Above Base of Wall (mm)	**Repaired Steel Bars in Boundary Region**		**Repaired Steel Bars in Web Region**	
	Cross-Sectional Area (mm^2)	Reinforcement Diameter, D_b (mm)	Cros-Sectional Area (mm^2)	Reinforcement Diameter, D_b (mm)
50	194	11.1	197	11.2
250	194	11.1	197	11.2
450	197	11.2	197	11.2

5.5.4 Bond Definition

Bond was applied to all bars from an elevation of 900 mm above the base of the wall to 350 mm into the foundation. Bond was also applied to all but the bottom node of the starter bars. The specific inputs for the different bond properties are shown in Table 5.15. The starter bars use the same C_{min} of 40 mm as this is a more conservative value than the actual value of 69.35 mm while also keeping things more simplistic by avoid having to define another bond model.

Table 5.15 Bond model properties.

Bond Model	β	C_{min}	# Layers Through Depth	Walls Utilized
Embedded Deformed Rebar	1	40	1	RSWS/RSWN in boundary regions or foundation
Embedded Deformed Rebar	0.5	40	1	RSWS/RSWN in web
Embedded Smooth Rebar	1	40	1	RSWN for SMA

5.5.5 Constitutive Models

The constitutive models chosen for concrete and steel are shown in Table 5.16 and were kept default where possible the exception being the Palermo 2002 with decay hysteretic response as described previously. Compression pre- and post-peak, tension stiffening, and FRC tension models were varied between iterations of the RSWS and RSWN models to better isolate the impact individual modelling choices have on the response. The choice for these constitutive models will be clearly stated before the results for a given iteration are displayed and discussed later in the chapter.

Table 5.16 Constitutive Models for RSWS and RSWN.

Concrete Constitutive Models

Compression Pre-Peak	Varies	**Dilation**	Variable - Isotropic
Compression Post-Peak	Varies	**Cracking Criterion**	Mohr-Coulomb (Stress)
Compression Softening	Vecchio 1992	**Crack Stress Calc**	Basic (DSFM/MCFT)
Tension Stiffening	Varies	**Crack Width Calc**	Agg/2.5 Max Agg.
Tension Softening	Nonlinear (Hordijik)	**Crack Slip Calc**	Walvern
FRC Tension	Varies	**Creep and Relaxation**	Not Considered
Hysteretic Response*		Palermo 2002 (w /decay)	

Steel Constitutive Models

Hysteric Response	Bauschinger Effect (Seckin)	**Buckling**	Modified Dhakal-Maeka
Dowel Action	Tassios (Crack Slip)	**Concrete Bond**	Eligehuasen

* indicates non-default model choice

5.5.6 Initial Repaired Wall Models

The initial Formworks models for RSWS and RSWN are shown below in Figure 5.48 and Figure 5.49. All models were subjected to the same reverse cyclic loading protocol outlined in Section 5.3.9 through a single unit nodal displacement in the positive x-direction.

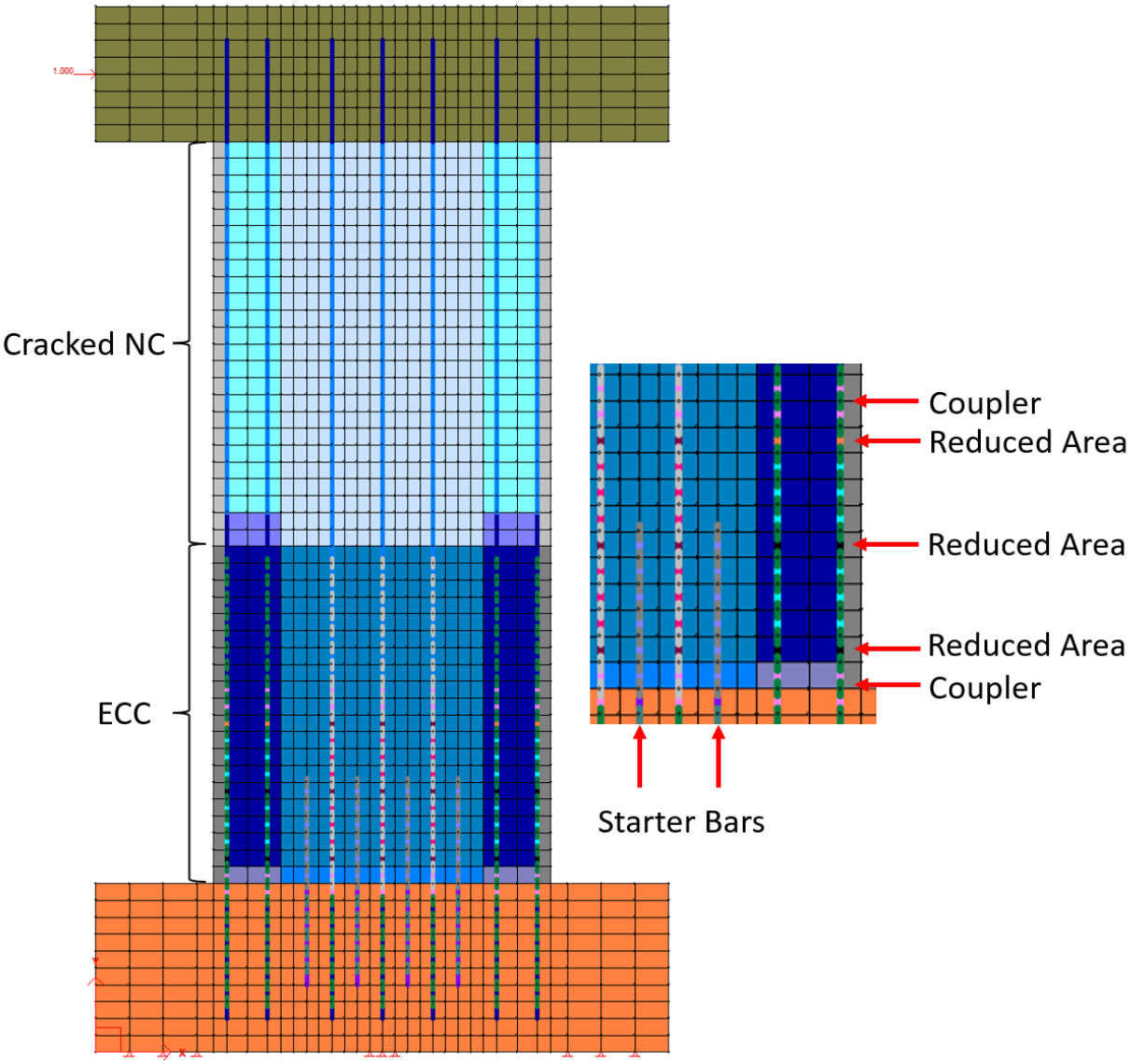

Figure 5.48 Initial Model for RSWS.

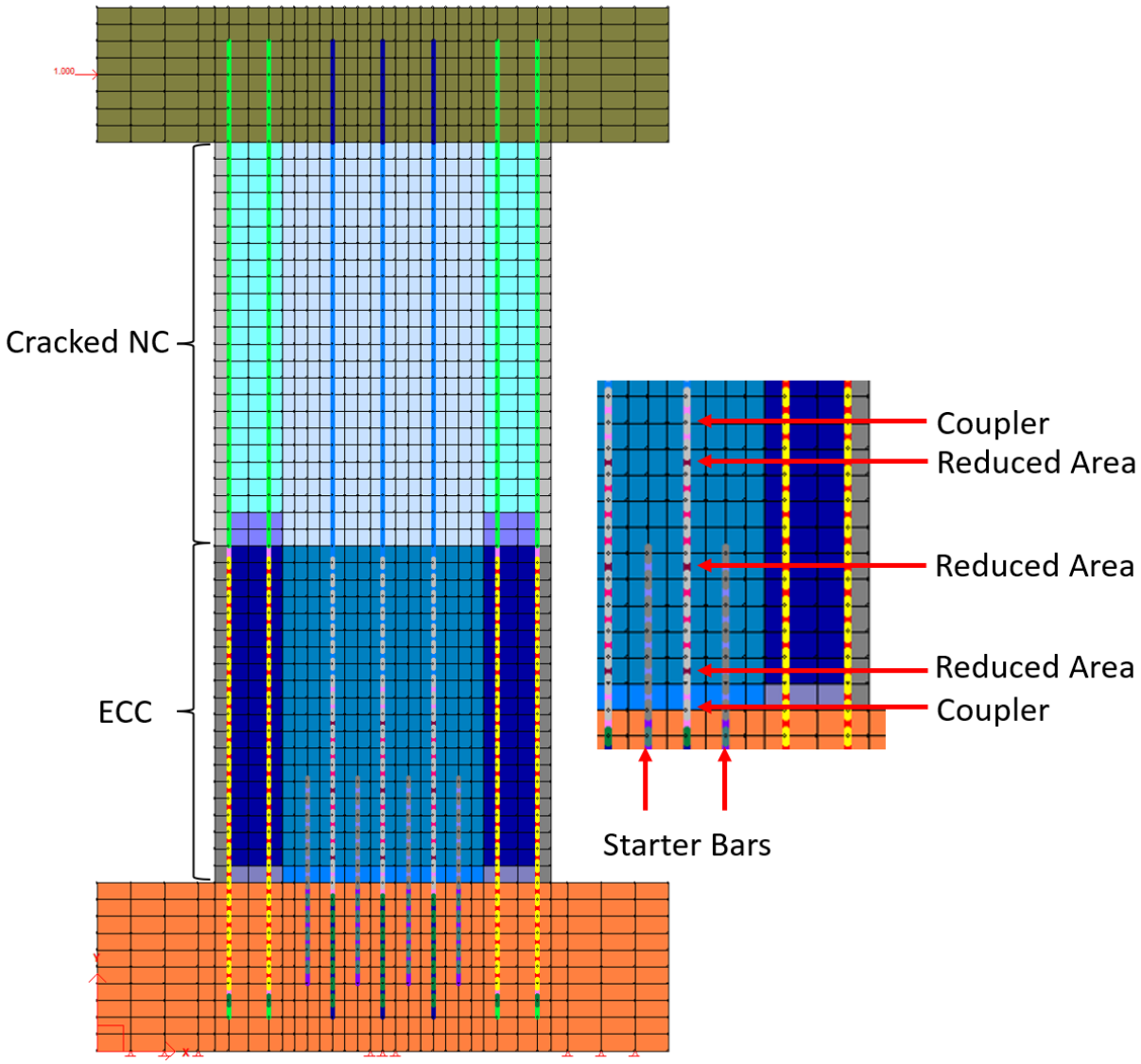

Figure 5.49 Initial Model for RSWN.

5.5.7 Models Considering ECC as High Strength Concrete

The first iteration of the RSWS and RSWN models, given the suffix V1, was designed to see what the impact of treating the ECC as a normal concrete without taking into consideration its fibre content. This was achieved by using all the material properties as described above but defining FRC tension as “not considered”, the compression pre and post-peak as Hognestad and Modified Pakr-Kent respectively and using Modified Bentz 2005 with local fracture for the tension stiffening model. The resulting load-displacement response is shown are shown in Figure 5.50 and Figure 5.51. Both models demonstrate an early failure with RSWS-V1 failing during the 36 mm displacement cycle and RSWN-V1 failing in the negative portion of the 48 mm displacement

cycles. The failure mode of both modes was rupture of replaced steel reinforcement sections with the specific element being at 300 mm, the same elevation where starter bars terminate, in RSWS and 400 mm in RSWN. Regarding load capacity, by the time RSWS-V1 failed it provided a decent load prediction of 147.3 kN and 138 kN in the positive and negative directions compared to experimental peak loads of 154.1kN and 136.9 kN. RSWN-V1 performs with similar accuracy of load: 141.2 kN and 133.2 kN in the positive and negative direction while in experimental testing the wall achieved peak loads of 144.5 kN and 129.4 kN.

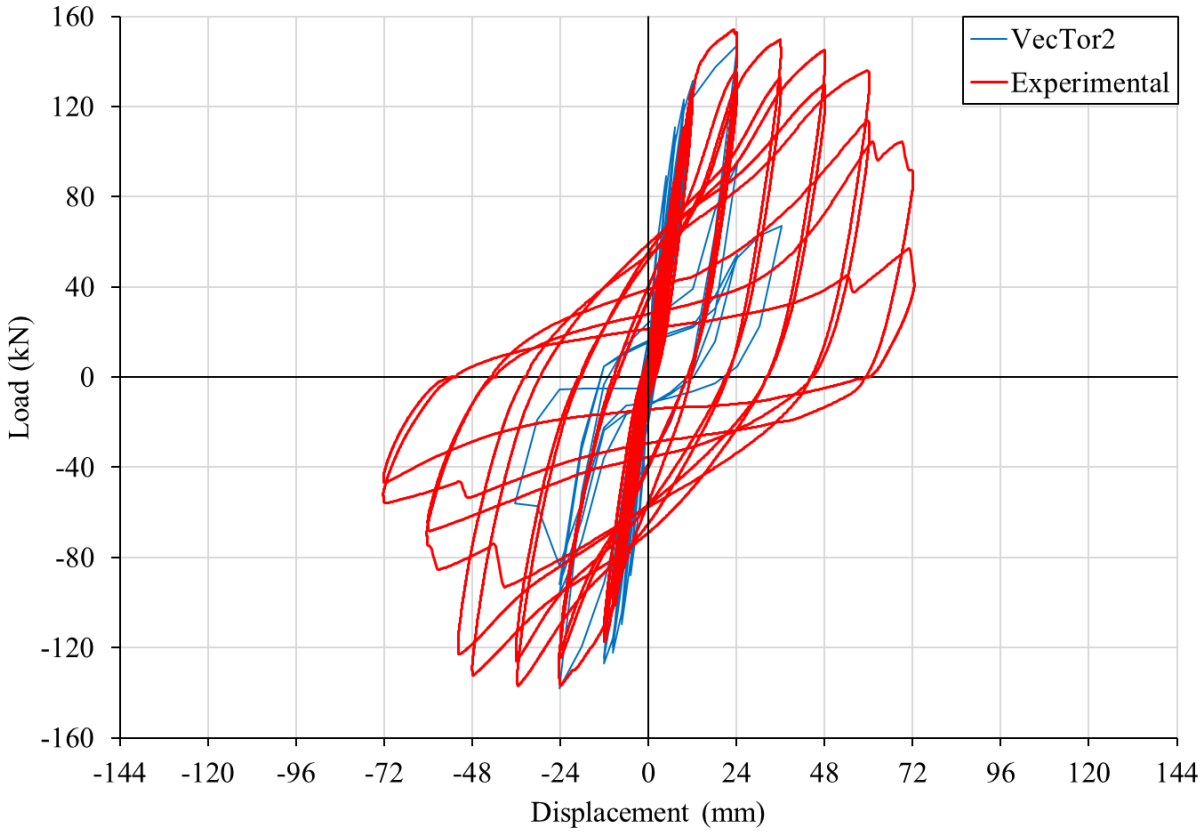

Figure 5.50 Load-displacement response of RSWS-V1.

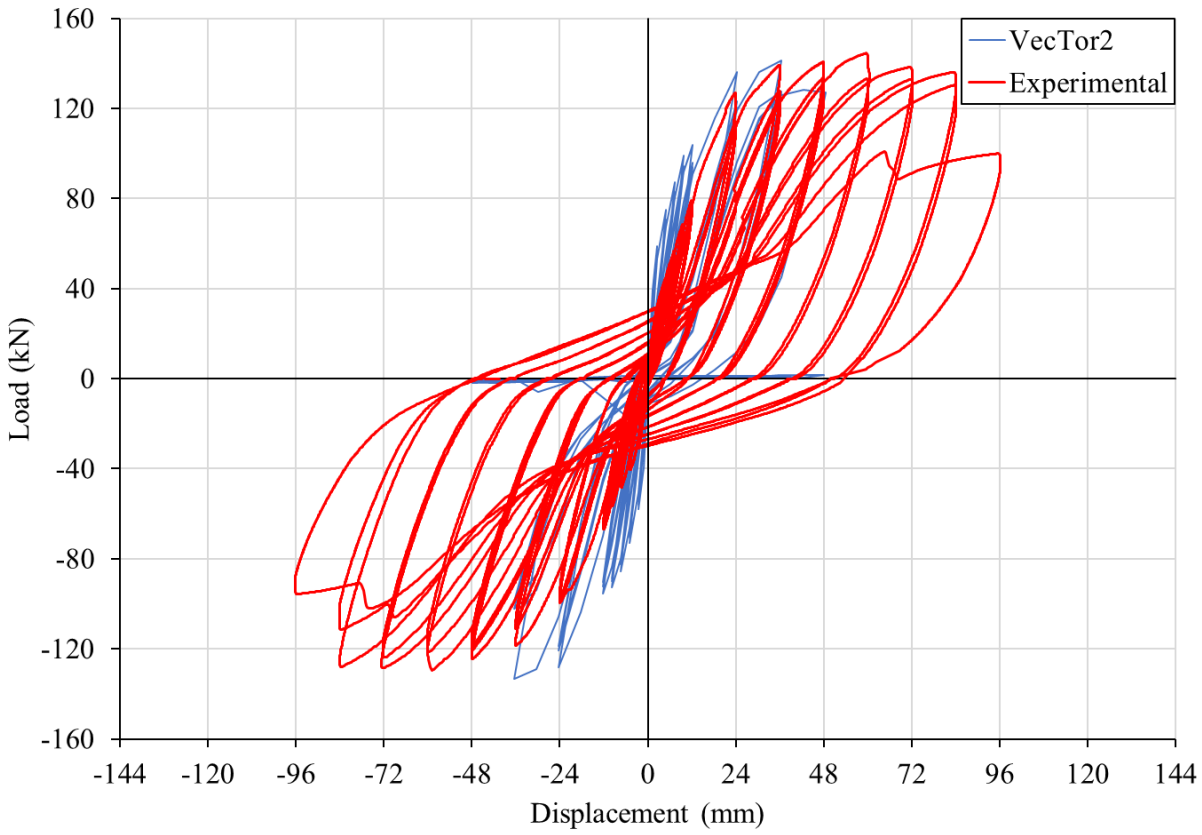

Figure 5.51 Load-displacement response of RSWN-V1.

5.5.8 Models Considering ECC Only in Compression

Looking at how to improve the ductility of V1, the next iteration considers lessons learnt from the comparison of unreinforced concrete elements from Chapter 3. From that chapter it was shown that the Lee et al 2011 (FRC) model for compression provided significantly greater ductility than other models which prompted its use as the compression pre- and post-peak for the second iteration of models, V2. All other constitutive models are kept the same as V1. The load-displacement responses of RSWS-V2 and RSWN-V2 are shown in Figure 5.52 and Figure 5.53. The load prediction values showed little variation from V1 models, but the ductility was impacted particularly in RSWN-V2 which was able to complete the 48 mm displacement cycle compared to V1 which was only able to complete a partial cycle at the same displacement before failing.

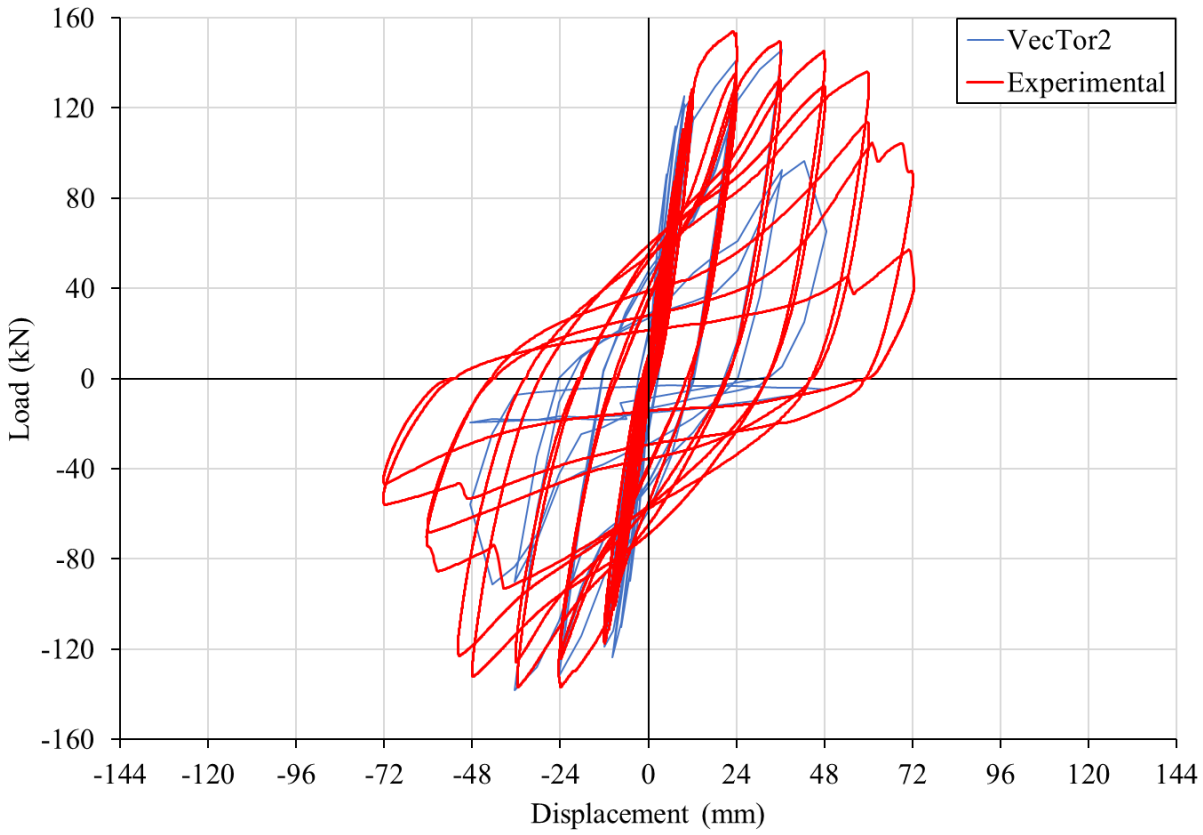

Figure 5.52 Load-displacement response of RSWS-V2.

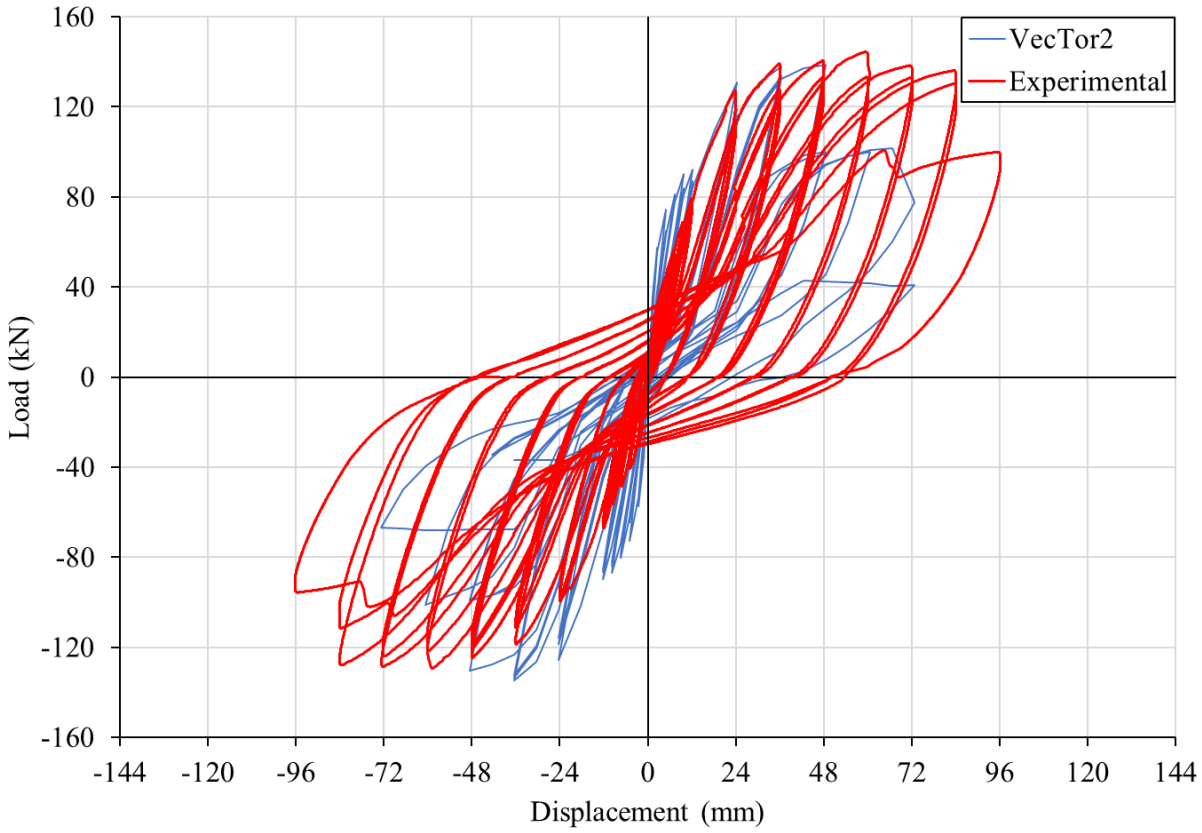

Figure 5.53 Load-displacement response of RSWN-V2.

5.5.8.1 Investigation of Tension Stiffening Model

The crack widths present in RSWS-V2 and RSWN-V2, shown in Figure 5.54, were examined with crack widths increase as colours change from blues to reds to greens. The visuals shown are from the peak of the 36 mm displacement cycle in the positive direction with RSWS-V2 having a predominate crack measuring 1.48 mm in width at an elevation between 250 and 350 mm while RSWN-V2 has an even more significant crack measuring 11.5 mm in width at an elevation of 400 mm. The presence of a single predominate crack in the plastic hinge without any other significant cracking was observed in experimental testing as well, shown in Figure 5.55. This large singular crack at the boundary region could present issues with the formulations of Modified Bentz 2005 with local fracture as now instead of having localization of tension stiffening across multiple smaller cracks it is only occurring at a singular large crack. The reduction in ultimate strain of the reinforcement bars could now be overestimating their failure.

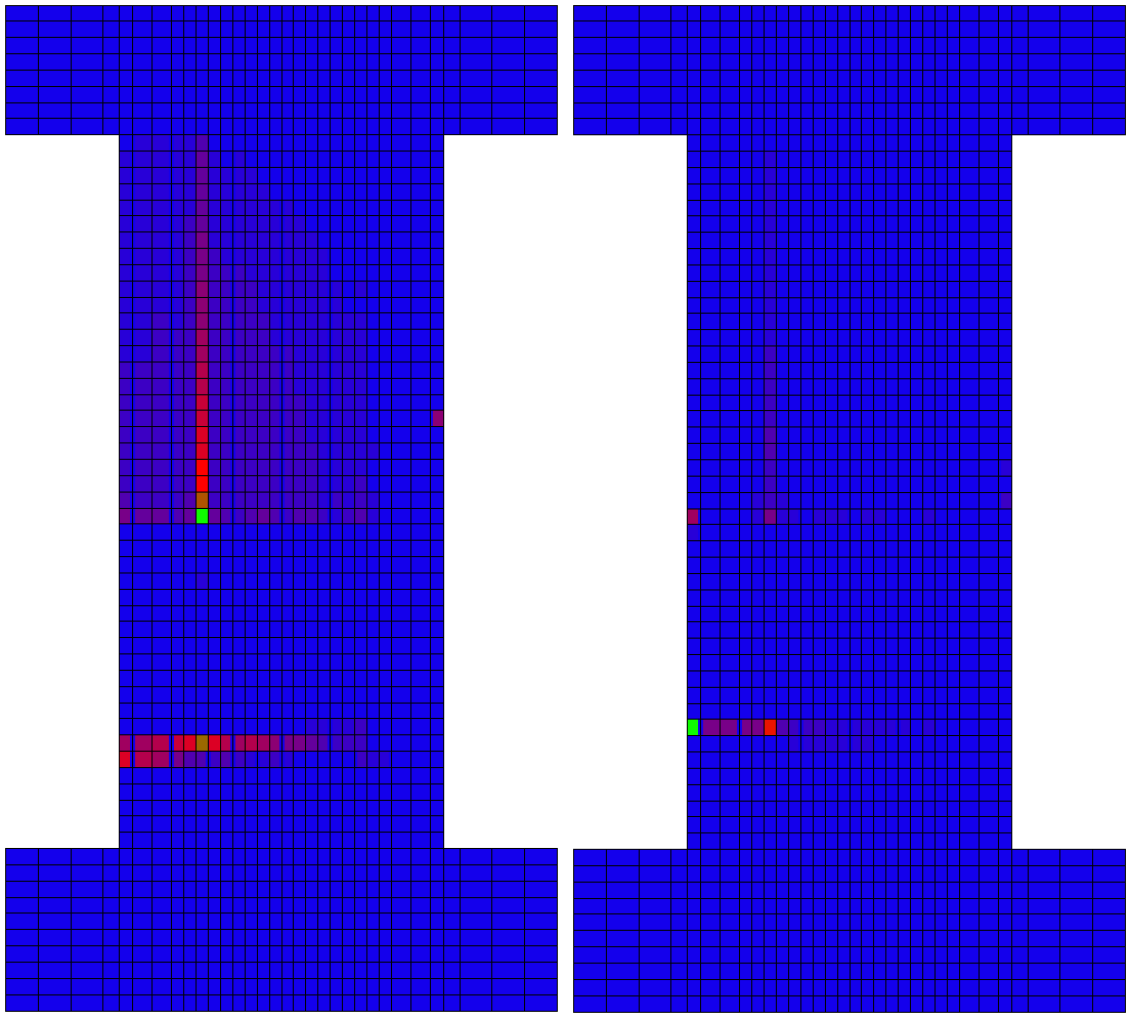

a) b)

Figure 5.54 Visualization of crack widths at 36 mm displacement cycle for a) RSWS-V2 and b) RSWN-V2.

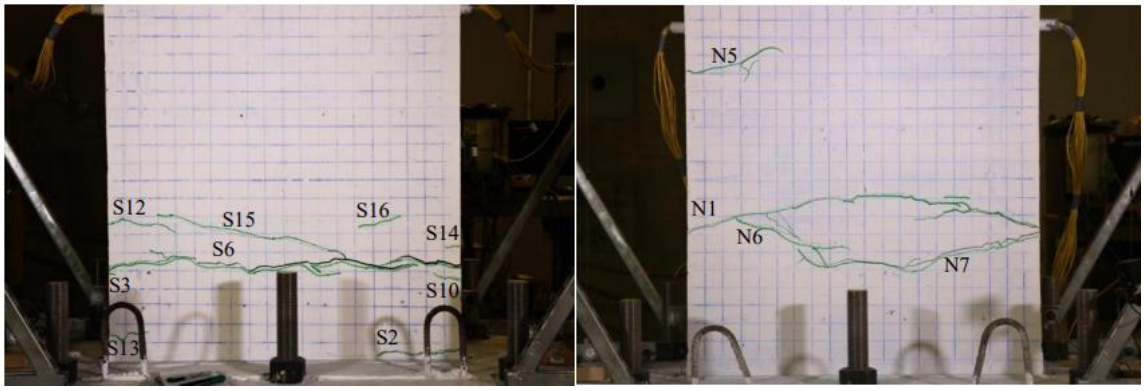

a) b)

Figure 5.55 Crack patter at 36 mm displacement cycle for a) RSWS and b) RSWN (M. A. Soto-Rojas, 2020).

Performing the calculations for the reduced ultimate strain of steel bars based on the local fracture formulations presented in Section 5.3.12 with properties of the RSWS and RSWN walls results in the embeded rupture strain being 37.8% of the bare bar rupture strain for both walls. Models RSWS-V2 and RSWN-V2 were modified such that the tension stiffening response is changed from the Modified Bentz 2005 with local fracture to the defualt of Modified Bentz 2005. The load displacement responses of these updated models are shown in Figure 5.56 and Figure 5.57. The load capacity of both models has no significant change which is ideal since the modification made should not affect the ultimate strength capacity of the sturcture. The ductility is improved significantly and to a point that is agreeagble to what was seen in experimnetal results. RSWS-V2 without local fracture failed on a the second 60 mm displacment cycle while RSWN-V2 with out local fracture completed the 96 mm displacement cycle before failing. Both failure methods consited of rupture of replacement steel reinforcment.

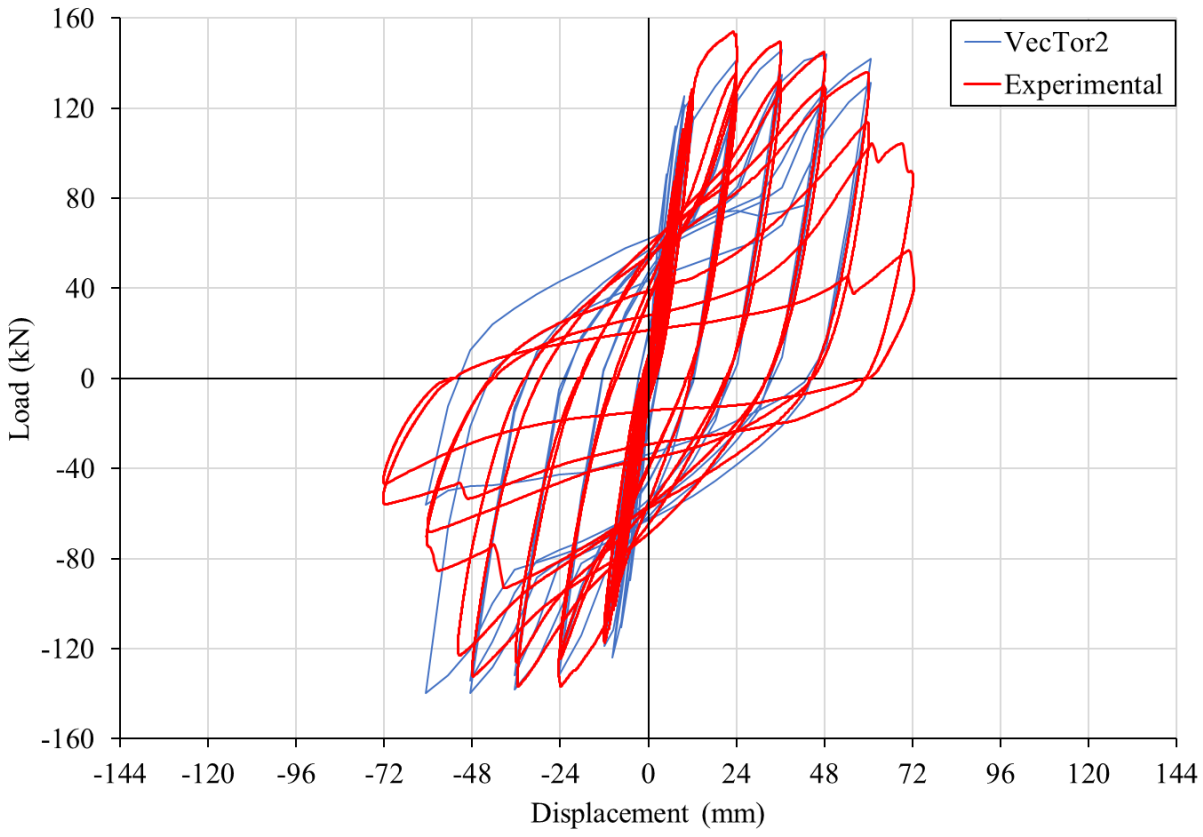

Figure 5.56 Load-displacement response of RSWS-V2 without local fracture.

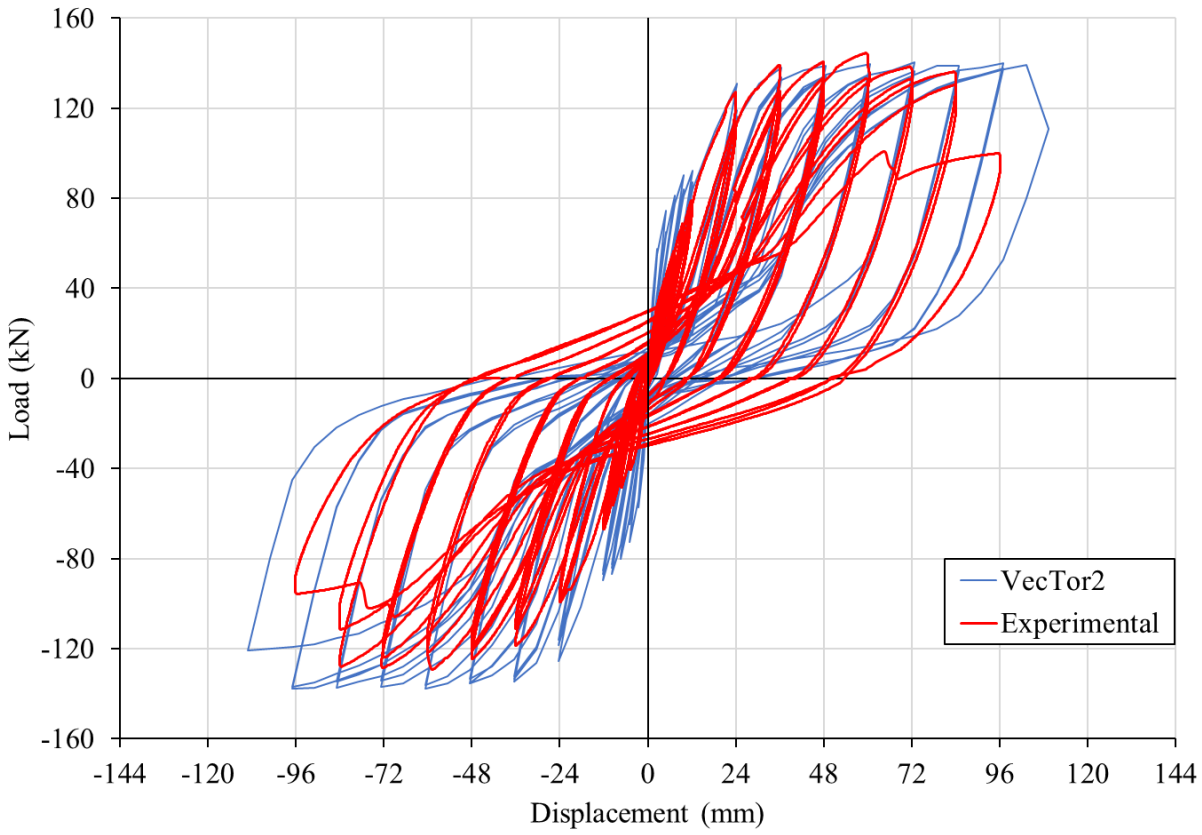

Figure 5.57 Load-displacement response of RSWN-V2 without local fracture.

5.5.9 Models Considering ECC Compression and Tension without Local Fracture

The final iteration of the models, V3, considered the tension properties of ECC by utilizing the FRC Tension constitutive mode options. The specific FRC tension model used was SDEM-Cyclic based on the fact that SDEM is the default and has been optimized to not require integration, like DEM and VEM models, which reduced the computational load. Additionally, the findings from Chapter 3 showed that no specific FRC tension model could fully capture the response of flexural prisms, so SDEM does not seem to present any significant disadvantages to other models at a face value. The load-displacement responses are shown in Figure 5.58 and Figure 5.59. Although the use of SDEM does not affect the ductility of RSWS-V3, only completing the 60 mm displacement cycles, the ductility of RSWS-V3 is severely impacted now only able to complete the 48 mm displacement cycles before failing. Additionally, there is a notable increase in the peak load predicted by RSWS-V3 of 164.3 kN and 162.7 kN in the positive and negative direction compared to the V2 iteration which had peak loads of 146 kN and 139.6 kN. This increase in the peak is

likely due to the increased strength and strain which ECC elements provide in the ascending portion of the hysteretic response. Although the RSWN-V3 model does not see such a rise in peak load, the response up to and including the 12 mm cycles displays far greater stiffness than the experimental values and RSWN-V2.

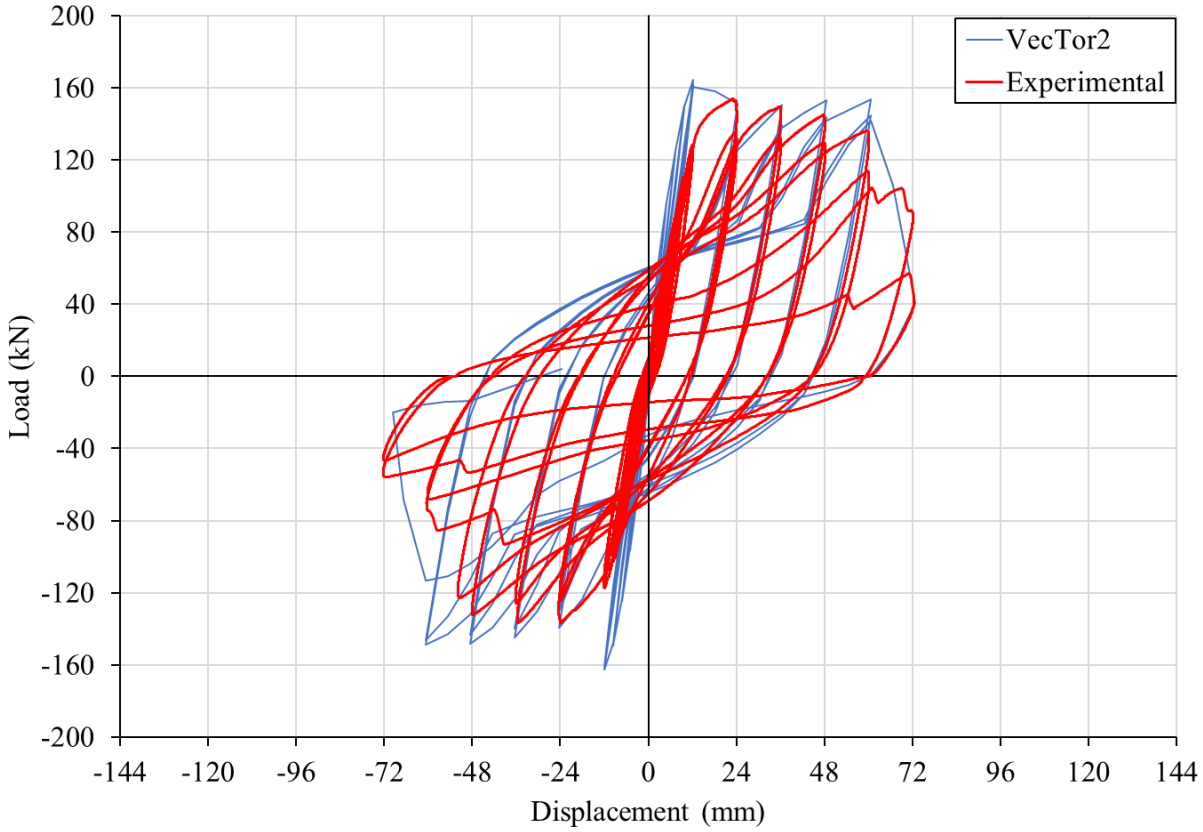

Figure 5.58 Load-displacement response of RSWS-V3.

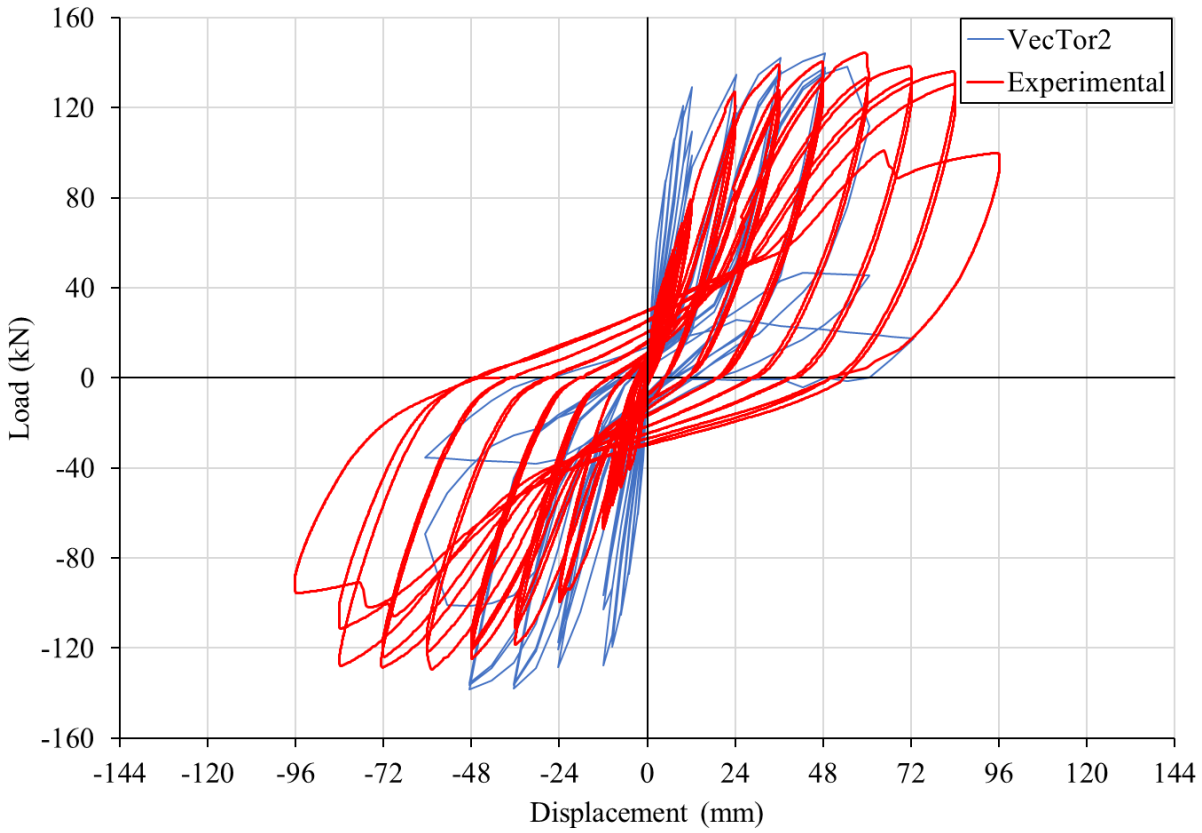

Figure 5.59 Load-displacement response of RSWN-V3.

5.6 Discussion of Results

5.6.1 SWS and SWN Walls

To more closely examine the finalized model for Morcos' walls the envelopes of the hysteretic load-displacement response of both wall SWS and SWN were compared against the numerical predictions of the V2 models with 3% reduction in area and local fracture in Figure 5.60 and Figure 5.61. The loads for the envelopes were taken as the load at the peak displacement in the first cycle at a given displacement. The errors between these peak load values were summarised in Table 5.17. It should be noted that there is no error for wall SWN in the 84 mm positive direction and in the 48 mm negative direction as these loading cycles was skipped over during experimental testing. Although the numerical models can provide acceptable peak load and ultimate displacement prediction values it appears that the ascending response before the load plateaus is problematic for SWN which is not within 10% error of the experimental data until the 96 mm and 48 mm cycles in the positive and negative directions respectively. This difficulty in the early stages is highly

dependant on the ability of VecTor2 to capture the proper strains of the materials up to their yielding and peak, for concrete and steel respectively. SWN in particular leaves much to be desired in the ascending section of the envelope with a significant overestimation of the response's stiffness.

Table 5.17 Errors in peak loads from load-displacement envelopes for walls SWS and SWN.

Cycle Displacement (mm)	SWS-V2 3% Reduction in Area		SWN-V2 3% Reduction in Area	
	% Error in Peak Load (+)	% Error in Peak Load (-)	% Error in Peak Load (+)	% Error in Peak Load (-)
1.2	36.3	32.3	108	69.7
2.4	17.9	37.5	40.4	43.9
4.8	24.4	35.2	31.2	42.3
7.2	14.7	23.8	49.9	59.3
9.6	16.8	16	48.7	58.8
12	11.8	8.8	46.9	62.7
24	1.2	8.3	47.4	63.7
36	1.1	6.8	21.5	29
48	3.5	8.9	NA	-3.3
60	8.8	11.5	22.6	-3.2
72	62.2*	70.5*	20.3	-2.2
84			NA	-0.2
96			5.7	51.8*
108			7	90.5*

* indicates that the experimental wall had started failing by this cycle

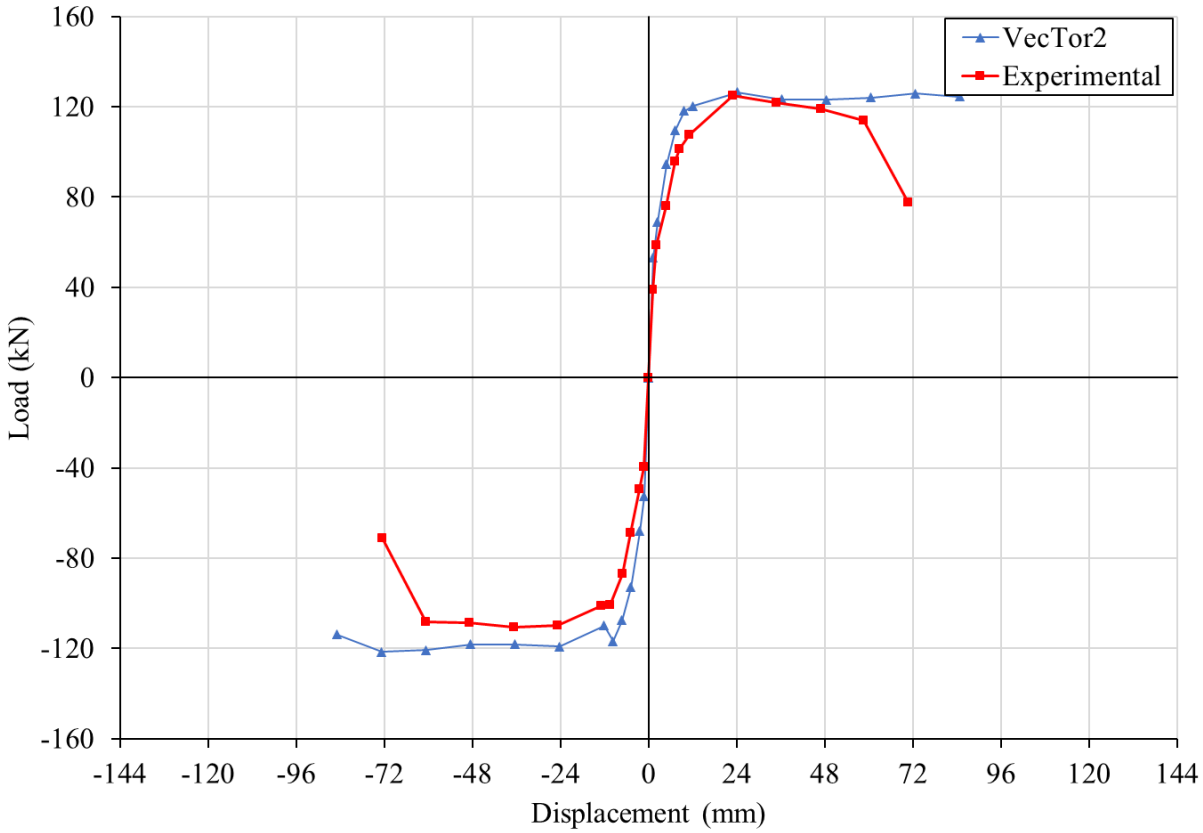

Figure 5.60 Envelope of load displacement response SWS-V2 based on 3% reduced area with local fracture.

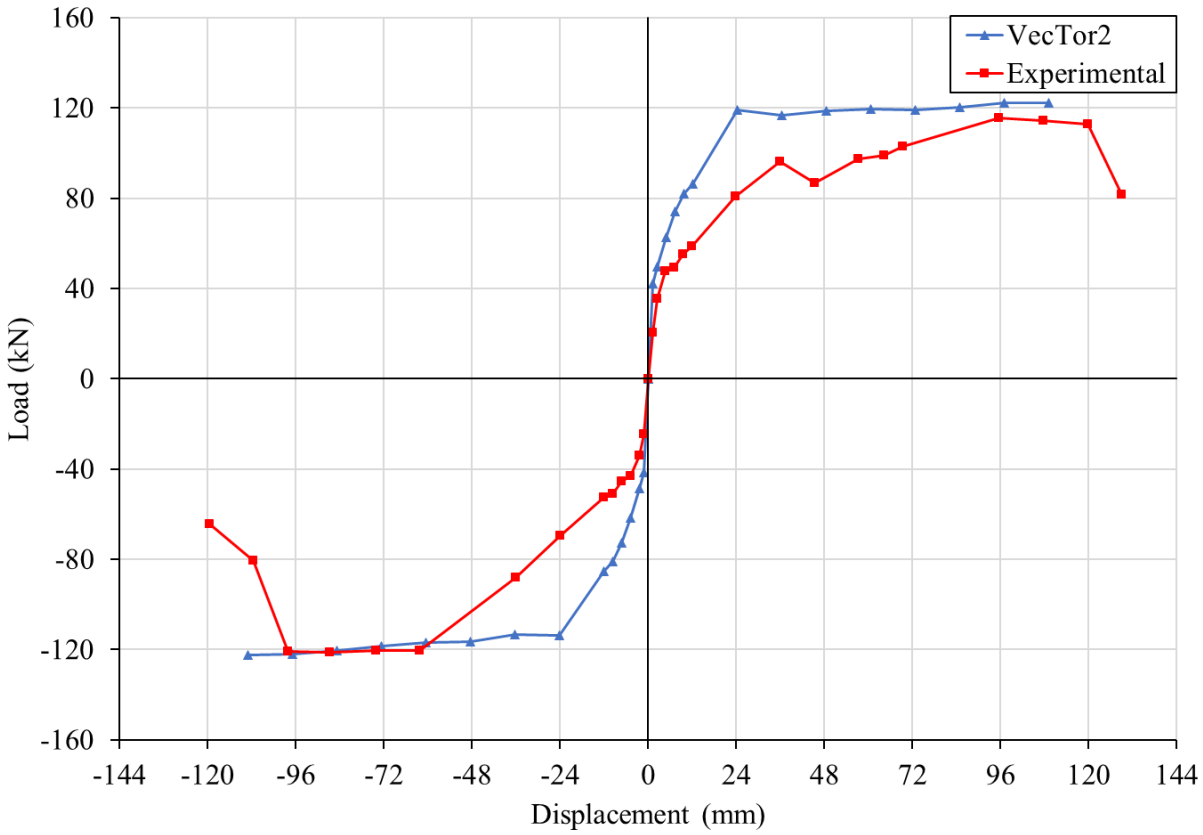

Figure 5.61 Envelope of load displacement response SWN-V2 based on 3% reduced area with local fracture.

5.6.2 RSWS and RSWN Walls

The iterative modelling approach demonstrated the importance proper modelling of the compression response of ECC can have on prediction capabilities. Although the Lee et al 2011 (FRC) model was chosen and provided reasonable results it would be beneficial to have had compressive stress-strain data for the ECC mixes provided. Based on the results of Chapter 3 it would also be prudent to try to capture any time dependant behaviour changes if ECC testing is undertaken.

The SDEM model was utilized for the third iterative step of incorporating FRC Tension response, but other options were considered on how to best capture the beneficial tension stiffening and softening that can be present in ECC. The other viable option considered consisted of using a "Custom Input" tension softening response similar to what was implemented in Chapter 3 using stress-strain values proposed Tolou-Kian (2020). Investigating this option caused several issues due to current input limitations of VecTor2. The first issue was alluded to in Chapter 3 and consists

of the fact that the Custom Input model cannot override the initial tension stiffening response until cracking had occurred. This can result in the reinforced concrete elements having an initial stiffness different from what was intended. Methods for correction of the ascending branch without impacting other aspects of the response were also unsuccessful. One method to change the initial tension stiffening is to input the target stiffness as the Elastic Modulus but this would then become the elastic modulus of the compression response as well. Another method would be to input a small non-zero value for the tensile strength when defining the material properties. This once again would have other impacts on different constitutive models which use f'_t anywhere in their formulation. This is not necessarily an issue but should be considered when trying to use experimental data as the backbone for the tensile stress-strain response being implanted in VecTor2.

The second issue with implementation of "Custom Input" for ECC in the context of Soto-Rojas' walls is the fact that it is applied to all reinforced concrete elements unlike the FRC Tension constitutive models, which is only applied to the tension response of reinforced concrete elements with smeared fibre reinforcement. This results in the NC, which is meant to be cracked and provide no tensile resistance to the wall, having the same tension response as the ECC and greatly over strengthens the response of the wall. The use of the "Custom Input" tension softening approach is appropriate in instances where all reinforced concrete materials consist of ECC, such was the case with Tolou-Kian (2020), but currently it should not be used when modelling structures where only some reinforced concrete elements are ECC. The fix to this may be as straight forward as implementing another Tension Softening constitutive model that is Custom Input but has a check that limits its implementation to materials with smeared fibres present, otherwise calculations revert to the default model.

6 Development of ECC Mix

6.1 History of ECC at York University

The ECC that was tested in this thesis was specifically created by Soto-Rojas for his Master's thesis but was based on the work of other researchers. The origin of the ECC mix can be traced back to the ECC M45 mix developed by Lepech & Li (2008). Lepech and Li wanted to develop an ECC mix that could be produced locally in Michigan at a scale that was commercially feasible and only made use of construction mixing equipment (gravity mixers, paddle mixers, or concrete transit mixing trucks). Construction mixing equipment imparts relatively lower energy compared to high-speed mixers often used in smaller laboratory testing, requiring additional consideration to ensure all constituents of ECC are thoroughly mixed. Part of this challenge is the fact that ECC lack large aggregate which traditionally helps break up clumping of finer aggregates. Ensuring that the ECC mix had an optimal grain size distribution would assist in this endeavor, resulting in three additional mixes, denoted ECC 46 through ECC 48, being developed. The only variation between mixes was the portion of sand being used as shown in Table 6.1. All mixes were first subjected to flow tests with only the ECC 46 mix providing better flowability than ECC 45; leading to ECC 45 and ECC 46 being the two mixes that advanced to further testing. After tensile coupon testing of both mixes, ECC 46 was not shown to provide any significant increase in tensile strain capacity, and it was decided to continue with ECC 45. Lepech and Li were able to outline an optimal mixing procedure for transit mixing trucks and demonstrated that the ECC had little variation in material properties irrespective of when it was poured any time before an hour time limit.

Table 6.1 Mix designs based on weight ratios from Lepech & Li (2008).

Mix	Cement	Fly Ash	Sand	Water	Super plasticizer	Fiber (% Volume)
M45	1.00	1.20	0.80	0.56	0.012	2
M46	1.00	1.20	1.2	0.58	0.012	2
M47	1.00	1.20	1.4	0.59	0.012	2
M48	1.00	1.20	1.6	0.60	0.012	2

Work by Georgiou & Pantazopoulou (2016) aimed to use the ECC 45 mix design and tailor it to local materials available in Europe. The large amount of fly ash, a waste by product of coal-power generation, incorporated in ECC 45 make it attractive in the fight against climate change by decreasing the amount of cement and carbon dioxide released during its production. The use of local materials allowed Georgiou & Pantazopoulou (2016) to replace the ordinary Portland cement (OPC) with the more impermeable and dense Portland Composite Cement En 197-1 Cem Ii / A-M (L-S) 42.5 R resulting in a higher workability and a reduction in plastic shrinkage. This composite cement also contains silica fume and slag. Where Lepech and Li had used an 8mm long PVA fibre Georgiou & Pantazopoulou (2016) used the more common 12 mm long 39μm diameter PVA. The ECC mix (SHCC for Strain Hardening Cementitious Composite) and a complementary mix that lacks any fibers (HVFA for High Volume Fly Ash) are shown in Table 6.2. Material testing of both materials was extensive with direct tension, uniaxial compression, split cylinder, four-point bending, and push off tests being performed. The inclusion of fibres was shown to provided additional ductility across tension, compression, split cylinder and four bending tests by bridging cracks as they form and allowing for the formation of multiple cracks. The push off tests demonstrated that even SHCC without reinforcement could greatly improve shear deformation.

Table 6.2 Mix designs based on weight ratios from Georgiou & Pantazopoulou (2016).

Mix	Cement	Fly Ash	Sand	Water	Super plasticizer	Fiber (% Volume)
SHCC	1.00	1.20	0.80	0.60	0.017	2
HVFA	1.00	1.20	0.80	0.55	0.012	NA

Building on this work Eshghi (2019) sought to create an improved ECC with strain hardening properties using materials local to Ontario, Canada. Selection of an appropriate ECC mix was done by examining eight variables in materials used across 39 different batches. The effective variables looked at types of cement, type of sand, combination of different sands, percentage/presence of slag and silica fume, deduction of silica fume and slag from cement or fly ash, coated or uncoated fiber, amount/presence of defoamer, and types of superplasticizers. The addition of slag and silica fume was done to replicate the presence of these two waste by-product materials in the Portland Composite Cement En 197-1 Cem Ii / A-M (L-S) 42.5 R used by

Georgiou & Pantazopoulou (2016). Preliminary testing of the 39 batches revealed that the best results were obtained using #730 Bell & McKenzie sand which had a maximum grain size of 300μm in line with the grain size of sand used by Georgiou & Pantazopoulou (2016). It was also noted that one specific batch using #730 McKenzie sand was able to achieve fibre pull-out, and strain hardening behavior, without the use of any coating agents. It is common practice to use coating agents to tailor the bond between fibers and the concrete matrix, however the process of coating fibers is an additional complication in the production of ECC. For this reason, Eshghi (2019) decided on using the mix that did not require any coating and scaled the design up to a 40-litre batch as shown in Table 6.3 that was batched five times. The mix design was converted into ratios of weight as done in previous work, shown in Table 6.4, to allow for easier comparison. General use Portland-limestone (GUL) cement was used along with MasterGlenium® 7700 acting as the superplasticizer. The additional pozzolans consisted of Type F fly ash, Ground Granulated Blast Furnace slag, and SF 100 Densified Silica Fume. The PVA fiber used was Kuralon K-II RECS100 × 12 which had a length of 12 mm, diameter of 0.1 mm, density of 1100 kg/m^3, tensile strength of 1200 MPa, and modulus of 28 GPa.

Table 6.3 Mix design from Eshghi (2019).

Cement (kg)	Fly Ash (kg)	Silica Fume (kg)	Slag (kg)	Sand (kg)	Water (kg)	Super Plasticizer (kg)	Fiber (kg)	Total Volume (L)
16	26.7	4.4	1.8	17.8	12.44	0.4	1	40

Table 6.4 Mix design based on weight ratios from Eshghi (2019).

Cement	Fly Ash	Silica Fume	Slag	Sand	Water	Super Plasticizer	Fiber (% Volume)
1	1.67	0.28	0.11	1.11	0.78	0.025	2

The mixing procedure which Eshghi (2019) employed is as follows:

1. All dry ingredients were mixed together for **1-2 minutes**.

2. The super plasticizer was added to half the water before slowly being added to the mixer over **2-3 minutes** until the mixture showed no visible clumping.
3. Fibers were then added while the mixer was running for another **5-10 minutes**.
4. The remaining half of the water was added slowly until all fibers were evenly distributed at which point it was considered ready to cast.

Soto-Rojas (2020) utilized the work of Eshghi (2019) for the ECC used in the repair of slender shear walls. To improve the workability of the mix Soto-Rojas settled on replacing half the PVA specified in Eshghi's (2019) design, by weight, with the smaller diameter Kuralon K-II REC15 x 12 PVA fibre which maintained a length of 12mm but had a reduced diameter of 0.04 mm, and tensile strength of 1560 MPa. Additionally, Soto-Rojas (2020) replaced the MasterGlenium® 3400 with MasterGlenium® 7700 since it had demonstrated higher workability in previous trails. The remainder of the constituents were kept consistent with what was used by Eshghi (2019). A small scale 2 litre mix, shown in Table 6.5 and converted to a weight ratio in Table 6.6, was cast as a trail mix and demonstrated acceptable flowability.

Table 6.5 Small scale mix design from M. A. Soto-Rojas (2020).

PVA Fibres (kg)		**Cement (kg)**	**Fly Ash (kg)**	**Silica Fume (kg)**	**Slag (kg)**	**Sand (kg)**	**Water (kg)**	**Super Plasticizer (kg)**	**Volume (L)**
∅=0.1 mm	**∅=0.04 mm**								
0.025	0.025	0.8	1.33	0.22	0.09	0.89	0.622	0.02	2

∅ = fibre diameter

Table 6.6 Small scale mix design based on weight ratios from M. A. Soto-Rojas (2020).

PVA Fibres (% Volume)		**Cement**	**Fly Ash**	**Silica Fume**	**Slag**	**Sand**	**Water**	**Super Plasticizer**
∅=0.1 mm	**∅=0.04 mm**							
1.0	1.0	1	1.66	0.28	0.11	1.11	0.78	0.025

∅ = fibre diameter

The trail mix was also compared to a commercially available steel fibre-reinforced concrete ready mix that was modified by Soto-Rojas (2020); replacing the steel fibres with the Kuralon K-

II RECS100 × 12 PVA fibres. The modified ready mix had a significantly higher 28 days compressive strength of 102.59 MPa compared to the ECC mix which reached 57.38 MPa. The flexural response of the two mixes under four point-bending, Figure 6.1, also differed greatly with the modified ready mix, Modified-Com K, demonstrating a peak load followed by a significant drop corresponding to the formation of a single dominate crack which propagated the height of the prism. The ECC (in-house) mix instead demonstrated a ductile strain-hardening behaviour due to the formation of microcracking before localization of a single crack led to failure.

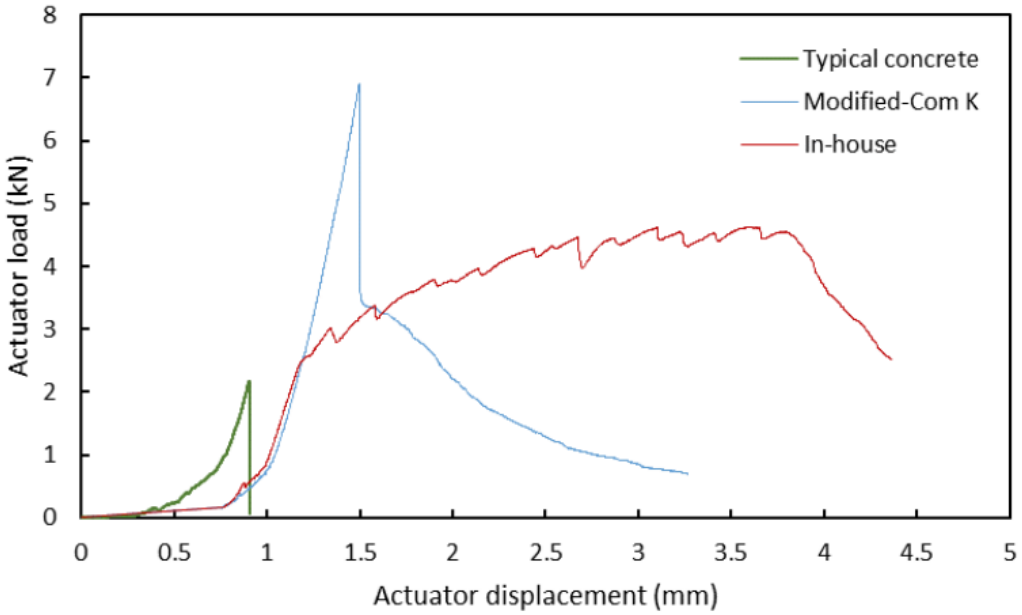

Figure 6.1 Load-displacement response of different concrete mixes (M. A. Soto-Rojas, 2020).

Successfully demonstrating strain-hardening behaviour and flowability inline with a self consolidating concrete Soto-Rojas (2020) scaled his mix up to 75 litre batches for repairs of the shear wall. The mixing procedure used by Soto-Rojas was as follows:

1. All dry ingredients were mixed together for **5 minutes**.
2. Half the super plasticizer was added to half the water before slowly being added to the mixer over **2-3 minutes** until the mixture showed no visible clumping.
3. Fibers were then added while the mixer was running for another **5-10 minutes**.
4. The remaining half of the water and super plasticizer were combined and added slowly until all fibers were evenly distributed at which point it was considered ready to cast.

The main two modifications made were the increase in the initial mixing time of the dry ingredients as well as splitting the super plasticizer equally between the two halves of water.

6.2 Recreating Soto-Rojas' ECC

The results of Chapter 4 and 5 demonstrated that additional material testing of ECC would be beneficial to corroborate and expand on the material properties which were derived in Chapter 3. Casting of tensile coupon specimens in particular could provide additional information and guidance into the tensile response of the ECC created and used by Soto-Rojas (2020). This prompted efforts into recreating the ECC mix. Testing started with small scale batches to ensure that appropriate compressive strength and strain hardening of the material could be achieved before committing to large scale mixes. The first attempt was a 13.24 litre mix, which was sized to allow for casting of six 75 mm x 150 mm compression cylinders, three 75 mm x 75 mm x 280 mm flexural prisms, and a 75 mm x 75 mm x 500 mm flexural prism as well as 15% extra material for a factor of safety. The material proportions were scaled from the 2 L mix outlined by Soto-Rojas (2020) and the materials were sourced from surplus leftover from Soto-Rojas' work except for the cement which was replaced for newer GUL. Mixing was done in an industrial stand mixer with a capacity of roughly 30 litres and used the same mixing procedure as Soto-Rojas (2020).

Table 6.7 Trial 1 mix design.

PVA Fibres (kg)		**Cement (kg)**	**Fly Ash (kg)**	**Silica Fume (kg)**	**Slag (kg)**	**Sand (kg)**	**Water (kg)**	**Superplasticizer (kg)**	**Volume (L)**
∅=0.1 mm	∅=0.04 mm								
0.116	0.116	5.3	8.8	1.456	0.596	5.89	4.2	0.132	13.24

∅ = fibre diameter

While the industrial mixer was able to handle all the dry ingredients, once the first half of the water and super plasticizer was added the mixture became too difficult to handle and strained the motor causing the fuse to trip and the mixer to be reset. The process of resetting the fuse increased the time that the mix had started to hydrate and would affect the flowability of the mix so a flow test was omitted. To ensure that the mixer would not overwork itself a portion of the

second half of the water and super plasticizer was added prior to adding fibres to liquify the mixture further. Once all the fibres were incorporated the remaining water and super plasticizer was added although there seemed to be slight bleeding of water when mixing was stopped. To help combat this bleeding the mixture was allowed to run for additional time until bleeding seemed to be reduced. Cylinders and prims were cast with the cylinders being placed on a vibration table shortly to remove voids. All specimens were demolded the following day and placed in water to cure for 28-days before being removed and tested. All cylinders were tested according to ASTM C39 (2016) at a constant stress rate of 0.265 MPa/sec in a Pilot Controls compression testing machine. The stated diameter and height of each cylinder was taken as an average of four measurements. The average compressive strength of the cylinders at 28 days was 30.93 MPa which is significantly lower (35.0%) than the 47.57 MPa average compressive strength achieved by Soto-Rojas (2020) at 28-days.

To address the issues around the ECC mix being too large for the industrial stand mixer, which lead to a fuse being tripped and complications to the mixing times, a new batch size of 10 litres was used for the second trial. This amount of ECC was enough for casting of six 75 mm x 150 mm compression cylinders, two 75 mm x 75 mm x 280 mm flexural prisms, and a 75 mm x 75 mm x 500 mm flexural prism. The mix design for the trial can be found in Table 6.8. When the first half of the water and superplasticiser was added into the mix, roughly two-thirds of this water was added in the first minute with the remainder of being added after 2.5 minutes had elapsed instead of adding it evenly over the full 5 minutes as done by Soto-Rojas (2020) and Eshghi (2019). This was found to avoid tripping a fuse. After all fibres had been incorporated and the final half of the water was added the mix was still too stiff for an ECC and required an additional 0.3 kg of water was required to achieve a flowable state during the slump test. The 28-day compressive strength of the mix averages 25.92 MPa, 45.5% the strength recorded by Soto-Rojas (2020).

Table 6.8 Trial 2 mix design.

PVA Fibres (kg)		Cement (kg)	Fly Ash (kg)	Silica Fume (kg)	Slag (kg)	Sand (kg)	Water (kg)	Superplasticizer (kg)	Volume (L)
∅=0.1 mm	∅=0.04 mm								
0.125	0.125	4	6.65	1.1	0.450	4.45	3.11	0.1	10

∅ = fibre diameter

Table 6.9 28-day compressive strength of trial 2 mix.

ID	Cylinder Size (diameter x height)	f_c (MPa)	f_c Average (Standard Deviation) (MPa)
2.1	76.82 x 147.65	24.92	25.92 (0.74)
2.2	76.56 x 147.80	29.15	
2.3	76.72 x 148.30	28.27	
2.4	77.32 x 149.48	35.56	
2.5	76.70 x 147.63	36.30	
2.6	76.84 x 149.20	40.29	

Noticing the variability in the flowability between the first two trials, an additional three batches were conducted using the same mix as Table 6.8. The super plasticizer had been shaken in its container by hand to that point but wanting to ensure there had been no separation of its chemical compounds the super plasticizer was then mixed with an electric drill utilizing a mixing attachment. Additionally, the mixing procedure was modified to ensure proper mixing of constituents. At all steps the mixer was paused at half the mixing time to allow for the sides of the mixing bowl and mixing paddle to be scrapped of any dry constituents. The bowl and paddle where

also scrapped between steps. The three batches were mixed on the same day and used the identifiers AM, PM, and B3.

During mixing of the AM batch, the industrial stand mixer was overworked partway through the mixing of the fibres and resulted in a fuse being tripped again. Similar to the first trial part of the remaining water and super plasticizer were added prematurely to allow for mixing to continue. The ECC seemed to be more flowable than previous batches during the second addition of water, suggesting that the improved mixing of super plasticizer had some impact, and 112 g of water/super plasticizer mixture was not added to avoid excessive water bleeding as seen in trail 1.

The fact that the mixer's fuse was tripped and that not all of the second addition of water/super plasticizer mixture was needed in the last step prompted the decision to add all the super plasticizer to the first half measure of water. This would ideally reduce the likelihood of the fuse being tripped again as well as allow for easier modification of the ECC's flowability during the last step. These changes resulted in the next two mixes being completed without overworking the mixer. Looking to understand the early age strength of the ECC batches, a cylinder from each batch was tested at 7 days after curing, Table 6.10, with results being indicative that all three batches would not attain compression strengths comparable to those of Soto-Rojas. The compressive strength of PM could not be determined as the cylinder was not able to support a sustained force applied by the Pilot Compression machine. The compressive strength of each batch is shown in Table 6.11 with the highest average strength being 22.45 MPa achieved by batch AM followed by B3 and PM reflecting the same pattern seen in the 7-day tests. Only 3 cylinders from each batch were tested at 28-days since the results were consistent but far below the target. Batches prior to AM, PM, and B3 had felt lighter than expected for a material that should have a density of 1900 kg/m^3, based on reports from Soto-Rojas (2020). All cylinders used in the 28-day testing were weighed before testing to investigate if the ECC batches made for this work were a lower-than-expected density. The average densities for batches AM, PM, and B3 were all well below the 1900 kg/m^3 target only having densities of 1405 kg/m^3, 1586 kg/m^3, and 1518 kg/m^3 respectively.

Table 6.10 7-day compressive strength of trials AM, PM, and B3.

ID	Cylinder Size (diameter x height)	f'_c (MPa)
AM	76.84 x 144.40	16.76
PM	77.28 x 145.94	NA
B3	76.69 x 145.31	6.49

Table 6.11 28-day compressive strength of trials AM, PM, and B3.

ID	Cylinder Size (diameter x height)	f_c (MPa)	f_c Average (MPa)
AM1	76.66 x 149.47	22.36	22.45
AM2	76.73 x 145.78	22.17	
AM3	76.78 x 148.35	22.83	
PM1	76.51 x 145.17	6.65	6.95
PM2	76.65 x 144.62	6.87	
PM3	76.75 x 144.22	7.33	
B3.1	76.96 x 150.22	11.72	11.09
B3.2	76.86 x 150.55	10.86	
B3.3	77.45 x 149.71	10.70	

The continued reduction in strength of the new mixes compared to Soto-Rojas and the inconsistency in flowability raised question on the integrity of the super plasticizer used as it had been over two years since its original procurement. New MasterGlenium® 3400 was procured from BASF as well as new silica fume since it is also produced by BASF and the surplus available in the lab was running low. The new superplasticizer and silica fume were used in another round of batches. These newer batches would not include fibres, making them a mortar, in order to avoid wasting PVA fibres which are imported from Japan. Additionally, there should not be a noticeable

impact on testing since it had previously been shown that the fibres in ECC do not contribute significantly to the compressive strength of the material (Georgiou & Pantazopoulou, 2016). The three batches of the ECC mortar would also examine how replacing a portion of fly ash with an equal mass of cement would affect the 28-day age of the concrete. This was done as the Eshghi (2019) and Soto-Rojas (2020) mixes had a higher than typical weight ratio of fly ash: 1.66 to 1.2 found in mixes by Lepech & Li (2008) and Georgiou & Pantazopoulou (2016). The first batch, referred to as M0, used the original proportions of all constituents while the remaining two batches, M10 and M20, were modified to use 10% and 20% less fly ash than M0 which was replaced with an equal mass of cement. Mixes M0, M10, and M20 are found in Table 6.12, Table 6.13, and Table 6.14 and each had a volume of 4 litres allowing for the casting of six 75 mm x 150 mm cylinders. The cylinders from each batch were split in sets of 3 which were tested in compression in at 7 and 28 days after casting.

Table 6.12 Mix design for batch M0.

Cement (g)	Fly Ash (g)	Silica Fume (g)	Slag (g)	Sand (g)	Water (g)	Superplasticizer (g)	Volume (L)
1600	2660	440	180	1880	1244	40	4

Table 6.13 Mix design for batch M10.

Cement (g)	Fly Ash (g)	Silica Fume (g)	Slag (g)	Sand (g)	Water (g)	Superplasticizer (g)	Volume (L)
1866	2394	440	180	1880	1244	40	4

Table 6.14 Mix design for batch M20.

Cement (g)	Fly Ash (g)	Silica Fume (g)	Slag (g)	Sand (g)	Water (g)	Superplasticizer (g)	Volume (L)
2128	2132	440	180	1880	1244	40	4

The compressive strengths at 7 days and 28 days after casting are shown in Table 6.15, Table 6.16, and Table 6.17 and demonstrate that the replacement of fly ash for an equal mass of cement provided significant strength increases with just a change in 10% reduction in fly ash causing an increase of 32.4% and 35.6% increase in the 7-day and 28-day compressive strength results. A 20% reduction in fly ash results in a strength increase of 84.6% and 62.6% at 7 and 28 days respectively when compared to the original mix. The densities of the cylinder were once again taken before testing and the average for M0, M10, and M20 were 2039 kg/m^3, 2082 kg/m^3, and 2111 kg/m^3 respectively which is more inline with the expected density of 1900 kg/m^3. The fact that there is only a 3.5% increase in density between the M0 and M20 mix demonstrates that the density of fly ash used was not an issue. The density of fly ash had been a consideration for the decreased density of the cylinders since fly ash represents a significant portion of the mix's mass and is stated by Lafarge (2023) to have a density anywhere between 2000-2900 kg/m^3. It was thought perhaps the bags of fly ash used in this work happened to be on the lower range while fly ash used by Eshghi (2019) and/or Soto-Rojas (2020) skewed to the higher range.

Table 6.15 Compressive strength of batch M0.

Age (Days)	Cylinder Size (diameter x height)	f_c (MPa)	f_c Average (MPa)
7	76.65 x 131.15	24.92	27.45
7	76.50 x 130.33	29.15	
7	76.58 x 131.33	28.27	
28	76.51 x 125.62	35.56	37.39
28	76.65 x 129.59	36.30	
28	76.75 x 129.35	40.29	

Table 6.16 Compressive strength of batch M10.

Age (Days)	Cylinder Size (diameter x height)	f_c (MPa)	f_c Average (MPa)
7	76.25 x 122.05	37.23	36.35
7	76.55 x 121.78	34.55	
7	76.95 x 119.8	37.29	
28	76.58 x 121.73	52.60	50.70
28	76.58 x 119.72	52.49	
28	76.52 x 118.14	46.99	

Table 6.17 Compressive strength of batch M20.

Age (Days)	Cylinder Size (diameter x height)	f_c (MPa)	f_c Average (MPa)
7	76.82 x 113.60	51.02	50.68
7	76.43 x 114.75	50.62	
7	76.45 x 114.30	50.39	
28	76.44 x 113.95	55.82	60.81
28	76.48 x 113.39	66.71	
28	76.56 x 115.67	59.88	

6.3 Lessons Learned from Trial Mixes

The density calculations from AM, PM, and B3 mixes as well as those from the mortar mixes demonstrated that there was an underlying problem with the density of the trial mixes that was not present in work by Eshghi (2019) and Soto-Rojas (2020). For all ECC mixes it appeared that small perfectly spherical voids were present and visible in the side (Figure 6.2 a), b), and c)) and top

(Figure 6.3 a), b), and c)) profiles of cylinders and that these voids were distributed throughout the depth of the cylinders. Photos were taken of all concrete specimens tested in this chapter but for brevity those shown in this discussion were chosen to be representative of specimens from their mix. The mortar cylinders displayed a strange behaviour that can be linked to these voids. During removal of the cylinders from the molds, the day after casting, all mortar cylinders had developed two distinct sections, a top "puck" section (Figure 6.4) that cleanly detached from the bottom cylinders which were tested and presented in Section 6.2. The top "pucks" were found to float in water and had an approximate density of 632 kg/m^3. Further, the bottom sections of the mortar cylinders (Figure 6.2 d) and Figure 6.3 d)) did not have as many small voids present. The voids that were present did appear to increase towards the top of the mortar cylinder.

a) b) c) d)

Figure 6.2 Side profile of cylinders: a) Trail 1.1, b) Trial 2.1, c) AM.1, and d) M20.1.

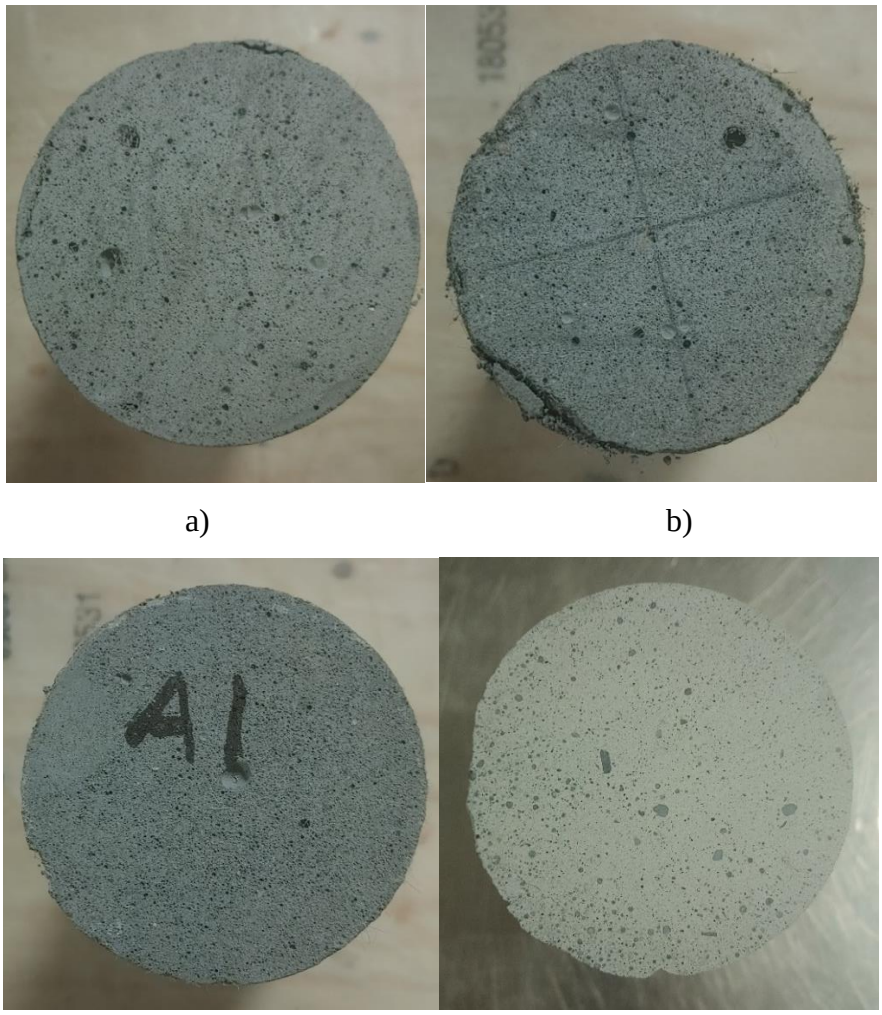

a) b)

c) d)

Figure 6.3 Top profile of cylinders: a) Trail 1.1, b) Trial 2.1, c) AM.1, and d) M20.1.

These observations suggests that the decreased density is being caused by the release of gases during the initial setting time of the ECC which was not present in previous work. These gases in the ECC mixes are likely suspended within the cylinder due to the influence of the PVA fibres but once these fibres are removed in the mortar mixes the gases can more freely ascend due to buoyancy and concentrate in the top portions of the mix, causing the formation of the low density "pucks". The density observed in the lower portion of the mortar cylinders align with the density previously stated by Soto-Rojas (2020). The increased porosity due to the voids may also be partially responsible for the lower strength of the ECC trial mixes. It can also be observed from the heights of cylinders in the M0, M10, and M20 mixes that increasing the amount of cement used also increased the size of the "pucks" and likely the amount of gas produced. The increased

amount of cement in M20 also resulted in cylinders being a lighter gray and revealed the presence of black specks, as seen in Figure 6.4. d) that are most likely from the fly ash and suggest possible impurities. These specks are larger than the maximum aggregate size of 0.3 mm which the ECC should have due to the sand being the largest grain size. The mechanism causing the gas formation as well as an investigation of possible impurities in the materials used are out of the scope of this work.

a) b) c)

Figure 6.4 Top "pucks" from cylinders: a) M0 mix, b) M10 mix, and c) M20 mix.

Flexural prims from the first two trial mixes were tested to investigate their ability to develop microcracking and strain-hardening behaviour. The underside of the tested 280 mm long (Figure 6.5) and 500 mm long (Figure 6.6) prisms are shown. It is seen that only Trial 1 presented multiple cracks before localization and propagation of a single predominate crack and even then, in the 250 mm long prims of Trial 1 the degree of cracking varies with SP1 have significant cracking, SP2 having ~4 cracks, and SP3 only having a single crack. Due to the inconsistent cracking behaviour, along with the low compressive strengths, all mixes after Trail 2 focused on reaching a compressive strength target based on Soto-Rojas (2020). The lack of multiple cracks in some specimens may have been caused by the porosity and density issues discussed for the cylinders but would require further investigation in future trials involving this particular ECC mix.

a) b)

c) d)

e) f)

Figure 6.5 Bottom face of 280 mm long flexural prisms: a) Trial 1.SP1, b) Trial 1.SP2, c) Trial 1.SP3, d) Trial 2.SP1, e) Trial 2.SP2, and f) Trial 2.SP3.

a)

b)

Figure 6.6 Bottom face of 500 mm long flexural prisms: a) Trial 1.LP1 and b) Trial 2.LP1.

7 Conclusions and Future Work

The work contained in this thesis sought to accurately model the repair of novel SMA-steel hybrid slender shear walls using Engineered Cementitious Composites (ECC) in VecTor2, a 2-D non-linear finite element analysis software. In undertaking this goal, it was necessary to perform experimental testing of ECC materials including flexural prisms and compression cylinders. The material properties and responses were able to provide insight into the applicability and accuracy of available built-in constitutive models of VecTor2 in modelling small scale flexural prisms. Lessons learned from the small-scale modelling were incorporated into modelling of slender shear walls with varied reinforcement, using traditional deformed rebar or a SMA-steel hybrid reinforcement layout, in both an original state with normal concrete and after repairs which made use of the ductility and self-consolidating properties of ECC. The created models were compared against experimental data from two previous theses. Looking to improve the material properties input into the models, replication of the ECC mixes used for testing was undertaken in the aim of providing additional tension data.

7.1 Conclusions

Considering the work that was completed the following conclusions were reached:

- The testing of surplus ECC cylinders and flexural prisms demonstrated the time dependent nature of the material's strength and ductility. Two variations of the mix used for these specimens had previously demonstrated strain hardening as evident in the response of flexural prims which had been observed to have micro-cracking before localization and propagation of a predominate crack at 28 days after testing. The surplus ECC flexural prisms, which were tested at 134 and 141 days, no longer demonstrated multiple cracks but were able to provide some tension softening effects while bridging the crack.
- Modelling ECC as a single compression element demonstrated some inconsistencies in the stress strain responses provided by VecTor2. The use of Hogenstad and Montoya 2003 compression post-peak constitutive models appeared to default to the Popovic/Mander model despite being different formulations. Additionally, the response of the Lee et al 2011 (FRC) is shown to provide different values if the model is only used for the pre-peak response as opposed to the full response.

- Modelling of ECC as a single tension element demonstrated that the VEM constitutional model for FRC tension cannot be used for ECC in its present state. Currently, the VEM model will treat any ECC defined with an aggregate size less than 2 mm as a mortar and apply a coefficient which results in a tensile response identical to unreinforced NC.
- Currently available FRC tension models, which were calibrated using steel fibre reinforced concrete, in VecTor2 were shown to be inaccurate at predicting the response of unreinforced ECC flexural prims. This inaccuracy was greatest when trying to capture the gradual decrease in load after the peak with all but one model predicting a sudden drop in load after the peak.
- Modelling predictions of RC and SMA-steel hybrid shear walls in VecTor2 were improved by implementing a combination of a non-default tension stiffening model, modified Bentz 2005 with local fracture, and the application of a reduction factor to steel reinforcement truss elements reflecting the impact of strain gauge instillation has on the cross-sectional area of rebar. The exact reduction factor, 3%, was calibrated by an iterative approach benchmarked against experimental data. This new methodology improved ductility predictions while not impacting peak strength predictions.
- Application of the modified Bentz 2005 with local fracture model to models of ECC repaired RC and SMA-steel hybrid shear walls must be done carefully as the cracking behavior of these structures can cause for an overcorrection in ultimate strain of reinforcement. For the structures repaired with ECC examined in this work, the default model ,modified Bentz 2005, was demonstrated to work best.
- Use of the Lee et al. 2011 (FRC) compression models were shown to greatly improve the ductility prediction of ECC shear walls modelled in this work. Conversely use of built in FRC tension models resulted in premature failure of walls due to increased stiffness and rupture of reinforcement.
- Defining an ECC material's tension softening response using a custom input in VecTor2 is not a valid approach in models that also contain NC elements based on current limitations. This is notable since all literature, to the author's knowledge, that use VecTor2 to model ECC structures only consist of ECC elements without any NC and make use of the custom input for tension softening.

- Current SMA bond models in VecTor2 have been shown to overestimate the initial stiffness of shear walls which use the novel materials. This does not affect the peak load prediction capabilities but does present room for improvement, especially at lower displacements.

7.2 Future Work

SE-SMAs and ECC are both relatively novel materials in the scope of RC structures which require experimental and numerical testing to gain confidence for use at a commercial scale. Though the literature on these materials separately has been increasing, their combined use in seismic force resisting structures is still limited. Taking this and the aforementioned conclusions into account there are multiple avenues which the work in this thesis can be expanded on in the future:

- Conduct further testing into the repeatability of the ECC mix design outlined in this work to determine the cause of significant gas production during curing. This testing should also look into the inclusion of additional admixtures that can prolong the setting time which is necessary when account for transit time required when batching and mixing in concrete trucks.
- Conducting experimental testing of ECC over larger time periods to better understand the time-dependent nature of the tension stiffening response.
- Investigate how specific constitutive models, such as Hogenstad and Montoya 2003 compression post-peak, are implemented within VecTor2 to ensure that there are no errors in the formulation. This is important since it has been shown by Zhang (2020) that it is possible for variables to be incorrectly attributed resulting in deviations from the intended theoretical values.
- Modify current built-in FRC tension models in VecTor2 so that coefficients applied based on polymer fiber type and aggregate size are reflective of ECC materials. This would require corroboration against direct tension tests available in literature to capture the use of different fibers and mix designs.
- Investigate constitutive models for ECC in compression and tension that have been proposed in reviewed literature and assess their applicability within VecTor2.
- Attempt to implement a method in VecTor2 that allows for the application of custom tension softening responses to specific reinforced concrete elements instead of being

applied to every element. This would allow for greater flexibility in the modelling of materials with different tension responses, something that may become pertinent as more structures are repaired/retrofitted with FRCs and ECCs.

- Extend the methodology of applying an area reduction factor to reinforcement trusses in modelling of other shear walls found in literature. This could provide additional baselines for what is an appropriate range for the percent reduction applied.

References

Abdulridha, A., & Palermo, D. (2017). Behaviour and modelling of hybrid SMA-steel reinforced concrete slender shear wall. *Engineering Structures*, *147*. https://doi.org/10.1016/j.engstruct.2017.04.058

Abdulridha, A., Palermo, D., & Foo, S. (2011). Superelastic sma reinforced concrete elements: Applicability and practicality. *Fib Symposium PRAGUE 2011: Concrete Engineering for Excellence and Efficiency, Proceedings*, *1*.

Abraik, E. (2020). Seismic performance of shape memory alloy reinforced concrete moment frames under sequential seismic hazard. In *Structures* (Vol. 26). https://doi.org/10.1016/j.istruc.2020.04.025

Abraik, E., El-Fitiany, S. F., & Youssef, M. A. (2020). Seismic performance of concrete core walls reinforced with shape memory alloy bars. *Structures*, *27*. https://doi.org/10.1016/j.istruc.2020.07.053

Alam, M. S., Moni, M., & Tesfamariam, S. (2012). Seismic overstrength and ductility of concrete buildings reinforced with superelastic shape memory alloy rebar. *Engineering Structures*, *34*. https://doi.org/10.1016/j.engstruct.2011.08.030

Almeida, J. P. de, Steinmetz, M., Rigot, F., & de Cock, S. (2020). Shape-memory NiTi alloy rebars in flexural-controlled large-scale reinforced concrete walls: Experimental investigation on self-centring and damage limitation. *Engineering Structures*, *220*. https://doi.org/10.1016/j.engstruct.2020.110865

ASTM. (2021). ASTM E8/E8M standard test methods for tension testing of metallic materials. *Annual Book of ASTM Standards*, *C*.

ASTM C39. (2016). ASTM Standard C39/C39M-16, Standard Test Method for Compressive Strength of Cylindrical Concrete Specimens. In *ASTM International*.

ASTM International. (2017). ASTM C1856/C1856M-17 - Standard Practice for Fabricating and Testing Specimens of Ultra-High Performance Concrete. *ASTM International*, *04.02*.

ATC. (1992). Guidelines for cyclic seismic testing of components of steel structures. In *ATC-24*.

Billah, A. H. M. M., & Alam, M. S. (2018). Probabilistic seismic risk assessment of concrete bridge piers reinforced with different types of shape memory alloys. *Engineering Structures*, *162*. https://doi.org/10.1016/j.engstruct.2018.02.034

Cheng, Z., Hu, Y., Chu, L., Yuan, C., & Feng, H. (2021). Peridynamic modeling of engineered cementitious composite with fiber effects. *Engineering Fracture Mechanics*, *245*. https://doi.org/10.1016/j.engfracmech.2021.107601

Cortés-Puentes, L., Zaidi, M., Palermo, D., & Dragomirescu, E. (2018). Cyclic loading testing of repaired SMA and steel reinforced concrete shear walls. *Engineering Structures*, *168*. https://doi.org/10.1016/j.engstruct.2018.04.044

Cortés-Puentes, W. L., & Palermo, D. (2017). SMA tension brace for retrofitting concrete shear walls. *Engineering Structures*, *140*. https://doi.org/10.1016/j.engstruct.2017.02.045

Cortés-Puentes, W. L., & Palermo, D. (2018). Seismic Retrofit of Concrete Shear Walls with SMA Tension Braces. *Journal of Structural Engineering*, *144*(2). https://doi.org/10.1061/(asce)st.1943-541x.0001936

Cruz Noguez, C. A., & Saiidi, M. S. (2012). Shake-Table Studies of a Four-Span Bridge Model with Advanced Materials. *Journal of Structural Engineering*, *138*(2). https://doi.org/10.1061/(asce)st.1943-541x.0000457

Deng, M., Pan, J., & Sun, H. (2018). Bond behavior of steel bar embedded in Engineered Cementitious Composites under pullout load. *Construction and Building Materials*, *168*. https://doi.org/10.1016/j.conbuildmat.2018.02.165

Deng, M., Pan, J., & Sun, H. (2019). Bond behavior of deformed bar embedded in Engineered Cementitious Composites under cyclic loading. *Construction and Building Materials*, *197*. https://doi.org/10.1016/j.conbuildmat.2018.11.200

Dhakal, R. P., & Maekawa, K. (2002). Path-dependent cyclic stress-strain relationship of reinforcing bar including buckling. *Engineering Structures*, *24*(11). https://doi.org/10.1016/S0141-0296(02)00080-9

Ding, Y., Yu, K., & Mao, W. (2020). Compressive performance of all-grade engineered cementitious composites: Experiment and theoretical model. *Construction and Building Materials*, *244*. https://doi.org/10.1016/j.conbuildmat.2020.118357

Eshghi, N. (2019). *Behaviour and Analysis of Strain Hardening Fiber Reinforced Cementitious Composites Under Shear and Flexure* [Masters]. York University.

Fan, J. S., Zhang, Z. Y., Ding, R., Nie, X., & Liu, C. (2021). Numerical simulation of shear-critical engineered cementitious composites structural members using a new two-dimensional fixed crack constitutive model. *Engineering Structures*, *240*. https://doi.org/10.1016/j.engstruct.2021.112375

(FEMA), F. E. M. A. (2007). Interim Protocols For Determining Seismic Performance Characteristics of Structural and Nonstructural Components Through Laboratory Testing. In *FEMA 461* (Issue June).

Franssen, R., Guner, S., Courard, L., & Mihaylov, B. I. (2021). Numerical modeling approach for uhpfrc members including crack spacing formulations. *Engineering Structures*, *238*. https://doi.org/10.1016/j.engstruct.2021.112179

Gencturk, B., & Elnashai, A. S. (2013). Numerical modeling and analysis of ECC structures. *Materials and Structures/Materiaux et Constructions*, *46*(4). https://doi.org/10.1617/s11527-012-9924-0

Georgiou, A., & Pantazopoulou, S. (2016, March). *Use of Waste Fly Ash from Power Plants for Use in Cementitious Composites for Structural Elements*.

Han, T. S., Feenstra, P. H., & Billington, S. L. (2003). Simulation of Highly Ductile Fiber-Reinforced Cement-Based Composite Components Under Cyclic Loading. *ACI Structural Journal*, *100*(6). https://doi.org/10.14359/12841

Herrezeel, T., & Rigot, F. (2019). *Dimensionnement parasismique et performance de voiles en béton armé contenant des armatures en alliage à mémoire de forme* [Masters]. Ecole polytechnique de Louvain.

Hosseini, F., Gencturk, B., Jain, A., & Shahzada, K. (2019). Optimal design of bridge columns constructed with engineered cementitious composites and Cu-Al-Mn superelastic alloys. *Engineering Structures*, *198*. https://doi.org/10.1016/j.engstruct.2019.109531

Hoult, R. D., & de Almeida, J. P. (2022). Residual displacements of reinforced concrete walls detailed with conventional steel and shape memory alloy rebars. *Engineering Structures*, *256*. https://doi.org/10.1016/j.engstruct.2022.114002

Hoult, R., & de Almeida, J. P. (2022). From experimental strain and crack distributions to plastic hinge lengths of RC walls with SMA rebars. *Engineering Structures*, *268*, 114731. https://doi.org/10.1016/j.engstruct.2022.114731

Htut T.N.S., & Foster, S. J. (2010). Unified model for mixed mode fracture of steel fibre reinforced concrete. *Fracture Mechanics of Concrete and Concrete Structures*, 1469–1477.

Hung, C. C., & Li, S. H. (2013). Three-dimensional model for analysis of high performance fiber reinforced cement-based composites. *Composites Part B: Engineering*, *45*(1). https://doi.org/10.1016/j.compositesb.2012.08.004

Kang, L., Qian, H., Guo, Y., Li, Z., Zhang, S., & Song, G. (2021). Seismic performance of SMA/ECC concrete shear wall with self-centering and self-repairing. *Earth and Space 2021: Materials, Structures, Dynamics, and Control in Extreme Environments - Selected Papers from the 17th Biennial International Conference on Engineering, Science, Construction, and Operations in Challenging Environments*. https://doi.org/10.1061/9780784483381.030

Khan, M. K. I., Lee, C. K., & Zhang, Y. X. (2020). Numerical modelling of engineered cementitious composites-concrete encased steel composite columns. *Journal of Constructional Steel Research*, *170*. https://doi.org/10.1016/j.jcsr.2020.106082

Lafarge. (2023). *Fly Ash and Bottom Ash Safety Data Sheet*.

Lee, S. C., Cho, J. Y., & Vecchio, F. J. (2011a). Diverse embedment model for steel fiber-reinforced concrete in tension: Model development. *ACI Materials Journal*, *108*(5). https://doi.org/10.14359/51683261

Lee, S. C., Cho, J. Y., & Vecchio, F. J. (2011b). Diverse embedment model for steel fiber-reinforced concrete in tension: Model verification. *ACI Materials Journal*, *108*(5).

Lee, S. C., Cho, J. Y., & Vecchio, F. J. (2013). Simplified diverse embedment model for steel fiber-reinforced concrete elements in tension. *ACI Materials Journal*, *110*(4). https://doi.org/10.14359/51685787

Lepech, M. D., & Li, V. C. (2008). Large-scale processing of engineered cementitious composites. *ACI Materials Journal*, *105*(4). https://doi.org/10.14359/19897

Li, L., Cai, Z., Yu, K., Zhang, Y. X., & Ding, Y. (2019). Performance-based design of all-grade strain hardening cementitious composites with compressive strengths from 40 MPa to 120 MPa. *Cement and Concrete Composites*, *97*. https://doi.org/10.1016/j.cemconcomp.2019.01.001

Li, X., Zhou, X., Tian, Y., & Li, M. (2019). A modified cyclic constitutive model for engineered cementitious composites. *Engineering Structures*, *179*. https://doi.org/10.1016/j.engstruct.2018.09.030

Maciel, M., Cortes-Puentes, W. L., & Palermo, D. (2019). Seismic performance analysis of high-rise RC shear walls reinforced with superelastic shape memory alloys. *Proceedings, Annual Conference - Canadian Society for Civil Engineering*, *2019-June*.

Mas, B., Cladera, A., & Ribas, C. (2016). Experimental study on concrete beams reinforced with pseudoelastic Ni-Ti continuous rectangular spiral reinforcement failing in shear. *Engineering Structures*, *127*. https://doi.org/10.1016/j.engstruct.2016.09.022

Meng, D., Huang, T., Zhang, Y. X., & Lee, C. K. (2017). Mechanical behaviour of a polyvinyl alcohol fibre reinforced engineered cementitious composite (PVA-ECC) using local ingredients. *Construction and Building Materials*, *141*. https://doi.org/10.1016/j.conbuildmat.2017.02.158

Meng, D., Lee, C. K., & Zhang, Y. X. (2017). Flexural and shear behaviours of plain and reinforced polyvinyl alcohol-engineered cementitious composite beams. *Engineering Structures*, *151*. https://doi.org/10.1016/j.engstruct.2017.08.036

Morcos, M. (2021). *Seismic Behaviour of SMA-Reinforced Slender Concrete Shear Walls* [Masters]. York University.

Morcos, M., & Palermo, D. (2018). Numerical modelling of slender superelastic-shape memory alloy reinforced concrete shear walls. *6th International Structural Specialty Conference 2018, Held as Part of the Canadian Society for Civil Engineering Annual Conference 2018*, 528–538.

Morcos, M., & Palermo, D. (2019). SMA-Reinforced Concrete Shear Walls Subjected to Reverse Cyclic Loading. *SMAR 2019 - Fifth Conference on Smart Monitoring, Assesment and Rehabilitation of Civil Structures*, 1–8. https://www.smar2019.org/

Muntasir Billah, A. H. M., & Shahria Alam, M. (2012). Seismic performance of concrete columns reinforced with hybrid shape memory alloy (SMA) and fiber reinforced polymer (FRP) bars. *Construction and Building Materials*, *28*(1). https://doi.org/10.1016/j.conbuildmat.2011.10.020

Naaman, A. E. (2018). *Fiber reinforced concrete: five decades of progress*. https://doi.org/10.21452/bccm4.2018.02.01

Nehdi, M., Alam, M. S., & Youssef, M. A. (2010). Development of corrosion-free concrete beam-column joint with adequate seismic energy dissipation. *Engineering Structures*, *32*(9). https://doi.org/10.1016/j.engstruct.2010.04.020

Nelson, R. B. (2007). *Experimental evaluation of performance of conventional bridge systems* [Masters]. University of Nevada.

Oudah, F. (2014). *Development of self-centering concrete beam-column connections reinforced using shape memory alloys*. University of Calgary.

Oudah, F., & El-Hacha, R. (2017). Joint performance in concrete beam-column connections reinforced using SMA smart material. *Engineering Structures*, *151*. https://doi.org/10.1016/j.engstruct.2017.08.054

Palermo, D., & Vecchio, F. J. (2007). Simulation of Cyclically Loaded Concrete Structures Based on the Finite-Element Method. *Journal of Structural Engineering*, *133*(5). https://doi.org/10.1061/(asce)0733-9445(2007)133:5(728)

Pan, Z., Zhu, Y., Qiao, Z., & Meng, S. (2020). Seismic behavior of composite columns with steel reinforced ECC permanent formwork and infilled concrete. *Engineering Structures*, *212*. https://doi.org/10.1016/j.engstruct.2020.110541

Park, R. (1989). Evaluation of ductility of structures and structural assemblages from laboratory testing. *Bulletin of the New Zealand Society for Earthquake Engineering*, *22*(3). https://doi.org/10.5459/bnzsee.22.3.155-166

Pereiro-Barceló, J., Bonet, J. L., Gómez-Portillo, S., & Castro-Bugallo, C. (2018). Ductility of high-performance concrete and very-high-performance concrete elements with Ni-Ti reinforcements. *Construction and Building Materials*, *175*. https://doi.org/10.1016/j.conbuildmat.2018.04.172

Saikali, E. R. (2019). *Bond Behaviour of Steel Reinforcing Bars Embedded in Ultra-High-Performance Steel Fiber Reinforced Concrete* [Masters]. York University.

Shahverdi, M., Czaderski, C., Annen, P., & Motavalli, M. (2016). Strengthening of RC beams by iron-based shape memory alloy bars embedded in a shotcrete layer. *Engineering Structures*, *117*. https://doi.org/10.1016/j.engstruct.2016.03.023

Shrestha, K. C., Saiidi, M. S., & Cruz, C. A. (2015). Advanced materials for control of post-earthquake damage in bridges. *Smart Materials and Structures*, *24*(2). https://doi.org/10.1088/0964-1726/24/2/025035

Siddiquee, K. N., Billah, A. M., & Issa, A. (2021). Seismic collapse safety and response modification factor of concrete frame buildings reinforced with superelastic shape memory alloy (SMA) rebar. *Journal of Building Engineering*, *42*. https://doi.org/10.1016/j.jobe.2021.102468

Song, G., Ma, N., & Li, H. N. (2006). Applications of shape memory alloys in civil structures. *Engineering Structures*, *28*(9). https://doi.org/10.1016/j.engstruct.2005.12.010

Soto-Rojas, M. A. (2020). *Behavior of Engineered Cementitious Composite-Repaired Superelastic-Shape Memory Alloy Reinforced Shear Walls* [Masters]. York University.

Soto-Rojas, M., & Palermo, D. (2020a, March). *MODELLING OF ENGINEERED CEMENTITIOUS COMPOSITE- REPAIRED SUPERELASTIC-SHAPE MEMORY ALLOY REINFORCED SHEAR WALLS*.

Soto-Rojas, M., & Palermo, D. (2020b, July). Modelling of Engineered Cementitious Composite-Repaired Superelastic-Shape Memory Alloy Reinforced Shear Walls. *The 17th World Conference on Earthquake Engineering*.

Tariq, H., Jampole, E. A., & Bandelt, M. J. (2019). Fiber-hinge modeling of engineered cementitious composite flexural members under large deformations. *Engineering Structures*, *182*. https://doi.org/10.1016/j.engstruct.2018.11.076

Tian, J., Wu, X., Zheng, Y., Hu, S., Du, Y., Wang, W., Sun, C., & Zhang, L. (2019). Investigation of interface shear properties and mechanical model between ECC and concrete. *Construction and Building Materials*, *223*. https://doi.org/10.1016/j.conbuildmat.2019.06.188

Tian, L. min, Kou, Y. feng, Lin, H. liang, & Li, T. ji. (2021). Interfacial bond–slip behavior between H-shaped steel and engineered cementitious composites (ECCs). *Engineering Structures*, *231*. https://doi.org/10.1016/j.engstruct.2020.111731

Tolou Kian, M. J., & Cruz-Noguez, C. A. (2020). Seismic design of three damage-resistant reinforced concrete shear walls detailed with self-centering reinforcement. *Engineering Structures*, *211*. https://doi.org/10.1016/j.engstruct.2020.110277

Tolou-Kian, M. J. (2020). *Reinforced Concrete Shear Walls with Improved Self-Centering and Damage Resistance Properties: Experimental Testing and Numerical Modeling* [PhD]. University of Alberta.

Tolou-Kian, M. J., & Cruz-Noguez, C. (2022). Performance design of reinforced concrete shear walls detailed with self-centering reinforcement. *Engineering Structures*, *252*. https://doi.org/10.1016/j.engstruct.2021.113533

Vecchio, F. J. (2000). Disturbed Stress Field Model for Reinforced Concrete: Formulation. *Journal of Structural Engineering*, *126*(9). https://doi.org/10.1061/(asce)0733-9445(2000)126:9(1070)

Vecchio, F. J., & Collins, M. P. (1986). MODIFIED COMPRESSION-FIELD THEORY FOR REINFORCED CONCRETE ELEMENTS SUBJECTED TO SHEAR. *Journal of the American Concrete Institute*, *83*(2). https://doi.org/10.14359/10416

VecTor Analysis Group. (2019). *Consulting Services*. VecTor Analysis Group.

Voo, J. Y. L., & Foster, S. (2003). Variable Engagement Model for the Design of Fibre Reinforced Concrete Structures. *Advanced Materials for Construction of Bridges, Buildings, and Other Structures III*.

Wong, P. S., Vecchio, F. J., & Trommels, H. (2002a). VecTor2 and FormWorks User's Manual. In *University of Toronto: Toronto, ON, Canada*.

Wong, P. S., Vecchio, F. J., & Trommels, H. (2002b). VecTor2 and FormWorks User's Manual. In *University of Toronto: Toronto, ON, Canada*.

Wyckmans, T., & Steinmetz, M. (2019). *Conception d'un dispositif expérimental pour des essais cycliques d'unités à grande échelle au LEMSC* [Masters]. Ecole polytechnique de Louvain.

Yan, S., Lin, M. Y., Xiao, Z. F., & Niu, J. (2018). Experimental research on resilient performances of Fe-based SMA-reinforced concrete shear walls. *IOP Conference Series: Earth and Environmental Science*, *189*(3). https://doi.org/10.1088/1755-1315/189/3/032028

Yang, Y., Pantazopoulou, S., & Palermo, D. (2020, August). *TENSILE BEHAVIOUR AND DURABILITY PERFORMANCE OF UHPFRC*.

Youssef, M. A., Alam, M. S., & Nehdi, M. (2008). Experimental investigation on the seismic behavior of beam-column joints reinforced with superelastic shape memory alloys. *Journal of Earthquake Engineering*, *12*(7). https://doi.org/10.1080/13632460802003082

Yuan, F., Chen, M., Zhou, F., & Yang, C. (2018). Behaviors of steel-reinforced ECC columns under eccentric compression. *Construction and Building Materials*, *185*. https://doi.org/10.1016/j.conbuildmat.2018.07.100

Zareie, S., Issa, A. S., Seethaler, R. J., & Zabihollah, A. (2020). Recent advances in the applications of shape memory alloys in civil infrastructures: A review. In *Structures* (Vol. 27). https://doi.org/10.1016/j.istruc.2020.05.058

Zhang, Z. (2020). *Finite Element Modelling of Ultra-High Performance Fibre Reinforced Concrete* [Masters]. University of Toronto.